Wireless Communication Networks Powered by Energy Harvesting

Wanchun Liu

September 2017

A thesis submitted for the degree of
Doctor of Philosophy of
The Australian National University

Research School of Engineering
College of Engineering and Computer Science
The Australian National University

To my family

Declaration

The contents of this thesis are the results of original research and have not been submitted for a higher degree to any other university or institution.

Much of the work in this thesis has been published or has been submitted for publication as book chapter or journal papers or conference papers.

The research work presented in this thesis has been performed jointly with Dr. Xiangyun Zhou (The Australian National University), Dr. Salman Durrani (The Australian National University), Prof. Kaibin Huang (The University of Hong Kong, Hong Kong), Prof. Petar Popovski (Aalborg University, Denmark), Prof. Steven D. Blostein (Queen's University, Canada), and Asst. Prof. Hani Mehrpouyan (Boise State University, USA). The substantial majority of this work was my own.

Wanchun Liu
Research School of Engineering,
College of Engineering and Computer Science,
The Australian National University,
Canberra, ACT 2601,
AUSTRALIA

Acknowledgments

First of all, I would like to express my sincere appreciation to my primary supervisor Dr. Xiangyun (Sean) Zhou for his great support and guidance throughout the past three years. I would also thank him for always being patient during numerous discussions on research problems and paper writing. I am also very grateful to my co-supervisor Dr. Salman Durrani, who has always been a wonderful supporter for my research. I deeply appreciate his valuable advice on my research and future career. I indeed feel fortunate for being supervised by both Sean and Salman.

I would like to thank Prof. Kaibin Huang for kindly welcoming me to visit his research group for three months. The discussions with Prof. Huang have stimulated many interesting ideas in the broad area of Internet-of-Things and have further brought us fruitful research outputs.

I would like to thank Profs. Petar Popovski, Steven D. Blostein and Hani Mehrpouyan for providing me lots of expert comments and feedback during our collaborations. Collaborating with them has significantly further improved my research and writing skills, and has broadened my research horizon.

I would like to thank my ANU colleagues for helpful discussions and friendships, especially Dr. Jing Guo, Dr. Hanchi Chen, Xiaohui Zhou, Yirui Cong, Dr. Ni Ding, Dr. Alice Bates, Dr. Mingchao Yu, Dr. Biao He, Xiang Wu, Khurram Shahzad, Dr. Yifei Huang, Noman Akbar, Sheeraz Alvi, Abbas Koohian, Jihui Zhang, Yuting Fang, Dr. Shama Islam, Chunhui Li and Simin Xu. Special thanks to Drs. Nan Yang, Shihao Yan, Wen Zhang, and Prasanga Samarasinghe, and Profs. Parastoo Sadeghi, Thushara D. Abhayapala and Rodney A. Kennedy. I would also like to thank the members of Prof. Huang's group for treating me like family during my visit, especially Dongzhu Liu, Changsheng You, Bin Lyu, Guangxu Zhu, Kaifeng Han, Yong Wang and Dr. Juan Wen.

I would like to express my deepest gratefulness to my dear parents, Ying Zhou and Shuzhi Liu, who are the source of my strength. Last but not least, I would like to thank my husband, Dawei Tan, for his unconditional trust, support and love.

Abstract

This thesis focuses on the design, analysis and optimization of various energy-constrained wireless communication systems powered by energy harvesting (EH). In particular, we consider ambient EH wireless sensor networks, wireless power transfer (WPT) assisted secure communication network, simultaneous wireless information and power transfer (SWIPT) systems, and WPT-based backscatter communication (BackCom) systems.

First, we study the delay issue in ambient EH wireless sensor network for status monitoring application scenarios. Unlike most existing studies on the delay performance of EH sensor networks that only consider the energy consumption of transmission, we consider the energy costs of both sensing and transmission. To comprehensively study the delay performance, we consider two complementary metrics and analyze their statistics: (i) update age - measuring how timely the updated information at the sink is, and (ii) update cycle - measuring how frequently the information at the sink is updated. We show that the consideration of sensing energy cost leads to an important tradeoff between the two metrics: more frequent updates result in less timely information available at the sink.

Second, we study WPT-assisted secure communication network. Specifically, we propose to use a wireless-powered friendly jammer to enable low-complexity secure communication between a source node and a destination node, in the presence of an eavesdropper. We propose a WPT-assisted secure communication protocol, and analytically characterize its long-term behavior. We further optimize the encoding-rate parameters for maximizing the throughput subject to a secrecy outage probability constraint. We show that the throughput performance differs fundamentally between the single-antenna jammer case and the multi-antenna jammer case.

Third, exploiting the fact that the radio-frequency (RF) signal can carry both information and energy, we study a point-to-point simultaneous wireless information and power transfer (SWIPT) system adopting practical M-ary modulation for both the power-splitting (PS) and the time-switching (TS) receiver architectures. Unlike most existing studies, we take into account the receiver's sensitivity level of the RF-EH circuit. We show several interesting results, such as for the PS scheme, modulations with high peak-to-average power ratio achieve better EH performance. Then, inspired by the PS-based SWIPT receiver, we propose a novel information receiver, which involves joint processing of coherently and non-coherently received signals, and hence, creates a three-dimensional received signal space. We show that the achievable rate of a splitting receiver provides a 50% rate gain compared to either the conventional coherent

or non-coherent receiver in the high SNR regime.

Last, we propose the design of WPT-based full-duplex backscatter communication (BackCom) networks for energy-constrained Internet-of-Things applications, where a novel multiple-access scheme based on time-hopping spread-spectrum (TH-SS) is designed to enable both one-way power transfer and two-way information transmission in coexisting backscatter reader-tag links. Comprehensive performance analysis of BackCom networks is presented. We show some interesting design insights, such as: a longer TH-SS sequence reduces the bit error rates (BERs) of the two-way information transmission but results in lower energy-harvesting rate at the tag; a larger number of BackCom links improves the energy-harvesting rate at the tags but also increase the BERs for the information transmission.

List of Publications

The work in this thesis has been published or has been submitted for publication as journal/-conference papers. These papers are:

Book chapter:

B1 **W. Liu**, S. Durrani, X. Zhou "Wireless Powered Sensor Networks" in *Wireless Energy Harvesting for Future Wireless Communications*, Springer Press, 2017.

Journal papers:

J1 **W. Liu**, X. Zhou, S. Durrani, P. Popovski, "Secure Communication with a Wireless-Powered Friendly Jammer," *IEEE Trans. Wireless Commun.*, vol. 15, no. 1, pp. 401–415, Jan. 2016.

J2 **W. Liu**, X. Zhou, S. Durrani, H. Mehrpouyan and S. D. Blostein, "Energy Harvesting Wireless Sensor Networks: Delay Analysis Considering Energy Costs of Sensing and Transmission," *IEEE Trans. Wireless Commun.*, vol. 15, no. 7, pp. 4635-4650, July 2016.

J3 **W. Liu**, K. Huang, X. Zhou, and S. Durrani, "Full-Duplex Backscatter Interference Networks Based on Time-Hopping Spread Spectrum," in *IEEE Trans. Wireless Commun.*, vol. 16, no. 7, pp. 4361-4377, July 2017.

J4 **W. Liu**, X. Zhou, S. Durrani, P. Popovski, "A Novel Receiver Design with Joint Coherent and Non-Coherent Processing," in *IEEE Trans. Commun.*, vol. 65, no. 8, pp. 3479-3493, Aug. 2017.

J5 **W. Liu**, K. Huang, X. Zhou, and S. Durrani, "Next Generation Backscatter Communication: Theory and Applications," submitted to *IEEE Wireless Commun.*, Aug. 2017.

Conference papers:

C1 **W. Liu**, X. Zhou, S. Durrani, "Wireless-Powered Friendly Jammer for Physical Layer Security," in *Proc. IEEE WCSP*, Oct. 2015, pp. 1–5.

C2 **W. Liu**, X. Zhou, S. Durrani, H. Mehrpouyan and S. D. Blostein, "Performance of Wireless-Powered Sensor Transmission Considering Energy Cost of Sensing," in *Proc. IEEE GLOBECOM*, Dec. 2015, pp. 1–7.

C3 **W. Liu**, X. Zhou, S. Durrani, and P. Popovski,“SWIPT with practical modulation and RF energy harvesting sensitivity," in *Proc. IEEE ICC*, May 2016, pp. 1–7.

C4 **W. Liu**, K. Huang, X. Zhou, and S. Durrani, “Time-Hopping Multiple-Access for Backscatter Interference Networks," to appear in *Proc. IEEE GLOBECOM*, Dec. 2017, pp. 1-7.

The papers **J1-J4** and **C3** are used in the thesis. The other conference papers are produced during the thesis but not explicitly used in this thesis.

List of Acronyms

ADC	analog to digital converter
AM	amplitude modulation
AWGN	additive white Gaussian noise
BER	bit-error rate
BPSK	binary-phase-shift keying
BS	base station
BackCom	backscatter communications
CCD	charge coupled device
ccdf	complementary cumulative distribution function
CD	coherent detection
cdf	cumulative distribution function
CMOS	complementary metal oxide semiconductor
CSI	channel state information
CW	continuous wave
D2D	device-to-device
DARPA	Defense Advanced Research Projects Agency
DC	direct current
EH	energy harvesting
EHB	energy harvesting block
FCE	fixed chip energy
FCP	fixed chip power
FTB	failed transmission block
ID	identification
i.i.d.	independently and identically distributed
IoT	Internet-of-Things
I-Q	in-phase-quandrature
I-Q-P	in-phase-quandrature-power
IT	information transmission
MIMO	multiple-input-multiple-output
MISO	multiple-input-single-output

PAM	pulse-amplitude modulation
PAPR	peak-to-average power ratio
PB	power beacon
PD	power detection
pdf	probability density function
pmf	probability mass function
PPP	Poisson point process
PT	power transfer
PTR	power-transfer rate
QAM	quadrature amplitude modulation
QoS	quality-of-service
RF	radio frequency
RFID	radio-frequency identification
Rx	receiver
SB	sensing block
SER	symbol error rate
SINR	signal-to-interference-plus-noise ratio
SIR	signal-to-interference ratio
SNR	signal-to-noise ratio
SWIPT	simultaneous wireless information and power transfer
TB	transmission block
TH-SS	time-hopping spread spectrum
Tx	transmitter
UAV	unmanned aerial vehicle
UWB	ultra-wide band
WIT	wireless information transmission
WPCN	wireless powered communication network
WPT	wireless power transfer
WSN	wireless sensor network

List of Notations

$\|\mathcal{A}\|$	size of set $\mathcal{A}$
$\mathcal{CN}\left(\mu, \sigma^2\right)$	Complex Normal distribution with mean μ and variance σ^2
$\mathcal{N}\left(\mu, \sigma^2\right)$	Real Normal distribution with mean μ and variance σ^2
$f_X(\cdot)$	PDF of a random variable X
$F_X(\cdot)$	CDF of a random variable X
$\mathbb{E}_X[\cdot]$	expectation operator with respect to X
$\mathrm{erfc}(\cdot)$	complementary error function
P_{out}	outage probability
λ	path-loss exponent
$\Pr\{\cdot\}$	probability measure
$Q()$	Q-function, i.e., $Q(x) = \frac{1}{2}\mathrm{erfc}\left(\frac{x}{\sqrt{2}}\right)$
j	$\sqrt{-1}$
$\mathrm{Real}\{\cdot\}$	real part of a complex-valued number
$\mathrm{Imag}\{\cdot\}$	imaginary part of a complex-valued number
$h(\cdot)$	differential entropy
$h(\cdot)$	joint differential entropy
$h(\cdot)$	conditional differential entropy
$\mathcal{I}(\cdot;\cdot)$	mutual information
$\tilde{x}$	x is a complex number
$(x)^*$	conjugate of a number x
$\|x\|$	absolute-value norm of a number x
$\mathbf{1}\{\cdot\}$	indicator function
$\max\{\cdot,\cdot\}$	the maximum value
$\min\{\cdot,\cdot\}$	the minimum value
$\mathrm{Pois}(\cdot,\kappa)$	pmf of Poisson distribution with parameter κ
$\setminus$	set exclusion operator
$\triangleq$	defined as
$\lceil\cdot\rceil$	ceiling operator
$\lfloor\cdot\rfloor$	floor operator
$(\cdot)\star(\cdot)$	continuous convolution operator

$(\cdot) * (\cdot)$	discrete convolution operator
$\cap$	intersect operator
$\cup$	union operator
Σ	summation operator
Π	product operator

Contents

List of Figures

List of Tables

Chapter 1

Introduction

1.1 Motivation

In the future, wireless access will not only be about connectivity for people but for anything that benefits from being connected [3]. We are already at the beginning of a transition into a fully connected networked society that will provide access to information and sharing of data anywhere and anytime for anyone and anything.

For example, Internet-of-Things (IoT) is an emerging concept of network connectivity anytime and anywhere for billions of everyday objects, which has recently attracted tremendous attention from both the industry and academia. However, keeping the massive number of devices alive poses a key design challenge for IoT. This is especially challenging given a large population of the devices are hidden (e.g., in the walls or appliances) or deployed in remote or hazardous environments (e.g., in radioactive areas or pressurized pipes), making battery recharging or replacement difficult if not impossible. In general, such *energy-constrained* wireless communication networks bring new challenges for contemporary wireless communications.

To fully realize future energy-constrained wireless communication networks, four challenges need to be tackled from the aspects of energy replenishment, low-complexity IoT security, efficient device-to-device communication and smart networking.

1.1.1 Research Challenges in Energy-Constrained Wireless Communication Networks

1.1.1.1 Energy Replenishment

Due to the limited battery storage of energy-constrained devices and the inconvenience of battery replacement for massive number of devices, the lifetime of such networks may not meet the demand from a certain application scenario. Energy harvesting (EH), converting ambient energy (i.e., solar, wind and thermal energy) to electrical energy, has emerged as an alternative to power sensor nodes [4]. In theory, a sensor node can be powered perpetually as

long as the harvested energy source is continuously available.

However, for devices powered by EH from the ambient environment, the energy arrival process is inherently time-varying in nature. Such fluctuations in the energy arrival process may affect the transmission delay of an EH device, i.e., there may not be sufficient energy available at the device when it has to transmit information, thus, it has to wait until there is sufficient harvested energy. Therefore, how to accurately measure and control the delay in EH wireless communication network is a very important problem, especially for time-relevant wireless applications, such as a status-monitoring wireless sensor network (WSN).

Moreover, conventional EH methods rely on various renewable energy sources in the environment, such as solar, vibration, thermoelectric and wind, which are usually uncontrollable. Also, a solar-energy based node is equipped with heavy solar panel, a vibration-energy based node is equipped with relatively complex mechanical construction, a thermal-energy based node is equipped with relatively large area thermoelectric generators, and a wind-energy based node is equipped with big size wind turbine. These conventional EH devices may not be suitable for many applications that have constraints on the form factors and the costs. Therefore, proactive wireless power transfer (WPT), an emerging EH method that only requires a radio-frequency (RF) EH circuit with low cost and small form factor, needs to be considered, and how to jointly design WPT and wireless information transmission (WIT) in a WPT-enabled network is a key problem.

1.1.1.2 Low-Complexity Security

Due to the massive number of devices in future wireless communication networks, a central controller or a network coordinator may not be available to distribute security keys to each of the devices to enable encrypted transmission [5]. Moreover, due to the broadcast nature of the wireless channel, the security keys can also be intercepted by the nearby eavesdroppers. Furthermore, energy-constrained wireless communication networks also require the security methods to be simple and low complexity, and thus, the conventional sophisticated cryptographic methods may not be suitable. Therefore, the security issue of energy-constrained network brings us new research challenges.

Recently, physical layer security has become an emerging technique to complement and significantly improve the communication security of wireless networks. Comparing to the conventional cryptographic approaches, physical layer security is a very different paradigm where secrecy is achieved by exploiting the physical layer properties of the wireless communication system, such as thermal noise, interference, and the time-varying nature of fading channels [6]. Since physical layer security does not rely on sophisticated cryptographic methods, it has low complexity and hence is more suitable for energy-constrained networks compared to the con-

ventional approaches.

Among all the physical layer security approaches, the proactive approach, i.e., emitting jamming noise/interference, is a popular one, such that the quality of the eavesdropping channel is deteriorated. Although using a nearby legitimate device, say a jammer, to send some jamming noise can effectively reduce the probability that the ongoing D2D information transmission is eavesdropped by an eavesdropper, the jammer in an energy-constrained network may not have sufficient energy nor want to consume its own energy for emitting jamming noise. Thus, it is desirable to make the transmitter wirelessly charge the jammer first and then recruit it to protect the secure information transmission. Therefore, the main challenge is how to optimally design the WPT and the secure communication process such that the secure communication is well protected while the energy consumption for WPT at the transmitter is minimized.

1.1.1.3 Information Transmission

Since radio signals can carry energy as well as information at the same time, *simultaneous* wireless information and power transfer (SWIPT) is a natural but significant idea. As proposed and elaborated in [7], a SWIPT receiver consists of one conventional information-reception circuit and one RF-EH circuit, and SWIPT is a more energy efficient way compared with doing WPT and WIT separately. Therefore, for an energy-constrained network, it is desirable to make some of the transmitters that are connected to the power grid, transfer power and information to the energy constraint receivers at the same time.

However, most of the existing study only consider ideal assumptions when studying the SWIPT system. Considering a practical SWIPT system, which has finite alphabet transmit signal input, different sensitivity level of the input power of the information-reception and RF-EH circuits and the non-linear property of the RF-EH circuit, it is desirable to jointly optimize and design the transmit signal and the parameters of the SWIPT receiver to meet the requirements of both the WIT and WPT.

1.1.1.4 Smart Networking

As future IoT is expected to wirelessly connect billions of low-complexity devices, the high density of IoT devices and their ad hoc communication without network coordinator results in strong interference which acts as a bottleneck on WIT. In general, there are two schemes to handle the interference: one is interference cancellation, and the other is interference suppression/avoidance by spread spectrum. The first scheme is not suitable for energy-constrained IoT since both the transmitter and the receiver are meant to be simple devices and are not able to apply complex analog circuits and digital algorithms to cancel the interference. Hence, it is

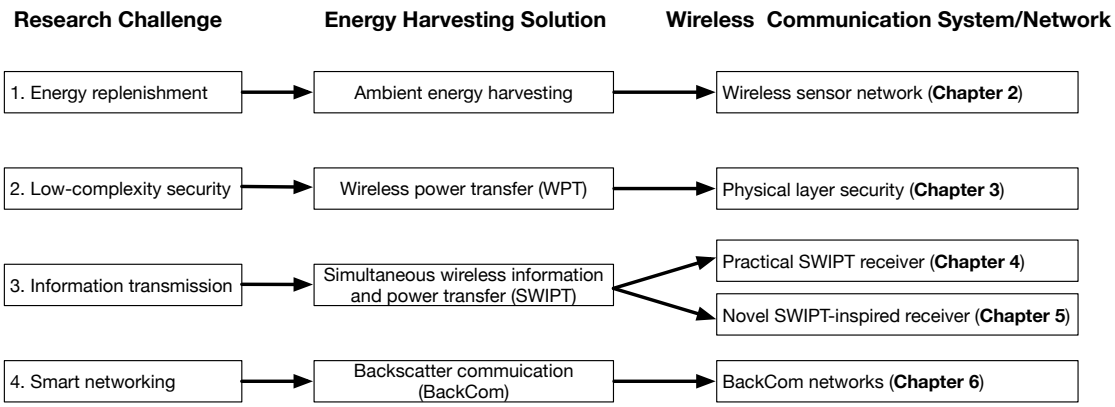

Figure 1.1: The thesis outline.

better to adopt the second scheme and make the interference unlikely to happen.

However, the conventional spread-spectrum methods may not be suitable in the energy-constrained IoT applications mainly due to their high complexity. Therefore, low-complexity spread-spectrum method, which also facilitates the WPT to charge the energy-constrained receivers, are desirable.

Many application scenarios in the future IoT require low-latency transmissions, such as e-healthcare and public safety [8]. Therefore, adopting full-duplex device-to-device (D2D) communications between IoT devices such that each IoT node can speak and listen at the same time is desirable since the latency of information transmission can be reduced significantly.

However, the conventional approach for enabling full-duplex transmission relies on sophisticated self-interference cancellation methods cannot be adopted in energy-constraint IoT devices. Thus, how to enable low-complexity full-duplex communication in energy-constrained IoT network is a key challenge.

This thesis tackles these research challenges in Chapters 2-6, and the thesis outline is shown in Fig. 1.1.

1.2 Background of Energy Harvesting Techniques

In this section, we review the energy harvesting techniques employed in this thesis, i.e., ambient energy harvesting, wireless power transfer, simultaneous wireless information and power transfer and backscatter communication.

1.2.1 Ambient Energy Harvesting

Generally speaking, EH means harvesting energy from the ambient environment such as solar, wind, vibration, thermal energy or RF signals, or other energy sources such as foot strike,

Table 1.1: Environmental Energy Harvesting Power (Reproduced from [1]).

Source	Average harvested energy
Solar panel	15 mW/cm^2
Light (indoor)	10-100 μW/cm^2
Airflow	0.4-1 mW/cm^3
Vibrations	200-380 μW/cm^3
Thermoelectric	40-60 μW/cm^2
Piezoelectric	100-330 μW/cm^3

finger strokes and body heat, and converting it to electrical power/energy [4]. An EH device first needs to convert the ambient energy arrival into a direct current (DC) signal by the EH module, which is then used to charge the battery of the device.

The EH rate of different energy sources are listed in Table 1.1. It is straightforward to see that EH from a solar panel can provide the highest EH rate. In addition, solar energy is the most easily accessible energy source and there are lots of existing WSN applications based on it. For example, the outdoor multi-target tracking networks, such as the zebra tracking and the turtle habitat monitoring networks in US [4].

1.2.1.1 Energy Harvesting Models

In order to evaluate the performance of EH based communications, we need to model the EH process first. Most of the studies have modeled EH processes as a time-discrete process or a block-by-block process, due to the fact that sensors, in practice, operate in a time-block based manner, i.e., transmission and sensing tasks are processed in one or several time blocks. In other words, we care about how much energy is harvested in different EH time blocks, rather than the entire time-continuous EH process within each of the block. In general, the harvested energy in each EH block could either remain constant or change from block to block. These EH fluctuations in time-domain are characterised by the coherent time. The coherence time is the time interval (i.e., the number of EH time blocks) within which the harvested energy does not change much.

There are three EH models listed below, as illustrated in Fig. 1.2.

1. Deterministic EH Model. Deterministic energy arrival is the most simple EH model. It is a proper model when the coherence time of the EH process is much larger than the duration of the entire communication session, such as EH by solar panel on clear days. Since the deterministic EH model is very simple, it is commonly adopted to evaluate the performance of EH based WSN communications [9, 10, 11].

2. Non-Causal EH Model. Non-causal EH model is an ideal EH model that the future

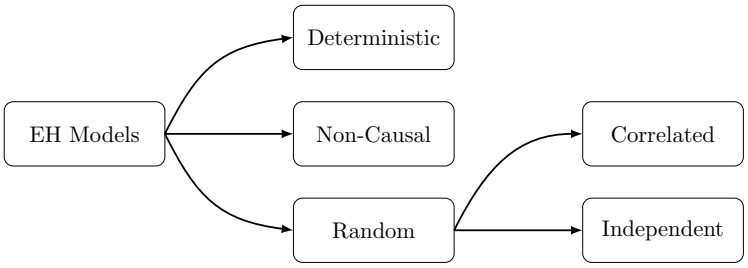

Figure 1.2: Classification of EH models.

EH process is entirely known at the beginning of transmission. If the non-causal EH information is known at a node, it can adopt the optimal energy scheduling strategy and achieves the maximum communication performance. Therefore, non-causal EH model is useful to provide a performance upper bound.

3. Random EH Models. The most popular EH model in the recent years is the random EH model in which the EH process are regarded as random processes. In general, random EH process can be treated as a causal EH model. They are divided into two categories:

   (a) Correlated EH process is an EH process that the harvested energy in the current time block, which is a random variable, is related to the harvested energy in the previous time blocks, i.e., a Markov EH model [12, 13, 14]. For example, in [15, 16], the EH process is modeled as a ON-OFF two-state a first-order discrete-time Markov process, where the harvested energy during an ON block is constant while there is no energy harvested in OFF blocks.

   (b) Independent EH process is an EH process that the harvested energy in the current time block is independent to the harvested energy in the previous time blocks, i.e., a i.i.d. EH model. For the i.i.d. energy arrival model, the available harvested energy in each time block follows i.i.d. continuous distribution [17, 18, 19]. In [20, 19], Bernoulli i.i.d. discrete EH process is considered.

1.2.1.2 Design, Optimization and Performance Analysis of EH Communication

Most of the EH WSN design problems can be treated as power scheduling problems under dynamic EH processes. If the allocated power usage in one time block is very high, an energy outage may happen in the next few time blocks in which the EH rate is very low and cannot support the relevant power consumption, and thus causes performance losses. While if the allocated power usage is very low in one time block, an energy overflow may happen in the next a few time blocks in which the EH rate is very high and a finite battery cannot store all the

available energy, and thus causes a waste of energy. Therefore, it is very important to carefully design the power scheduling protocols.

The power scheduling problem has basically two scenarios: offline and online, corresponding to non-causal and causal EH processes, respectively. The design targets of the power scheduling problems are mostly focused on average transmission throughput maximization during a certain time duration and transmission completion time minimization, and average delay minimization, such as [21, 22, 23], respectively. The required constraints of the optimization problems include the energy causality, i.e., not using energy in the future, and the battery capacity.

For the offline optimization problems, where the full knowledge of both the energy state information and the transmission channel state information are known before the beginning of transmission, when both the object function is a concave and the constraints are convex, the optimal power scheduling strategy can be found by solving Karush-Kuhn-Tuchher conditions [21]. However, most of the EH power scheduling problems are not convex, and in this case, optimal (deterministic) dynamic programming policy and greedy policy are helpful [24]. The approach in the optimal dynamic programming policy is to break an optimization problem into sub-problems and then recursively find the optimal solutions to the sub-problems. The greedy policy also first breaks down the problem into sub-problems, but then it simply picks optimal choices for each sub-problem as the solution. However, such locally optimal (i.e., greedy) choices may result in a bad global solution. On the other hand, the greedy policy has a much lower computation and space complexity compared to the optimal dynamic programming policy and usually provides an acceptable sub-optimal solution in some scenarios.

For the online optimization problems, the optimization only accounts for partial or full statistical knowledge of the EH and transmission channel fading dynamic processes, and the problem is usually solved as an online optimal power control problem. The most commonly used method is the stochastic dynamic programming [24, 25]. Formally, the stochastic dynamic policy has the same components as the deterministic one. The only difference is that for the stochastic dynamic programming, when evaluating each sub-problem, the long-term effect caused by the adopted strategy should be taken into account.

1.2.1.3 Low-Complexity Harvest and Use Protocols

There are two kinds of low-complexity transmission protocols for EH communications:

(i) Harvest-use protocol, where the harvested energy in one time block is assumed to be used entirely within the same block. The harvest-use protocol can be adopted by WSNs with small battery storage [7, 26, 27, 17, 28], where the harvested energy should be used immediately, otherwise, the battery energy overflow occurs and leads to communication

performance losses. On the other hand, the performance analysis of harvest-use protocol-based WSNs are often tractable, which is why they have been adopted by many research studies. Therefore, the performance of a harvest-use protocol-based WSN can be treated as a lower bound of that obtained by an optimal transmission protocol.

(ii) Harvest-store-use protocol, where the harvested energy in one time block can be stored for future use. Since the harvested energy does not need to be consumed entirely, the harvest-store-use protocol provides a better transmission performance compared with the harvest-use protocol. The harvest-store-use protocol is adopted by WSNs with large battery storage [29, 30, 31]. In this case, the sensors do not need to use all the available energy at each time block, and thus can better utilize the available harvested energy and schedule its power consumption to improve the communication performance. In theory, in order to achieve a globally optimal performance of transmission, a sensor can adaptively change the transmit power in each time block depending on the current energy storage and the length of data queue. However, most of the WPT-based WSNs are simple devices, which require low-complexity protocols that do not allow adaptively changing the transmit power. Therefore, the widely adopted harvest-store-use protocol is a threshold based protocol, which transmits with a constant power within a time block as long as there is sufficient energy for the transmission [29, 30, 31].

1.2.2 Wireless Power Transfer and Simultaneous Wireless Information and Power Transfer

Leveraging the far-field radiative properties of electromagnetic waves, wireless receivers are able to harvest energy remotely from RF signals radiated by RF signal emitters. This simple invention has been known long (a century ago) before the recent excitement about WPT. WPT techniques are considered popular because of following two properties:

(i) Wireless, which enables conveniently powering large-scale ubiquitous nodes without battery replacements or specific conventional EH sources, particularly for implanted in-body sensors. In other words, WPT technologies have the potential to make people's life truly wire free.

(ii) RF signals carry both energy and information at the same time, which enables wireless power and information transfer at the same time.

Compared to conventional EH techniques, WPT has another two advantages:

(i) WPT is more controllable and does not rely on environmental EH sources.

Table 1.2: Wireless Power Transfer Experimental Data [2].

Source	Source Power	Distance	Amount of Energy Harvested (uW)
Isotropic RF transmitter	4 W	15 m	5.5
Isotropic RF transmitter	1.78 W	25 m	2.3
Isotropic RF transmitter	1.78 W	27 m	2
TX91501 Powercaster transmitter	3 W	5 m	189
TX91501 Powercaster transmitter	3 W	11 m	1
Tokyo TV Tower	48 kW	6.3 km	0.1-0.25
KING-TV Tower (Seattle)	960 kW	4.1 km	60
KING-TV Tower (Seattle)	960 kW	10.4 km	$\geq$15.8

(ii) RF-EH devices, i.e., rectifier based simple passive components, are suitable for large scale WSNs and IoT nodes. This is in contrast to: solar-energy based node is equipped with heavy solar panel, vibration-energy based node is equipped with relatively complex mechanical construction, thermal-energy based node is equipped with relatively large area thermoelectric generators, wind-energy based node is equipped with big size wind turbine.

A summary of some of the industry studies about the available harvested RF power is listed in Table 1.2. Compared with the EH rate provided by the conventional ambient EH methods shown in Table 1.1, we see that the EH rate of the WPT techniques in general is much lower and decays rapidly with the distance with the RF signal emitter. This is the main problem of WPT. However, for low power WSNs, WPT is viable and an attractive solution.

1.2.2.1 Receiver Design for WPT

The receiver architecture for WPT consists of an RF antenna, and an RF-EH device which harvest and store the RF energy that is further used to power the other circuits of the receiver, such as for information transmission, sensing and computing. Specifically, the RF-EH device first converts an RF signal to DC signal via a rectifier architecture, and then uses the DC signal to charge a battery. The architecture of the RF-EH device is quite simple. It consists of a Schottky diode and a low pass filter (LPF), as illustrated in Fig. 1.3. To accurately measure how much available RF power captured by the antenna can be harvested, a proper model is required for the non-linear power conversion property introduced by the Schottky diode.

The I-V curve of a Schottky diode is illustrated in Fig. 1.4(a), and it shows that only the positive part of the receive signal that is beyond a certain threshold, can be harvested. The harvested power increases monotonically from zero when the receive signal power increases and is larger than the threshold. More precisely, the non-truncated part of the non-linear model

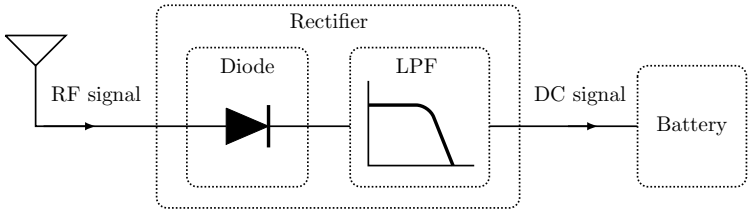

Figure 1.3: Illustration of a RF-EH device.

can be written as

$$I = I_s \left(e^{\gamma V} - 1 \right), \tag{1.1}$$

where I_s is the saturation current, V is the voltage drop across the diode and γ is the reciprocal of the thermal voltage.

Although the model in (1.1) is precise, it is not tractable for general analysis. In [32], the authors take a Taylor expansion of the exponential function in (1.1), and the optimal waveform design is considered based on the simplified model. In [33], in order to better capture the truncated property of the Schottky diode, a non-linear model is considered as

$$\mathcal{P}_{\mathrm{DC}} = \frac{M}{1 + \exp\left(-a\left(\mathcal{P}_{\mathrm{RF}} - b\right)\right)}, \tag{1.2}$$

where M, a, b are the constant diode parameters, and $\mathcal{P}_{\mathrm{RF}}$ and $\mathcal{P}_{\mathrm{DC}}$ are the input RF power and the output DC power, respectively. Then an optimal resource allocation problem is considered for a multi-user simultaneous wireless information and power transfer system based on the non-linear model.

There are another two commonly considered simplified models for RF-DC power conversion, as illustrated in Figs. 1.4(a) and (b).

(i) For the near-practical model (Fig. 1.4(b)), the converted DC power is assumed to increase linearly with the received RF power only if it passes a threshold [34, 35].

(ii) For the ideal model (Fig. 1.4(c)), the converted DC power is assumed to be proportional to the RF power only if it is beyond the threshold [7, 26].

1.2.2.2 Network Model Based on WPT

There are three network models for WPT.

1. *WPT only network*, where energy transfer is in the downlink. In [36], the authors proposed a power beacon based hybrid cellular network. In the network, mobile users are wirelessly powered by randomly deployed power beacons, which enables mobile users

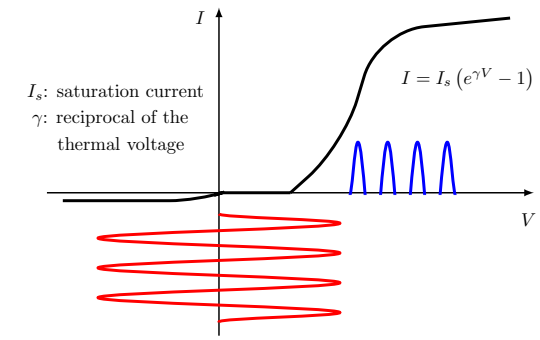

(a) Accurate non-linear behaviour of the Schottky diode

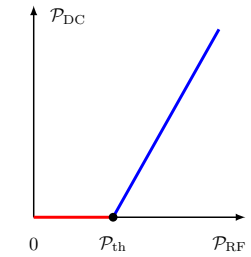

(b) Near-practical approximation

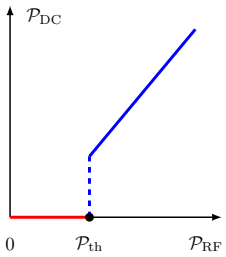

(c) Ideal approximation

Figure 1.4: Illustration of the models for RF-DC converter.

to have a much longer lifetime without battery replacement. The outage and coverage probability with power beacons was analyzed in [37].

Different scenarios such as single-/multi-user, relays, multi-carrier have been considered with WPT [7, 38, 39, 40, 41, 31, 42, 32].

In [7], wirelessly power transfer from a multi-antenna PB to single/multiple energy receivers is studied, where the optimal WPT strategy are obtained. In [38], a system consisting of a single power beacon and multiple energy receivers was considered, where the energy receiver can only do one-bit feedback. The optimal channel learning algorithm was also proposed for such a WPT system. In [39], the distributed WPT system with limited-feedback was studied, where a distributed channel learning method was proposed. In [40], WPT-based sensor networks were considered, where a large-scale sensor network are powered by randomly deployed power beacons. The sensor-active probability was also studied.

In [41], the multiple power beacon placement problem was considered. The location of the power beacons was optimized which maximized the WPT powered communication network. In [31] and [42], WPT-based single- and bi-directional relay networks were considered, respectively, where the relay is wirelessly powered by the transmitter for relaying the information to the destination. The maximal throughput of such a relay

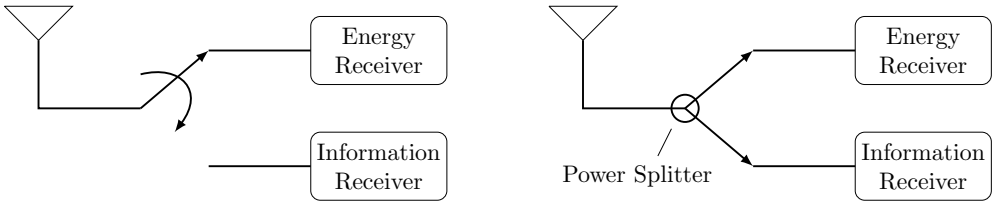

(a) Time-switching receiver. (b) Power-splitting receiver.

Figure 1.5: SWIPT receivers.

networks was derived.

In [32], WPT with multi-carrier waveform was considered, where waveform optimization method was proposed.

2. *SWIPT network*, where energy and information are transferred simultaneously in the downlink by leveraging the property that RF signal carries both information and energy. In [7], the authors first proposed a practical SWIPT system, where the receiver can obtain information and energy simultaneously from the received signal by using a time-switching or power-splitting method, as illustrated in Fig. 1.5.

   For the time-switching-based SWIPT receiver, the RF antenna periodically switches between an information receiver and an energy receiver for information detection and EH, respectively. In this way, the SWIPT receiver is able to detect information for a certain percentage of time, and harvest energy in the rest of the time. For the power-splitting-based SWIPT receiver, the received RF signal is first splitted into two streams by a passive power splitter, and then one signal is sent to the information receiver and the other signal is sent to the energy receiver. Note that there are some other SWIPT architectures, such as the antenna-switching based SWIPT architecture, see [43].

   The network with multiple randomly deployed SWIPT links was analyzed in [44] SWIPT for a multiple-input-single-output (MISO) broadcast channel was investigated in [45]. SWIPT in OFDM-based systems were further investigated in [46, 47]. Such systems are important, since 4G systems are based on OFDM. In [46], downlink OFDM-SWIPT in a multi-user system was studied, where the optimal resource allocation problem was solved. In [47], the resource allocation problem of an OFDM cellular system, which performs downlink SWIPT and uplink information transmission, was comprehensively studied.

   Current studies on SWIPT often consider an ideal information transmission model (i.e., Gaussian signaling) and investigate the tradeoff between the information capacity and harvested energy [7, 48, 49]. In reality, SWIPT receivers are typically energy constrained

and may be incapable of performing high-complexity capacity-achieving coding/decoding scheme. Recently, SWIPT with practical coherent modulations was analyzed in [26].

Another commonly applied assumption in the SWIPT literature is that the average received signal power at the radio-frequency (RF) EH circuit is well above the RF-EH sensitivity level [7, 26, 48]. Hence, these studies ignore the impact of the RF-EH sensitivity level. In reality, practical state-of-the-art RF-EH circuits have power sensitivity requirement in the range of -10 dBm to -30 dBm [2]. Guaranteeing a much higher received signal power than the RF-EH sensitivity level often requires an extremely short communication range, which largely limits the application of SWIPT. Therefore, we consider a more general SWIPT system with M-ary modulation where the received signal power is not necessarily larger than the RF-EH sensitivity level. Since different constellation symbols may have different power levels, the amount of harvested energy may vary from symbol by symbol, and it is possible that some symbols can activate the RF-EH circuit but others cannot. Hence, it is important to accurately capture the effect of the RF-EH sensitivity level in analyzing the performance of SWIPT.

3. *WPCN (wireless powered communication network)*, where energy is transferred in the downlink and information is transfer in the uplink [50]. In [27], the authors first proposed the WPCN network model. In this network, mobile users harvest RF energy emitted by a base station, and transmit information to the base station when it has harvested enough energy. The WPCN is particularly useful in wireless sensor networks, since wireless sensors usually have very low downlink data rate but high uplink data rate, e.g., updating the sensed information to the sink. In [51], the authors further considered a full-duplex WPCN, where an access point operating in a full-duplex manner, i.e., broadcasting wireless energy to a set of distributed users in the downlink and, and receiving independent information from the users via time-division multiple access in the uplink simultaneously.

   However, this WPCN architecture suffers from a “doubly near-far" problem[1]: due to both the downlink and uplink distance dependent signal attenuation, where a far user from the access point, which receives less wireless energy than a nearer user in the downlink, has to transmit with more power in the downlink for reliable information transmission. To tackle the challenge of “doubly near-far" problem, the direct solution is the decoupling of the uplink and the downlink [52, 36], i.e., the energy emitter and information receiver should be separated. In [52], the authors proposed a novel WPCN consisting of a primary and a secondary network. The low-power mobiles in a secondary network, i.e., the secondary transmitters, harvest ambient RF energy from transmissions

[1] The doubly near-far problem is also applicable to SWIPT systems.

by nearby active transmitters in a primary network, i.e., primary transmitters, while opportunistically transit information to the secondary receivers by accessing the spectrum licensed to the primary network. In [36], the authors propose a cellular network consisting of base stations, mobile users and power beacons (PBs). Therefore, the users are able to harvest RF energy from the nearby PBs and transmit information to their associated base stations.

1.2.2.3 Performance Metrics and Analysis

There is one important metric for each of the WPT network, SWIPT network and WPCN, as shown below.

WPT efficiency is considered in WPT only networks, which is defined as

$$\eta_{\text{WPT}} = \frac{\mathcal{P}_{\text{tx}}}{\mathcal{P}_{\text{rx}}}, \tag{1.3}$$

where $\mathcal{P}_{\text{tx}}$ and $\mathcal{P}_{\text{rx}}$ are the transmit signal power and the harvested signal power at the transmitter and the receiver, respectively. WPT efficiently indicates the quality of a WPT protocol design, such as channel training-based energy transfer [53, 54], and multi-antenna energy beamforming [38, 55, 39].

Rate-energy region is considered in SWIPT networks, which is the boundary of all the achievable tradeoff for maximal information rate versus energy transfer [7, 26]. A large rate-energy region means the SWIPT network is more capable for simultaneously harvesting RF energy and detecting information, or the performance losses on information detection due to the RF EH is smaller.

Uplink throughput is the key metric for a WPCN. WPCNs encounter a doubly near-far problem due to the fact that a far sensor from the sink, which receives less wireless energy than a nearer sensor in the downlink, has to transmit with more power in the uplink to achieve the same reliable information transmission rate [27]. Therefore, in order to achieve a better uplink throughput of a WSN, one needs to properly design the downlink WPT and the uplink information transmission protocols. A time-division-multiple-access based uplink-downlink user scheduling scheme is proposed in [27].

1.2.3 Backscatter Communications

Keeping the massive number of energy-constrained IoT smart devices alive poses a key design challenge for IoT, as mentioned before, it is highly desirable to power IoT nodes by ambient EH [4] or WPT [56]. Another promising solution is BackCom that allows an IoT node to transmit data by reflecting and modulating an incident RF wave [57]. The conventional

radio architecture comprises power-hungry RF chains having oscillators, mixers and digital-to-analog converters, which results in non-compact form factors and limiting the battery lives of IoT devices. In contrast, a backscatter node has no active RF components and as a result can be made to have miniature hardware with extremely low power consumption, facilitating large-scale deployment at flexible location or even in-body implantation.

Specifically, a basic BackCom system consists of two devices: a mobile backscatter node, i.e., a Tag, and a Reader [58]. The Tag is a passive node that harvests energy from an incident single-tone sinusoidal continuous wave (CW) radiated by the Reader, and also modulates and reflects a fraction of the wave back to the Reader. Specifically, the wave reflection is due to an intentional mismatch between the antenna and load impedance. Varying the load impedance makes the reflection coefficient to vary following a random sequence that modulates the reflected wave with Tag's information bits. Such a modulation scheme is named as the backscatter modulation. Therefore, the passive Tag is powered by RF EH and does not require any active RF component. On the contrary, the Reader has its own power supply and a full set of conventional RF components for emitting CW and information transmission/reception.

In the past two decades, the basic point-to-point BackCom has been widely deployed in the application of radio-frequency identification (RFID) for a passive RFID Tag to report an ID to an enquiring Reader over the near field (typically several centimeters). In its early stage, IoT comprised of primarily RFID devices for logistics and inventory management. However, IoT is expected to connect tens of billions of devices and accomplish much more sophisticated and versatile tasks with city-wise or even global-scale influences. This demands the communication capabilities and ranges (tens of meters) between IoT nodes to be way beyond the primitive RFID operations supporting bursty and low-rate (several-bytes pre-written ID sequence) uni-directional transmission over several meters. This can be achieved via a full-fledged BackCom theory leveraging the existing well-developed communication technologies such as small-cell networks, full-duplexing, multi-antenna communications and wireless PT, as well as advancements in electronics such as miniature radios (e.g., button-size radios) and low-power electronics. Furthermore, instead of supporting a single RFID link, a BackCom networking theory has to be developed for allowing multiple access by a massive number of simultaneous IoT nodes. From the computing perspective, it is desirable for IoT sensors to pre-process sensing data to reduce its redundancy and latency while RFID Tags have no such capabilities. Despite the constraint on their form factors, IoT sensors can acquire powerful computing capabilities leveraging the advancements in miniature computers e.g., computer on a stick. These IoT design challenges present many promising research opportunities, resulting in a recent surge in research interests in BackCom.

1.3 Literature Review

In this section, we review the relevant work in the literature on wireless sensor networks, physical layer security, and passive backscatter communications.

1.3.1 Wireless Sensor Network

The first WSN was originally invented by the United States Military in the 1950s to detect and track Soviet submarines [59]. The network, which consisted of acoustic sensors, was distributed in the Atlantic and Pacific oceans. In the 1980s, the United States Defense Advanced Research Projects Agency (DARPA) started the distributed sensor network program which boosted the civilian and scientific research on WSNs. Thanks to the advances in semiconductor, networking and material science technologies in the past a few decades, the ubiquitous deployment of large-scale WSNs has finally come true. The state-of-the-art WSNs have many applications such as micro-climates measurement on farms, habitat monitoring, volcano monitoring, structural monitoring, vehicle tracking, human presence detection in homes and offices, electrical/gas/water metering.

The future IoT, which is going to connect tens of billions of low-complexity wireless devices such as sensors and wearable computing devices, can be treated as an advanced evolution of WSN. The IoT will enable new applications such as smart cities, home automation and e-healthcare. One of the most important implementation challenge of the IoT is that the finite battery capacity sensor nodes have a limited lifetime and thus require regular battery replacements [60]. This kind of battery replacement for massive number of IoT nodes is difficult or even infeasible as many sensors are deployed in hazardous environments or hidden in walls, furniture and even in human bodies.

One immediate solution is to use large batteries for longer lifetimes, however, the increased size, weight and cost may not be affordable for the massive number of sensors. Another solution is to adopt low-power hardware, but at the cost of lesser computation ability and lower transmission ranges. To effectively address the finite node lifetime problem, an alternative technique, i.e., EH powered WSN is the most promising solution. Fig. 1.6 illustrates the basic architecture of an EH WSN, which consists of multiple sensors and one sink. The sensors are able to harvests energy from a solar panel and may also harvests energy from other energy sources such as RF signals emitted by power beacons or base stations.

More precisely, an EH sensor consists of six modules: a micro-controller, EH module, battery, sensing modulo, transmitter(and receiver) and data buffer. The sensor first needs to convert the ambient energy arrival into a direct current (DC) signal by the EH module, which is then used to charge the battery of the sensor. Powered by the harvested energy, the sensing module senses its relevant parameters and saves the sensed data into the data buffer, and the

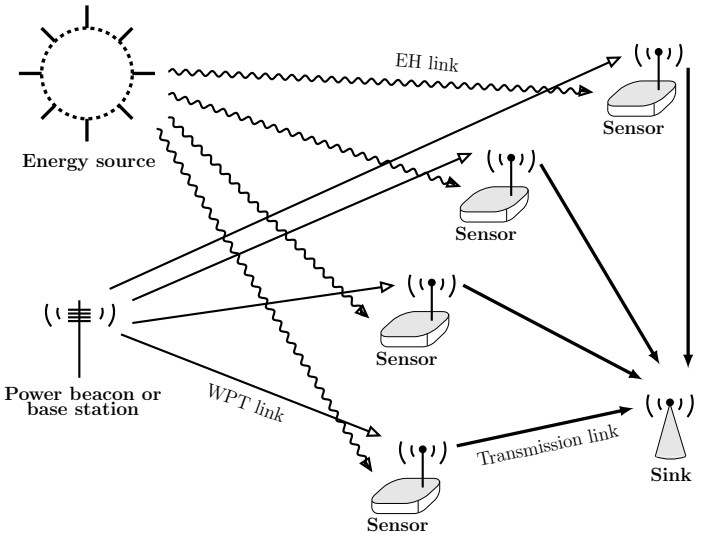

Figure 1.6: Illustration of EH WSN.

transmitter transmits the sensed data to the sink.

1.3.1.1 Power Consumption of Wireless Sensor

There are three main energy costs in wireless sensors, which are summarized in [1] as

(i) Energy cost of RF transmission and reception. This is the energy consumption of the RF components of the transmitter (and also the receiver), such as the mixer and the analog to digital converter (ADC).

(ii) Energy cost of information sensing and processing. This is the energy consumption of the sensor chip and the ADC of the sensing module.

(iii) Energy cost of other basic processing while being active. This is the energy consumption of the micro-controller of the wireless sensor node. The processing unit, which is generally associated with a small storage unit, performs tasks, processes data, and controls the functionality of other components in the sensor node.

The power consumption for processing, sensing, and transmission/reception for most commonly used WSN nodes are summarized in Tables 1.3, 1.4 and 1.5, respectively. In Table 1.3, we list two micro-controllers PXA271 and ATmega 128/L, which are used in two popular WSN nodes Inote2 and MicaZ, respectively. We also include three micro-controllers of TI's low voltage low power series. Comparing TI's MSP430F2132 with ATmel's ATmega 128/L, we see that the active power consumption is significantly reduced. In Table 1.4, we list five sensor chips with the functions of three-axis accelerometer, pressure sensing, light sensing,

temperature sensing, and thermopile sensing. We see that the power consumption of different types of sensors varies greatly. In Table 1.5, we list five commonly used 2.4 GHz Low Power Transceiver for the IEEE 802.15.4 standard. Comparing TI's CC2520 with Freescale's MC1321, it is easy to see that MC1321's power consumption is almost doubled compared to CC2520 in the receive mode, while the transmit power consumption are almost the same.

We see that the energy cost of processing and sensing is much smaller compared to the energy cost of transmission, and this is the reason why majority of the current work on EH WSNs has considered only the energy cost of transmission, while ignoring the energy cost of processing and sensing [12, 13].

However, the IoT will require various more complicated sensing functions, such as charge coupled device (CCD) or complementary metal oxide semiconductor (CMOS) image sensors that adopt array sensing, and high-rate and high-resolution acoustic and seismic sensors [61] (and references therein). The energy cost of sensing in this scenario can actually be higher than the energy cost of transmission. Moreover, as an emerging low power communication technique, BackCom, which does not have any active RF components and relies on passive RF signal reflection, has an ultra low power consumption roughly within a μW level when active for transmissions [57, 62]. Therefore, in these application scenarios, power consumption for sensing is comparable to or even much higher than that of transmission/reception. The first study is [63] that considers an WSN energy allocation problem taken into account both the sensing and transmission power consumption.

Table 1.3: Processor Consumption

	PXA271	ATmega 128/L	TMS320c5535	MSP430F2132
Features	CPU	MCU	DSP	MCU
Company	Intel	Atmel	TI	TI
Voltage Supply	3 V	5 V	1.05 V	2.2 V
CPU Frequency	13 MHz	12MHz	50 MHz	1M
Active Mode Power	44.2 mW	125 mW	7.5 mW	0.55 mW
Standby Mode Power	1.72 mW (idle 8.5 mW)	8.5 mW	0.26 mW	1.54 uW

Table 1.4: Sensor Consumption

Features	ADXL345	MS5534AM	TSL2550D	PGA309-ht	LMP91051
Manufacturer	Analog Devices	Intersema	TAOS	TI	TI
Function	three-axis Accelerometer	Barometric Pressure Sensor	Ambient Light Sensor	Temperature and pressure Sense	thermopile sensor
Voltage Supply	2.5 V	3 V	3.3 V	3 V	3.3 V
Active Mode Power	58 uW	3 mW	1 mW	3.6 mW	11.88 mW
Standby Mode Power	0.25 uW	0.01 mW	$<$ 0.03 mW	0	0.247mW

Table 1.5: Transceiver Consumption (Reproduced from [1])

Features	CC2520	CC2590	JN5139	MC1321	EM1250
manufacturer	TI	TI	Jennic	Freescale	Ember
Bit Rate (kbps)	250	250	250	250	250
Supply Voltage (V)	1.8-3.8	2.2-3.6	2.2-3.7	2.0-3.4	2.1-3.6
Sleep Current (uA)	1	0.1	0.2	1	1
Rx Current (mA)	18.5	3.4	34	37	29
Tx Current Min (mA)	16.2(-18 dBm)	-	-	20.9(-28 dBm)	19(-32 dBm)
Tx Current Max (mA)	33.6 (5 dBm)	22.1 (12 dBm)	35 (3 dBm)	30 (0 dBm)	33 (5 dBm)

1.3.1.2 Delay in Energy Harvesting Wireless Sensor Networks

The recent IoT brings ubiquitous wireless sensors together, which monitor environmental data and update them to the users. In this status monitoring application, we need the sensors to update their monitored status as timely as possible. The conventional metric to measure the timeliness of a WSN is update cycle, which measures the time elapsed from one status update at the sink to the next. Update cycle captures how frequently the status information is updated at the user. For example, if the average update cycle of a WSN is 10 sec, then we can expect that the status updates successfully at the user every 10 sec.

However, from the 10 sec update cycle, we cannot see when the status was originally generated. For example, when a successful status is received/updated at the user, the status

could be collected 9 sec ago, which is not a fresh status, or 1 sec ago, which is a fresh status. Measuring the freshness of the updated status has long been desirable, but it is only recently that it have been seriously considered and modeled in [64, 65, 66], and named as update age. Since both the update frequency and freshness are related to determine how timely a status monitoring WSN is, one need both the update cycle and update age to accurately measure the timeliness of the status monitoring WSN [30].

1.3.2 Physical Layer Security

Physical layer security has been recently proposed as a complement to cryptography method to provide secure wireless communications [67, 6]. It is a very different paradigm where secrecy is achieved by exploiting the physical layer properties of the wireless communication system, especially interference and fading. Several important physical layer security techniques have been investigated in the past decade (see a survey article [68] and the references therein). Inspired by cooperative communication without secrecy constraints, user cooperation is a promising strategy for improving secrecy performance. There are mainly two kinds of cooperation: cooperative relaying and cooperative jamming. As for cooperative relaying, the well-known decode-and-forward and amplify-and-forward schemes were discussed in [69, 70, 71] with secrecy considerations. Following the idea of artificial noise in [72], cooperative jamming was investigated as an effective method to enhance secrecy [73, 74, 75, 76, 77, 78, 79, 80, 81]. In this scheme, a friendly jammer transmits a jamming signal to interfere with the eavesdropper's signal reception at the same time when the source transmits the message signal. In [73, 74, 75], the authors focused on the design of a single-antenna jammer. In [76] and [77], multiple single-antenna jammers were considered to generate distributed cooperative jamming signals. In [78], the authors studied multi-antenna jammer (called relay in [78]) in secure wireless networks. Motivated by this work, the authors in [79, 80, 81] considered multi-antenna jammers in MIMO (multiple-input and multiple-output) networks.

In [82, 83], the authors considered secure communications with one information receiver and one (or several) wireless EH eavesdropper(s). In [84], the authors studied the coexistence of three destination types in a network: an information receiver, a receiver for RF EH and an eavesdropper. In [85], the authors considered the wireless communication network with eavesdroppers and two types of legal receivers which can receive information and harvest RF energy at the same time: desired receiver and idle receiver, while the idle receivers are treated as potential eavesdroppers. All these works on secure communication did not explicitly study how the harvested energy at the receiver is used.

1.3.3 Backscatter Communication Networks

1.3.3.1 BackCom Systems

Recently, active research has been conducted on designing techniques for various types of BackCom systems and networks which are more complex than the traditional RFID systems [86, 87, 88, 89, 90]. One focus of the research is to design multiple-access BackCom networks where a single reader serves multiple tags. As proposed in [86], collision can be avoided by directional beamforming at the reader and decoupling tags covered by the same beam using the frequency-shift keying modulation. Subsequently, alternative multiple-access schemes were proposed in [87] and [88] based on time-division multiple access and collision-detection-carrier-sensing based random access, respectively. A novel approach for collision avoidance was presented in [89] which treats backscatter transmissions by tags as a sparse code and decodes multi-tag data using a compressive-sensing algorithm.

1.3.3.2 Energy Transfer in BackCom Systems

IoT devices having the capabilities of sensing and computing consume more power than simple RFID tags and also require much longer WIT/WPT ranges (RFID ranges are limited to only several meters). This calls for techniques for enhancing the WPT efficiency in BackCom systems by leveraging the rich results from the popular area of wireless power transfer (e.g., see the surveys in [56, 91]). In [92], it was proposed that a reader is provisioned with multi-antennas to beam energy to multiple tags. An algorithm was also provided therein for the reader to estimate the forward-link channel, which is required for energy beamforming, using the backscattered pilot signal also transmitted by the reader.

The WPT efficiency can be also enhanced by reader cooperation. For example, multiple readers are coordinated to perform WPT (and WIT) to multiple tags as proposed in [93]. The implementation of such designs require BackCom network architectures with centralized control. However, IoT relies primarily on distributed *device-to-device* (D2D) communication. Large-scale distributed D2D BackCom are modeled and analyzed in [90] using stochastic geometry, where tags are wirelessly powered by dedicated stations (called power beacons). In particular, the network transmission capacity that measures the network spatial throughput was derived and maximized as a function of backscatter parameters including duty cycle and reflection coefficient. Instead of relying on peer-to-peer WPT, an alternative approach of powering IoT devices is to harvest ambient RF energy from transmissions by WiFi access points or TV towers [94].

1.3.3.3 BackCom Systems with D2D Communication

Conventional BackCom techniques designed for RFID applications mostly target simple single-tag systems and one-way IT from a tag to a reader. Nevertheless, for future IoT supporting D2D communications, many distributed reader-tag links will coexist. This prompts researcher to design more sophisticated and versatile BackCom techniques to improve the data rates and mitigate interference. An EH D2D BackCom system was designed in [95] that features a full-duplex BackCom link where high-rate data and a low-rate control signal are transmitted in the opposite directions using on-off keying and binary *amplitude modulation* (AM), respectively, which are superimposed exploiting their asymmetric bit-rates. In BackCom systems with co-existing links, interference is a much more severe issue than that in conventional systems due to *interference regeneration* by reflection at all nodes having backscatter antennas. The time-hopping spread spectrum (TH-SS) scheme was first proposed in an *ultra-wide band* (UWB) system [96], and the idea of mitigating interference using TH-SS was further applied to UWB RFID (BackCom) systems [97]. The drawback of such a system is that the required accurate analog detection of ultra-sharp UWB pulses places a stringent requirement for hardware implementation and may not be suitable for low complexity IoT devices.

Many application scenarios in the future IoT require low-latency transmissions, such as e-healthcare and public safety [8]. Therefore, adopting full-duplex D2D communications between IoT devices such that each IoT node can speak and listen at the same time is desirable since the latency of information transmission can be reduced significantly. The conventional approach for enabling full-duplex transmission over a single link relies on self-interference cancellation [98]. The implementation requires sophisticated adaptive analog-and-digital signal processing that is unsuitable for low-complexity and low-power IoT devices. Since in conventional BackCom systems, the reader/tag is able to transfer/receive energy and receive/transfer information simultaneously, it is natural to design a full-duplex BackCom system enabling simultaneous two-way information transmission/reception. A simple full-duplex BackCom design, supporting low data rates for IoT links, was proposed in [95]. However, the drawback of the design is the requirement of asymmetric rates for transmissions in the opposite directions since it targets mixed transmissions of data and control signals. Though information flow in RFID applications is usually uni-directional, message exchange between nodes is common in IoT. Therefore, the reader-to-tag and tag-to-reader ITs are equally important for future IoT applications, which require symmetric communication links between the massive number of devices.

1.3.4 Limitation of Existing Studies

Although the existing studies have focused on and solved many problems in wireless communication networks powered by EH, there are still various remaining open problems in this area. In the thesis, we aim to fill in several important blanks in the literature by raising and tackling the following key questions:

- What are the proper delay metrics for a status-monitoring WSN powered by EH, that are able to comprehensively capture the quality of the status-updating process? How does the energy consumption of a sensor node, such as that for transmission and sensing, effect the delay performance?
- How to design an energy-constrained secure communication network, where the friendly jammer may not have energy for jamming? What is the secure performance and how to maximize the performance of this network?
- What is the performance of EH and information decoding of a practical SWIPT system, which has finite-alphabet inputs and a non-linear RF-EH receiver? How to optimize the performance of the SWIPT system with these practical constraints?
- Is it possible to make a SWIPT-like receiver that also benefit information reception compared with the conventional receivers, and how to do it?
- How to design a communication protocol for a passive backscatter interference network consisting of multiple reader-tag pairs, such that the readers and the tags are able to listen and speak at the same time, and the network interference is effectively suppressed as well? What is the communication performance of such a network?

1.4 Thesis Overview and Contributions

The main focus of the thesis is on the design, analysis and optimization of wireless communication systems powered by EH for the application of energy-constrained IoT. In particular, we consider EH wireless sensor networks, WPT-based secure communication network, SWIPT systems, and WPT-based BackCom system. The specific contributions of each chapter are detailed below:

Chapter 2-Energy Harvesting Wireless Sensor Networks with Delay Constraints

In Chapter 2, we consider a status *monitoring* scenario in a WSN, e.g., monitoring some property of a target environment, with one sensor-sink pair. The sensor is solely powered by EH

from an ambient energy source. The sensor periodically monitors and senses the current environment, i.e., it generates current status information about one or more variables of interest, and then transmits a status-information-containing packet to the sink[2]. Once the packets are successfully transmitted to the sink, which may occur after several failed retransmissions due to fading in the transmission channel, the status under monitoring is *updated* at the sink.

We adopt two different metrics to assess the delay performance: (i) update age[3] which measures the time duration between the time of generation of the current status information at the sink and the time at which it is updated at the sink, and (ii) update cycle which measures the time duration between one status update at the sink to the next. The update age (or freshness) and update cycle (or frequency) are complementary measures. For instance, a smaller update age means the updated status information at the sink is much more timely, but does not indicate when the next update status information will be received. A smaller update cycle means more frequent status updates at the sink, but does not indicate when the current updated status information was originally generated or how old it is. Thus, the quality of a status monitoring system, i.e., the status update freshness and frequency, is comprehensively captured by the update age and update cycle, respectively.

We account for the fact that sensing and transmission operations both consume energy. Inspired from the harvest-then-use and save-then-transmit communication protocols for EH nodes in wireless networks [17, 31, 34], which are simple to implement in practice, we consider a harvest-then-use protocol for the EH sensor. In our proposed protocol, the sensor performs sensing and transmission as soon as it has harvested sufficient energy. In order to limit the delay due to retransmissions, we impose a time window for retransmissions. The delay performance of the considered harvest-then-use protocol is analyzed. The main contributions of this chapter are summarized as follows:

- We provide a comprehensive study on the delay performance of EH sensor networks. Apart from the commonly considered delay due to the information transmission from the sensor to the sink, defined as the update age, we also characterize the frequency of updating the information held by the sink, defined as the update cycle.

- Considering a Rayleigh fading wireless channel, we analytically derive the statistics of both the update cycle and the update age. We consider both a deterministic energy arrival model and a random energy arrival model with a general distribution, so that our results can be applied to model a wide range of EH processes.

[2]Due to the fluctuation in the energy arrival process, strictly periodic sensing and transmission is not possible. Thus, 'periodic' is used to indicate that the sensor alternates between sensing and transmission(s) in order to keep status updating at the sink.

[3]The term update age is inspired by [65] and indicates the age or timeliness of the transmitted information, since an outdated message may lose its value in a communication system when the receiver has interest in fresh information [64]. Note that this notion of the delay is in fact the same as the transmission delay in [34].

- We take the energy costs of both sensing and transmission into account when studying the delay performance. Such a consideration brings up an interesting question of whether to increase or reduce the number of allowed retransmission attempts for each sensed information, because both sensing and transmission consume energy. This in turn results in a tradeoff between the update cycle and the update age. The tradeoff emphasizes the importance of modeling the energy cost of sensing.

The results in this chapter have been presented in [30] and [99], which are listed again for ease of reference:
[30] **W. Liu**, X. Zhou, S. Durrani, H. Mehrpouyan and S. D. Blostein, "Energy Harvesting Wireless Sensor Networks: Delay Analysis Considering Energy Costs of Sensing and Transmission," *IEEE Trans. Wireless Commun.*, vol. 15, no. 7, pp. 4635-4650, July 2016.
[99] **W. Liu**, X. Zhou, S. Durrani, H. Mehrpouyan, and S. D. Blostein, "Performance of wireless-powered sensor transmission considering energy cost of sensing" in *Proc. IEEE GLOBECOM*, Dec. 2015, pp. 1-7.

Chapter 3-Wireless Power Transfer Assisted Secure Communication

In Chapter 3, we consider a scenario that the network designer wants to establish secure communication between a pair of source-destination devices with minimal cost. To this end, a simple passive device is deployed nearby as a helper. Such a device does not have connection to power line and is only activated during secure communication. The requirements of simplicity and low cost bring important challenges: the helping device should have low complexity in its design and operation, with a low-cost EH method to enable its operation when needed. Consequently, the helping device should ideally have very little workload of online computation and minimal coordination or information exchange with the source-destination pair.

To solve the above-mentioned secure communication design problem, we propose to use a wireless-powered friendly jammer as the helping device, where the jammer harvests energy via wireless power transfer from the source node. The EH circuit (consisting of diode(s) and a passive low-pass filter [2, 26]) is very simple and cost effective. More importantly, such a design allows us to control the EH process for the jammer, which is very different from the conventional EH methods that rely on uncontrollable energy sources external to the communication network. We use a simple time-switching protocol [7, 27, 31], where WPT and WIT are separated in time. In this regard, the time allocation between PT and IT must be carefully designed in order to achieve the best possible throughput performance. We solve this problem by optimizing the jamming power, which indirectly gives the best time allocation for achieving the maximum throughput while satisfying a given secrecy constraint. We further optimize the

rate parameters of secure communication. All design parameters are optimized offline with only statistical knowledge of the wireless channels.

The main contributions of this chapter are summarized as follows:

- The novelty of the work lies in the design of a communication protocol that provides secure communication using an energy-constrained jamming node wirelessly powered by the source node. The protocol sets a target jamming power and switches between IT and PT depending on whether the available energy at the jammer meets the target power or not.

- We study the long-term behavior of the proposed communication protocol and derive a closed-form expression of the probability of IT. Based on this, we obtain the achievable throughput of the protocol with fixed-rate transmission.

- We optimize the rate parameters to achieve the maximum throughput while satisfying a constraint on the secrecy outage probability. Further design insights are obtained by considering the high SNR regime and the large number of antennas regime. We show that when the jammer has a single antenna, increasing the source transmit power quickly makes the throughput converge to an upper bound. However, when the jammer has multiple antennas, increasing the source transmit power or the number of jammer antennas improves the throughput significantly.

The results in this chapter have been presented in [29] and [100], which are listed again for ease of reference:

[29] **W. Liu**, X. Zhou, S. Durrani, P. Popovski, “Secure Communication with a Wireless-Powered Friendly Jammer," *IEEE Trans. Wireless Commun.*, vol. 15, no. 1, pp. 401–415, Jan. 2016.

[100] **W. Liu**, X. Zhou, S. Durrani, “Wireless-Powered Friendly Jammer for Physical Layer Security," in *Proc. IEEE WCSP*, Oct. 2015, pp. 1-5.

Chapter 4-SWIPT System with Practical Constraints

In Chapter 4, we consider a transmitter-receiver pair adopting SWIPT with either PS or TS scheme. In the PS scheme, the transmitter transfers modulated data signal to the receiver, then the receiver splits the received signal into two separate streams, one to draw energy and one to acquire information, respectively. In the TS scheme, for a given percentage of time, the transmitter transfers energy signal to the receiver, and the receiver draws energy from it. For the remaining portion of time, the transmitter transfers modulated data signal to the receiver, and the receiver acquires information from the signal. Assuming a Nakagami-m fading channel, we derive the average harvested power and the average number of successfully transmitted

symbol per unit time (i.e., the symbol success rate), at the receiver. We study the performance tradeoff between information decoding and EH using these metrics.

The main contributions of this chapter are summarized as follows:

- For the PS scheme, a modulation scheme with high peak-to-average power ratio (PAPR) leads to a better EH performance, e.g., M-PAM performs better than M-QAM, which performs better than M-PSK. This modulation performance order is very different from that of information decoding.

- For the TS scheme, we propose an optimal energy signal for the power transfer phase, which maximizes the available harvested energy. This is done by minimizing the duration of time for wireless power transfer since in this way one minimizes the amount of energy that is not harvested due to the impact of the RF-EH sensitivity level.

- For both the PS and TS schemes, we show that channel fading is beneficial for EH when the RF-EH sensitivity level is considered in the analysis. This is in contrast to previous studies, which ignored the sensitivity level.

The results in this chapter have been presented in [35], which is listed again for ease of reference:
[35] **W. Liu**, X. Zhou, S. Durrani, and P. Popovski,"SWIPT with practical modulation and RF energy harvesting sensitivity," in *Proc. ICC*, May 2016, pp. 1–7.

Chapter 5-A Novel SWIPT-Inspired Information Receiver

In Chapter 5, inspired by the PS-based SWIPT receiver, we consider a basic point-to-point communication system and revisit the design of the communication receiver. We propose a novel receiver with joint coherent and PD-based non-coherent processing. To the best of our knowledge, this is an open problem in the literature and it is not immediately clear whether joint processing will be better than either coherent or PD-based non-coherent processing alone. In this work, we show that it can in fact significantly improve the achievable rate and also reduce the symbol error rate (SER).

The main contributions of the chapter are summarized as follows:

- We propose a novel information receiver architecture for a K-antenna receiver called *splitting receiver*. The received signal at each antenna is split into two streams by a passive power splitter with a certain *splitting ratio*. One stream is processed by a conventional coherent detection (CD) circuit, and the other is processed by a (non-coherent) PD circuit, and then the $2K$ streams of processed signal are jointly used for information detection.

- As a variant of the splitting receiver, we also propose a simplified receiver where no power splitters are required and a fixed number of antennas are connected to CD circuits and the remaining antennas are connected to PD circuits. Analytically, the simplified receiver can be treated as a special case of a splitting receiver, where the splitting ratio at each antenna can only take 1 or 0.

- From an information-theoretic perspective, we model the channel introduced by the splitting receiver as a splitting channel. Assuming a Gaussian input to the splitting channel, in the high signal-to-noise-ratio (SNR) regime, we show analytically that: (i) The asymptotic maximum mutual information of the splitting channel is $3/2$ times that of either the coherent AWGN channel or the non-coherent AWGN channel, under the same average received signal power constraint. (ii) For a splitting receiver with a single receiver antenna, the asymptotic optimal power splitting ratio is $1/3$. (iii) For the simplified receiver with a large number of receiver antennas, connecting half the antennas to the CD circuits and the other half to the PD circuits is the optimal strategy.

- For transmissions based on practical modulations, we analyze the symbol decision region and the SER at the splitting receiver. Considering high SNR regime, we derive the SER expression for a general modulation scheme. The analytical results show that, compared with the conventional coherent receiver, the splitting receiver achieves asymptotic SER reduction by a factor of $M-1$ for M-PAM (pulse amplitude modulation) and $\sqrt{M}-1$ for M-QAM (quadrature amplitude modulation).

The results in this chapter have been presented in [101], which is listed again for ease of reference:
[101] **W. Liu**, X. Zhou, S. Durrani, P. Popovski, “A Novel Receiver Design with Joint Coherent and Non-Coherent Processing," in *IEEE Trans. Commun.*, vol. 65, no. 8, pp. 3479-3493, Aug. 2017.

Chapter 6-WPT-Based Backscatter Interference Networks

In Chapter 6, we consider a BackCom interference network comprising K coexisting pairs reader-tag. Each reader is provisioned with reliable power supply and performs both WPT and WIT to an intended tag that transmits data back to the reader by backscatter. Targeting this network, a novel multiple-access scheme, called *time-hopping full-duplex BackCom*, is proposed to simultaneously mitigate interference and enable full-duplex communication. These two features are realized by two components of the scheme.

The main contributions of this chapter are summarized as follows:

- We propose the novel *sequence-switch modulation* scheme where a bit is transmitted from a reader to a tag by switching between a pair of TH-SS sequences each containing a single random nonzero *on-chip*. Besides reducing the interference power by the TH-SS sequence [102], the design not only supports WPT for every symbol via the transmission of a nonzero chip but also satisfies the constraint of non-coherent detection at tags using energy detectors [103]. Each tag also continuously harvests energy from interference.

- To realize the full-duplex feature of time-hopping BackCom, the backward transmission from a tag to a reader is implemented such that each tag modulates the transmitted on-chip in the corresponding TH-SS sequence using the binary-phase-shift keying (BPSK) and a reader performs coherent demodulation to detect the bit thus transmitted. The BPSK modulation at a tag is operated by switching two impedances chosen according to the reflection coefficients having zero and 180-degree phase shifts. Compared with the previous design of full-duplex BackCom in [95], the proposed technique has the advantages of supporting symmetric full-duplex data rates and interference mitigation.

- The performance of the proposed time-hopping full-duplex BackCom scheme is thoroughly analyzed in this chapter in terms of *bit-error rate* (BER) for WIT and the expected *power-transfer rate* (PTR) and the *energy-outage probability* for WPT. The main results are summarized as follows:

    1) (Synchronous Transmissions) First, consider a typical link in a two-link BackCom interference system where the time-hopping full-duplex BackCom scheme is deployed. Assume chip synchronization between links. From the WIT perspective, the BERs for the forward (reader-to-tag) and the backward (tag-to-reader) transmissions are derived for both the cases of static and fading channels. The results quantify the effects of TH-SS on mitigating the original and regenerated interference.

    2) (Asynchronous Transmissions) Next, the assumption of chip synchronization is relaxed. The preceding results are extended to the case of (chip) asynchronous transmissions. It is found that the lack of synchronization between coexisting links degrades the BER performance for both forward and backward transmissions. For example, in the high SNR regime, the BER for backward transmission is approximately doubled. Nevertheless, the effects of asynchronous transmissions on WPT are negligible.

    3) (K-Link Systems) Last, the performance analysis for the two-link systems is generalized to a K-link system. It is shown that the BER for forward transmission as well as the expected PTRs are approximately proportional to $(K-1)$.

The results in this chapter have been presented in [62] and [104], which are listed again for ease of reference:

[62] **W. Liu**, K. Huang, X. Zhou, and S. Durrani, “Full-Duplex Backscatter Interference Networks Based on Time-Hopping Spread Spectrum", in *IEEE Trans. Wireless Commun.*, vol. 16, no. 7, pp. 4361-4377, July 2017.

[104] **W. Liu**, K. Huang, X. Zhou, and S. Durrani, “Time-Hopping Multiple-Access for Backscatter Interference Networks", to appear in *IEEE GLOBECOM 2017*.

Finally, Chapter 7 gives a summary of results and provides suggestions for future research work.

Chapter 2

Energy Harvesting Wireless Sensor Networks with Delay Constraints

Energy harvesting provides a means of greatly enhancing the lifetime of wireless sensor nodes. However, the randomness inherent in the EH process may cause significant delay for performing sensing operation and transmitting the sensed information to the sink. In this chapter, unlike most existing studies on the delay performance of EH sensor networks, where only the energy consumption of transmission is considered, we consider the energy costs of both sensing and transmission. Specifically, we consider an EH sensor that monitors some status property and adopts a harvest-then-use protocol to perform sensing and transmission. To comprehensively study the delay performance, we consider two complementary metrics and analytically derive their statistics: (i) update age - measuring the time taken from when information is obtained by the sensor to when the sensed information is successfully transmitted to the sink, i.e., how timely the updated information at the sink is, and (ii) update cycle - measuring the time duration between two consecutive successful transmissions, i.e., how frequently the information at the sink is updated. Our results show that the consideration of sensing energy cost leads to an important tradeoff between the two metrics: more frequent updates result in less timely information available at the sink.

This chapter is organized as follows. Section 2.1 presents the system model and the harvest-then-use protocol with a time window for retransmissions. Section 2.2 defines the proposed delay related metrics. Sections 2.3 and 2.4 are the main technical sections in the chapter which analyze the update age and update cycle, respectively. Section 2.5 presents the numerical results. Finally, Section 2.6 concludes the chapter.

2.1 System Model

We consider the transmission scenario where a sensor periodically transmits its sensed information to a sink, as illustrated in Fig. 2.1. The sensor is an EH node which harvests energy

from the ambient environment such as solar, wind, vibration or RF signals. The sensor has two main functions, i.e., sensing and transmission, each having individual energy cost. We assume half-duplex operation, i.e., sensing and transmission cannot occur at the same time. In order to perform either sensing or transmission, the sensor first needs to spend a certain amount of time on EH. The harvested energy is stored in a battery. We assume that the battery cannot charge and discharge at the same time [17]. In addition, the battery has sufficient charge capacity such that the amount of energy stored in the battery never reaches its maximum capacity. This assumption is reasonable since battery capacity typically ranges from joules to thousands of joules [4], while the energy level in the battery in our system is only in the μJ range as shown in Section 2.5.

Following the state-of-the-art EH sensor design practice [105], we adopt a time-slotted or block-wise operation. We assume that one sensing operation or one transmission is performed in one time block of duration T seconds.[1] At the beginning of each block, we assume that the sensor checks the battery energy state and makes a decision to perform either sensing, transmission, or energy harvesting. Thus, we define the following types of time blocks with the associated amount of energy cost/harvesting:

- Sensing Block (SB): the sensor samples the status information and then processes and packs sensed information into a data packet. The energy cost in an SB is denoted by $\mathcal{E}_{\mathrm{SB}}$.
- Transmission Block (TB): the sensor transmits the newest generated data packet (from the last sensing operation) to the sink with energy cost $\mathcal{E}_{\mathrm{TB}}$, i.e., the transmit power is $\mathcal{P}_{\mathrm{TB}} = \mathcal{E}_{\mathrm{TB}}/T$. Then the sink sends a one-bit feedback signal to the sensor to indicate successful packet reception. We assume that the time consumed for receiving the feedback signal at the sensor is negligible as compared to its packet transmission time. If the transmission is successful, we have a successful transmission block (STB); otherwise, we have a failed transmission block (FTB). We assume that successes/failures of each TB are mutually independent [34, 31]. *The probability of a TB being a FTB, i.e., transmission outage, is denoted by P_{out}.*
- Energy-harvesting block (EHB): the sensor harvests energy from the ambient environment and stores the energy in its battery.

2.1.1 Proposed Sensing and Transmission Protocol

Since the time-varying EH process results in randomness in the delay for performing sensing and transmission, we propose a harvest-then-use protocol with a time window for retransmis-

[1] In general a sensor may spend different amounts of time on one sensing operation [61]. Thus, the assumed protocol and analysis can be generalized to different sensing time durations other than T, which is outside the scope of this work.

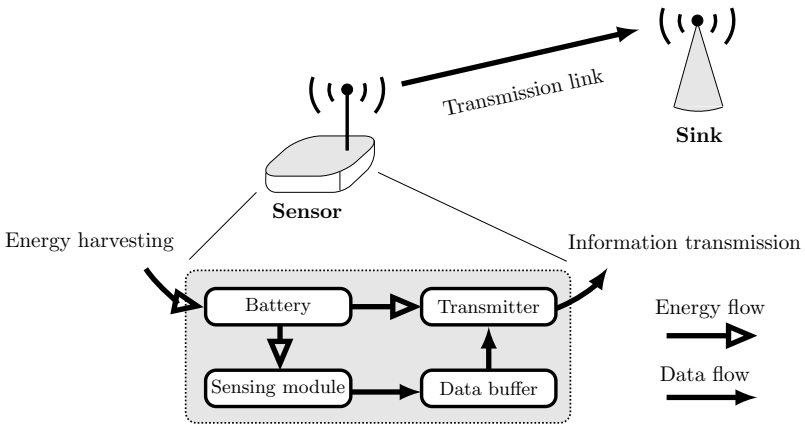

Figure 2.1: Illustration of system model and sensor components.

sions in order to improve the delay-related performance.

The protocol is motivated as follows. *Firstly*, considering the energy cost of sensing, it is necessary to harvest sufficient energy, $\mathcal{E}_{\mathrm{SB}}$, before sensing can occur. However, it is unwise to perform sensing as soon as the harvested energy reaches $\mathcal{E}_{\mathrm{SB}}$ because there will be insufficient energy left for transmission after the sensing operation. The time spent on EH due to insufficient energy for transmitting the sensed information will result in unnecessary delay. To avoid such delay, we define the condition for the sensing operation to be when the harvested energy in the battery exceeds $\mathcal{E}_{\mathrm{SB}} + \mathcal{E}_{\mathrm{TB}}$. In this way, a transmission of sensed information occurs immediately after the sensing operation (i.e., an SB is always followed by a TB). *Secondly*, in the event that the transmission is not successful due to the fading channel between the sensor and sink, we need to allow for retransmissions, which are a common feature in conventional (non-EH) WSNs [106]. In this chapter, we impose a time window for retransmissions to control the delay caused by unsuccessful transmissions because it is unwise to spend an indefinite amount of time trying to transmit outdated information. We denote W as the maximum number of time blocks after an SB, within which transmissions of the currently sensed information can take place. Since the first transmission attempt always happens immediately after the SB, the time window for retransmissions is $W - 1$ time blocks.

Under the proposed protocol, the sensor operates as follows:

1. First, the sensor uses several EHBs to harvest enough energy, $\mathcal{E}_{\mathrm{SB}} + \mathcal{E}_{\mathrm{TB}}$, and then an SB and a TB occur.

2. If the transmission in the TB is successful, i.e., we have a STB, the sensor harvests energy (taking several EHBs) for the next sensing period until the battery energy exceeds $\mathcal{E}_{\mathrm{SB}} + \mathcal{E}_{\mathrm{TB}}$.

3. If the transmission in the TB fails, i.e., we have a FTB, the sensor goes back to harvest

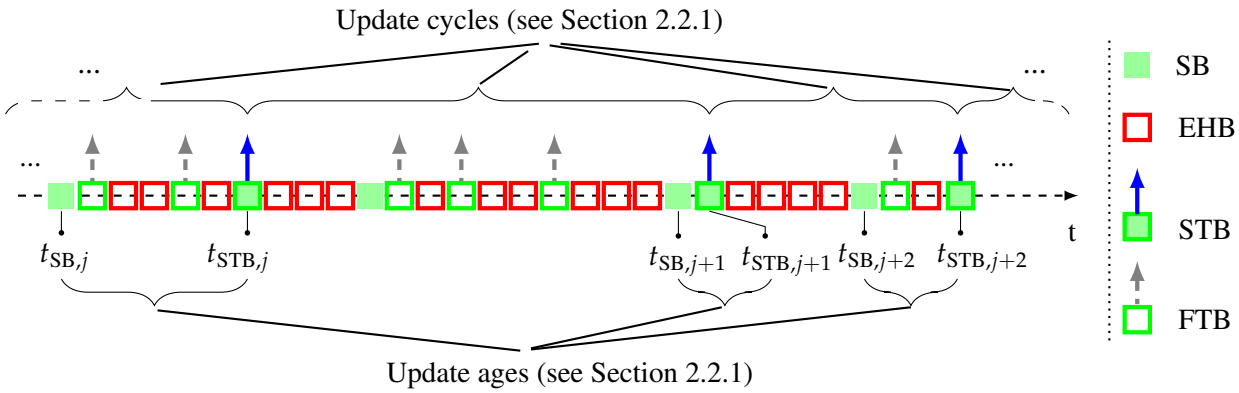

Figure 2.2: Illustration of update cycle and update age.

energy (taking several EHBs) and performs a retransmission when the battery energy exceeds $\mathcal{E}_{\mathrm{TB}}$.

4. Retransmission may occur several times until the sensed information is successfully transmitted to the sink or the time window for retransmissions $W-1$ is reached. Then, the data packet at the sensor is dropped and the sensor goes back to harvest the energy for a new sensing operation.

Fig. 2.2 illustrates this protocol with $W=7$. In the example shown, the first block in Fig. 2.2 is an SB, followed by two FTBs (and two EHBs in between). Since the third TB is a STB, the sensed information in the first SB is successfully transmitted to the sink. Then, the sensor uses three EHBs to harvest energy to conduct sensing in the next SB. After the second SB, there are three TBs during 7 time blocks, and all of them are FTBs. Thus, the retransmission process is terminated after $W=7$ is reached. As a result, the sensed information in the second SB is not transmitted to the sink. The time indices shown in Fig. 2.2 will be defined in the following section.

2.1.2 Proposed Models for Energy Arrival

In this chapter, we consider that the harvested energy in each EHB could either *remain constant* or *change* from block to block. The former is referred to as deterministic energy arrival, while the latter is referred to as random energy arrival.

Deterministic energy arrival is an appropriate model when the coherence time of the EH process is much larger than the duration of the entire communication session, such as EH by solar panel on clear days [9, 10, 11]. In this chapter, we denote this as *deterministic energy arrival process*. For tractability, we also assume that $\mathcal{E}_{\mathrm{SB}}$ and $\mathcal{E}_{\mathrm{TB}}$ represent integer multiples of the harvested energy by one EHB, ρ.

For random energy arrivals, we consider independent and identically distributed (i.i.d.) random energy arrival model[2] with a general probability distribution function for the amount of energy harvested in each EHB. This energy arrival model is referred to as *general random energy arrival process*. The previously considered exponential and gamma distributions in [34, 31, 17] become as special cases of the general probability distribution in this work. Since the exponential distribution is commonly studied for wireless power transfer using RF signals, we will also provide results for this important special case and referred to it as *exponential energy arrival process*.

2.2 Delay-Related Metrics

As described in the previous section, both sensing and (re)transmission requires a variable amount of EH time, which may result in significant delays in obtaining the sensed information at the sink. In this section, we consider two metrics to measure the delay performance of the considered sensing and transmission protocol.

For the convenience of describing the two metrics, as shown in Fig. 2.2, we use $t_{\mathrm{STB},j}$ to denote the block index for the jth STB during the entire sensing and transmission operation. Note that a successful transmission also induces an information update at the sink. Also, it is important to associate each transmission with its information content. To this end, we use $t_{\mathrm{SB},j}$ to denote the block index for the SB in which the sensed information is transmitted in the jth STB. In other words, status information sensed at $t_{\mathrm{SB},j}$ is successfully transmitted to the sink at $t_{\mathrm{STB},j}$. Next, we define two delay-related metrics, expressed in terms of the number of time blocks.

2.2.1 Update Age and Update Cycle

Definition 1. *For the jth STB, the update age is given by the number of time blocks from $t_{\mathrm{SB},j}$ to $t_{\mathrm{STB},j}$ (shown in Fig. 2.2). The jth update age is*

$$T_{\mathrm{UA},j} = t_{\mathrm{STB},j} - t_{\mathrm{SB},j},\ j = 1, 2, 3, ... \tag{2.1}$$

Remark 1. The update age measures the time elapsed from the generation of a status-information-containing packet at the sensor to the reception of the packet, i.e., status update, at the sink. This metric is referred to as the status update age in [65]. A larger update age implies that a more outdated status is received by the sink. The update age, which captures

[2]The i.i.d. energy arrival model is commonly considered in the literature [17, 18, 19]. There are other energy arrival models captures the temporal correlation of the energy arrival process, such as discrete-Markovian modeling [12, 13, 14], which are beyond the scope of this work.

the freshness of the updated status information, however, does not reflect the update frequency at the sink. Rather, the update frequency is captured by the update cycle which is presented below:

Definition 2 (Update cycle)**.** For the jth STB, the update cycle is given by the number of time blocks from $t_{\mathrm{STB},j-1}$ to $t_{\mathrm{STB},j}$ (shown in Fig. 2.2). The jth update cycle is

$$T_{\mathrm{UC},j} = t_{\mathrm{STB},j+1} - t_{\mathrm{STB},j},\ j = 1, 2, 3, ... \tag{2.2}$$

Remark 2. The update cycle measures the time elapsed from one status update at the sink to the next. The update cycle, however, does not reflect the update freshness at the sink. Unlike the update age, the update cycle takes into account the delay due to dropped data packets. Therefore, update cycle complements update age, and they jointly capture the update frequency and freshness, to provide comprehensive metrics on the delay performance of a status monitoring system.

2.2.2 Modeling Delay-Related Metrics as i.i.d. Random Variables

To model each of the update age/update cycle as i.i.d. random variables, we focus on the steady-state behavior as characterized in Lemma 1.

Lemma 1. *For a deterministic energy arrival process, the energy level after each TB is zero. For a general random energy arrival process with pdf containing at least one positive right-continuous point, $f(\epsilon)$, the steady-state distribution of the energy level after each TB has pdf*

$$g(\epsilon) = \frac{1}{\rho}\left(1 - F(\epsilon)\right), \tag{2.3}$$

where ρ is the average harvested energy, and $F(\epsilon)$ is the cumulative distribution function (cdf) corresponding to $f(\epsilon)$.

Proof. For a deterministic energy arrival process, Lemma 1 is straightforward. For a general random energy arrival process, the proof is given in Appendix A.2. □

According to the sensing and transmission protocol defined in the previous section, each SB is directly followed by a TB. From Lemma 1, the steady-state distribution of available energy after any TB is the same. Hence, the steady-state distribution of the available energy after $t_{\mathrm{STB},j}$ is the same for all j. Because the successes/failures of each TB are mutually independent, and $T_{\mathrm{UC},j}$ is determined by both the available energy after $t_{\mathrm{STB},j}$ and the successes/failures of the following TBs, $T_{\mathrm{UC},j}$ are i.i.d. for all j. Similarly, it is also easy to show that $T_{\mathrm{UA},j}$ are i.i.d. for all j. For convenience, we remove subscript j for T_{UC} and T_{UA} in (2.2) and (2.1), respectively.

2.3 Update Age

In this section, considering the dynamics of an energy arrival process and the probability of successful/failed transmission in our proposed harvest-then-use protocol, the update age for deterministic, general random and exponential energy arrival processes are analyzed.

2.3.1 Deterministic Energy Arrival Process

Theorem 1. *For a deterministic energy arrival process, the update age pmf is given by*

$$\Pr\{T_{\mathrm{UA}}=k\}=\frac{(1-P_{out})\,(P_{\mathrm{out}})^{n-1}}{P_{\mathrm{suc}}},\quad k=1+(n-1)\left(\frac{\mathcal{E}_{\mathrm{TB}}}{\rho}+1\right), \tag{2.4}$$

where

$$n=1,2,...\hat{n},\ \hat{n}=1+\left\lfloor\frac{W-1}{1+\frac{\mathcal{E}_{\mathrm{TB}}}{\rho}}\right\rfloor, P_{\mathrm{suc}}=1-(P_{\mathrm{out}})^{\hat{n}}, \tag{2.5}$$

and P_{out} is the probability of a TB being a FTB, defined in Section 2.1.

Proof. See Appendix A.4. □

From Theorem 1, the average update age, $\bar{T}_{\mathrm{UA}}$ for a deterministic energy arrival process is straightforwardly obtained as in Corollary 1.

Corollary 1. *For a deterministic energy arrival process, average update age is given by*

$$\bar{T}_{\mathrm{UA}}=\sum_{n=1}^{\hat{n}}\left(1+(n-1)\left(\frac{\mathcal{E}_{\mathrm{TB}}}{\rho}+1\right)\right)\frac{(1-P_{out})\,(P_{\mathrm{out}})^{n-1}}{P_{\mathrm{suc}}}, \tag{2.6}$$

where P_{suc} is given in (2.5)*.*

2.3.2 General Random Energy Arrival Process

Theorem 2. *For a general random energy arrival process, the update age pmf*[3] *is given by*

$$\Pr\{T_{\mathrm{UA}}=k\}=\begin{cases}\dfrac{1-P_{out}}{P_{\mathrm{suc}}}, & k=1,\\ \dfrac{(1-P_{out})}{P_{\mathrm{suc}}}\displaystyle\sum_{n=2}^{k}(P_{\mathrm{out}})^{n-1}\left(G_{k-n-1}((n-1)\mathcal{E}_{\mathrm{TB}})-G_{k-n}((n-1)\mathcal{E}_{\mathrm{TB}})\right), & 2\le k\le W,\end{cases} \tag{2.7}$$

[3] Although the general expression in Theorem 2 contains multiple integrals in Eq. (9), for special cases, such as deterministic and exponential energy arrival processeses, the results given in Theorems 1 and 3 are closed-form expressions.

where

$$P_{\text{suc}} = 1 - P_{out} + (1 - P_{out}) \sum_{l=2}^{W} \sum_{n=2}^{l} (P_{\text{out}})^{n-1} \left(G_{l-n-1}((n-1)\mathcal{E}_{\text{TB}}) - G_{l-n}((n-1)\mathcal{E}_{\text{TB}}) \right), \tag{2.8}$$

and

$$G_i(x) = \begin{cases} 1, & i = -1, \\ \int_0^x (g \underbrace{\star f \star f \star \ldots \star f}_{i \text{ convolutions}})(u) \mathrm{d}u, & i \geq 0. \end{cases} \tag{2.9}$$

$g(x)$ and $f(x)$ are defined in Lemma 1.

Proof. See Appendix A.4. □

From Theorem 2, the average update age, $\bar{T}_{\text{UA}}$ for a general random energy arrival process is obtained straightforwardly as in Corollary 2.

Corollary 2. *For a general random energy arrival process, average update age is given by*

$$\bar{T}_{\text{UA}} = \frac{1 - P_{out}}{P_{\text{suc}}} \left(1 + \sum_{l=2}^{W} l \sum_{n=2}^{l} (P_{\text{out}})^{n-1} \left(G_{l-n-1}((n-1)\mathcal{E}_{\text{TB}}) - G_{l-n}((n-1)\mathcal{E}_{\text{TB}}) \right) \right), \tag{2.10}$$

where P_{suc} is given in (2.8)*.*

2.3.3 Exponential Energy Arrival Process

Theorem 3. *For an exponential energy arrival process, the update age pmf is given by*

$$\Pr\{T_{\text{UA}} = k\} = \begin{cases} \frac{1 - P_{out}}{P_{\text{suc}}}, k = 1, \\ \frac{(1 - P_{out})}{P_{\text{suc}}} \sum_{n=2}^{k} (P_{\text{out}})^{n-1} \operatorname{Pois}\left(k - n, (n-1)\mathcal{E}_{\text{TB}}/\rho\right), 2 \leq k \leq W, \end{cases} \tag{2.11}$$

where

$$P_{\text{suc}} = 1 - P_{out} + (1 - P_{out}) \sum_{l=2}^{W} \sum_{n=2}^{l} (P_{\text{out}})^{n-1} \operatorname{Pois}\left(l - n, (n-1)\mathcal{E}_{\text{TB}}/\rho\right), \tag{2.12}$$

Proof. See Appendix A.4. □

From Theorem 3, the average update age, $\bar{T}_{\text{UA}}$ for an exponential energy arrival process is straightforwardly obtained as in Corollary 3.

Corollary 3. *For an exponential energy arrival process, average update age is given by*

$$\bar{T}_{\mathrm{UA}} = \frac{(1-P_{out})}{P_{\mathrm{suc}}} \left(1 + \sum_{l=2}^{W} l \sum_{n=2}^{l} \left(P_{\mathrm{out}}\right)^{n-1} \mathrm{Pois}\left(l-n,(n-1)\mathcal{E}_{\mathrm{TB}}/\rho\right) \right) \tag{2.13}$$

where P_{suc} *is given in* (2.12).

From Theorems 1, 2 and 3 and Corollaries 1, 2 and 3, we see that different energy arrival processes induce different pmfs and average values of update age. For benchmarking with the existing studies on delay without imposing a constraint on the time window for retransmissions [34], we let $W \to \infty$, so that all sensed information is eventually transmitted to the sink, the average update age is the same under different energy arrival processes as in Corollary 4.

Corollary 4. *For a deterministic or general random energy arrival process,* $\bar{T}_{\mathrm{UA}}$ *increases with* W*, and as* W *gets large, the asymptotic upper bound of* $\bar{T}_{\mathrm{UA}}$ *is independent with energy arrival distribution and is given by*

$$\lim_{W\to\infty} \bar{T}_{\mathrm{UA}} = 1 + \frac{P_{out}}{1-P_{out}} \left(\frac{\mathcal{E}_{\mathrm{TB}}}{\rho} + 1 \right). \tag{2.14}$$

Proof. See Appendix A.7. □

Remark 3. From the above analytical results, we have that:

i) From Theorems 1, 2 and 3, T_{UA} is independent of the energy cost of sensing, $\mathcal{E}_{\mathrm{SB}}$, because the delay is only affected by the energy harvesting and retransmissions that happen after the sensing operation. This might give the impression that energy cost of sensing does not affect delay. However, update age is only one of the two delay metrics, and the energy cost of sensing has important impacts on update cycle, which will be investigated in the next section.

ii) Allowing a larger window for retransmissions increases the average update age. This might suggest that retransmissions should be avoided, i.e., $W = 1$. However, the update age does not take into account cases where sensed information is not successfully transmitted to the sink. In this regard, the update cycle implicitly captures such cases.

2.4 Update Cycle

In this section, considering the dynamics of an energy arrival process and the probability of successful/failed transmission in our proposed harvest-then-use protocol, the update cycle for deterministic, general random and exponential energy arrival processes are analyzed.

2.4.1 Deterministic Energy Arrival Process

Theorem 4. *For a deterministic energy arrival process, the update cycle pmf is given by*

$$\begin{aligned}&\Pr\{T_{\mathrm{UC}}=k\}=(1-P_{out})\,(P_{\mathrm{out}})^{n-1+m\hat{n}},\\&k=\left(\frac{\mathcal{E}_{\mathrm{SB}}+n\mathcal{E}_{\mathrm{TB}}}{\rho}\right)+n+1+m\left(\frac{\mathcal{E}_{\mathrm{SB}}+\hat{n}\mathcal{E}_{\mathrm{TB}}}{\rho}+(\hat{n}+1)\right),\end{aligned}\tag{2.15}$$

where $n=1,2,...\hat{n}, m=0,1,2,...$, *and* $\hat{n}$ *is given in* (2.5).

Proof. See Appendix A.5. □

Corollary 5. *For a deterministic energy arrival process, average of update cycle is given by*

$$\begin{aligned}\bar{T}_{\mathrm{UC}}=&\frac{(P_{\mathrm{out}})^{\hat{n}}}{1-(P_{\mathrm{out}})^{\hat{n}}}\left(1+\hat{n}+\frac{\mathcal{E}_{\mathrm{SB}}+\hat{n}\mathcal{E}_{\mathrm{TB}}}{\rho}\right)+\frac{\mathcal{E}_{\mathrm{SB}}}{\rho}+1\\&+(1+\frac{\mathcal{E}_{\mathrm{TB}}}{\rho})\frac{1-P_{out}}{1-(P_{\mathrm{out}})^{\hat{n}}}\sum_{n=1}^{\hat{n}}(P_{\mathrm{out}})^{n-1}\,n.\end{aligned}\tag{2.16}$$

Proof. See Appendix A.6. □

2.4.2 General Random Energy Arrival Process

Theorem 5. *For a general random energy arrival process, the update cycle pmf is given by*

$$\Pr\{T_{\mathrm{UC}}=k\}=\sum_{m=0}^{\hat{m}}\left(\zeta(\mathcal{E}_{\mathrm{SB}}+\mathcal{E}_{\mathrm{TB}})\underbrace{*\zeta(\mathcal{E}_{\mathrm{SB}})*\cdots*\zeta(\mathcal{E}_{\mathrm{SB}})}_{m\ convolutions}\underbrace{*\vartheta*\cdots*\vartheta}_{m\ convolutions}*\iota\right)(k-m(1+W)-1),\qquad k=2,3,....\tag{2.17}$$

where $\hat{m}=\left\lfloor\frac{k-2}{W+1}\right\rfloor$, *and functions* $\zeta(\mathcal{E},i)$, $\iota(i)$ *and* $\vartheta(i)$ *are given by*

$$\zeta(\mathcal{E},i)=G_{i-1}(\mathcal{E})-G_i(\mathcal{E}),\tag{2.18a}$$

$$\iota(i)=P_{\mathrm{suc}}\Pr\{T_{\mathrm{UA}}=i\},\tag{2.18b}$$

$$\begin{aligned}\vartheta(i)=&P_{out}\,(G_{W+i-2}(\mathcal{E}_{\mathrm{TB}})-G_{W+i-1}(\mathcal{E}_{\mathrm{TB}}))\\&+\sum_{l=2}^{W}\sum_{n=2}^{l}(P_{\mathrm{out}})^{n}\,(G_{l-n-1}((n-1)\mathcal{E}_{\mathrm{TB}})-G_{l-n}((n-1)\mathcal{E}_{\mathrm{TB}}))\,(G_{W+i-l-1}(\mathcal{E}_{\mathrm{TB}})-G_{W+i-l}(\mathcal{E}_{\mathrm{TB}}))\,.\end{aligned}\tag{2.18c}$$

$\Pr\{T_{\mathrm{UA}}=i\}$, P_{suc} *and* $G_i(\mathcal{E})$ *are given in* (2.7), (2.8) *and* (2.9), *respectively.*

Proof. See Appendix A.5. □

Corollary 6. *For a general random energy arrival process, average update cycle is given by*

$$\bar{T}_{\mathrm{UC}} = \frac{1-P_{\mathrm{suc}}}{P_{\mathrm{suc}}}\left(\frac{\mathcal{E}_{\mathrm{SB}}}{\rho}+\bar{V}+W+1\right)+\frac{\mathcal{E}_{\mathrm{SB}}+\mathcal{E}_{\mathrm{TB}}}{\rho}+\bar{T}_{\mathrm{UA}}+1, \tag{2.19}$$

where P_{suc} and $\bar{T}_{\mathrm{UA}}$ are respectively given in (2.8) *and* (2.10)*, and*

$$\begin{aligned}\bar{V} =& \frac{P_{out}}{1-P_{\mathrm{suc}}}\left(\frac{\mathcal{E}_{\mathrm{TB}}}{\rho}-\sum_{i=0}^{W-2} i(G_{i-1}(\mathcal{E}_{\mathrm{TB}})-G_i(\mathcal{E}_{\mathrm{TB}}))-(W-1)\left(1-\sum_{i=0}^{W-2}(G_{i-1}(\mathcal{E}_{\mathrm{TB}})-G_i(\mathcal{E}_{\mathrm{TB}}))\right)\right)\\ &+\frac{1}{1-P_{\mathrm{suc}}}\sum_{l=2}^{W}\sum_{n=2}^{l}(P_{out})^n\left(G_{l-n-1}((n-1)\mathcal{E}_{\mathrm{TB}})-G_{l-n}((n-1)\mathcal{E}_{\mathrm{TB}})\right)\times\\ &\left(\frac{\mathcal{E}_{\mathrm{TB}}}{\rho}-\sum_{i=0}^{W-l-1} i\left(G_{i-1}(\mathcal{E}_{\mathrm{TB}})-G_i(\mathcal{E}_{\mathrm{TB}})\right)-(W-l)\left(1-\sum_{i=0}^{W-l-1}\left(G_{i-1}(\mathcal{E}_{\mathrm{TB}})-G_i(\mathcal{E}_{\mathrm{TB}})\right)\right)\right).\end{aligned} \tag{2.20}$$

Proof. See Appendix A.6. □

2.4.3 Exponential Energy Arrival Process

Theorem 6. *For an exponential energy arrival process, the update cycle pmf is given by*

$$\Pr\{T_{\mathrm{UC}}=k\}=\sum_{m=0}^{\hat{m}}\left(\zeta((m+1)\mathcal{E}_{\mathrm{SB}}+\mathcal{E}_{\mathrm{TB}})\underbrace{*\vartheta*\cdots*\vartheta}_{m\ \text{convolutions}}*\iota\right)(k-m(1+W)-1), \quad k=2,3,.... \tag{2.21}$$

where $\hat{m}=\left\lfloor\frac{k-2}{W+1}\right\rfloor$, and functions $\zeta(\mathcal{E},i)$, $\iota(i)$ and $\vartheta(i)$ are given by

$$\zeta(\mathcal{E},i)=\mathrm{Pois}\left(i,\mathcal{E}/\rho\right), \tag{2.22a}$$

$$\iota(i)=P_{\mathrm{suc}}\Pr\{T_{\mathrm{UA}}=i\}, \tag{2.22b}$$

$$\begin{aligned}\vartheta(i)=&P_{out}\mathrm{Pois}\left(W+i-1,\mathcal{E}_{\mathrm{TB}}/\rho\right)\\ &+\sum_{l=2}^{W}\sum_{n=2}^{l}(P_{\mathrm{out}})^n\,\mathrm{Pois}\left(l-n,(n-1)\mathcal{E}_{\mathrm{TB}}/\rho\right)\mathrm{Pois}\left(W+i-l,\mathcal{E}_{\mathrm{TB}}/\rho\right),\end{aligned} \tag{2.22c}$$

and $\Pr\{T_{\mathrm{UA}}=i\}$ and P_{suc} are given in (2.11) *and* (2.12)*, respectively.*

Proof. See Appendix A.5. □

Corollary 7. *For an exponential energy arrival process, average update cycle is given by*

$$\bar{T}_{\mathrm{UC}} = \frac{1-P_{\mathrm{suc}}}{P_{\mathrm{suc}}}\left(\frac{\mathcal{E}_{\mathrm{SB}}}{\rho}+\bar{V}+W+1\right)+\frac{\mathcal{E}_{\mathrm{SB}}+\mathcal{E}_{\mathrm{TB}}}{\rho}+\bar{T}_{\mathrm{UA}}+1, \tag{2.23}$$

where $\bar{T}_{\mathrm{UA}}$ *and* P_{suc} *are given in* (2.13) *and* (2.12)*, and*

$$\bar{V} = \frac{P_{out}}{1-P_{\mathrm{suc}}}\left(\frac{\mathcal{E}_{\mathrm{TB}}}{\rho} - \sum_{i=0}^{W-2} i\mathrm{Pois}\left(i, \frac{\mathcal{E}_{\mathrm{TB}}}{\rho}\right) - (W-1)\left(1 - \sum_{i=0}^{W-2}\mathrm{Pois}\left(i, \frac{\mathcal{E}_{\mathrm{TB}}}{\rho}\right)\right)\right)$$
$$+ \frac{1}{1-P_{\mathrm{suc}}}\sum_{l=2}^{W}\sum_{n=2}^{l}(P_{\mathrm{out}})^n \mathrm{Pois}\left(l-n, (n-1)\frac{\mathcal{E}_{\mathrm{TB}}}{\rho}\right)\times$$
$$\left(\frac{\mathcal{E}_{\mathrm{TB}}}{\rho} - \sum_{i=0}^{W-l-1} i\mathrm{Pois}\left(i, \frac{\mathcal{E}_{\mathrm{TB}}}{\rho}\right) - (W-l)\left(1 - \sum_{i=0}^{W-l-1}\mathrm{Pois}\left(i, \frac{\mathcal{E}_{\mathrm{TB}}}{\rho}\right)\right)\right). \tag{2.24}$$

Proof. See Appendix A.6. □

Similar to the case of update age, different energy arrival processes induces different pmfs and average values of update cycle. However, for benchmarking with the existing studies on delay without imposing a constraint on the maximum allowable retransmission time, when we consider removing the constraint of retransmission, i.e., $W \to \infty$, so that all sensed information is eventually transmitted to the sink, the average update cycle is the same under different energy arrival processes as in Corollary 8.

Corollary 8. *For a deterministic or general random energy arrival process,* $\bar{T}_{\mathrm{UC}}$ *decreases with W, and as W grows large, the asymptotic lower bound of* $\bar{T}_{\mathrm{UC}}$ *is independent with energy arrival distribution and is given by*

$$\lim_{W\to\infty} \bar{T}_{\mathrm{UC}} = 2 + \frac{\mathcal{E}_{\mathrm{SB}} + \mathcal{E}_{\mathrm{TB}}}{\rho} + \frac{P_{out}}{1-P_{out}}\left(\frac{\mathcal{E}_{\mathrm{TB}}}{\rho} + 1\right). \tag{2.25}$$

Proof. See Appendix A.7. □

Remark 4. From the above analytical results, we have that:

i) From Theorems 4, 5 and 6, we know that T_{UC} is affected by the energy cost of sensing, $\mathcal{E}_{\mathrm{SB}}$. A larger $\mathcal{E}_{\mathrm{SB}}$ means more EHBs are required to harvest a sufficient amount of energy to perform sensing operation(s) between adjacent STBs.

ii) A larger window for retransmissions shorten the average update cycle, because allowing more retransmissions increases the chance of having a successful transmission. This might suggest that it is also better to increase W to reduce the update cycle. But increasing W also increases the update age as discussed earlier. Therefore, there is clearly a tradeoff between the two metrics.

2.5 Numerical Results

In this section, we present numerical results for the update age and update cycle, using the results in Theorems 1, 2, 3, 4, 5 and 6, and Corollaries 1, 2, 3, 4, 5, 6, 7, and 8. The typical outdoor range for a wireless sensor is from 75 m to 100 m [107]. Hence, we set the distance between the sensor and the sink as $d = 90$ m and the path loss exponent for the sensor-sink transmission link as $\lambda = 3$ [34]. The duration of a time block is $T = 5$ ms[10]. The noise power at the sink is $\sigma^2 = -100$ dBm [31]. The average harvested power is 10 mW [108], i.e., average harvested energy per time block, $\rho = 50$ μJ. Unless otherwise stated, (i) we set the power consumption in each TB, $\mathcal{P}_{\text{TB}} = 40$ mW, i.e., $\mathcal{E}_{\text{TB}} = 200$ μJ. Note that this includes RF circuit consumption (main consumption) and the actual RF transmit power $\mathcal{P}_{\text{tx}} = -5$ dBm[4] and (ii) we set the power consumption in each SB as $\mathcal{P}_{\text{SB}} = 50$ mW[61], i.e., $\mathcal{E}_{\text{SB}} = 250$ μJ. In the following calculations, power and SNR related quantities use a linear scale. We assume that a transmission outage from the sensor to the sink occurs when the SNR at the sink γ, is lower than SNR threshold $\gamma_0 = 40$ dB [109]. The outage probability is

$$P_{\text{out}} = \Pr\left\{\gamma < \gamma_0\right\}. \tag{2.26}$$

The SNR at the sink is [110]

$$\gamma = \frac{|h|^2 \mathcal{P}_{\text{tx}}}{\Gamma d^{\lambda} \sigma^2}, \tag{2.27}$$

where h is the source-sink channel fading gain, $\Gamma = \frac{P_L(d_0)}{d_0^{\lambda}}$, is a path loss factor relative to reference distance d_0 of the antenna far field, and $P_L(d_0)$ is linear-scale path loss, which depends on the propagation environment [34]. Following [34, 31], we assume $\Gamma = 1$, for simplicity.

For the numerical results, we assume that h is block-wise Rayleigh fading. Using (2.27), the outage probability can be written as

$$P_{\text{out}} = 1 - \exp\left(-\frac{d^{\lambda}\sigma^2\gamma_0}{\mathcal{P}_{\text{tx}}}\right). \tag{2.28}$$

By applying (2.28) to the theorems and corollaries in Sections 2.3 and 2.4, we compute the expressions of the pmfs of T_{UA} and T_{UC} as well as their average values $\bar{T}_{\text{UA}}$ and $\bar{T}_{\text{UC}}$.

Pmfs of update age and update cycle with different energy arrival processes: First, we consider a deterministic energy arrival process with harvested energy in each EHB, ρ. Also we consider two special cases of the general random energy arrival process: (i) exponential energy arrival processes with average harvested energy in each EHB, ρ and (ii) random energy arrival processes with gamma distribution [17], $\text{Gamma}(0.05, 1000)$. We term this as the *gamma*

[4]The values we chose for $\mathcal{P}_{\text{TB}}$ and $\mathcal{P}_{\text{tx}}$ are typical for commercial sensor platforms, such as MICAz [107].

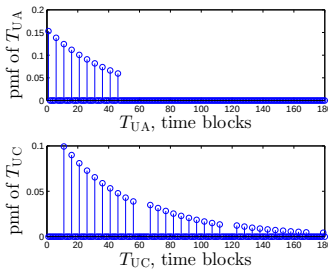

Figure 2.3: pmfs for $T_{\rm UA}$ and $T_{\rm UC}$ with deterministic energy arrival process.

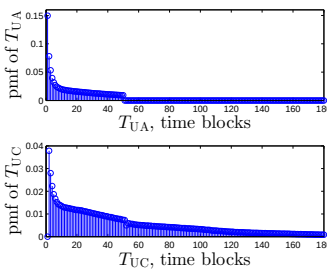

Figure 2.4: pmfs for $T_{\rm UA}$ and $T_{\rm UC}$ with gamma energy arrival process.

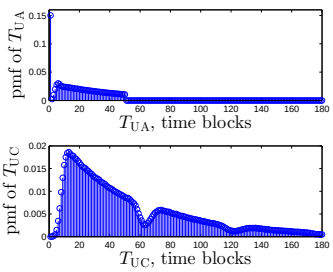

Figure 2.5: pmfs for $T_{\rm UA}$ and $T_{\rm UC}$ with exponential energy arrival process.

energy arrival process, and it is easy to verify that this gamma energy arrival process has the same average harvested energy in each EHB as the deterministic and exponential energy arrival processes.

Figs. 2.3-2.5 plot the pmfs of update age, $T_{\rm UA}$, and update cycle, $T_{\rm UC}$, for the deterministic, gamma and exponential energy arrival process, respectively. The analytical results are plotted using Theorems 1, 2, 3, 4, 5 and 6, and we set $W = 50$, i.e., the time window for retransmissions is $W - 1 = 49$ time blocks. In particular, in Fig. 2.4 the analytical pmfs of $T_{\rm UA}$ and $T_{\rm UC}$ for the general random arrival process are obtained using Theorems 2 and 5. The results in Figs. 2.4-2.5 also illustrate the importance of the general random energy arrival process, which is used in this work. This is because gamma and exponential energy arrival processes, which have been used in the literature [34, 31, 109, 17], are special cases of the general random energy arrival process. *We see that different energy arrival processes result in different pmfs of update age and update cycle. Hence, a statistical analysis of the two metrics will provide insight into the design of future EH WSNs.*

In the following figures (Figs. 6-9), we only present the numerical results for the average values of the two delay metrics, which have been presented in Corollaries 1, 2, 3, 4, 5, 6, 7, and 8.

Average update age and average update cycle with different energy arrival processes: Figs. 2.6 and 2.7 show the average update age, $\bar{T}_{\rm UA}$, and the average update cycle, $\bar{T}_{\rm UC}$, for different W, i.e., different time windows for retransmissions, $W - 1$, and energy arrival processes. The results in Figs. 2.6 and 2.7 are generated using Corollaries 1-4 and Corollaries 5-8, respectively. We can see that the different energy arrival models result in almost the same values of the average update age and especially the average update cycle. As the time window for retransmissions increases, the average update age increases monotonically and approaches its analytical upper bound given by Corollary 4, while the average update cycle decreases monotonically and approaches its analytical lower bound given by Corollary 8. *Thus, with a smaller time window for retransmissions, the updated status is more fresh, but the update frequency is*

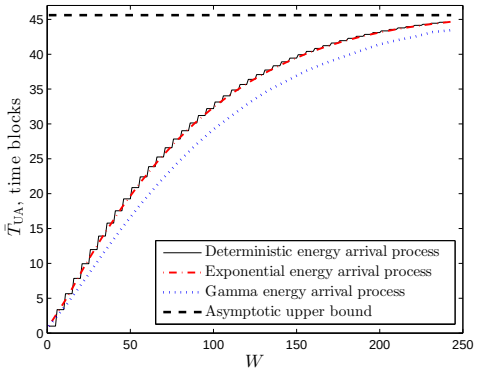

Figure 2.6: Average update age, $\bar{T}_{\mathrm{UA}}$, versus W, with different energy arrival processes.

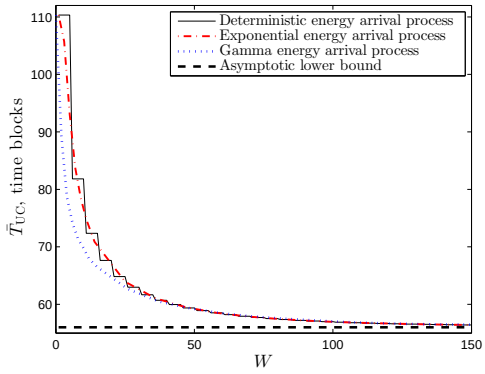

Figure 2.7: Average update cycle, $\bar{T}_{\mathrm{UC}}$, versus W, with different energy arrival processes.

lower.

Average update age and average update cycle with different average harvested power: Fig. 2.8 shows the average update age, $\bar{T}_{\mathrm{UA}}$, and the average update cycle, $\bar{T}_{\mathrm{UC}}$, for different average harvested power values, ρ, with an exponential energy arrival process. The results are plotted using Corollaries 3 and 7. For the update age, we see that when the average harvested power is very low, i.e., less than -2 dBm, the update age is one time block. This is expected since sufficiently low average harvested power cannot enable any retransmission during time window $W-1$, i.e., a packet is either successfully transmitted in the first transmission block right after the sensing block (an update age of one) or dropped due to no chance of retransmission. With an increase of average harvested power, retransmissions are enabled, which makes the update age increases beyond one. However, when the average harvested power is higher than 8 dBm, the average update age monotonically decreases with an increase of the average harvested power. This is as expected: the sensor requires fewer energy harvesting blocks to perform retransmissions, and hence, the sink is likely to receive the packet in a more timely manner (i.e., with a smaller update age). For the update cycle, we see that the average update cycle monotonically decreases with average harvested power. Again, this is expected since a higher average harvested power enables more transmission blocks within a certain time duration, and hence, more successful block transmissions are likely to occur within a given time duration, i.e., the update cycle decreases. Also we see that when the average harvested power is very high, i.e., $\rho \geq 30$ dBm, both update age and update cycle converge to constant values which can be obtained by letting $\rho \to \infty$ in Corollaries 3 and 7, respectively. *Thus, without changing the parameters of the communication protocol, the improvement in delay performance is limited when increasing the average harvested power.*

Effect of energy cost of sensing on average update cycle: We illustrate the effect of energy cost of sensing on average update cycle with exponential energy arrival process as a

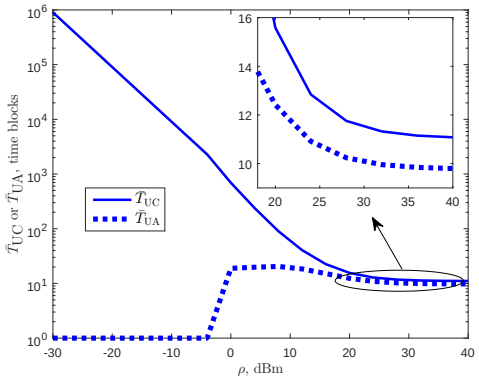

Figure 2.8: $\bar{T}_{\rm UC}$ and $\bar{T}_{\rm UA}$ versus ρ with exponential energy arrival process.

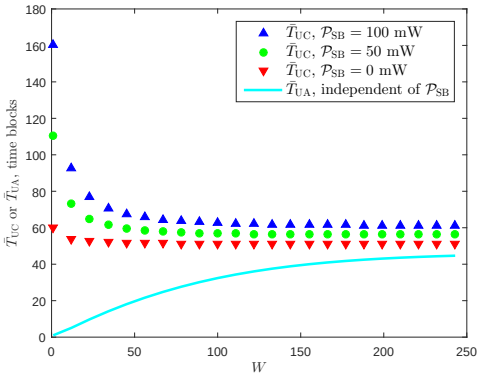

Figure 2.9: $\bar{T}_{\rm UC}$ and $\bar{T}_{\rm UA}$ versus W for different sensing power, $\mathcal{P}_{\rm SB}$.

special case of the random energy arrival process. Fig. 2.9 shows the average update age, $\bar{T}_{\rm UA}$, and the average update cycle, $\bar{T}_{\rm UC}$, as a function of W, with different energy cost of sensing, $\mathcal{P}_{\rm SB}$. The figure shows that the average update age increases as W increases (consistent with Fig. 2.6) but it does not change with the energy cost of sensing, i.e., *the energy cost of sensing has no effect on the update age*. This is in perfect agreement with our earlier observations and explanations provided in Remark 3. We can see that for a fixed value of W, the average update cycle increases as the sensing power consumption increases from 50 mW to 100 mW, i.e., *the higher the energy cost of sensing the lower update frequency.* This is in perfect agreement with our earlier observations and explanations provided in Remark 4. To place these results in context with existing studies in the literature that commonly ignore the energy cost of sensing, we also include the result with zero energy cost of sensing. When $\mathcal{P}_{\rm SB} = 0$ mW, we can see that $\bar{T}_{\rm UC}$ is almost constant around the value of 50 and does not vary much with W.

Tradeoff between average update age and average update cycle: Fig. 2.10 shows the tradeoff between average update age, $\bar{T}_{\rm UA}$, and average update cycle, $\bar{T}_{\rm UC}$ with exponential energy arrival process. The different points on the same curve are achieved with different W. We can see that when the energy cost of sensing is comparable to or larger than the energy cost of transmission, e.g., $\mathcal{P}_{\rm SB} = 50$ mW and $\mathcal{P}_{\rm SB} = 100$ mW, the reduction in $\bar{T}_{\rm UA}$ can result in a significant increase in $\bar{T}_{\rm UC}$, and vice versa. For example, when $\mathcal{P}_{\rm SB} = 100$ mW, decreasing $\bar{T}_{\rm UA}$ from 15 to 5 time blocks, causes the $\bar{T}_{\rm UC}$ to increase from 75 to 95 time blocks. However, when the energy cost for sensing is negligible, e.g., $\mathcal{P}_{\rm SB} = 0$ mW, such a tradeoff is almost barely noticeable. For example, decreasing $\bar{T}_{\rm UA}$ from 15 to 5 time blocks, results in $\bar{T}_{\rm UC}$ increasing by two time blocks, i.e., a significant change in $\bar{T}_{\rm UA}$ does not result in a noticeable change in $\bar{T}_{\rm UC}$. These trends in Fig. 2.10 are in accordance with our earlier observations in Remark 4. *Thus, with the consideration of sensing energy cost, an increase of update frequency is achieved at the expense of update freshness, and vice versa.*

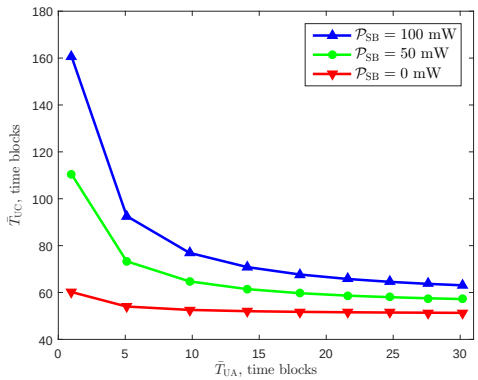

Figure 2.10: Tradeoff between $\bar{T}_{\rm UC}$ and $\bar{T}_{\rm UA}$.

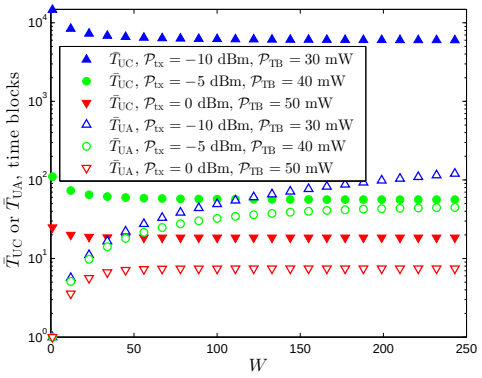

Figure 2.11: $\bar{T}_{\rm UC}$ and $\bar{T}_{\rm UA}$ versus W with different $\mathcal{P}_{\rm tx}$ and $\mathcal{P}_{\rm TB}$.

Effect of transmit power consumption on average update age and averge update cycle. Fig.2.11 shows the impact of power consumption on $\bar{T}_{\rm UA}$ and $\bar{T}_{\rm UC}$, for different values of transmit power $\mathcal{P}_{\rm TB}$ and RF transmit power $\mathcal{P}_{\rm tx}$, with an exponential energy arrival process. In reality, $\mathcal{P}_{\rm TB}$ and $\mathcal{P}_{\rm tx}$ do not have a linear relationship. Three pairs of typical values found in [25] are chosen. We see that both $\bar{T}_{\rm UA}$ and $\bar{T}_{\rm UC}$ decrease with $\mathcal{P}_{\rm TB}$ or $\mathcal{P}_{\rm tx}$. This is as expected: if the transmit power is small, $P_{\rm out}$ is high, resulting in a large number of retransmissions until the sensed information is successfully transmitted or $W-1$ time blocks are reached. As a result, $\bar{T}_{\rm UA}$ and $\bar{T}_{\rm UC}$ are large when the transmit power is small. *Thus, under these above parameter choices, a higher transmit power results in better delay performance.*

2.6 Summary

In this chapter, we have analysed the delay performance of an EH sensor network, focusing on the operation of a single EH sensor and its information transmission to a sink. The energy costs of both sensing and transmission were taken into account. Two metrics were proposed, namely the update age and update cycle. In order to limit the delay due to retransmissions, a time window for retransmissions was imposed. Using both a deterministic and a general random energy arrival model, the exact probability mass functions and the mean values of both metrics were derived. The results showed that the average update age increases while the average update cycle decreases with increasing retransmission window length. The average update age is independent of the energy cost of sensing but the average update cycle increases as the energy cost of sensing increases. In addition, a tradeoff between update age and update cycle was illustrated when the energy cost of sensing is comparable to the energy cost of transmission.

Chapter 3

Wireless Power Transfer Assisted Secure Communication

In Chapter 2, we have studied the delay issue of WSN powered by ambient EH. For low-complexity IoT applications, security if often another critical concern due to the lack of sophisticated cryptographic protection. To protect the desired communication security, physical layer techniques can be used as an extra layer of protection.

In this chapter, we propose to use a wireless-powered friendly jammer to enable low-complexity secure communication between a source node and destination node, in the presence of an eavesdropper. We consider a two-phase communication protocol with fixed-rate transmission. In the first phase, wireless power transfer is conducted from the source to the jammer. In the second phase, the source transmits the information-bearing signal under the protection of a jamming signal sent by the jammer using the harvested energy in the first phase. We analytically characterize the long-term behavior of the proposed protocol and derive a closed-form expression for the throughput. We further optimize the rate parameters for maximizing the throughput subject to a secrecy outage probability constraint. Our analytical results show that the throughput performance differs significantly between the single-antenna jammer case and the multi-antenna jammer case. For instance, as the source transmit power increases, the throughput quickly reaches an upper bound with single-antenna jammer, while the throughput grows unbounded with multi-antenna jammer. Our numerical results also validate the derived analytical results.

This chapter is organized as follows. Section 3.1 presents the system model. Section 3.2 proposes the secure communication protocol. Section 3.3 analyzes the protocol and derives the achievable throughput. Section 3.4 formulates an optimization problem for secrecy performance, and gives the optimal design. Section 3.5 presents numerical results. Finally, conclusions are given in Section 3.6.

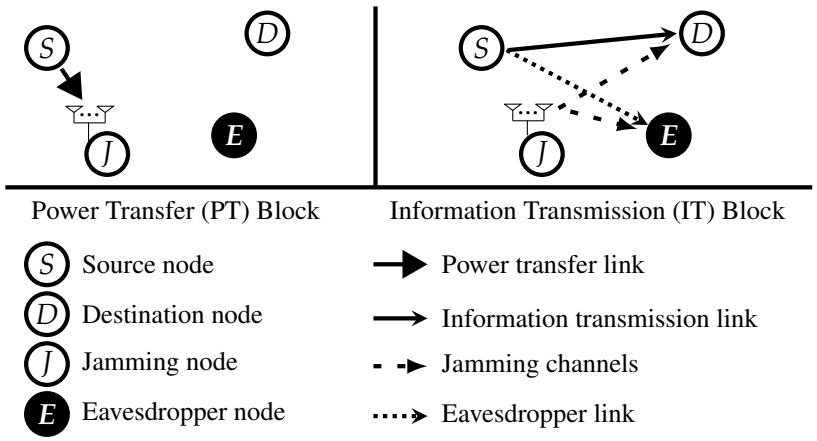

Figure 3.1: System model with illustration of the power transfer and information transmission phases.

3.1 System Model

We consider a communication scenario where a source node (S) communicates with a destination node (D) in the presence of a passive eavesdropper (E) with the help of a friendly jammer (J), as illustrated in Fig. 3.1. We assume that the jammer has N_J antennas ($N_J \geq 1$), while all the other nodes are equipped with a single antenna only. *Also we assume that the eavesdropper is just another communication node in the same network which should not have access to the information transmitted from the source to the destination. Therefore, the locations of all nodes are public knowledge.*

3.1.1 Jammer Model

In this work, the jammer is assumed to be an energy constrained node with no power of its own and having a rechargeable battery with infinite capacity [111, 112, 31]. In order to make use of the jammer, the source node wirelessly charges the jammer via wireless power transfer. Once the jammer harvests sufficient energy, it can be used for transmitting friendly jamming signals to enhance the security of the communication between the source and the destination. We assume that the jammer's energy consumption is dominated by the jamming signal transmission, while the other energy consumption, e.g., due to the signal processing, is relatively insignificant and hence ignored for simplicity [113, 26].

3.1.2 Channel Assumptions

We assume that all the channel links are composed of large-scale path loss with exponent λ and statistically independent small-scale Rayleigh fading. We denote the inter-node distance of links $S \to J$, $S \to D$, $J \to D$, $S \to E$ and $J \to E$ by d_{SJ}, d_{SD}, d_{JD}, d_{SE} and d_{JE}, respectively.

The fading channel gains of the links $S \to J$, $S \to D$, $S \to E$, $J \to E$ and $J \to D$ are denoted by $\boldsymbol{h}_{SJ}$, h_{SD}, h_{SE}, $\boldsymbol{h}_{JE}$, $\boldsymbol{h}_{JD}$, respectively. These fading channel gains are modeled as quasi-static frequency non-selective parameters, which means that they are constant over the block time of T seconds and independent and identically distributed between blocks. Consequently, each element of these complex fading channel coefficients are circular symmetric complex Gaussian random variables with zero mean and unit variance. In this chapter, we make the following assumptions on channel state information (CSI) and noise power:

- The CSI (h_{SD} and $\boldsymbol{h}_{JD}$) is assumed to be perfectly available at both the transmitter and receiver sides. This allows benchmark system performance to be determined.
- The CSI of the eavesdropper is only known to itself.
- Noise power at the eavesdropper is zero in line with [114], which corresponds to the worst case scenario.

3.1.3 Transmission Phases

The secure communication with wireless-powered jammer takes places in two phases: (i) power transfer (PT) phase and (ii) information transmission (IT) phase, as shown in Fig. 3.1. During the PT phase, the source transfers power to the jammer by sending a radio signal with power $\mathcal{P}_s$. The jammer receives the radio signal, converts it to a direct current signal and stores the energy in its battery. During the IT phase, the jammer sends jamming signal to the eavesdropper with power $\mathcal{P}_J$ by using the stored energy in the battery. At the same time, the source transmits the information signal to the destination with power $\mathcal{P}_s$ under the protection of the jamming signal. We define the *information transmission probability* as the probability of the communication process being in the IT phase and denote it by p_{tx}.

3.1.4 Secure Encoding and Performance Metrics

We consider confidential transmission between the source and the destination, using Wyner's wiretap code [115]. Specifically, there are two rate parameters of the wiretap code, namely the rate of codeword transmission, denoted by R_t, and the rate of secret information, denoted by R_s. The positive rate difference $R_t - R_s$ is the cost to provide secrecy against the eavesdropper. A M-length wiretap code is constructed by generating 2^{MR_t} codewords $x^M(w, v)$ of the length M, where $w = 1, 2, ..., 2^{MR_s}$ and $v = 1, 2, ..., 2^{M(R_t - R_s)}$. For each message index w, the value of v is selected randomly with uniform probability from $\left\{1, 2, ..., 2^{M(R_t - R_s)}\right\}$, and the constructed codeword to be transmitted is $x^M(w, v)$. Clearly, reliable transmission from the source to the destination cannot be achieved when $R_t > C_d$, where C_d denotes the channel capacity of $S \to D$ link. This event is defined as connection outage event. From [115], perfect

secrecy cannot be achieved when $R_t - R_s < C_e$, where C_e denotes the fading channel capacity of $S \rightarrow E$ link. This event is defined as secrecy outage event. In this work, we consider fixed rate transmission, which means R_t and R_s are fixed and chosen offline following [116, 117].

Since we consider quasi-static fading channel, we use outage based measures as considered in [116, 117]. Specifically, the connection outage probability and secrecy outage probability are defined, respectively, as

$$p_{co} = \Pr\{R_t > C_d\}, \tag{3.1}$$

$$p_{so} = \Pr\{R_t - R_s < C_e\}, \tag{3.2}$$

where $\Pr\{\nu\}$ denotes the probability for success of event ν. Note that the connection outage probability is a measure of the fading channel quality of the $S \rightarrow D$ link. Since the current CSI is available at the legitimate nodes, the source can always suspend transmission when connection outage occurs. This is easy to realize by one-bit feedback from the destination. Therefore, in this work, connection outage leads to suspension of IT but not decoding error at the destination.

Our figure of merit is the throughput, π, which is the average number of bits of confidential information received at the destination per unit time [118, 117], and is given by

$$\pi = p_{tx} R_s. \tag{3.3}$$

As we will see in Section 3.3, the information transmission probability p_{tx} contains the connection outage probability p_{co}.

It is important to note that a trade-off exists between throughput achieved at the destination and secrecy against the eavesdropper (measured by the secrecy outage probability). For example, increasing R_s would increase π in (3.3), but also increase p_{so} in (3.2). This trade-off will be investigated later in Section 3.4 in this chapter.

3.2 Proposed Secure Communication Protocol

In this section, we propose a simple fixed-power and fixed-rate secure communication protocol, which employs a wireless-powered jammer. Note that more sophisticated power and rate adaptation strategies at the source are possible but outside the scope of this chapter.

3.2.1 Transmission Protocol

We consider the communication in blocks of T seconds, each block being either a PT or an IT block. Intuitively, IT should happen when the jammer has sufficient energy for jamming

and the $S \rightarrow D$ link is in a good condition to ensure successful information reception at the destination. We define the two conditions for a block to be used for IT as follows:

- At the beginning of the block, the jammer has enough energy, $\mathcal{P}_J T$, to support jamming with power $\mathcal{P}_J$ over an information transmission block of T seconds, and
- the link $S \rightarrow D$ does not suffer connection outage, which means it can support the codeword transmission rate R_t from the source to the destination.

Note that both conditions are checked at the start of each block using the knowledge of the actual amount of energy in the jammer's battery and the instantaneous CSI of $S \rightarrow D$ link, and both conditions must be satisfied simultaneously for the block to be an IT block. If the first condition is not satisfied, then the block is used for PT and we refer to it as a *dedicated PT block*. If the first condition is satisfied while the second condition is not, then the block is still used for PT but we refer it as an *opportunistic PT block*. Note that $\mathcal{P}_J$ is a design parameter in the proposed protocol.

For an accurate description of the transmission process, we define a PT-IT cycle as a sequence of blocks which either consists of a single IT block or a sequence of PT blocks followed by an IT block. Let discrete random variables X and Y ($X, Y = 0, 1, 2, ...$) denote the number of dedicated and opportunistic PT blocks in a PT-IT cycle, respectively. In our proposed protocol, the following four types of PT-IT cycles are possible:

1. $X > 0,\ Y = 0$, i.e., PT-IT cycle contains X dedicated PT blocks followed by an IT block. This is illustrated as the kth PT-IT cycle in Fig. 3.2.
2. $X > 0,\ Y > 0$, i.e., PT-IT cycle contains X dedicated PT blocks and Y opportunistic PT blocks followed by an IT block. This is illustrated as the $(k+1)$ th PT-IT cycle in Fig. 3.2.
3. $X = 0,\ Y > 0$, i.e., PT-IT cycle contains Y opportunistic PT blocks followed by an IT block. This is illustrated as the $(k+2)$ th PT-IT cycle in Fig. 3.2.
4. $X = 0,\ Y = 0$, i.e., PT-IT cycle contains one IT block only. This is illustrated as the $(k+3)$ th PT-IT cycle in Fig. 3.2.

3.2.2 Long-Term Behavior

We are interested in the long-term behavior (rather than that during the transition stage) of the communication process determined by our proposed protocol. After a sufficiently long time, the behavior of the communication process falls in one of the following two cases:

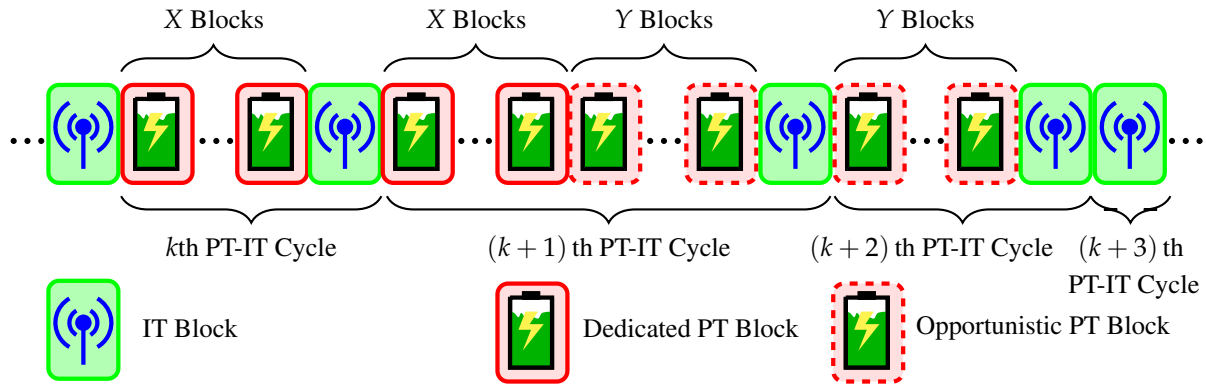

Figure 3.2: Illustration of four types of PT-IT cycles.

- *Energy Accumulation*: In this case, on average, the energy harvested at the jammer during opportunistic PT blocks is higher than the energy required during an IT block. Thus, after a long time has passed, the energy steadily accumulates at the jammer and there is no need for dedicated PT blocks (the harvested energy by opportunistic PT blocks fully meet the energy consumption requirement at the jammer). Consequently, only PT-IT cycles with $X = 0$ can occur.

- *Energy Balanced*: In this case, on average, the energy harvested at the jammer during opportunistic PT blocks is lower than the energy required during an IT block. Thus, after a long time has passed, dedicated PT blocks are sometimes required to make sure that the energy harvested from both dedicated and opportunistic PT blocks equals the energy required for jamming in IT blocks on average. Consequently, all four types of PT-IT cycles can occur.

Remark 5. *Although we have assumed infinite battery capacity for simplicity in the analysis, it is important to discuss the effect on finite battery capacity. In fact, our analytical result is valid for finite battery capacity as long as the battery capacity in much higher than the required jamming energy* $\mathcal{P}_J T$.[1] *To be specific:*

i) When the communication process is in the energy accumulation case, the harvested energy steadily accumulates at the jammer, thus, the energy level will always reach the maximum battery capacity after a sufficient long time and stay near the maximum capacity for the remaining time period. This means that the energy level in the battery is always much larger than the required jamming energy level. Thus, having a finite battery capacity has hardly any effect on the communication process, as compared with infinite capacity.

[1] From [4], for typical energy storage, including super-capacitor or chemical battery, the capacity easily reaches several Joules, or even several thousand Joules. While in our work, from the simulation results to be presented later, the optimal value of required jamming energy is only several micro Joules. Therefore, it is reasonable to say that the battery capacity in practice is much larger than the required jamming energy.

ii) When the communication process is in the energy balanced case, on average, the harvested energy equals the required (consumed) jamming energy. Therefore, the energy level mostly stays between zero and the required jamming energy level, $\mathcal{P}_J T$. This also means that the energy level in the battery can hardly approach the maximum battery capacity. Thus, having a finite battery capacity has almost no effect on the communication process, compared with infinite capacity.

Therefore, although our analysis is based on the assumption of infinite battery capacity, the analytical results still hold with practical finite battery capacity.

In the next section, the mathematical model for the proposed protocol is presented. The boundary condition between the energy accumulation and energy balanced cases is derived. In Section 3.5, we will also verify the long-term behavior through simulations.

3.3 Protocol Analysis

In this section, we analyze the proposed secure communication protocol and derive the achievable throughput for the proposed secure communication protocol.

3.3.1 Signal Model

In a PT block, the source sends radio signal x_{SJ} with power $\mathcal{P}_s$. Thus, received signal at the jammer, $\boldsymbol{y}_J$ is given by

$$\boldsymbol{y}_J = \frac{1}{\sqrt{d_{SJ}^{\lambda}}} \sqrt{\mathcal{P}_s} \boldsymbol{h}_{SJ} x_{SJ} + \boldsymbol{n}_J, \tag{3.4}$$

where x_{SJ} is the normalized signal from the source in an PT block, and $\boldsymbol{n}_J$ is the additive white Gaussian noise (AWGN) at the jammer. From equation (4), by ignoring the noise power, the harvested energy is given by [22]

$$\rho_J(\boldsymbol{h}_{SJ}) = \eta \left| \frac{1}{\sqrt{d_{SJ}^{\lambda}}} \sqrt{\mathcal{P}_s} \boldsymbol{h}_{SJ} \right|^2 T,$$

where η is the energy conversion efficiency of RF-DC conversion operation for energy storage at the jammer. Because the elements of $\boldsymbol{h}_{SJ}$ are independent identically distributed complex Gaussian random variable with normalized variance, we have $\mathbb{E}\left[|\boldsymbol{h}_{SJ}|^2\right] = N_J$. Therefore, the average harvested energy ρ_J is given by

$$\rho_J = \mathbb{E}\left[\rho_J(\boldsymbol{h}_{SJ})\right] = \mathbb{E}\left[\eta \frac{1}{d_{SJ}^{\lambda}} \mathcal{P}_s \left|\boldsymbol{h}_{SJ}\right|^2 T\right] = \frac{\eta N_J \mathcal{P}_s T}{d_{SJ}^{\lambda}}. \tag{3.5}$$

During an IT block, the source transmits information-carrying signal with the protection from the jammer. The jammer applies different signaling methods depending on its number of antennas. When $N_J = 1$, the jammer sends a noise-like signal x_{JD} with power $\mathcal{P}_J$, affecting both the destination and the eavesdropper. When $N_J > 1$, by using the artificial interference generation method in [114], the jammer generates an $N_J \times (N_J - 1)$ matrix $\boldsymbol{W}$ which is an orthonormal basis of the null space of $\boldsymbol{h}_{JD}$, and also an vector $\boldsymbol{v}$ with $N_J - 1$ independent identically distributed complex Gaussian random elements with normalized variance.[2] Then the jammer sends $\boldsymbol{W}\boldsymbol{v}$ as jamming signal. Thus, the received signal at the destination, y_D, is given by

$$y_D = \begin{cases} \frac{\sqrt{\mathcal{P}_s}}{\sqrt{d_{SD}^{\lambda}}} h_{SD} x_{SD} + \frac{\sqrt{\mathcal{P}_J}}{\sqrt{d_{JD}^{\lambda}}} h_{JD} x_{JD} + n_d, & N_J = 1, \\ \frac{\sqrt{\mathcal{P}_s}}{\sqrt{d_{SD}^{\lambda}}} h_{SD} x_{SD} + n_d, & N_J > 1, \end{cases} \tag{3.6}$$

where x_{SD} is the normalized information signal from the source in an IT block and n_d is the AWGN at the destination with variance σ_d^2. *Note that for $N_J > 1$, the received signal is free of jamming, because the jamming signal is transmitted into the null space of $\boldsymbol{h}_{JD}$.*

Similarly, the received signal at the eavesdropper, y_E, is given by

$$y_E = \begin{cases} \frac{\sqrt{\mathcal{P}_s}}{\sqrt{d_{SE}^{\lambda}}} h_{SE} x_{SD} + \frac{\sqrt{\mathcal{P}_J}}{\sqrt{d_{JE}^{\lambda}}} h_{JE} x_{JD} + n_e, & N_J = 1, \\ \frac{\sqrt{\mathcal{P}_s}}{\sqrt{d_{SE}^{\lambda}}} h_{SE} x_{SD} + \frac{\sqrt{\mathcal{P}_J}}{\sqrt{d_{JE}^{\lambda}}} \boldsymbol{h}_{JE} \frac{\boldsymbol{W}\boldsymbol{v}}{\sqrt{N_J - 1}} + n_e, & N_J > 1, \end{cases} \tag{3.7}$$

where n_e is the AWGN at the eavesdropper which we have assumed to be 0 as a worst-case scenario.

From (3.6), the SINR at the destination is

$$\gamma_d = \begin{cases} \frac{\frac{\mathcal{P}_s}{d_{SD}^{\lambda}} |h_{SD}|^2}{\sigma_d^2 + \frac{\mathcal{P}_J}{d_{JD}^{\lambda}} |h_{JD}|^2}, & N_J = 1 \\ \frac{\mathcal{P}_s |h_{SD}|^2}{d_{SD}^{\lambda} \sigma_d^2}, & N_J > 1 \end{cases} \tag{3.8}$$

Hence the capacity of $S \to D$ link is given as $C_d = \log_2(1 + \gamma_d)$.

Since $|h_{SD}|$ and $|h_{JD}|$ are Rayleigh distributed, $|h_{SD}|^2$ and $|h_{JD}|^2$ are exponential dis-

[2] With the assumption of zero additive noise at the eavesdropper, the null-space artificial jamming scheme works when the number of jamming antennas in larger than the number of eavesdropper antennas, as discussed in [36]. This condition is satisfied in this work when $N_J > 1$.

tributed and γ_d has the cumulative distribution function (cdf) as

$$F_{\gamma_d}(x) = \begin{cases} 1 - \dfrac{e^{-\frac{x}{\rho_d}}}{1+\varphi x}, & N_J = 1, \\ 1 - e^{-\frac{x}{\rho_d}}, & N_J > 1, \end{cases} \tag{3.9}$$

where

$$\varphi = \frac{\mathcal{P}_J}{\mathcal{P}_s} \frac{d_{SD}^{\lambda}}{d_{JD}^{\lambda}}. \tag{3.10}$$

For convenience, we define the SNR at the destination (without jamming noise) as

$$\rho_d \triangleq \frac{\mathcal{P}_s}{d_{SD}^{\lambda} \sigma_d^2}. \tag{3.11}$$

From (3.7), the SINR at the eavesdropper is

$$\gamma_e = \begin{cases} \dfrac{1}{\phi} \dfrac{|h_{SE}|^2}{|h_{JE}|^2}, & N_J = 1, \\ \dfrac{1}{\phi} \dfrac{|h_{SE}|^2}{\frac{\|\boldsymbol{h}_{JE}\mathbf{W}\|^2}{N_J - 1}}, & N_J > 1, \end{cases} \tag{3.12}$$

where

$$\phi = \frac{\mathcal{P}_J}{\mathcal{P}_s} \frac{d_{SE}^{\lambda}}{d_{JE}^{\lambda}}. \tag{3.13}$$

Hence, the capacity of $S \to E$ link is given as $C_e = \log_2(1 + \gamma_e)$. Using the fact that h_{SE}, h_{JE} and the entries of $\boldsymbol{h}_{JE}\mathbf{W}$ are independent and identically distributed (i.i.d.) complex Gaussian variables, from [118], γ_e has the probability density function (pdf) as

$$f_{\gamma_e}(x) = \begin{cases} \phi \left(\dfrac{1}{\phi x + 1} \right)^2, & N_J = 1, \\ \phi \left(\dfrac{N_J - 1}{\phi x + N_J - 1} \right)^{N_J}, & N_J > 1. \end{cases} \tag{3.14}$$

Using the pdf of γ_e in (3.14), the secrecy outage probability defined in (3.2) can be evaluated.

3.3.2 Information Transmission Probability

Focusing on the long-term behavior, we analyze the proposed secure communication protocol and derive the information transmission probability p_{tx}, which in turn gives the throughput in (3.3). Note that p_{tx} is the probability of an arbitrary block being used for IT. As discussed in the last section, the communication process falls in either energy accumulation or energy balanced

case. Thus, p_{tx} will have different values for the two different cases. First we mathematically characterize the condition of being in either case in the lemma below.

Lemma 2. The communication process with the proposed secure communication protocol leads to energy accumulation if

$$\frac{p_{co}}{1-p_{co}} > \frac{\mathcal{P}_J T}{\rho_J} \tag{3.15}$$

is satisfied. Otherwise, the communication process is energy balanced.

Proof. See Appendix B.1. □

Using Lemma 2, we can find the general expression for p_{tx} as presented in Theorem 7 below.

Theorem 7. The information transmission probability for the proposed secure communication protocol is given by

$$p_{tx} \triangleq 1-(1-p_{co})(1-p_{so}) = \frac{1}{1+\max\left\{\frac{\mathcal{P}_J T}{\rho_J}, \frac{p_{co}}{1-p_{co}}\right\}}, \tag{3.16}$$

where

$$p_{co} = \begin{cases} 1-\dfrac{e^{-\frac{2^{R_t}-1}{\rho_d}}}{1+\frac{\mathcal{P}_J}{\mathcal{P}_s}\frac{d_{SD}^{\lambda}}{d_{JD}^{\lambda}}\left(2^{R_t}-1\right)}, & N_J = 1, \\ 1-e^{-\frac{2^{R_t}-1}{\rho_d}}, & N_J > 1. \end{cases} \tag{3.17}$$

Proof. We first model the communication process in both energy accumulation and energy balanced cases as Markov chains and show the ergodicity of the process. This then allows us to derive the stationary probability of a block being used for IT either directly or by using time averaging. The detailed proof can be found in Appendix B.2. □

By substituting (3.16) in (3.3), we obtain the achievable throughput of the proposed protocol.

3.4 Optimal Design for Throughput

In the last section, we derived the achievable throughput with given design parameters. Specifically the jamming power $\mathcal{P}_J$ is a design parameter of the protocol. A different value of $\mathcal{P}_J$ results in a different impact on the eavesdropper's SINR, hence leads to different secrecy outage probability defined in (3.2). Also the rate parameters of the wiretap code, R_t and R_s, affect the secrecy outage probability. Hence, it is interesting to see how one can optimally design

these parameters to maximize the throughput while keeping the secrecy outage probability below a prescribed threshold. In this section, we present such an optimal fixed-rate design of the proposed secure communication protocol. The optimization is done offline, hence does not increase the complexity of the proposed protocol.

3.4.1 Problem Formulation

We consider the optimal secure communication design as follows:

$$\begin{aligned} &\max_{\mathcal{P}_J, R_t, R_s} \quad \pi \\ &\text{s.t.} \quad p_{so} \leq \varepsilon,\ \mathcal{P}_J \geq 0,\ R_t \geq R_s \geq 0, \end{aligned} \tag{3.18}$$

where ε is the secrecy outage probability constraint. This design aims to maximize the throughput with the constraint on the secrecy outage probability[3].

From (3.2), the secrecy outage probability should meet the requirement that

$$p_{so} = \Pr\left\{R_t - R_s < \log_2\left(1+\gamma_e\right)\right\} \leq \varepsilon. \tag{3.19}$$

By substituting (3.14) into (3.19), and after some simplification manipulations, the jamming power $\mathcal{P}_J$ should satisfy the condition

$$\mathcal{P}_J \geq \hat{\mathcal{P}}_J \triangleq \begin{cases} \mathcal{P}_s \dfrac{d_{JE}^{\lambda}}{d_{SE}^{\lambda}} \dfrac{\left(\varepsilon^{-1}-1\right)}{2^{R_t-R_s}-1}, & N_J = 1, \\ \mathcal{P}_s \dfrac{d_{JE}^{\lambda}}{d_{SE}^{\lambda}} \dfrac{\left(N_J-1\right)\left(\varepsilon^{-\frac{1}{N_J-1}}-1\right)}{2^{R_t-R_s}-1}, & N_J > 1. \end{cases} \tag{3.20}$$

From (3.16), we can see that π decreases with $\mathcal{P}_J$. Thus, the maximum π is obtained when

$$\mathcal{P}_J^{\star} = \hat{\mathcal{P}}_J. \tag{3.21}$$

The jammer harvests energy from the source in each PT block. The dynamically harvested and accumulated energy at the jammer must exceed $\mathcal{P}_J^{\star} T$, before it can be used to send jamming signal with power $\mathcal{P}_J^{\star}$.

Substituting (3.21) and (3.16), into (3.3), the throughput with optimal jamming power $\mathcal{P}_J^{\star}$

[3]Note that the problem is to optimize a long-term performance and does not require the instantaneous CSI.

satisfying the secrecy outage constraint of $p_{so} \leq \varepsilon$, is given by

$$\pi\left(\mathcal{P}_J^{\star}\right) = \begin{cases} \dfrac{R_s}{1+\max\left\{\underbrace{\dfrac{d_{SJ}^{\lambda}}{\eta}\dfrac{d_{JE}^{\lambda}}{d_{SE}^{\lambda}}\dfrac{\left(\varepsilon^{-1}-1\right)}{2^{R_t-R_s}-1}}_{(a)}, \underbrace{e^{\frac{\left(2^{R_t}-1\right)}{\rho_d}}\left(1+\dfrac{d_{JE}^{\lambda}}{d_{SE}^{\lambda}}\dfrac{d_{SD}^{\lambda}}{d_{JD}^{\lambda}}\dfrac{\left(\varepsilon^{-1}-1\right)}{2^{R_t-R_s}-1}\left(2^{R_t}-1\right)\right)-1}_{(b)}\right\}}, & N_J = 1, \\ \dfrac{R_s}{1+\max\left\{\underbrace{\dfrac{d_{SJ}^{\lambda}}{N_J\eta}\dfrac{d_{JE}^{\lambda}}{d_{SE}^{\lambda}}\dfrac{\left(N_J-1\right)\left(\varepsilon^{-\frac{1}{N_J-1}}-1\right)}{2^{R_t-R_s}-1}}_{(a)}, \underbrace{e^{\frac{2^{R_t}-1}{\rho_d}}-1}_{(b)}\right\}}, & N_J > 1. \end{cases} \tag{3.22}$$

Note that the terms (a) and (b) in (3.22) are the terms $\frac{\mathcal{P}_J T}{\rho_J}$ and $\frac{p_{co}}{1-p_{co}}$ in Lemma 2, respectively. Thus, if we choose (R_t, R_s) to make $(a) > (b)$, the communication process is energy balanced; while if (R_t, R_s) make $(a) \leq (b)$, the communication process leads to energy accumulation. For analytical convenience, we define three 2-dimension rate regions:

$$\mathcal{D}_1 \triangleq \left\{(R_t, R_s)\,|(a) < (b), R_t \geq R_s \geq 0\right\}, \tag{3.23}$$

$$\hat{\mathcal{D}} \triangleq \left\{(R_t, R_s)\,|(a) = (b), R_t \geq R_s \geq 0\right\}, \tag{3.24}$$

$$\mathcal{D}_2 \triangleq \left\{(R_t, R_s)\,|(a) > (b), R_t \geq R_s \geq 0\right\}, \tag{3.25}$$

where rate region $\hat{\mathcal{D}}$ denotes the boundary between regions $\mathcal{D}_1$ and $\mathcal{D}_2$. From the discussion above, if $(R_t, R_s) \in \mathcal{D}_1$, the communication process leads to energy accumulation, while if $(R_t, R_s) \in \mathcal{D}_2 \cup \hat{\mathcal{D}}$, it is energy balanced.

Using (3.22), the optimization problem in (3.18) is equivalently converted to the following problem:

$$\begin{aligned} &\max_{R_t, R_s} \ \pi\left(\mathcal{P}_J^{\star}\right) \\ &\text{s.t. } R_t \geq R_s \geq 0. \end{aligned} \tag{3.26}$$

The optimization problem in (3.26) can be solved with global optimal solution. The solution for $N_J = 1$ and $N_J > 1$ are presented in the next two subsections.

3.4.2 Optimal Rate Parameters with Single-Antenna Jammer

Proposition 1. When $N_J = 1$, the optimal R_t and R_s can be obtained by using the following facts:

IF $(R_t^\star, R_s^\star) \in \mathcal{D}_1$, i.e., the case of energy accumulation, $R_s^\star$ is the unique root of equation (monotonically increasing on the left side):

$$k_2\left(2^{R_s}+\frac{2^{R_s}-1}{\xi}\right)\left(R_s\ln 2-1+\frac{R_s\ln 2}{\xi}\right)=1, \tag{3.27}$$

and $R_t^\star$ is given by

$$R_t^\star = R_s^\star + \log_2\left(1+\xi^\star\right), \tag{3.28}$$

where

$$\xi=\frac{1}{2}\left(-\frac{k_2\left(2^{R_s}-1\right)}{1+k_2 2^{R_s}}+\left(\left(\frac{k_2\left(2^{R_s}-1\right)}{1+k_2 2^{R_s}}\right)^2+\frac{4\rho_d k_2\left(1-\frac{1}{2^{R_s}}\right)}{1+k_2 2^{R_s}}\right)^{\frac{1}{2}}\right), \tag{3.29}$$

and $\xi^\star$ is obtained by taking $R_s^\star$ into (3.29).

ELSE, $(R_t^\star, R_s^\star) \in \hat{\mathcal{D}}$, i.e., the energy balanced case, and $R_t^\star$ is the root of following equation which can be easily solved by a linear search:

$$\zeta'\left(\frac{1+\frac{k_1}{\zeta}}{\ln 2\,(1+\zeta)}-\frac{k_1\left(R_t-\log_2\left(1+\zeta\right)\right)}{\zeta^2}\right)=1, \tag{3.30}$$

where

$$\zeta=\frac{k_1-k_2 e^{\frac{2^{R_t}-1}{\rho_d}}\left(2^{R_t}-1\right)}{e^{\frac{2^{R_t}-1}{\rho_d}}-1}, \tag{3.31}$$

$$\zeta'=\frac{\ln 2\, e^{\frac{2^{R_t}-1}{\rho_d}}}{\left(e^{\frac{2^{R_t}-1}{\rho_d}}-1\right)^2}\left(k_2\,2^{R_t}\left(1+\frac{1}{\rho_d}-e^{\frac{2^{R_t}-1}{\rho_d}}\right)-\frac{k_1+k_2}{\rho_d}\right), \tag{3.32}$$

$$k_1=\frac{d_{SJ}^\lambda}{\eta}\frac{d_{JE}^\lambda}{d_{SE}^\lambda}\left(\varepsilon^{-1}-1\right), \tag{3.33}$$

$$k_2=\frac{d_{JE}^\lambda}{d_{SE}^\lambda}\frac{d_{SD}^\lambda}{d_{JD}^\lambda}\left(\varepsilon^{-1}-1\right), \tag{3.34}$$

and $R_s^\star = R_t^\star - \log_2\left(1+\zeta^\star\right)$, where $\zeta^\star$ is calculated by taking $R_t^\star$ into (3.31).

Proof. See Appendix B.3. □

Note that the optimal (R_t, R_s) never falls in region $\mathcal{D}_2$. This is because the throughput in

$\mathcal{D}_2$ increases towards the boundary of $\mathcal{D}_1$ and $\mathcal{D}_2$, that is $\hat{\mathcal{D}}$. The detailed explanation is given in Appendix B.3.

Proposition 1 can then be used to obtain the optimal values of R_t and R_s as follows. We firstly assume the optimal results are in the region $\mathcal{D}_1$, thus, R_s and R_t can be obtained by equation (3.27) and (3.28). Then, we check whether the results are really in $\mathcal{D}_1$. If they are, we have obtained the optimal results. If not, we solve equation (3.30) to obtain the optimal R_t and R_s.

3.4.2.1 High SNR Regime

We want know whether we can largely improve throughput by increasing the transmit power at the source, $\mathcal{P}_s$, thus, we consider the high SNR regime. Note that we have defined SNR at the destination (without the effect of jamming noise) as ρ_d in (3.11).

Corollary 9. When $N_J = 1$ and the SNR at the destination is sufficiently high, the asymptotically optimal rate parameters and an upper bound of throughput are given by

$$\tilde{R}_s^\star = \frac{1 + \mathrm{W}_0\left(\frac{1}{ek_2}\right)}{\ln 2}, \tag{3.35a}$$

$$\tilde{R}_t^\star = \tilde{R}_s^\star + \log_2\left(1 + \tilde{\xi}^\star\right), \tag{3.35b}$$

$$\tilde{\pi}^\star = \frac{\mathrm{W}_0\left(\frac{1}{ek_2}\right)}{\ln 2}, \tag{3.35c}$$

where k_2 is defined in (3.34),

$$\tilde{\xi}^\star = \left(\frac{\rho_d k_2\left(1 - \frac{1}{2^{\tilde{R}_s^\star}}\right)}{1 + k_2 2^{\tilde{R}_s^\star}}\right)^{\frac{1}{2}}, \tag{3.36}$$

and $\mathrm{W}_0(\cdot)$ is the principle branch of the Lambert W function [119].

Proof. See Appendix B.4. □

Remark 6. *From Corollary 9, the following insights are obtained.*

i) The upper bound of throughput implies that one cannot effectively improve the throughput by further increasing $\mathcal{P}_s$ when the SNR at the destination is already high.

ii) It can be checked that when $\mathcal{P}_s$ is sufficiently high, the optimized communication process leads to energy accumulation. Intuitively, this implies that when the available harvested energy is very large, the jammer should store a significant portion of the harvested energy

in the battery rather than fully using it, because too much jamming noise can have adverse impact on SINR at the destination in this single-antenna jammer scenario. This behavior will also be verified in Section 3.5, Fig. 3.4.

3.4.3 Optimal Rate Parameters with Multiple-Antenna Jammer

Proposition 2. When $N_J > 1$, the optimal R_s and R_t are in region $\hat{\mathcal{D}}$ which also means that the optimal communication process is in the energy balanced case, and the optimal values are given by

$$\begin{aligned} R_t^\star &= \log_2 z^\star, \\ R_s^\star &= \log_2 \frac{z^\star}{1+\frac{M}{e^{\frac{z^\star-1}{\rho_d}}-1}}, \end{aligned} \tag{3.37}$$

where $z^\star$ is calculated as the unique solution of

$$\frac{\rho_d}{z} - \ln z + \ln\left(1+\frac{M}{e^{\frac{z-1}{\rho_d}}-1}\right) + \frac{Me^{\frac{z-1}{\rho_d}}}{\left(e^{\frac{z-1}{\rho_d}}-1\right)^2+M\left(e^{\frac{z-1}{\rho_d}}-1\right)} = 0, \tag{3.38}$$

and

$$M = \frac{d_{SJ}^\lambda}{N_J\eta}\frac{d_{JE}^\lambda}{d_{SE}^\lambda}(N_J-1)\left(\varepsilon^{-\frac{1}{N_J-1}}-1\right). \tag{3.39}$$

Proof. See Appendix B.5. □

We can see that the left side of (3.38) is a monotonically decreasing function of z. Thus, z can be easily obtained by using numerical methods.

3.4.3.1 High SNR Regime

Similar to the single-antenna jammer case, we are interested in whether increasing the source transmission power $\mathcal{P}_s$, is an effective way of improving throughput. Hence the high SNR regime is considered:

Corollary 10. When $N_J > 1$ and the SNR at the destination is sufficiently high, the asymptotically optimal rate parameters and an upper bound of throughput are given by

$$\tilde{R}_t^\star = \log_2(2\rho_d) - \log_2(\mathrm{W}_0(2\rho_d)), \tag{3.40a}$$

$$\tilde{R}_s^\star = \frac{2\mathrm{W}_0(2\rho_d)}{\ln 2} - \log_2(M\rho_d), \tag{3.40b}$$

$$\tilde{\pi}^\star = \tilde{R}_s^\star, \tag{3.40c}$$

where $z^\star = \frac{2\rho_d}{\mathrm{W}_0(2\rho_d)}$ and M is defined in (3.39).

Proof. See Appendix B.6. □

Remark 7. *From Corollary 10, we have the following insights.*

i) The throughput will always increase with increasing transmit power $\mathcal{P}_s$ (because ρ_d increases as $\mathcal{P}_s$ increases). This is in contrast to the single-antenna jammer case, because the multi-antenna jamming method only interferes the $S \to E$ link.

ii) From Proposition 2 and Corollary 10, when $\mathcal{P}_s$ is sufficiently large, the optimized communication process is still energy balanced, which is different from the single-antenna jammer scenario. Intuitively, storing extra energy is not a good choice, because we can always use the accumulated energy to jam at the eavesdropper without affecting the destination, which in turn improves the throughput.

3.4.3.2 Large Number of Jammer Antenna Regime

We also want to know that whether we can largely improve the throughput by increasing the number of antennas at the jammer.

Corollary 11. In large N_J scenario, the asymptotically optimal rate parameters and an upper bound of throughput are given by

$$\tilde{R}_t^\star = \frac{\mathrm{W}_0\left(\rho_d\right)}{\ln 2}, \tag{3.41a}$$

$$\tilde{R}_s^\star = \log_2 \frac{e^{\mathrm{W}_0(\rho_d)}}{1 + \frac{M}{e^{\frac{\mathrm{W}_0(\rho_d)-1}{\rho_d}}-1}}, \tag{3.41b}$$

$$\tilde{\pi}^\star = \frac{\mathrm{W}_0\left(\rho_d\right)}{\ln 2\, e^{\frac{1}{\mathrm{W}_0(\rho_d)}-\frac{1}{\rho_d}}}, \tag{3.41c}$$

where M is defined in (3.39).

Proof. See Appendix B.6. □

Remark 8. *Corollary 11 gives an asymptotic upper bound on throughput for this protocol, thus, π does not increase towards infinity with N_J. Intuitively, the throughput cannot always increase with N_J, because it is bounded by the $S \to D$ channel capacity which is independent with N_J.*

3.5 Numerical Results

In this section, we present numerical results to demonstrate the performance of the proposed secure communication protocol. We set the path loss exponent as $\lambda = 3$ and the length of

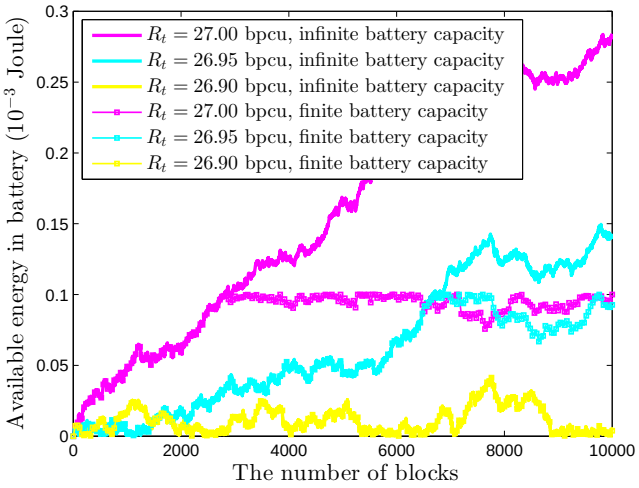

Figure 3.3: Available energy in battery during the communication process. Since the channel power gain of the source-to-jammer link changes independently block-by-block, the harvested energy per block changes randomly and the curves are not smooth.

time block as $T = 1$ millisecond. We set the energy conversion efficiency as $\eta = 0.5$ [7, 27, 26]. Note that the practical designs of rectifier for RF-DC conversion achieve the value of η between 0.1 and 0.85 [2]. Such a range makes wireless energy harvesting technology meaningful. A rectifier design with $\eta < 0.1$ is unlikely to be used in practice. We assume that the source, jammer, destination and eavesdropper are placed along a horizontal line, and the distances are given by $d_{SJ} = 25$ m, $d_{SE} = 40$ m, $d_{SD} = 50$ m, $d_{JE} = 15$ m, $d_{JD} = 25$ m, in line with [78]. Unless otherwise stated, we set $\sigma_d^2 = -100$ dBm, and the secrecy outage probability requirement $\varepsilon = 0.01$. We do not specify the bandwidth of communication, hence the rate parameters are expressed in units of *bit per channel use* (bpcu).

To give some ideas about the energy harvesting process at the jammer under this setting: When $N_J = 1$ and $\mathcal{P}_s = 30$ dBm, the average power that can be harvested (after RF-DC conversion) is -15 dBm, thus, the overall energy harvesting efficiency (i.e., the ratio between the harvested power at the jammer and the transmit power at the source) is $(-15 \text{ dBm})/(30 \text{ dBm}) \approx 3 \times 10^{-5}$. Note that, although the average harvested power at the jammer is relatively small, a small jamming power is sufficient to achieve good secure communication performance. For instance, the optimal jamming power under this setting is only -13 dBm based on the analytical results in Section refsecurity:optimal. In order to transmit the jamming signal at the optimal power of -13 dBm with the average harvested power of -15 dBm, roughly 61% of time is used for charging and 39% of time is used for secure communication with jamming.

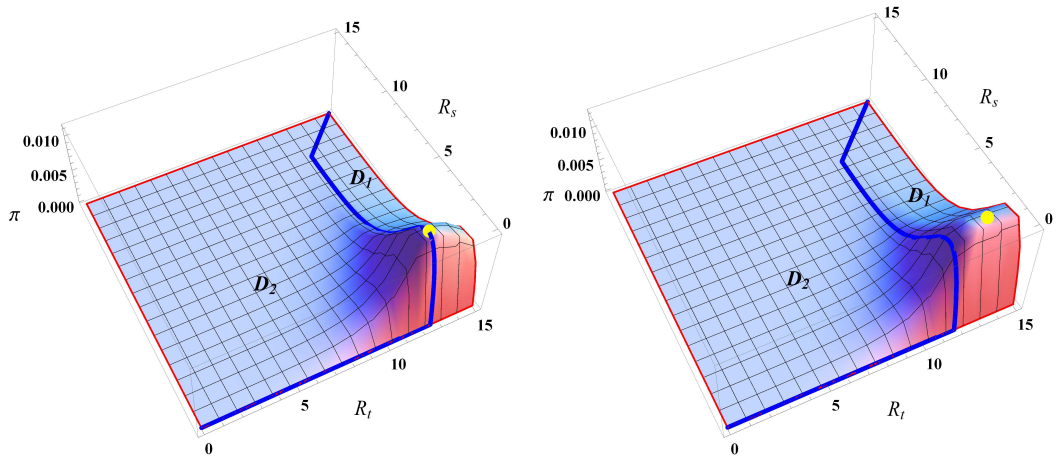

(a) $N_J = 1, \mathcal{P}_s = 0$ dBm (b) $N_J = 1, \mathcal{P}_s = 30$ dBm

Figure 3.4: Optimal rate parameters for $N_J = 1$. The regions $\mathcal{D}_1$ and $\mathcal{D}_2$ are separated by the blue curve, $\mathcal{D}_1$ is on the right side, while $\mathcal{D}_2$ is on the left side

3.5.1 Energy Accumulation and Energy Balanced Cases

Fig. 3.3 shows the simulation results on the available energy in the battery in the communication process. The jammer has 8 antennas ($N_J = 8$) and the target jamming power is $\mathcal{P}_J = 0$ dBm. The source transmit power is $\mathcal{P}_s = 30$ dBm. Thus, the energy consumption in one IT block at the jammer, $\mathcal{P}_J T$, is 10^{-6} Joule, and the average harvested energy in one PT block, ρ_J, is 2.56×10^{-7} Joule. From Lemma 2 and (3.17), when $\frac{p_{co}}{1-p_{co}} > \frac{\mathcal{P}_J T}{\rho_J}$ which means $R_t > 26.92$ bpcu, the communication process leads to energy accumulation, while if $R_t \leq 26.92$ bpcu, it is the energy balanced.

First, we focus on the curves with infinite battery capacity. We can see that when $R_t = 26.9$ bpcu, the available energy goes up and down, but does not have the trend of energy accumulation. Thus, the communication process is energy balanced. When $R_t = 26.95$ and 27 bpcu, the available energy grows up, and the communication process leads to energy accumulation. Therefore, the condition given in Lemma 2 is verified.

In Fig. 3.3, we also plot a set of simulation results with finite battery capacity as $E_{\max} = 0.1 \times 10^{-3}$ Joule. As we can see, for the energy accumulative cases, i.e., $R_t = 26.95$ and 27.00 bpcu, the energy level stays near the battery capacity (0.1×10^{-3} Joule) after experienced a sufficient long time, which is much higher than the required jamming energy level $\mathcal{P}_J T = 10^{-6}$ Joule. Therefore, in practice, having a finite battery capacity has hardly any effect on the communication process, as compared with infinite capacity.

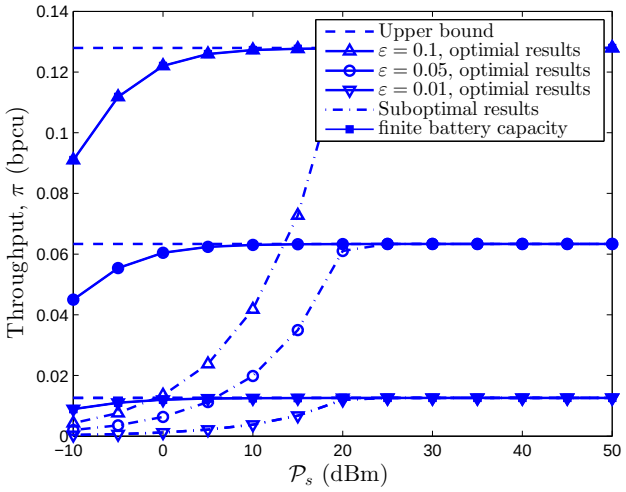

Figure 3.5: Throughput versus source transmit power $\mathcal{P}_s$ for $N_J = 1$.

3.5.2 Rate Regions with Single-Antenna Jammer

Fig. 3.4 plots the throughput in (3.22) with different R_t and R_s in the single-antenna jammer scenario. In Fig. 3.4(a), we set $\mathcal{P}_s = 0$ dBm. The optimal rate parameters $(R_t^\star, R_s^\star)$ are obtained in the region $\hat{\mathcal{D}}$, which is the boundary of $\mathcal{D}_1$ and $\mathcal{D}_2$. This implies that the optimized communication process is energy balanced. In Fig. 3.4(b), we increase $\mathcal{P}_s$ to 30 dBm. The optimal rate parameters $(R_t^\star, R_s^\star)$ are obtained in the region $\mathcal{D}_1$. This implies that the optimized communication process leads to energy accumulation. This observation agrees with the remarks after Corollary 9 regarding the optimal operating point when the SNR at the destination is sufficiently large.

3.5.3 Throughput Performance with Single-Antenna Jammer

Fig. 3.5 plots the throughput with optimal designs given by Proposition 1. We also include the suboptimal performance which is achieved by using the asymptotically optimal rate parameters in Corollary 9, as well as the upper bound on throughput in Corollary 9.

First, we focus on the curves with infinite battery capacity. We can see that when $\mathcal{P}_s = 5$ dBm, the optimal throughput almost reaches the upper bound. Also we can see that when $\mathcal{P}_s < 20$ dBm, the suboptimal performance has a large gap with the optimal one, while when $\mathcal{P}_s > 20$ dBm, the suboptimal performance is very close to the optimal one.

In Fig. 3.5, we also plot a set of simulation results with finite battery capacity as $E_{\max} = 0.1 \times 10^{-3}$ Joule. It is easy to see that our analytical results for infinite battery capacity fit very well with the simulation results for finite battery capacity. Therefore, a practical finite battery capacity have negligible effect on the performance of the protocol, and our analysis are valid

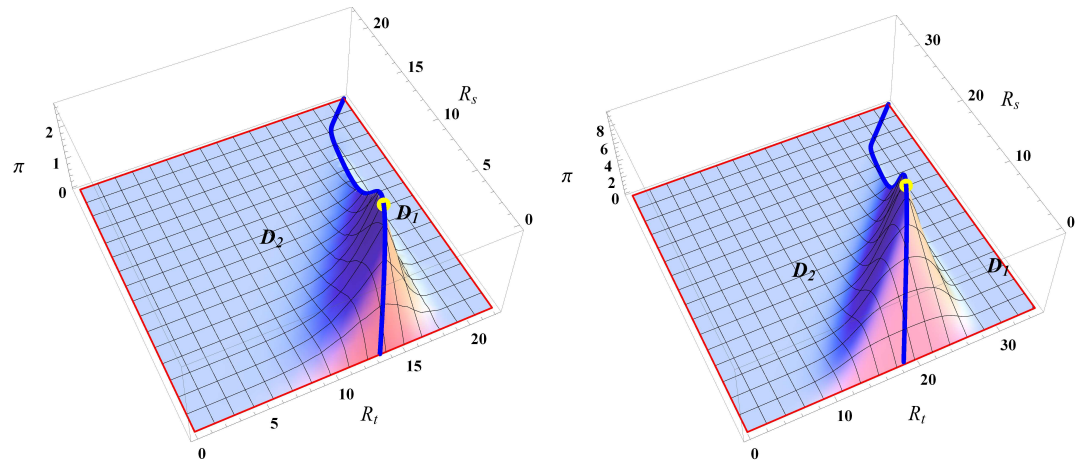

(a) $N_J = 8, \mathcal{P}_s = 0$ dBm (b) $N_J = 8, \mathcal{P}_s = 30$ dBm

Figure 3.6: Optimal rate parameters for $N_J = 8$.

in the practical scenario.

3.5.4 Rate Regions with Multiple-Antenna Jammer

Fig. 3.6 plots the throughput in (3.22) with different R_t and R_s in the multiple-antenna jammer scenario. In Fig. 3.6(a) and Fig. 3.6(b), we set $\mathcal{P}_s = 0$ dBm and 30 dBm, respectively. The optimal rate parameters $(R_t^\star, R_s^\star)$ are both obtained in the region $\hat{\mathcal{D}}$. This implies that the optimized communication process is energy balanced, which agrees with the remarks after Corollary 10.

3.5.5 Throughput Performance with Multiple-Antenna Jammer

Fig. 3.7(a) plots the optimal throughput from Proposition 2. We also present the suboptimal performance which is achieved by the asymptotically optimal rate parameters obtained in Corollary 10. We can see that the throughput increases with $\mathcal{P}_s$ unbounded. Also we can see that the suboptimal performance is reasonably good when $\mathcal{P}_s > 20$ dBm.

Fig. 3.7(b) plots the throughput achieved with the optimal design given in Proposition 2 for different N_J. The source transmit power is $\mathcal{P}_s = 30$ dBm. We also include the suboptimal performance achieved by the asymptotically optimal rate parameters in the large N_J regime (Corollary 11) as well as the upper bound on throughput in Corollary 11.

We can see that with the increment of N_J, although theoretically the throughput is upper bounded as $N_J \to \infty$, the available throughput within practical range of N_J is far from the upper bound. Hence, increasing N_J is still an efficient way to improve the throughput with practical antenna size. Also we can see that the suboptimal performance is acceptable but the

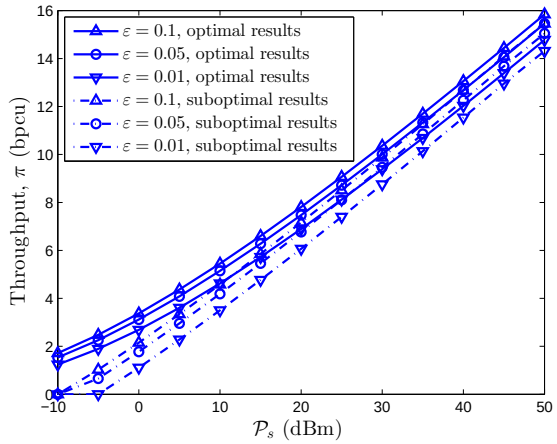

(a) Throughput vs. source transmit power $\mathcal{P}_s$ for $N_J = 8$.

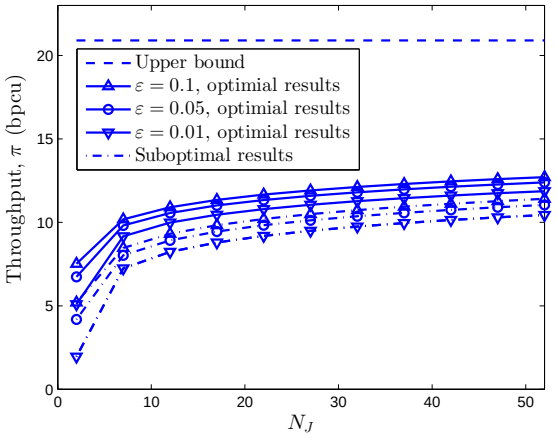

(b) Throughput vs. number of antennas at the jammer, $N_J \geq 2$.

Figure 3.7: Throughput for $N_J > 1$.

gap from the optimal throughput performance is still noticeable.

3.6 Summary

In this chapter, we investigated secure communication with the help from a wireless-powered jammer. We proposed a simple communication protocol and derived its achievable throughput with fixed-rate transmission. We further optimized the rate parameters to achieve the best throughput subject to a secrecy outage probability constraints. As energy harvesting and wireless power transfer become emerging solutions for energy constrained networks, this work has demonstrated how to make use of an energy constrained friendly jammer to enable secure communication without relying on an external energy supply.

Chapter 4

SWIPT System with Practical Constraints

In Chapter 3, we investigated a WPT-assisted secure communication system, where the energy receiver, i.e., the jammer, can only harvest RF energy from the received signal. As the RF wave can carry both energy and information, it is desirable to consider a receiver that is able to absorb energy and extract information from the received signal.

In this chapter, we shift our focus on a point-to-point SWIPT system adopting practical M-ary modulation, where the receiver leverages the received RF signal for both RF EH an information detection. We take into account the fact that the receiver's radio-frequency (RF) energy harvesting circuit can only harvest energy when the received signal power is greater than a certain sensitivity level. For both power-splitting (PS) and time-switching (TS) schemes, we derive the energy harvesting performance as well as the information decoding performance for the Nakagami-m fading channel. We also analyze the performance tradeoff between energy harvesting and information decoding by studying an optimization problem, which maximizes the information decoding performance and satisfies a constraint on the minimum harvested energy. Our analysis shows that (i) for the PS scheme, modulations with high peak-to-average power ratio achieve better energy harvesting performance, (ii) for the TS scheme, it is desirable to concentrate the power for wireless power transfer in order to minimize the non-harvested energy caused by the RF energy harvesting sensitivity level, and (iii) channel fading is beneficial for energy harvesting in both PS and TS schemes.

This chapter is organized as follows. Section 4.1 presents the system model. Sections 4.2 and 4.3 analyze the performance tradeoff between energy harvesting and information decoding for the PS and TS schemes, respectively. Section 4.4 presents the numerical results. Finally, Section 4.5 concludes the chapter.

4.1 System Model

We consider a SWIPT system consisting of a transmitter (Tx) and a receiver (Rx). The receiver comprises an information-decoding circuit and an RF-EH circuit [7]. Each node is equipped with a single omnidirectional antenna. The transmitter and receiver adopt block-wise operation with block time duration, T. We assume that the receiver is located in the far field, at a distance d from the transmitter. Thus, the channel link between the two nodes is composed of large scale path loss with exponent λ and small-scale Nakagami-m fading. Note that m represents the fading parameter, which controls the severity of the fading. The fading channel gain, h, is assumed to be constant within one block time and independent and identically distributed from one block to the next [7, 48, 34]. We assume instantaneous channel state information (CSI) is available only at the receiver.

We consider that the transmitter adopts a practical modulation scheme for information transmission (IT). Let the signal constellation set be denoted by $\mathcal{X}$. The size of $\mathcal{X}$ is denoted by M with $M = 2^l$, and $l \geq 1$ being an integer. The ith constellation point in $\mathcal{X}$ is denoted by x_i, $i = 1, 2, ..., M$, with equal probability $p_i = 1/M$,[1] and the average power of signal set $\mathcal{X}$ is normalized to one, i.e., $\sum_{i=1}^{M} |x_i|^2/M = 1$. In this work, we consider three most commonly used coherent modulation schemes for IT: M-PSK, M-PAM, and M-QAM.[2]

At the receiver, during a symbol period T_s, assuming the receive power at the RF-EH circuit is $\mathcal{P}_{\text{rx}}$, the amount of harvested energy can be represented as [34]

$$\mathcal{E} = \eta T_s \left(\mathcal{P}_{\text{rx}} - \mathcal{P}_{\text{th}}\right)^+, \tag{4.1}$$

where $0 \leq \eta \leq 1$ is the RF-EH efficiency, and $(z)^+ = \max\{z, 0\}$. We assume that the harvested energy at the receiver is stored in an ideal battery [7, 34, 120]. Note that in (4.1), according to the existing studies [34, 120, 121], the RF-EH circuit can only harvest energy when its receive signal power, $\mathcal{P}_{\text{rx}}$, is greater than the RF-EH sensitivity level, $\mathcal{P}_{\text{th}}$, and the harvested energy is proportional to $\mathcal{P}_{\text{rx}} - \mathcal{P}_{\text{th}}$.

4.1.1 PS and TS Schemes

The operation of SWIPT using PS or TS scheme is described as follows:

- *PS*: In each time block, the transmitter sends modulated data signal with average transmit power $\mathcal{P}_{\text{tx}}$. The receiver splits the received signal with a PS ratio, ρ_{PS}, for separate EH and information decoding.

[1] Consideration of modulation schemes with non-uniform probability distribution among all symbols is outside the scope of this work.

[2] For M-QAM, we assume that $M = 2^l$, and l is an even integer.

- *TS*: Each time block is divided into a power transfer (PT) phase and an IT phase. First, the transmitter transmits an energy signal with average transmit power $\mathcal{P}_{\text{tx},1}$ during the first $\rho_{\text{TS}}T$ seconds, i.e., PT phase. The receiver harvests energy from this received signal. Then, the transmitter transmits modulated signal with average transmit power $\mathcal{P}_{\text{tx},2}$ during the remaining $(1-\rho_{\text{TS}})T$ seconds, i.e., IT phase, and the receiver decodes the received information.

4.1.2 Transmit Power Constraints

We consider both average and peak power constraints at the transmitter for SWIPT [7, 48], denoted by $\mathcal{P}_{\text{ave}}$ and $\mathcal{P}_{\text{peak}}$, respectively. From [122] and references therein, the peak-to-average ratio of a practical RF circuit can be as large as 13 dB. In this chapter, we assume that $\mathcal{P}_{\text{peak}}/\mathcal{P}_{\text{ave}} \geq 3$, i.e., 4.77 dB.

4.1.2.1 PS Scheme

First, the average transmission power $\mathcal{P}_{\text{tx}}$ should satisfy the average power constraint, i.e., $\mathcal{P}_{\text{tx}} \leq \mathcal{P}_{\text{ave}}$.

Second, different transmitted symbols have different power. Thus, the highest transmit power of the symbols in $\mathcal{X}$ should also be no larger than $\mathcal{P}_{\text{peak}}$. From [123], the PAPR of M-PSK/PAM/QAM are given by

$$\varphi_{\text{PSK}} = 1, \varphi_{\text{PAM}} = 3\frac{M-1}{M+1}, \varphi_{\text{QAM}} = 3\frac{\sqrt{M}-1}{\sqrt{M}+1}, \tag{4.2}$$

respectively. Therefore, peak power constraint should be satisfied as $\varphi_j \mathcal{P}_{\text{tx}} \leq \mathcal{P}_{\text{peak}}$, $j = \text{PSK, PAM, QAM}$, i.e., j is the index of the modulation scheme

From (4.2), we see that the PAPR is always less than 3. Thus, for the considered modulation schemes, the peak power constraint is automatically satisfied, as long as the average power requirement is met, i.e., $\mathcal{P}_{\text{tx}} \leq \mathcal{P}_{\text{ave}}$.

4.1.2.2 TS Scheme

First, the transmit power should satisfy average power constraint as $\rho_{\text{TS}}\mathcal{P}_{\text{tx},1} + (1-\rho_{\text{TS}})\mathcal{P}_{\text{tx},2} \leq \mathcal{P}_{\text{ave}}$.

Second, for the PT phase of the TS scheme, the peak power of the energy signal should be no larger than $\mathcal{P}_{\text{peak}}$, and a constraint for the average power of the energy signal, $\mathcal{P}_{\text{tx},1} \leq \mathcal{P}_{\text{peak}}$, is satisfied naturaly. For the IT phase of the TS scheme, as discussed above, peak power

constraint should be satisfied as

$$\varphi_j \mathcal{P}_{\text{tx},2} \leq \mathcal{P}_{\text{peak}},\ j = \text{PSK}, \text{PAM}, \text{QAM}. \tag{4.3}$$

4.1.3 Performance Metrics

For EH, we use the average harvested power $\bar{\mathcal{P}}$ as a performance metric [49, 48]. For information decoding, we adopt the average success symbol rate, $\overline{\text{SSR}}$, which is related to the average symbol error rate, $\overline{\text{SER}}$, as the performance metric. The $\overline{\text{SSR}}$ measures the average number of successfully transmitted symbols per unit time. Using $\bar{\mathcal{P}}$ and $\overline{\text{SSR}}$, we investigate the performance tradeoff between EH and information decoding. The exact mathematical definitions of $\bar{\mathcal{P}}$ and $\overline{\text{SSR}}$ are given in Sections III and IV for the PS and TS schemes, respectively.

4.2 Analytical Results for Power Splitting

Following [7, 113], after PS, the received RF signal at the RF-EH circuit is

$$y(t) = h(t)\sqrt{\frac{\rho_{\text{PS}}\mathcal{P}_{\text{tx}}}{d^{\lambda}}}\, x(t) + \tilde{n}(t), \tag{4.4}$$

where $h(t)$ represents the channel fading gain as described in Sec. II, $x(t)$ is the modulated information signal sent from the transmitter, and $\tilde{n}(t)$ is the circuit noise.

For information decoding, the RF signal is down converted to baseband. The received signal and the signal noise ratio (SNR) at the information-decoding circuit of the receiver are given by[3]

$$y = h\sqrt{\frac{(1-\rho_{\text{PS}})\mathcal{P}_{\text{tx}}}{d^{\lambda}}}\, x + n, \tag{4.5}$$

and

$$\gamma(\nu) = \frac{(1-\rho_{\text{PS}})\mathcal{P}_{\text{tx}}\nu}{d^{\lambda}\sigma^2}, \tag{4.6}$$

respectively, where n is the AWGN at the information-decoding circuit with power σ^2, and $\nu = |h|^2$ is the fading power gain of the channel. Since we consider Nakagami-m fading, the probability density function (pdf) of ν is given by

$$f_{\nu}(v) = \frac{v^{m-1}m^m}{\Gamma(m)} \exp\left(-mv\right),\ m = 1, 2, 3.... \tag{4.7}$$

In the following, we analyze the performance of EH and information decoding with M-PSK, M-PAM and M-QAM schemes.

[3] In (4.5), for notational simplification, we have represented the baseband signals, $y[k]$, $x[k]$ and $n[k]$ as y, x and n, respectively, where k denotes symbol index.

4.2.1 RF Energy Harvesting with the PS Scheme

Using (4.1) and (4.4), and assuming that the amount of energy harvested from the circuit noise $\tilde{n}$ is negligible [7, 26], the harvested energy under fading power gain v during one symbol time T_s is given by

$$\mathcal{E}(x_i, v) = \eta T_s \left(\frac{\rho_{\text{PS}} \mathcal{P}_i v}{d^\lambda} - \mathcal{P}_{\text{th}} \right)^+, \tag{4.8}$$

where $\mathcal{P}_i$ is the transmit power for the ith constellation point, and $\sum_{i=1}^{M} \mathcal{P}_i / M = \mathcal{P}_{\text{tx}}$. From [123], $\mathcal{P}_i$ can be obtained as

$$\mathcal{P}_i = \begin{cases} \mathcal{P}_{\text{tx}}, & \text{for } M\text{-PSK} \\ \dfrac{3\mathcal{P}_{\text{tx}}}{M^2-1} \left(2 \left\lceil \left| i - \dfrac{M+1}{2} \right| \right\rceil - 1 \right)^2, & \text{for } M\text{-PAM} \\ \dfrac{3\mathcal{P}_{\text{tx}}}{2(M-1)} \left((2 \left\lceil \left| \left\lceil \dfrac{i}{\sqrt{M}} \right\rceil - \dfrac{\sqrt{M}+1}{2} \right| \right\rceil - 1)^2 \right. \\ \left. + (2 \left\lceil \left| \left(i \mod \sqrt{M} \right) - \dfrac{\sqrt{M}+1}{2} \right| \right\rceil - 1)^2 \right), \\ & \text{for } M\text{-QAM} \end{cases} \tag{4.9}$$

where $\lceil \cdot \rceil$ is the ceiling operator, and the operator $z \mod Z$ has the definition as follows: if z is an integer multiple of Z, $z \mod Z$ is Z, while in other cases, it is equal to z modulo Z.

From (4.8), the average harvested power can be calculated as

$$\begin{aligned} \bar{\mathcal{P}}_{\text{PS}} &= \frac{1}{T_s} \sum_{i=1}^{M} p_i \int_0^\infty \mathcal{E}(x_i, v) f_\nu(v) \mathrm{d}v \\ &= \eta \sum_{i=1}^{M} p_i \int_{\bar{v}_i}^\infty \left(\frac{\rho_{\text{PS}} \mathcal{P}_i v}{d^\lambda} - \mathcal{P}_{\text{th}} \right) f_\nu(v) \mathrm{d}v, \\ &= \eta \sum_{i=1}^{M} p_i \left(\frac{\rho_{\text{PS}} \mathcal{P}_i}{d^\lambda} \left(1 - \int_{v=0}^{\bar{v}_i} v f_\nu(v) \mathrm{d}v \right) - \mathcal{P}_{\text{th}} \left(1 - \int_{v=0}^{\bar{v}_i} f_\nu(v) \mathrm{d}v \right) \right), \end{aligned} \tag{4.10}$$

where p_i is the transmit probability of symbol x_i, i.e., $1/M$, and $\bar{v}_i = \mathcal{P}_{\text{th}} d^\lambda / \rho_{\text{PS}} \mathcal{P}_i$. By taking (4.7), (4.9) and $p_i = 1/M$ into (4.10), after some simplification, we get

$$\begin{aligned} \bar{\mathcal{P}}_{\text{PS}} = \frac{\eta}{M} \sum_{i=1}^{M} \frac{\rho_{\text{PS}} \mathcal{P}_i}{d^\lambda} \exp \left(-m \mathcal{P}_{\text{th}} \frac{d^\lambda}{\rho_{\text{PS}} \mathcal{P}_i} \right) \times \\ \left(1 + \sum_{k=0}^{m-1} \left(\mathcal{P}_{\text{th}} \frac{d^\lambda}{\rho_{\text{PS}} \mathcal{P}_i} \right)^{k+1} \frac{m^k (m-k-1)}{(k+1)!} \right). \end{aligned} \tag{4.11}$$

Special case: For $m = 1$, i.e., Rayleigh fading channel, we have

$$\bar{\mathcal{P}}_{\text{PS}} = \frac{\eta}{M} \sum_{i=1}^{M} \frac{\rho_{\text{PS}} \mathcal{P}_i}{d^{\lambda}} \exp(-\frac{\mathcal{P}_{\text{th}} d^{\lambda}}{\rho_{\text{PS}} \mathcal{P}_i}). \tag{4.12}$$

For M-PSK, (4.12) further simplifies to

$$\bar{\mathcal{P}}_{\text{PS}}^{\text{PSK}} = \eta \frac{\rho_{\text{PS}} \mathcal{P}_{\text{tx}}}{d^{\lambda}} \exp\left(-\frac{\mathcal{P}_{\text{th}} d^{\lambda}}{\rho_{\text{PS}} \mathcal{P}_{\text{tx}}}\right). \tag{4.13}$$

Remark 9. *For the PS scheme, a modulation scheme with higher PAPR, or a fading channel with larger variation in its power gain, increases the average harvested power.*

The above observations in Remark 9 will be verified in Sec. V. They can be explained using the analysis as follows:

Due to the RF-EH sensitivity level, $\mathcal{P}_{\text{th}}$, (4.8) is a convex function w.r.t. symbol transmit power, $\mathcal{P}_i$, and channel power fading gain v. Thus, based on Jensen's inequality, taking (4.8) into the first line of (4.10), we have

$$\bar{\mathcal{P}}_{\text{PS}} \geq \eta \left(\frac{\rho_{\text{PS}}}{d^{\lambda}} \sum_{i=1}^{M} p_i \mathcal{P}_i \int_0^{\infty} v f_v(v) \mathrm{d}v - \mathcal{P}_{\text{th}} \right)^{+}. \tag{4.14}$$

We see that the equality holds in (4.14), i.e., average harvested power $\bar{\mathcal{P}}_{\text{PS}}$ is minimized, iff the variance of both the symbol power in the signal set and the channel fading power gain equal to zero, i.e., $\mathcal{P}_i = \mathcal{P}_{\text{tx}}$ for all i, and v is always equal to one (non-fading channel).

For practical modulations, M-PSK results in the worst EH performance since it has constant symbol power (lowest PAPR and zero variance of symbol power). In addition, our numerical results suggest that M-PAM (which has highest PAPR) performs better than M-QAM, which performs better than M-PSK. This will be verified in Sec. V.

For the Nakagami-m fading, we can easily prove using (4.11) that $\bar{\mathcal{P}}_{\text{PS}}$ decreases with increasing m. As m increases, the fading variance decreases. Hence, a channel with larger fading variance (smaller m) increases the average harvested power.

4.2.2 Information Decoding with the PS Scheme

The average symbol success rate, $\overline{\text{SSR}}$, can be calculated as

$$\overline{\text{SSR}} = \int_{v=0}^{\infty} (1 - \text{SER}(v)) f_v(v) \mathrm{d}v = 1 - \overline{\text{SER}}. \tag{4.15}$$

where

$$\overline{\text{SER}} = \int_{v=0}^{\infty} \text{SER}(v) f_v(v) \mathrm{d}v, \tag{4.16}$$

and $\mathrm{SER}(v)$ is given by [123] as[4]

$$\mathrm{SER}(v) = \begin{cases} 2\,Q\left(\sqrt{2g_{\mathrm{PSK}}\gamma(v)}\right), & \text{for } M\text{-PSK} \\ 2(M-1)/M\,Q\left(\sqrt{2g_{\mathrm{PAM}}\gamma(v)}\right), & \text{for } M\text{-PAM} \\ 4\left(1-1/\sqrt{M}\right)\,Q\left(\sqrt{2g_{\mathrm{QAM}}\gamma(v)}\right) & \\ \quad -4\left(1-1/\sqrt{M}\right)^2\,Q^2\left(\sqrt{2g_{\mathrm{QAM}}\gamma(v)}\right), & \\ & \text{for } M\text{-QAM} \end{cases} \tag{4.17}$$

where $Q(\cdot)$ is the Q-function, M is the modulation order, $g_{\mathrm{PSK}} = \sin^2(\pi/M)$, $g_{\mathrm{PAM}} = \frac{3}{M^2-1}$ and $g_{\mathrm{QAM}} = \frac{3}{2(M-1)}$.

Remark 10. Given ρ_{PS}, M and v, it is known that in the high SNR regime, M-QAM outperforms M-PSK, which outperforms M-PAM on SER [123]. Thus, from (4.15), the same order holds for average success symbol rate.

4.2.3 Optimal Transmission Strategy for the PS Scheme

It is interesting to investigate the problem that given a certain required average harvested power level, $\bar{\mathcal{P}}_0$, what is the achievable average symbol success rate ($\overline{\mathrm{SSR}}$). For the PS scheme, there are two design parameters: the PS ratio, ρ_{PS}, and the transmit power, $\mathcal{P}_{\mathrm{tx}}$.

We consider the following optimization problem:

$$\begin{aligned} \mathbf{P1}: \ \underset{\rho_{\mathrm{PS}},\mathcal{P}_{\mathrm{tx}}}{\mathsf{Maximize}} \quad & \overline{\mathrm{SSR}} = 1 - \overline{\mathrm{SER}} \\ \mathsf{Subject\ to} \quad & \bar{\mathcal{P}}_{\mathrm{PS}} \geq \bar{\mathcal{P}}_0, \\ & 0 \leq \rho_{\mathrm{PS}} \leq 1,\ 0 \leq \mathcal{P}_{\mathrm{tx}} \leq \mathcal{P}_{\mathrm{ave}}. \end{aligned} \tag{4.18}$$

where $\bar{\mathcal{P}}_{\mathrm{PS}}$ is defined in (4.11), and the required average harvested power, $\bar{\mathcal{P}}_0$, is no higher than the maximum range of average harvested power, $\bar{\mathcal{P}}_{\mathrm{PS,max}}$, which is obtained by taking $\rho_{\mathrm{PS}} = 1$ into (4.11).

The optimization problem can be solved as follows. From (4.15) and (4.11), it is easy to see that both $\bar{\mathcal{P}}_{\mathrm{PS}}$ and $\overline{\mathrm{SSR}}$ are monotonically increasing functions w.r.t. $\mathcal{P}_{\mathrm{tx}}$. Meanwhile, $\bar{\mathcal{P}}_{\mathrm{PS}}$ and $\overline{\mathrm{SSR}}$ increase and decrease with ρ_{PS}, respectively. Thus, in **P1**, we let $\mathcal{P}_{\mathrm{tx}} = \mathcal{P}_{\mathrm{ave}}$ and $\bar{\mathcal{P}}_{\mathrm{PS}} = \bar{\mathcal{P}}_0$. In order to obtain the optimal ρ_{PS}, $\rho_{\mathrm{PS}}^{\star}$, which yields $\bar{\mathcal{P}}_{\mathrm{PS}} = \bar{\mathcal{P}}_0$, a method of bisection for linear search can be adopted as $\bar{\mathcal{P}}_{\mathrm{PS}}$ is a monotonically increasing function of

[4]For simplicity, we adopt an accurate and widely used approximate closed-form expression for M-PSK.

ρ_{PS}. Taking $\rho_{\text{PS}}^{\star}$ into (4.15), the maximum achievable average symbol success rate, $\overline{\text{SSR}}^{\star}$, is obtained.

Special case: For M-PSK scheme with Rayleigh fading channel, we can obtain a closed-form expression for $\rho_{\text{PS}}^{\star}$. By taking $\mathcal{P}_{\text{tx}} = \mathcal{P}_{\text{ave}}$ into (4.13) and letting (4.13) $= \bar{\mathcal{P}}_0$, and solving we get

$$\rho_{\text{PS}}^{\star} = \frac{\mathcal{P}_{\text{th}} d^{\lambda}}{\mathcal{P}_{\text{ave}} W_0\left(\frac{\eta \mathcal{P}_{\text{th}}}{\bar{\mathcal{P}}_0}\right)}, \tag{4.19}$$

where $W_0(\cdot)$ is the principle branch of the Lambert W function.

In the following, we analyze the time-switching scheme and optimize the design parameters, i.e., the TS ratio, and the transmit power in the PT and IT phases.

4.3 Analytical Results for Time Switching

In the PT phase, i.e., ρ_{TS} portion of a time block, the transmitter transmits a pre-designed energy signal with average power $\mathcal{P}_{\text{tx},1}$. Thus, the received RF signal at the RF-EH circuit is given by

$$y(t) = h(t)\sqrt{\frac{1}{d^{\lambda}}}\,\omega(t) + \tilde{n}(t), \tag{4.20}$$

where $\omega(t)$ is the pre-designed energy signal, which will be investigated in the following subsection.

In the IT phase, i.e., $1 - \rho_{\text{TS}}$ portion of a time block, the baseband received signal and the SNR at the information-decoding circuit of the receiver are given by

$$y = h\sqrt{\frac{\mathcal{P}_{\text{tx},2}}{d^{\lambda}}}\,x + n, \tag{4.21}$$

and

$$\gamma(\nu) = \frac{\mathcal{P}_{\text{tx},2}\nu}{d^{\lambda}\sigma^2}, \tag{4.22}$$

respectively.

In the following, we analyze the performance of EH and information decoding.

4.3.1 RF Energy Harvesting with the TS Scheme

If the RF-EH sensitivity level is zero, any energy signal design will achieve the same harvested energy. On the other hand, with a non-zero RF-EH sensitivity level, different energy signals perform differently. Here, we propose an optimal energy signal which maximizes the harvested energy.

Proposition 3. For the PT phase, given the average transmit power, $\mathcal{P}_{\text{tx},1}$, and the RF-EH sensitivity level, $\mathcal{P}_{\text{th}}$, an optimal energy signal which achieves maximum harvested energy, is the signal with power $\mathcal{P}_{\text{peak}}$ for the first $\mathcal{P}_{\text{tx},1}/\mathcal{P}_{\text{peak}}$ portion of the phase, and with power zero for the rest of the phase.

Proof. Although the proposed optimal energy signal seems simple, to the best of our knowledge, prior studies have not provided an optimal energy signal design under the RF-EH model in (4.1). We provide the formal proof in Appendix C.1. □

Remark 11. In order to maximize the harvested energy with the consideration of RF-EH sensitivity level, the available power/energy is concentrated into the shortest possible duration of time, i.e., transmit with $\mathcal{P}_{\text{peak}}$. In this way, the amount of energy that is wasted during the harvesting process is minimized.

Similar to the PS scheme, the average harvested power for the TS scheme is given by

$$\begin{aligned}\bar{\mathcal{P}}_{\text{TS}} &= \eta\rho_{\text{TS}}\frac{\mathcal{P}_{\text{tx},1}}{\mathcal{P}_{\text{peak}}}\int_0^{\infty}\left(\frac{\mathcal{P}_{\text{peak}}v}{d^{\lambda}}-\mathcal{P}_{\text{th}}\right)^{+}f_v(v)\mathrm{d}v\\ &= \eta\rho_{\text{TS}}\frac{\mathcal{P}_{\text{tx},1}}{\mathcal{P}_{\text{peak}}}\int_{\bar{v}_{\text{peak}}}^{\infty}\left(\frac{\mathcal{P}_{\text{peak}}v}{d^{\lambda}}-\mathcal{P}_{\text{th}}\right)f_v(v)\mathrm{d}v\\ &= \eta\rho_{\text{TS}}\frac{\mathcal{P}_{\text{tx},1}}{d^{\lambda}}\,\Psi,\end{aligned} \tag{4.23}$$

where $\bar{v}_{\text{peak}} = \mathcal{P}_{\text{th}}d^{\lambda}/\mathcal{P}_{\text{peak}}$, and

$$\begin{aligned}\Psi = \exp\left(-m\frac{\mathcal{P}_{\text{th}}d^{\lambda}}{\mathcal{P}_{\text{peak}}}\right)\times\\ \left(1+\sum_{k=0}^{m-1}\left(\mathcal{P}_{\text{th}}\frac{d^{\lambda}}{\mathcal{P}_{\text{peak}}}\right)^{k+1}\frac{m^k(m-k-1)}{(k+1)!}\right).\end{aligned} \tag{4.24}$$

Because of the average power constraint, $\rho_{\text{TS}}\mathcal{P}_{\text{tx},1}+(1-\rho_{\text{TS}})\,\mathcal{P}_{\text{tx},2}\leq\mathcal{P}_{\text{ave}}$, taking $\rho_{\text{TS}}\mathcal{P}_{\text{tx},1}=\mathcal{P}_{\text{ave}}$ into (4.23), the maximum range of average harvested power is given by

$$\bar{\mathcal{P}}_{\text{TS,max}} = \eta\frac{\mathcal{P}_{\text{ave}}}{d^{\lambda}}\,\Psi. \tag{4.25}$$

Similar to the PS scheme, from (4.23), we can easily prove that $\bar{\mathcal{P}}_{\text{TS}}$ decreases with increasing m. Thus, fading channel with larger variation in its power gain will also increase the EH performance of the TS scheme, as it does for the PS scheme.

4.3.2 Information Decoding with the TS Scheme

Compared to the PS scheme, only $1-\rho_{\text{TS}}$ portion of a block time is used for IT in the TS scheme. Since the $\overline{\text{SSR}}$ in the PS scheme measures the average number of successfully transmitted symbols per unit time, we consider a normalized $\overline{\text{SSR}}$ for the TS scheme in order to measure the same quantity, which is given by

$$\begin{aligned}\overline{\text{SSR}} &= (1-\rho_{\text{TS}}) \int_{v=0}^{\infty} (1-\text{SER}(v))\, f_v(v)\text{d}v \\ &= (1-\rho_{\text{TS}}) \left(1-\overline{\text{SER}}\right),\end{aligned} \tag{4.26}$$

where $\text{SER}(v)$ and $\overline{\text{SER}}$ are obtained by taking (4.22) into (4.17) and (4.16) respectively.

4.3.3 Optimal Transmission Strategy for the TS Scheme

We investigate the problem that given a certain required minimum average harvested power level, $\bar{\mathcal{P}}_0$, what is the maximum achievable average symbol success rate. For the TS scheme, there are three design parameters: the TS ratio, ρ_{TS}, the power for PT, $\mathcal{P}_{\text{tx},1}$, and the power for IT, $\mathcal{P}_{\text{tx},2}$. We consider the following optimization problem:

$$\begin{aligned}\textbf{P2}: \underset{\rho_{\text{TS}},\mathcal{P}_{\text{tx},1},\mathcal{P}_{\text{tx},2}}{\text{Maximize}} \quad & \overline{\text{SSR}} = (1-\rho_{\text{TS}}) \left(1-\overline{\text{SER}}\right) \\ \text{Subject to} \quad & \bar{\mathcal{P}}_{\text{TS}} \geq \bar{\mathcal{P}}_0, \\ & \rho_{\text{TS}}\mathcal{P}_{\text{tx},1} + (1-\rho_{\text{TS}})\,\mathcal{P}_{\text{tx},2} \leq \mathcal{P}_{\text{ave}}, \\ & 0 \leq \mathcal{P}_{\text{tx},1}, \varphi_j \mathcal{P}_{\text{tx},2} \leq \mathcal{P}_{\text{peak}}, \\ & 0 \leq \rho_{\text{TS}} \leq 1,\end{aligned} \tag{4.27}$$

where $\bar{\mathcal{P}}_0$ is no higher than the maximum range of average harvested power $\bar{\mathcal{P}}_{\text{TS,max}}$ defined in (4.25). $\bar{\mathcal{P}}_{\text{TS}}$ and φ_j are defined in (4.23) and (4.3), respectively.

Proposition 4. For the TS scheme, given $\bar{\mathcal{P}}_0$, $\mathcal{P}_{\text{ave}}$, $\mathcal{P}_{\text{peak}}$ and $\mathcal{P}_{\text{th}}$, the optimal parameters are given by

$$\begin{aligned}\rho_{\text{TS}}^{\star} &= \frac{\bar{\mathcal{P}}_0 d^{\lambda}}{\eta \mathcal{P}_{\text{peak}} \Psi}, \; \mathcal{P}_{\text{tx},1}^{\star} = \mathcal{P}_{\text{peak}}, \\ \mathcal{P}_{\text{tx},2}^{\star} &= \frac{1}{1-\rho_{\text{TS}}^{\star}} \left(\mathcal{P}_{\text{ave}} - \frac{\bar{\mathcal{P}}_0 d^{\lambda}}{\eta\, \Psi}\right),\end{aligned} \tag{4.28}$$

where Ψ is defined in (4.24).

Proof. See Appendix C.2. □

Taking (4.28) into (4.26), optimal achievable average symbol success rate is obtained.

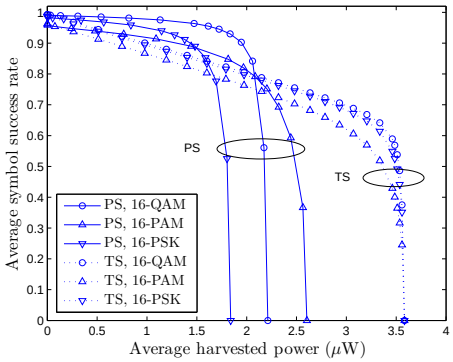

Figure 4.1: Tradeoff between the average symbol success rate and the average harvested power with different modulation schemes, M=16.

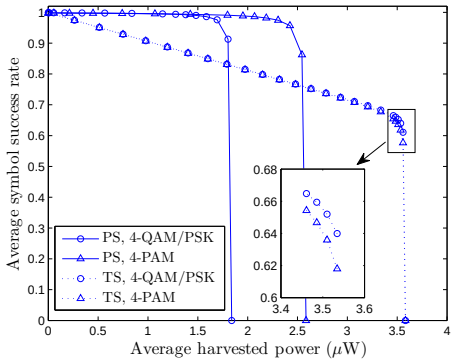

Figure 4.2: Tradeoff between the average symbol success rate and the average harvested power with different modulation schemes, M=4.

Remark 12. Recall that Proposition 3 suggests to transfer energy at a peak power and then turn the energy signal off during the remaining time if any. Contrary to this, after performing a joint optimization as done in Proposition 4, the resulting energy signal for PT is transmitted at constant power $\mathcal{P}_{\text{peak}}$ which occupies the entire PT phase.

4.4 Numerical Results

In this section, we illustrate the tradeoffs between the average symbol success rate and the average harvested power for the PS and TS schemes, which are obtained by using the optimal transmission strategies given in Sec. III-C and Sec. IV-C, respectively.

We set the average power constraint at the transmitter as $\mathcal{P}_{\text{ave}} = 10$ mW, peak power constraint as $\mathcal{P}_{\text{peak}} = 3\mathcal{P}_{\text{ave}}$ [124], distance between the transmitter and the receiver as $d = 10$ m, path loss exponent as $\lambda = 3$ [34]. We set the noise power at the receiver information-decoding circuit as $\sigma^2 = -50$ dBm. The receiver RF-EH conversion efficiency is 0.5 [2]. Unless otherwise stated, we set the modulation order at the transmitter as $M = 16$, the RF-EH sensitivity level as $\mathcal{P}_{\text{th}} = -20$ dBm [2], the Nakagami-m fading parameter as $m = 1$, i.e., Rayleigh fading channel. Under these setting, it can be proved that the average receive power at the receiver is no less than the RF-EH sensitivity level [7].

4.4.1 Effect of Modulation Schemes

Figs. 4.1 and 4.2 plot the tradeoffs between the average symbol success rate and the average harvested power using PS and TS schemes and different modulation schemes, with $M = 16$ and 4, respectively.

For the PS scheme, from Figs. 4.1 and 4.2, we see that the different modulation schemes

result in different performance tradeoff between information decoding and EH. When the required average harvested power is high, M-PAM performs better than M-QAM, and M-QAM performs better than M-PSK.[5] This order matches their order on PAPR, which is in line with Remark 9. When the required average harvested power is low, M-QAM performs better than M-PSK, and M-PSK performs better than M-PAM. This order matches their order on average symbol success rate in high SNR regime, which is in accordance with Remark 10. Thus, if we aim to harvest energy, a modulation scheme with higher PAPR performs better than the one with lower PAPR, while if we focus on information decoding, the modulation scheme with the highest PAPR performs the worst.

For the TS scheme, from Figs. 4.1 and 4.2, we see that the effect of different modulation schemes is smaller than that with the PS scheme. This is because only IT phase is affected by modulation. Thus, in general (high SNR regime), M-QAM performs better than M-PSK, and M-PSK performs better than M-PAM on average symbol success rate, as stated in Remark 10.

Also we see that given a modulation scheme, there is a crossover between the tradeoff curves of the PS and TS schemes. When the average harvested power requirement is high, the TS scheme always results in a better information-decoding performance than the PS scheme. This is due to the optimized energy signal for the TS scheme in Proposition 3, which makes the EH more efficient under the presence of RF-EH sensitivity level, while for the PS scheme, the signal for EH cannot be optimized. Note that this crossover has not been identified in the rate-energy tradeoff curves studied in [7].

4.4.2 Effect of RF-EH Sensitivity

Fig. 4.3 plots the tradeoffs between the average symbol success rate and the average harvested power under different RF-EH sensitivity level, using 16-QAM modulation scheme. We see that given a target average harvested power, the average symbol success rate varies significantly between $\mathcal{P}_{\text{th}} = 0$ and practical RF-EH sensitively level, i.e., $\mathcal{P}_{\text{th}} = -20$ dBm. When $\mathcal{P}_{\text{th}} = 0$, there is no crossover between the tradeoff curves of the PS and TS schemes, and the range of average harvested power is the same between the two schemes. This is similar to the results shown in [7], which ignored the effect of $\mathcal{P}_{\text{th}}$. If a practical RF-EH sensitivity level is set, e.g., $\mathcal{P}_{\text{th}} = -20$ dBm, the crossover is clearly observed, and we see that different SWIPT schemes result in different ranges of average harvested power. Thus, under a practical RF-EH sensitivity level, the performance tradeoff between information decoding and EH is very different from that obtained under ideal assumption. This highlights the importance of considering the RF-EH sensitivity level in this work.

[5] When $M = 4$, M-PSK is equivalent with M-QAM.

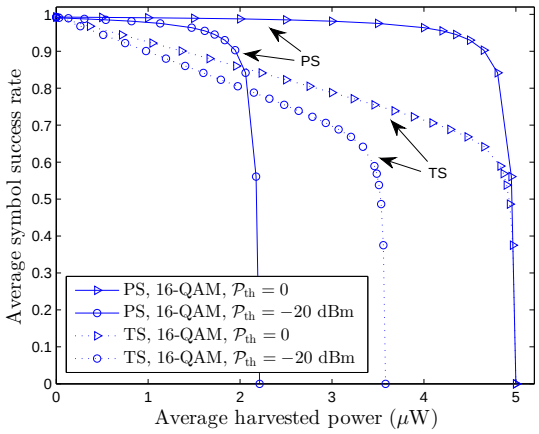

Figure 4.3: Tradeoff between the average symbol success rate and the average harvested power with different RF-EH sensitivity level.

4.4.3 Effect of Fading Channel

Fig. 4.4 plots the tradeoffs between the average symbol success rate and the average harvested power using 16-QAM modulation scheme, for different Nakagami-m fading channel parameters. The figure confirms that different values of m do not affect the general trends of the curves, as identified in Figs. 1-3 for $m = 1$. We see that if the required average harvested power is high, the channel with larger non-line-of-sight (NLOS) component, e.g., $m = 1$, leads to better information-decoding performance than the channel with smaller NLOS component, e.g., $m \to \infty$. However, if the required average harvested power is low, the channel with larger NLOS component, leads to worse information-decoding performance than the channel with smaller NLOS component. This implies that for SWIPT, fading is beneficial for EH as it creates a higher PAPR signal but detrimental for information decoding. This also verifies our observation in Remark 9.

4.5 Summary

In this chapter, we studied SWIPT between a transmitter and a receiver, using either PS or TS scheme, taking practical modulation and receiver RF-EH sensitivity level into account. For both the PS and TS schemes, we designed the optimal system parameters, which satisfy transmit average and peak power constraints and maximize the information-decoding performance with a constraint of minimum harvested energy. Our analysis showed that for the PS scheme, a modulation scheme with higher PAPR achieves better EH performance. For the TS scheme, we proposed an optimal energy signal for the PT phase, which maximizes the available harvested energy. In addition, channel fading is beneficial for EH when considering realistic values of

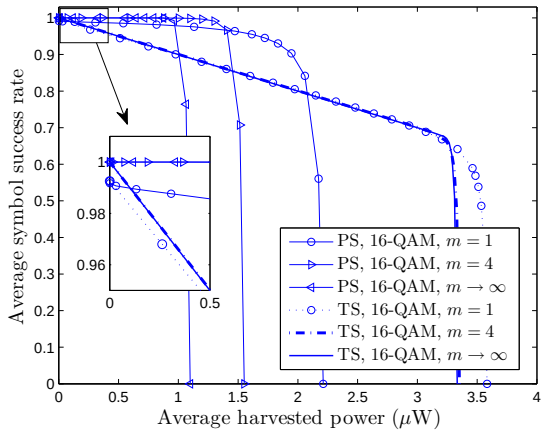

Figure 4.4: Tradeoff between the average symbol success rate and the average harvested power with different Nakagami-m fading parameters.

the RF-EH sensitivity level. The results highlight the importance of accurately characterizing the impact of RF-EH sensitivity level in SWIPT systems.

Chapter 5

A Novel SWIPT-Inspired Information Receiver

In Chapter 4, we have studied practical SWIPT systems. Exploring the fact a SWIPT receiver consists of a conventional information receiver and a RF-DC converter, can we also extract some information from the DC signal to assist information detection? We show in this chapter that the answer is 'yes'.

In this chapter, inspired by the receiver architecture of the PT-based SWIPT, we proposed a novel information receiver, which involves joint processing of coherently and non-coherently received signals. Using a passive RF power splitter, the received signal at each receiver antenna is split into two streams which are then processed by a conventional coherent detection (CD) circuit and a power-detection (PD) circuit[1], respectively. The streams of the signals from all the receiver antennas are then jointly used for information detection. We show that the splitting receiver creates a three-dimensional received signal space, due to the joint coherent and non-coherent processing. We analyze the achievable rate of a splitting receiver, which shows that the splitting receiver provides a rate gain of $3/2$ compared to either the conventional (CD-based) coherent receiver or the PD-based non-coherent receiver in the high SNR regime. We also analyze the symbol error rate (SER) for practical modulation schemes, which shows that the splitting receiver achieves asymptotic SER reduction by a factor of at least $\sqrt{M}-1$ for M-QAM compared to either the conventional (CD-based) coherent receiver or the PD-based non-coherent receiver.

This chapter is organized as follows. Section 5.1 presents the system model, the proposed receiver architectures and the splitting channel. Section 5.2 analyzes the mutual information of the splitting channel with a Gaussian input. Section 5.3 presents the received signal constellation at the splitting receiver for practical modulation schemes. Section 5.4 shows the SER results of practical modulation schemes. Finally, Section 5.5 concludes the chapter.

[1]The PD circuit is rectifier-based. The modeling of a rectifier circuit has been discussed in detail in Chapter 1.2.2.1.

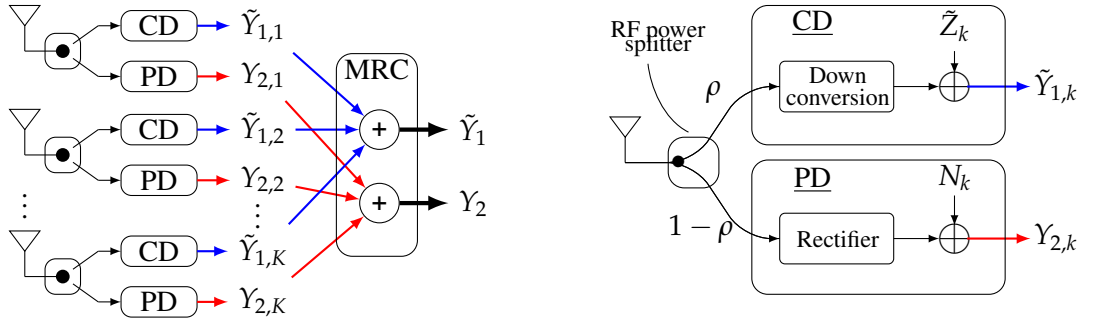

(a) K-antenna splitting receiver architecture.

(b) The kth antenna receiver architecture.

Figure 5.1: The proposed splitting receiver architecture.

5.1 System Model

Consider the communication between a single-antenna transmitter and a K-antenna receiver. The average received signal power at each antenna is denoted by $\mathcal{P}$. The channel coefficient at the kth receiver antenna is denoted by $\tilde{h}_k$.

5.1.1 Proposed Receiver Architecture

Splitting receiver: The proposed splitting receiver architecture is illustrated in Figs. 5.1(a) and (b). In the first stage, the received signal at each antenna is split into two streams by an ideal *passive RF power splitter*. We assume there is no power loss or noise introduced during the splitting process [125, 126, 26]. One stream is sent to the (conventional) CD circuit and the other to the PD circuit. The signals in the CD and PD circuits are first converted to the baseband signals and then sampled and digitized by the analog-to-digital converters (ADCs) accordingly, for further processing. Specifically, the rectifier-based PD circuit converts the RF signal into a DC signal with a conversion efficiency η. In the second stage, all the $2K$ streams of signal of the K antennas are jointly used for information detection.[2] Note that although we focus on the wireless communication application in this chapter, the proposed splitting receiver with single-antenna ($K = 1$) is also applicable to cable and fibre-optical communication systems.

Simplified receiver: We also propose a simplified receiver, as a variant of the splitting receiver, where no power splitters are required. This is illustrated in Fig. 5.2. In the simplified receiver, K_1 antennas ($1 \leq K_1 < K$) are connected to the CD circuit and the remaining antennas are connected to the PD circuits. This is illustrated in Fig. 5.2. We assume that

[2] Although the CD and PD circuits may have different detection sensitivity level in practice [35], we assume both the circuits are able to detect arbitrarily small power signal for tractability. In practice, the sensitivity levels of the circuits do not affect much on the system performance when the SNR is high, while the proposed receiver degrades to the conventional coherent receiver when the SNR is small as the sensitivity level of the PD circuit is higher than the CD circuit.

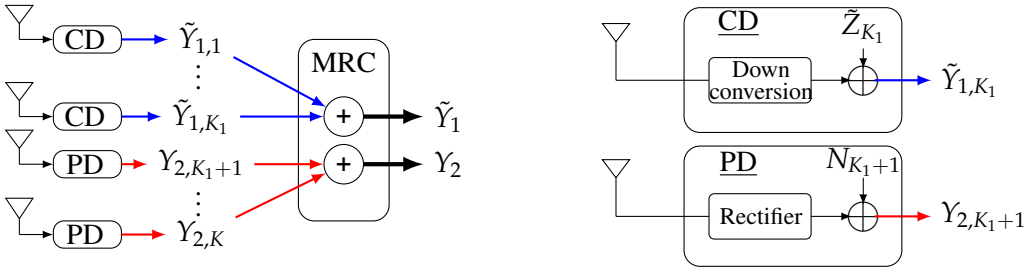

(a) K-antenna simplified receiver architecture.

(b) The K_1th and the (K_1+1)th antenna receiver architectures.

Figure 5.2: The proposed simplified receiver architecture.

the connections are determined offline, hence do not depend on the instantaneous channel coefficients at each antenna.

5.1.2 Signal Model

In this section, we present the signal model for the splitting receiver. Note that the simplified receiver can be analytically treated as a special case of the splitting receiver with power splitting ratios taking binary values only, i.e., $\rho_k \in \{0,1\}$, for all $k = 1,2,...,K$.

Based on [26, 127], the output signals from the CD and PD circuits at the kth antenna are given by, respectively,

$$\tilde{Y}_{1,k} = \sqrt{\rho_k \mathcal{P}}\tilde{h}_k \tilde{X} + \tilde{Z}_k, \tag{5.1}$$

$$Y_{2,k} = \eta(1-\rho_k)|\tilde{h}_k|^2 \mathcal{P}|\tilde{X}|^2 + N'_k, \tag{5.2}$$

where $\rho_k \in [0,1]$ is the power splitting ratio. $\tilde{X}$ is the transmitted signal with normalized variance and $\tilde{X} \in \mathcal{X}$, where $\mathcal{X}$ denotes the set of all possible transmitted signals. $\tilde{Z}_k$ is the post-processing complex AWGN of the CD circuit with the mean of zero and the variance of σ^2_{cov}, which includes both the RF band to baseband conversion noise and the ADC noise. N'_k is the post-processing noise of the PD circuit which is also assumed to be real Gaussian noise [127], which includes both the rectifier noise and the ADC noise. *Note that we only consider the post-processing noise $\tilde{Z}_k$ and N'_k, i.e., we ignore the pre-processing noise, such as the antenna noise which is almost at the thermal noise level and is much smaller than the post-processing noise [26].*

Without loss of generality, scaling (5.2) by η, the received signal $Y_{2,k}$ can be rewritten as

$$Y_{2,k} = (1-\rho_k)|\tilde{h}_k|^2 \mathcal{P}|\tilde{X}|^2 + N_k, \tag{5.3}$$

where $N_k \triangleq N'_k/(\eta)$ is the equivalent rectifier conversion AWGN with the mean of zero and

the variance σ_{rec}^2.

5.1.3 Maximal Ratio Combining of Splitting Receiver

To detect the transmitted signal $\tilde{X}$, similar with a conventional SIMO receiver, the optimal method is the maximal ratio combining (MRC). We assume that the receiver has perfect channel state information (CSI), i.e., knowledge of $\tilde{h}_k$. Since the K-antenna received signals $\tilde{Y}_{1,k}$ and $Y_{2,k}$, $k = 1, 2, ..., K$, lie in different signal spaces, we use MRC for coherently processed signals (i.e., $\tilde{Y}_{1,k}$) and non-coherent signals (i.e., $Y_{2,k}$) separately. Based on (5.1) and (5.3), the combined coherently and non-coherently processed signals are given by, respectively,

$$\begin{aligned} \tilde{Y}_1 &= \left(\sum_{k=1}^{K} \rho_k |\tilde{h}_k|^2\right) \sqrt{\mathcal{P}}\tilde{X} + \sum_{k=1}^{K} \sqrt{\rho_k}\tilde{h}_k^* \tilde{Z}_k, \\ Y_2 &= \left(\sum_{k=1}^{K} (1-\rho_k)^2 |\tilde{h}_k|^4\right) \mathcal{P}|\tilde{X}|^2 + \sum_{k=1}^{K} (1-\rho_k)|\tilde{h}_k|^2 N_k. \end{aligned} \tag{5.4}$$

For convenience of analysis, after linear scaling, (5.4) can be rewritten as

$$\tilde{Y}_1 = \sqrt{\Theta_1}\sqrt{\mathcal{P}}\tilde{X} + \tilde{Z},\ Y_2 = \sqrt{\Theta_2}\mathcal{P}|\tilde{X}|^2 + N, \tag{5.5}$$

where

$$\Theta_1 = \sum_{k=1}^{K} \rho_k |\tilde{h}_k|^2,\ \Theta_2 = \sum_{k=1}^{K} (1-\rho_k)^2 |\tilde{h}_k|^4, \tag{5.6}$$

and $\tilde{Z}$ and N follow the same distributions as $\tilde{Z}_k$ and N_k, respectively. The two-dimensional signal $\tilde{Y}_1$ and the one-dimensional signal Y_2 form a triple $(\tilde{Y}_1, Y_2)$, which is the equivalent received signal of the K-antenna splitting receiver.

It is interesting to see that since the two-dimensional signal $\tilde{Y}_1$ lies on the *in-phase-quadrature* (I-Q) plane and the one-dimensional signal Y_2 lines on the *power* (P)-axis, the equivalent received signal $(\tilde{Y}_1, Y_2)$ lies in the three-dimensional I-Q-P space. This is different from the conventional coherent (two-dimensional) and non-coherent (one-dimensional) receiver signal spaces. Thus, the splitting receiver expands the received signal space and fundamentally changes the way in which the signal is processed compared with the conventional receivers.

Considering the noiseless signal, i.e., letting $\tilde{Z}$ and $N = 0$ in (5.5), we have $Y_2 = \frac{\sqrt{\Theta_2}}{\Theta_1}|\tilde{Y}_1|^2$ from (5.5), which is a paraboloid equation. From a geometric point of view, defining $\vec{\rho} \triangleq [\rho_1, \rho_2, ... \rho_K]$, $\vec{1} \triangleq \underbrace{[1, 1, \cdots, 1]}_{K}$, and $\vec{0} \triangleq \underbrace{[0, 0, \cdots, 0]}_{K}$, the splitting receiver is actually bending the noiseless received signal space into a paraboloid with $\vec{\rho}$ as illustrated in Fig. 5.3. When $\vec{\rho} = \vec{1}$, i.e., a non-splitting case, the splitting receiver degrades to the coherent receiver. As the parameter $\sqrt{\Theta_2}/\Theta_1$ increases, e.g., each element of $\vec{\rho}$ decreases, the splitting receiver bends

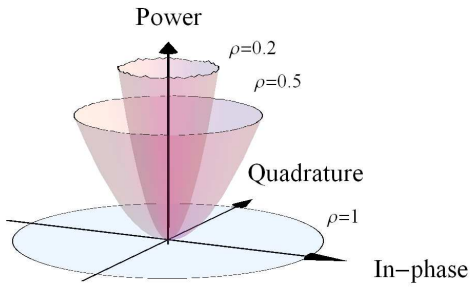

Figure 5.3: Illustration of the signal space of the splitting receiver, $\rho = 0.2, 0.5, 1$.

the signal plane to a paraboloid, which is taller and thinner with a larger $\sqrt{\Theta_2}/\Theta_1$, e.g., a smaller $\vec{\rho}$. When $\vec{\rho} = \vec{0}$, the splitting receiver degrades to the PD-based non-coherent receiver.

In this chapter, PD-based non-coherent receiver is named as *non-coherent receiver* for short, and we refer to both the K-antenna coherent receiver (i.e., $\vec{\rho} = \vec{1}$) and the K-antenna non-coherent receiver (i.e., $\vec{\rho} = \vec{0}$) as the *conventional receivers*.

5.1.4 Splitting Channel

From an information theory perspective, (5.5) can be rewritten as

$$\begin{bmatrix} \tilde{Y}_1 \\ Y_2 \end{bmatrix} = \begin{bmatrix} 1 & 0 \\ 0 & |\cdot|^2 \end{bmatrix} \begin{bmatrix} \sqrt{\Theta_1} \\ \sqrt[4]{\Theta_2} \end{bmatrix} \sqrt{\mathcal{P}}\tilde{X} + \begin{bmatrix} \tilde{Z} \\ N \end{bmatrix}, \tag{5.7}$$

where $|\cdot|^2$ is the squared magnitude operator. We name (5.7) as the *splitting channel*, and the input and output of the splitting channel regarded as random variables, are $\sqrt{\mathcal{P}}\tilde{X}$ and $(\tilde{Y}_1, Y_2)$, respectively.

The splitting channel can be treated as a SIMO channel, since the channel has one input $\sqrt{\mathcal{P}}\tilde{X}$ and two outputs $\tilde{Y}_1$ and Y_2. It can also be treated as a degraded (due to the power splitting) SISO channel with the output $\tilde{Y}_1$ and a side information Y_2.

5.1.5 Performance Metrics

We study the mutual information[3] between the input and output of the splitting channel for an ideal Gaussian input, and study the SER performance for practical modulation schemes.

[3]The mutual information is the reliable information transmission rate achieved by a certain random source.

For convenience of analysis, we define the operating SNR as

$$\mathsf{SNR} \triangleq \min\left\{\mathsf{SNR}_{\text{coh}}, \mathsf{SNR}_{\text{non-coh}}\right\}, \tag{5.8}$$

where

$$\mathsf{SNR}_{\text{coh}} \triangleq H_2\frac{\mathcal{P}}{\sigma_{\text{cov}}^2},\ \mathsf{SNR}_{\text{non-coh}} \triangleq \sqrt{H_4}\frac{\mathcal{P}}{\sigma_{\text{rec}}},\ H_2 \triangleq \sum_{k=1}^{K}|\tilde{h}_k|^2,\ H_4 \triangleq \sum_{k=1}^{K}|\tilde{h}_k|^4. \tag{5.9}$$

$\mathsf{SNR}_{\text{coh}}$ and $\mathsf{SNR}_{\text{non-coh}}$ are the SNRs of the conventional receivers, i.e., $\vec{\rho}=\vec{1}$ for the coherent receiver and $\vec{\rho}=\vec{0}$ for the non-coherent receiver, respectively. Specifically, the definition of $\mathsf{SNR}_{\text{non-coh}}$ is consistent with [127]. Note that although $\sqrt{H_4}\mathcal{P}$ and σ_{rec} correspond to the standard deviation (not variance) of the signal $\sqrt{H_4}\mathcal{P}|\tilde{X}|^2$ and the noise N at the PD receiver, respectively, $\sqrt{H_4}\mathcal{P}$ still has the physical meaning of "power". Thus, the signal-to-noise ratio is defined as $\sqrt{H_4}\frac{\mathcal{P}}{\sigma_{\text{rec}}}$ not $H_4\frac{\mathcal{P}^2}{\sigma_{\text{rec}}^2}$.

In the following, we refer to the high SNR regime as $\mathsf{SNR}\to\infty$ which is obtained by letting $\mathcal{P}\to\infty$. Our analysis will focus on the splitting receiver which includes the simplified receiver as a special case.

5.2 Splitting Channel: Mutual Information

In this section, we study the mutual information of the splitting channel to determine the gain due to the joint coherent and non-coherent processing. We also provide a discussion to intuitively explain this processing gain.

Based on (5.7), the mutual information between the input and outputs of the splitting channel with the splitting ratio $\vec{\rho}$ is

$$\begin{aligned}
&\mathcal{I}(\sqrt{\mathcal{P}}\tilde{X};\tilde{Y}_1,Y_2) = h(\tilde{Y}_1,Y_2) - h(\tilde{Y}_1,Y_2|\sqrt{\mathcal{P}}\tilde{X})\\
&=h(\tilde{Y}_1,Y_2) - h(\tilde{Z},N|\sqrt{\mathcal{P}}\tilde{X})=h(\tilde{Y}_1,Y_2) - h(\tilde{Z},N)=h(\tilde{Y}_1,Y_2) - h(\tilde{Z}) - h(N)\\
&= -\int_{Y_2}\int_{\tilde{Y}_1} f_{\tilde{Y}_1,Y_2}(\tilde{y}_1,y_2)\log_2(f_{\tilde{Y}_1,Y_2}(\tilde{y}_1,y_2))\mathrm{d}\tilde{y}_1\mathrm{d}y_2 - \log_2(\pi e\sigma_{\text{cov}}^2) - \frac{1}{2}\log_2(2\pi e\sigma_{\text{rec}}^2).
\end{aligned} \tag{5.10}$$

The joint probability density function (pdf) of $(\tilde{Y}_1,Y_2)$ is

$$f_{\tilde{Y}_1,Y_2}(\tilde{y}_1,y_2) = \int_{\tilde{X}} f_1(\sqrt{\Theta_1\mathcal{P}}\tilde{x},\tilde{y}_1)f_2(\sqrt{\Theta_2}\mathcal{P}|\tilde{x}|^2,y_2)f_{\tilde{X}}(\tilde{x})\mathrm{d}\tilde{x}, \tag{5.11}$$

where $f_{\tilde{X}}(\tilde{x})$ is the pdf of $\tilde{X}$, and $f_1(\sqrt{\Theta_1\mathcal{P}}\tilde{x},\cdot)$ and $f_2(\sqrt{\Theta_2}\mathcal{P}|\tilde{x}|^2,\cdot)$ are the pdfs of the distributions $\mathcal{CN}(\sqrt{\Theta_1\mathcal{P}}\tilde{x},\sigma_{\text{cov}}^2)$ and $\mathcal{N}(\sqrt{\Theta_2}\mathcal{P}|\tilde{x}|^2,\sigma_{\text{rec}}^2)$, respectively.

The mutual information expression in (5.10) needs five integrals to evaluate, which is cum-

bersome and thus the maximal mutual information theoretically achieved by the optimal distribution of $\tilde{X}$, cannot be obtained.

5.2.1 Mutual Information and Joint Processing Gain

For tractability, in the following analysis, we consider the mutual information with a Gaussian input, i.e., $\tilde{X} \sim \mathcal{CN}(0,1)$, and we have:

1) Letting $\vec{\rho} = \vec{1}$, the splitting channel is degraded to the coherent AWGN channel, and the mutual information is well-known as [128]

$$\mathcal{I}(\sqrt{\mathcal{P}}\tilde{X}; \tilde{Y}_1, Y_2) = h(\tilde{Y}_1) - h(\tilde{Z}) = \log_2\left(1 + H_2 \frac{\mathcal{P}}{\sigma_{\text{cov}}^2}\right), \tag{5.12}$$

which is exactly the capacity of the coherent AWGN channel, i.e., $\mathcal{C}(\vec{\rho} = \vec{1})$.

2) Letting $\vec{\rho} = \vec{0}$, the splitting channel is degraded to the conventional intensity channel in free-space optical communications [127]. Recall that we refer to the intensity channel as the non-coherent AWGN channel, echoing the coherent AWGN channel in this chapter[4]. The mutual information of the non-coherent AWGN channel is [127]

$$\begin{aligned}\mathcal{I}(\sqrt{\mathcal{P}}\tilde{X}; \tilde{Y}_1, Y_2) = h(Y_2) - h(N) &= -\int_{-\infty}^{\infty} f_{Y_2}(y_2)\log_2(f_{Y_2}(y_2))\mathrm{d}y_2 - \frac{1}{2}\log_2(2\pi e\sigma_{\text{rec}}^2) \\ &\overset{(a)}{\geq} \frac{1}{2}\log_2\left(1 + H_4\frac{\mathcal{P}^2 e}{2\pi\sigma_{\text{rec}}^2}\right),\end{aligned} \tag{5.13}$$

where $Y_2 = \sqrt{H_4}\mathcal{P}|\tilde{X}|^2 + N$ follows an exponential modified Gaussian distribution [129]:

$$f_{Y_2}(y_2) = \frac{1}{2\sqrt{H_4}\mathcal{P}} \exp\left(\frac{1}{2\sqrt{H_4}\mathcal{P}}\left(\frac{\sigma_{\text{rec}}^2}{\sqrt{H_4}\mathcal{P}} - 2y_2\right)\right) \operatorname{erfc}\left(\frac{\frac{\sigma_{\text{rec}}^2}{\sqrt{H_4}\mathcal{P}} - y_2}{\sqrt{2}\sigma_{\text{rec}}}\right). \tag{5.14}$$

The inequality (a) is given by [127], and (5.13) is the asymptotic mutual information in the high SNR regime, which is also the asymptotic capacity (with gap less than $|\frac{1}{2}\log_2\left(\frac{e}{2\pi}\right)|$ bits) of the non-coherent AWGN channel, i.e., $\mathcal{C}(\vec{\rho} = \vec{0})$.

Comparing (5.12) and (5.13), it is easy to see that as $\mathsf{SNR} \to \infty$, *the coherent and non-coherent AWGN channels have the same asymptotic capacity*, i.e., $\lim_{\mathsf{SNR}\to\infty} \mathcal{C}(\vec{\rho} = \vec{1})/\mathcal{C}(\vec{\rho} = \vec{0}) = 1$. In the following, we will show that the splitting receiver with $\vec{\rho} \neq \vec{0}$ nor $\vec{1}$ provides a gain

[4]Note that in this chapter, the non-coherent channel refers to the intensity channel, and it does not refer to the kind of channel without CSI at the transmitter or the receiver.

in the mutual information compared with the conventional receivers. Firstly, we need the following definition.

Definition 3. *The joint processing gain of the splitting receiver is*

$$G \triangleq \frac{\sup\{\mathcal{I}(\sqrt{\mathcal{P}}\tilde{X};\tilde{Y}_1,Y_2):\vec{\rho}\in[0,1]^K\}}{\max\{\mathcal{I}(\sqrt{\mathcal{P}}\tilde{X};\tilde{Y}_1,Y_2)|_{\vec{\rho}=\vec{0}},\mathcal{I}(\sqrt{\mathcal{P}}\tilde{X};\tilde{Y}_1,Y_2)|_{\vec{\rho}=\vec{1}}\}}, \tag{5.15}$$

where $\sup\{\cdot\}$ *denotes for the supremum, and* $[0,1]^K$ *is the K-product space generated by the interval* $[0,1]$.

If the joint processing gain $G > 1$, the splitting receiver achieves higher mutual information compared with the conventional receivers. If the joint processing gain $G = 1$ which means the joint coherent and non-coherent processing is unnecessary, the splitting receiver should be degraded to either one of the conventional receivers.

Due to the complicated form of (5.10), it is not possible to accurately evaluate the mutual information[5] for $\vec{\rho} \in [0,1]^K$ and prove whether G is greater than 1 or not. Hence, we first use Monte Carlo based histogram method to simulate the results. In Fig. 5.4, considering the $K = 1$ case, it is observed that when SNR is reasonably high, e.g., $\mathcal{P} = 10$, $\sigma_{\text{cov}}^2 = 1$ and $\sigma_{\text{rec}} = 1$, the joint processing gain G is greater than 1. Inspired by this, we will focus on the analysis on the mutual information in (5.10) and the joint processing gain in Definition 3 in the high SNR regime in the following subsection.

5.2.2 High SNR Analysis

Lemma 3. *In the high SNR regime,* $\mathcal{I}(\sqrt{\mathcal{P}}\tilde{X};\tilde{Y}_1,Y_2)$ *with* $\vec{\rho}\in[0,1]^K\setminus\{\vec{0},\vec{1}\}$ *is given by*

$$\mathcal{I}(\sqrt{\mathcal{P}}\tilde{X};\tilde{Y}_1,Y_2) \approx \log_2\left(\frac{\Theta_1\mathcal{P}}{\sigma_{\text{cov}}^2}\right) + \frac{1}{2\log(2)}\exp\left(\frac{\Theta_1\sigma_{\text{rec}}^2}{\Theta_2 2\sigma_{\text{cov}}^2\mathcal{P}}\right)\text{Ei}\left(\frac{\Theta_1\sigma_{\text{rec}}^2}{\Theta_2 2\sigma_{\text{cov}}^2\mathcal{P}}\right) \tag{5.16a}$$

$$\approx \log_2\left(\frac{\sqrt{2}\mathcal{P}^{\frac{3}{2}}\sqrt{\Theta_1\Theta_2}}{\sigma_{\text{cov}}\sigma_{\text{rec}}}\right) - \frac{\gamma}{2\ln 2}, \tag{5.16b}$$

where $\text{Ei}(x) \triangleq \int_x^\infty \frac{e^{-t}}{t}\mathrm{d}t$ *is the exponential integral function, and* γ *is Euler's constant.*

Proof. See Appendix D.1. □

From Lemma 3, it is clear that the mutual information of the splitting channel increases linearly with $\log_2(\mathcal{P})$ and decreases linearly with $\log_2(\sigma_{\text{cov}})$ and $\log_2(\sigma_{\text{rec}})$ in the high SNR

[5] A lower bound and an upper bound of $\mathcal{I}(\sqrt{\mathcal{P}}\tilde{X};\tilde{Y}_1,Y_2)$ with explicit expressions can be found based on the basic inequalities $\mathcal{I}(\sqrt{\mathcal{P}}\tilde{X};\tilde{Y}_1,Y_2) > \mathcal{I}(\sqrt{\mathcal{P}}\tilde{X};\tilde{Y}_1)$, $\mathcal{I}(\sqrt{\mathcal{P}}\tilde{X};\tilde{Y}_1,Y_2) > \mathcal{I}(\sqrt{\mathcal{P}}\tilde{X};Y_2)$ and $\mathcal{I}(\sqrt{\mathcal{P}}\tilde{X};\tilde{Y}_1,Y_2) < \mathcal{I}(\sqrt{\mathcal{P}}\tilde{X};\tilde{Y}_1)+\mathcal{I}(\sqrt{\mathcal{P}}\tilde{X};Y_2)$ [128]. Since the bounds are loose, we do not pursue them here.

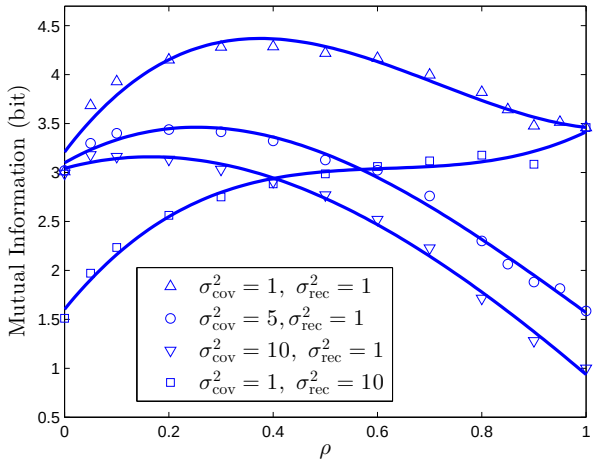

Figure 5.4: $\mathcal{I}(\sqrt{\mathcal{P}}\tilde{X};\tilde{Y}_1,Y_2)$ versus ρ, $\mathcal{P}=10$, $K=1$, $|\tilde{h}_1|=1$. The simulation results are marked with 'o's, and are curve fitted by polynomials of degree of 3.

regime. Moreover, since the mutual information depends on the power splitting ratio $\vec{\rho}$, which is contained in the term $\Theta_1\Theta_2$, it is interesting to find the optimal $\vec{\rho}$ that maximizes the mutual information.

Based on Lemma 3, the following optimization problem is proposed to obtain the optimal splitting ratio $\vec{\rho}$ in the high SNR regime:

$$\text{(P1)} \quad \max_{\vec{\rho}\in[0,1]^K\setminus\{\vec{0},\vec{1}\}} \Theta_1\Theta_2 \Leftrightarrow \max_{\vec{\rho}\in[0,1]^K\setminus\{\vec{0},\vec{1}\}} \sum_{k=1}^{K}\rho_k|\tilde{h}_k|^2 \sum_{k=1}^{K}(1-\rho_k)^2|\tilde{h}_k|^4. \tag{5.17}$$

It can be shown that (P1) is not a convex optimization problem. Thus, the optimal splitting ratio can be obtained by numerical methods. In what follows, we first focus on two special scenarios and then discuss the joint processing gain for a general splitting receiver.

5.2.2.1 Splitting receiver with single receiver antenna

When $K=1$, $\Theta_1=\rho_1|\tilde{h}_1|^2$ and $\Theta_2=(1-\rho_1)^2|\tilde{h}_1|^4$, and thus, the optimal power-splitting ratio is obtained by solving the equation $\frac{\partial\rho^{\frac{1}{3}}(1-\rho)^{\frac{2}{3}}}{\partial\rho}=0$. It is straightforward to obtain the following results.

Proposition 5. *For the splitting receiver with single receiver antenna, the optimal splitting ratio in the high SNR regime is*

$$\rho^\star=\frac{1}{3}, \tag{5.18}$$

and the maximal mutual information is given by

$$\mathcal{I}(\sqrt{\mathcal{P}}\tilde{X};\tilde{Y}_1,Y_2)|_{\rho^\star} \approx \log_2\left(\frac{2\sqrt{2}}{3\sqrt{3}}\frac{|\tilde{h}_1|^3\mathcal{P}^{\frac{3}{2}}}{\sigma_{\text{cov}}\sigma_{\text{rec}}}\right)-\frac{\gamma}{2\ln 2}. \tag{5.19}$$

5.2.2.2 Simplified receiver with a large number of antennas

For the simplified receiver with a large number of antennas, (5.17) can be rewritten as

$$\max_{1\le K_1<K}\sum_{k=1}^{K_1}|\tilde{h}_k|^2\sum_{k=K_1+1}^{K}|\tilde{h}_k|^4. \tag{5.20}$$

Assuming that $\tilde{h}_k$, $k=1,2,...K$, are independent and identically distributed (i.i.d.) random variables, i.e., *the uncorrelated scenario*, due to the law of large numbers when K is sufficiently large, we have

$$\lim_{K\to\infty}\sum_{k=1}^{K_1}|\tilde{h}_k|^2\sum_{k=K_1+1}^{K}|\tilde{h}_k|^4=\lim_{K\to\infty}K_1K_2\sum_{k=1}^{K_1}|\tilde{h}_k|^2/K_1\sum_{k=K_1+1}^{K}|\tilde{h}_k|^4/K_2\overset{(a)}{=}K_1K_2\mathbb{E}\left[|\tilde{h}_k|^2\right]\mathbb{E}\left[|\tilde{h}_k|^4\right], \tag{5.21}$$

where $K_2\triangleq K-K_1$, and (a) is because both K_1 and K_2 are sufficiently large. Assuming that $|\tilde{h}_k|$, $k=1,2,...K$, are identical with each other, i.e., *the free-space scenario which is also a fully-spatially-correlated scenario*, we have the same expression with (5.21). Thus, K_1K_2 is maximized when $K_1=K_2=K/2$, and we have the following proposition.

Proposition 6. *For the simplified receiver with a large number of antennas, the optimal strategy for the spatially-uncorrelated channel or the fully-spatially-correlated channel (i.e., the free-space scenario) in the high SNR regime is to connect half of the antennas to the CD circuits and the other half to the PD circuits, and the maximum mutual information is given by*

$$\mathcal{I}(\sqrt{\mathcal{P}}\tilde{X};\tilde{Y}_1,Y_2)|_{\vec{\rho}^\star} \approx \log_2\left(\frac{K\mathcal{P}^{\frac{3}{2}}\sqrt{\mathbb{E}\left[|\tilde{h}_k|^2\right]\mathbb{E}\left[|\tilde{h}_k|^4\right]}}{\sqrt{2}\sigma_{\text{cov}}\sigma_{\text{rec}}}\right)-\frac{\gamma}{2\ln 2}. \tag{5.22}$$

Note that for the general spatially-correlated scenario, the optimal strategy in the high SNR regime is not immediately clear. We will investigate this scenario for future study.

5.2.2.3 Joint processing gain of splitting receiver with K receiver antennas

We assume that $\vec{\rho} \neq \vec{0}$ nor $\vec{1}$, thus, $\Theta_1 \neq 0$ and $\Theta_2 \neq 0$. Then, based on (5.16b) of Lemma 3, (5.12) and (5.13), we can show that

$$\lim_{\mathsf{SNR}\to\infty} \frac{\mathcal{I}(\sqrt{\mathcal{P}}\tilde{X}; \tilde{Y}_1, Y_2)|_{\vec{\rho}\in[0,1]^K\setminus\{\vec{0},\vec{1}\}}}{\max\{\mathcal{I}(\sqrt{\mathcal{P}}\tilde{X}; \tilde{Y}_1, Y_2)|_{\vec{\rho}=\vec{0}}, \mathcal{I}(\sqrt{\mathcal{P}}\tilde{X}; \tilde{Y}_1, Y_2)|_{\vec{\rho}=\vec{1}}\}} = \frac{3}{2}. \tag{5.23}$$

In other words, the asymptotic gain is the same no matter what value $\vec{\rho}$ takes, as long as $\vec{\rho} \neq \vec{0}$ nor $\vec{1}$. Therefore, the asymptotic optimal splitting ratio $\vec{\rho}^\star \in [0,1]^K \setminus \{\vec{0}, \vec{1}\}$, and we have the following result based on Definition 3.

Proposition 7. *In the high SNR regime, the asymptotic joint processing gain for a splitting receiver with K receiver antennas is*

$$G = \lim_{\mathsf{SNR}\to\infty} \frac{\mathcal{I}(\sqrt{\mathcal{P}}\tilde{X}; \tilde{Y}_1, Y_2)|_{\vec{\rho}^\star}}{\max\{\mathcal{I}(\sqrt{\mathcal{P}}\tilde{X}; \tilde{Y}_1, Y_2)|_{\vec{\rho}=\vec{0}}, \mathcal{I}(\sqrt{\mathcal{P}}\tilde{X}; \tilde{Y}_1, Y_2)|_{\vec{\rho}=\vec{1}}\}} = \frac{3}{2}. \tag{5.24}$$

5.2.3 Explanation of the Joint Processing Gain

The result of Proposition 7 shows that in the high SNR regime, since $G = 3/2 > 1$, the splitting receiver provides a processing gain. Note that although the joint processing gain at any given SNR depends on the specific value of the received signal power $\mathcal{P}$, the noise variances σ^2_{cov} and σ^2_{rec}, the asymptotic joint processing gain is independent of the specific noise variances at the CD and PD circuits in the high SNR regime. *This implies that the reason for the performance improvement lies in the joint coherent and non-coherent processing.* This is explained in detail using intuitive and geometric arguments as follows.

Intuitive explanation of the rate improvement: Since the degrees of freedom of a channel is commonly defined as the dimension of the received signal space [130], the coherent AWGN channel has two degrees of freedom (I-Q plane) while the non-coherent AWGN channel has one degree of freedom (P-axis). For the splitting channel created by jointly utilizing both the coherent and non-coherent AWGN channels, the received signals are spread into a three-dimensional space, i.e., the I-Q-P space. Thus, the splitting channel can be treated as a channel with three degrees of freedom. Therefore, the splitting channel with a properly designed splitting ratio can take better advantage of the I-Q-P space, and achieve a better channel rate performance compared with either the coherent or non-coherent AWGN channel.

We would like to highlight that a 'splitting receiver', which splits the received signal at each antenna into two streams and sends both streams to CD circuits (i.e., two coherent AWGN channels), does not provide any rate improvement. After MRC, it is straightforward to see that the received signal space still lies on the I-Q plane. Thus, the received signal space is the same

as for the conventional coherent receiver. For instance, consider a single-antenna receiver for ease of illustration. It can be proved that the best 'splitting' strategy is to send the entire signal to the CD circuit with a smaller noise variance, instead of splitting and sending signals to both CD circuits [130]. Therefore, there is no joint processing gain by using two coherent AWGN channels, i.e., $G = 1$. The same argument holds for a 'splitting receiver' which splits the received signal at each antenna into two streams and sends them to two PD circuits (i.e., two non-coherent AWGN channels).

Therefore, the key to the rate improvement is the increased dimension of the received signal space achieved by joint coherent and non-coherent processing, where the coherent channel adds noise linearly to the signal, and the noncoherent channel adds noise to the square amplitude of the signal.

A geometric explanation of the asymptotic gain: As discussed in Section 5.1.3, a splitting receiver with the splitting ratio $\vec{\rho}$ maps the noiseless received signal space, i.e., the I-Q plane, to a paraboloid in the I-Q-P space with parameter $\sqrt{\Theta_2}/\Theta_1$ which depends on $\vec{\rho}$. Considering a disk with radius R and center $(0,0)$ in the I-Q plane, the area of the disk is πR^2, where R is proportional to $\sqrt{P}$ in this chapter. After the mapping, the disk is converted into a paraboloid with parameter $\sqrt{\Theta_2}/\Theta_1$ which is restricted by the condition that the projection of the paraboloid in the I-Q plane should lie within the disk with radius $\sqrt{\Theta_1}R$. When R is sufficiently large, the area of the paraboloid can be shown to be approximated by $3\pi\sqrt{\Theta_1\Theta_2}R^3$ for $\vec{\rho} \neq \vec{0}$ nor $\vec{1}$. It is well known that the optimal constellation design for the I-Q space is equivalent to a sphere-packing problem, i.e., packing two-dimensional spheres (disks) with a certain radius, which is related to the detection error rate, on the surface of the disk (i.e., the disk on the I-Q plane). The number of spheres that can be packed is proportional to the area of the disk. Thus, the communication rate can be written as $\mathcal{O}\left(\log(\pi R^2)\right) \sim 2\mathcal{O}(\log R)$. Similarly, for the paraboloid, the number of three-dimensional spheres[6] (balls) that can be packed on the surface is proportional to the paraboloid area, and the rate can be written as $\mathcal{O}\left(\log(3\pi\sqrt{\Theta_1\Theta_2}R^3)\right) \sim 3\mathcal{O}(\log R)$. Therefore, it is straightforward to see that there is a $3/2$ fold rate gain provided by the splitting receiver when R is sufficiently large. To sum up, bending the signal space from a two-dimensional plane to a three-dimensional paraboloid increases the effective area of the signal space which boosts the communication rate.

The complexity of splitting receiver: Although the splitting receiver is able to provide a performance gain, it is clear that for the information detection in the digital domain, the splitting receiver requires a three-dimensional detection, while the conventional CD/PD receiver only needs a two/one-dimensional detection, respectively. Specifically, when applying the minimum distance detection for practical modulation, the splitting receiver needs to calculate

[6]Note that sphere-packing is considered only if $\sigma^2_{\text{cov}} = 2\sigma^2_{\text{rec}}$, i.e., a uniform three-dimensional noise sphere, otherwise, it is ellipsoid-packing. Here we use sphere-packing for ease of illustration.

the distance between two signal points in the three-dimensional space, while the conventional CD/PD receiver only needs to calculate the distance in the two/one-dimensional space. Thus, the splitting receiver requires a higher computational complexity to achieve the performance gain. Regarding the circuit complexity, for each antenna branch, the splitting receiver requires two detection circuits, while the conventional CD/PD receiver only needs one detection circuit. On the other hand, the proposed simplified receiver has a lower complexity than the CD receiver and a higher complexity than the PD receiver. Therefore, we should consider both the performance gain and the complexity (and the cost) when adopting a splitting receiver in practical systems.

5.2.4 Numerical Results

In the last two subsections, we have shown and explained that the splitting receiver achieves a $3/2$ fold rate gain compared with the non-splitting channels in the high SNR regime. This suggests that a notable performance improvement can be found within a moderate SNR range, which is verified as follows. Also, we verify the tightness of the asymptotic analytical results presented in Section 5.2.2.

5.2.4.1 Single-antenna scenario

We set the channel power gain $|\tilde{h}_1|^2 = 1$ for simplicity.

Fig. 5.5 depicts the mutual information approximation given in (5.16a) and also the simulated mutual information with different received signal power. We see that the approximation and simulation results have the same general trend, and the percentage difference between the approximation and simulation results decreases as $\mathcal{P}$ increase (e.g., from $\mathcal{P} = 10$ to 100). Also we see that the optimal splitting ratios are (almost) the same for both the approximation and simulation results. When SNR is sufficiently large, e.g., 20 dB, $\rho = 0.33$ makes the mutual information at least 20% larger than that of the conventional cases (i.e., $\rho = 0$ or 1), and the joint processing gain is shown to be $G \approx 1.3$. When $\mathsf{SNR} = 30$ dB (i.e., $\mathcal{P} = 1000$), the approximation is tight, and the joint processing gain with $\rho = 0.33$ is close to 1.5. Thus, the tightness of the mutual information expressions in Lemma 3 and Proposition 5 (which is obtained by taking $\rho = 1/3$ into Lemma 3) and also the asymptotic joint processing gain given by Proposition 7 are verified.

Fig. 5.6 depicts the optimal splitting ratio ρ (obtained by simulation) versus the received signal power $\mathcal{P}$. It is observed that the optimal splitting ratio approaches $1/3$ quickly as $\mathcal{P}$ increases, i.e., $\rho = 1/3$ when $\mathcal{P} > 35$. *Thus, $\rho = 1/3$ is a near-optimal choice even at moderate SNRs, and the tightness of the asymptotic optimal splitting ratio in Proposition 5 is verified.*

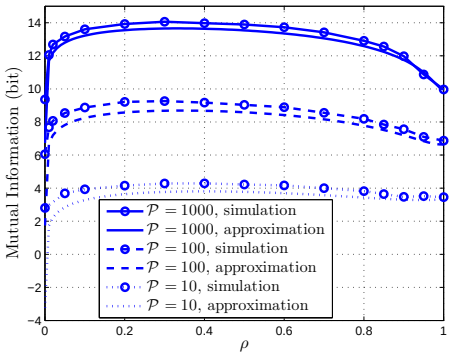

Figure 5.5: Mutual information versus $\rho, \sigma^2_{\text{cov}} = \sigma^2_{\text{rec}} = 1$.

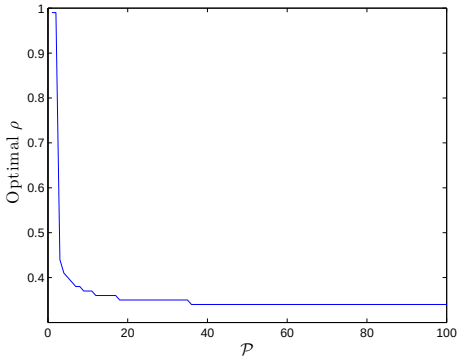

Figure 5.6: Optimal ρ versus $\mathcal{P}$, $\sigma^2_{\text{cov}} = \sigma^2_{\text{rec}} = 1$.

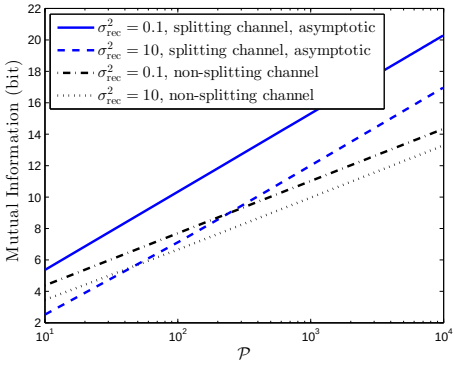

Figure 5.7: Mutual information of the splitting channel and the non-splitting channel versus $\mathcal{P}$, $\sigma^2_{\text{cov}} = 1$.

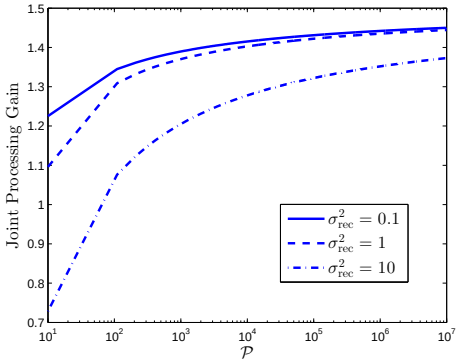

Figure 5.8: Joint processing gain versus $\mathcal{P}$, $\sigma^2_{\text{cov}} = 1$.

Fig. 5.7 depicts the approximation of the splitting channel mutual information given in (5.16a) with $\rho = 1/3$, and the optimal non-splitting channel mutual information, i.e., $\max\{(5.12), (5.13)\}$. It is observed that the splitting channel mutual information increases much faster w.r.t. $\mathcal{P}$ as compared with the coherent and non-coherent AWGN channels. When $\mathsf{SNR} > 20$ dB (e.g., $\mathcal{P} > 100$, $\sigma^2_{\text{cov}} = 1$ and $\sigma^2_{\text{rec}} = 0.1$, or $\mathcal{P} > 1000$, $\sigma^2_{\text{cov}} = 1$ and $\sigma^2_{\text{rec}} = 10$), one can clearly see the mutual information improvement due to splitting.

Fig. 5.8 depicts the joint processing gain obtained by taking (5.16a) into Definition 3. It is observed that the joint processing gain increases with $\mathcal{P}$ and slowly approaches the constant $3/2$. The gain at a practically high SNR, e.g., 30 dB, is notable, e.g., $1.2 \sim 1.4$.

5.2.4.2 Multi-antenna scenario

Fig. 5.9 depicts the average mutual information over 10^3 channel realizations using (5.16b), where the channel power gain $|\tilde{h}_k|^2$ is assumed to follow an exponential distribution with the

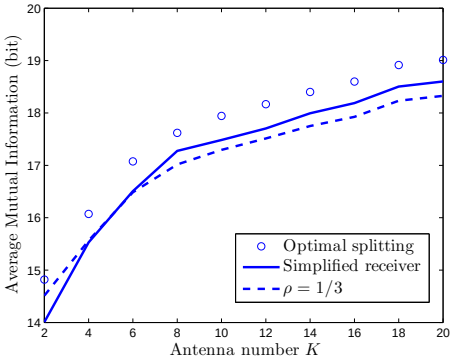

Figure 5.9: Mutual information of the splitting channel with different splitting strategies, $\sigma^2_{\text{cov}} = \sigma^2_{\text{rec}} = 1$.

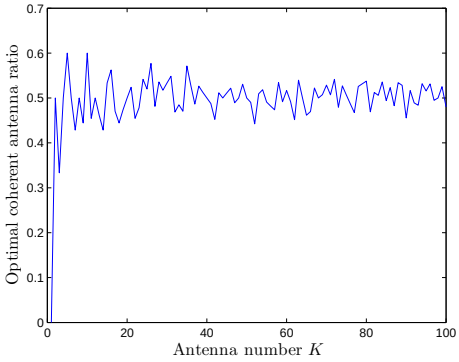

Figure 5.10: Average optimal ratio of antennas allocated for coherent processing versus K.

mean of 1, and $\mathcal{P} = 100$. Three splitting strategies are considered: (i) the numerically searched optimal splitting ratios by solving (P1) for every channel realization (i.e., optimal splitting), (ii) the simplified receiver with the strategy in Proposition 6, and (iii) $\rho_k = 1/3$ for all $k = 1, 2, ..., K$. It is observed that the splitting receiver with the optimal splitting strategy is better than the simplified receiver. On the other hand, the splitting receiver can perform worse than the simplified receiver if some sub-optimal splitting strategy is used, e.g., $\rho = 1/3$, which is the optimal for a single-antenna receiver, but generally not necessarily optimal for a multi-antenna receiver.

Fig. 5.10 depicts the optimal ratio of antennas allocated for coherent processing for a simplified receiver obtained by simulation using 10^4 random channel realizations. *It shows that the optimal ratio is within the range of* $(0.45, 0.55)$ *when* $K > 40$*, and the optimal ratio converges to* $1/2$ *as* K *increases further, which verifies Proposition 6.*

5.3 Splitting Receiver: Practical Modulation

In this section, we consider commonly used modulation schemes and assume that each signal of the constellation is transmitted with the same probability. Note that, in this section, x and y denote the in-phase and quadrature signals in the CD circuit, respectively, and z denotes the signal in the PD circuit, which are different from the notation in Section 5.2. This change of notation is adopted for ease of presentation of results.

5.3.1 Transmitted Signal Constellation

We consider the transmitted signal constellation of a general M-ary modulation scheme is Ω_{gen}, which is a two-dimensional constellation placed on the I-Q plane. The ith symbol is denoted by the tuple (x_i, y_i) on the I-Q plane, $i = 1, 2, ..., M$. Specifically:

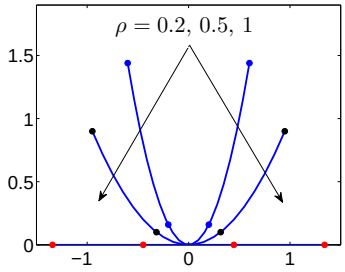

(a) 4-PAM on the I-P plane.

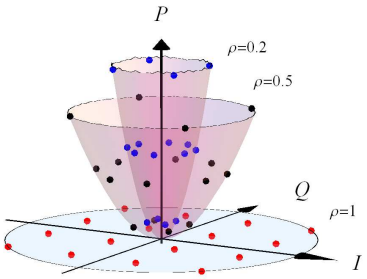

(b) 16-QAM on the I-Q-P space, $\rho = 0.2,\ 0.5,\ 1$.

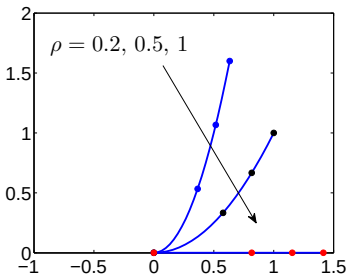

(c) 4-IM on the I-P plane.

Figure 5.11: Noiseless received signal constellation with different $\vec{\rho}$, $K = 1$, $|\tilde{h}_1| = 1$, $\mathcal{P} = 10$.

(i) For the M-PAM scheme [130], which is a one-dimensional modulation scheme on the I-axis, we have $x_i = 2i - 1$ for $i = 1, 2, ..., M/2$, and $x_i = -x_{i-M/2}$ for $i = M/2 + 1, ...M$, and $y_i = 0$ for all i.

(ii) For the M-QAM scheme, which is a two-dimensional modulation scheme on the I-Q plane, we have $x_i = 2\left(i \mod \frac{\sqrt{M}}{2}\right) - 1$, $y_i = 2\left\lfloor \frac{i-1}{\sqrt{M}/2} \right\rfloor - 1$, $i = 1, 2, ..., M/4$, which are the first quadrant symbols on the I-Q plane. Due to the symmetry property of M-QAM, the other quadrant symbol expressions are omitted for brevity.

(iii) For the M-IM scheme, which is a one-dimensional modulation scheme on the positive I-axis where the information is carried by the signal power but not phase, we have $x_i = \sqrt{2(i-1)}$ and $y_i = 0$, $i = 1, 2, ..., M$.

5.3.2 Noiseless Received Signal Constellation

Based on the received signal expression after MRC in (5.5), the average signal power of the coherently and non-coherently processed signals are $\Theta_1\mathcal{P}$ and $\sqrt{\Theta_2}\mathcal{P}$, respectively. Thus, with such average power constraints, we define the noiseless received signal constellation

$\breve{\Omega}_{\text{gen}}$, and the ith symbol in $\breve{\Omega}_{\text{gen}}$ is denoted by the tuple $(\breve{x}_i, \breve{y}_i, \breve{z}_i)$, and $\breve{x}_i = k_1\sqrt{\Theta_1\mathcal{P}}x_i$, $\breve{y}_i = k_1\sqrt{\Theta_1\mathcal{P}}y_i$, $\breve{z}_i = k_2\sqrt{\Theta_2}\mathcal{P}\left(x_i^2 + y_i^2\right)$. Here k_1 and $k_2 \triangleq k_1^2$ are the power normalization parameters determined only by the geometric property of a certain modulation scheme. Specifically, we have

$$k_1 = \begin{cases} \sqrt{\dfrac{3}{M^2-1}}, & M\text{-PAM}, \\ \sqrt{\dfrac{3}{2(M-1)}}, & M\text{-QAM}, \\ \sqrt{\dfrac{1}{M-1}}, & M\text{-IM}. \end{cases} \tag{5.25}$$

For the single-antenna scenario, Figs. 5.11(a) and 5.11(c) show that the splitting ratio $\rho \in (0,1)$ bends the received signal constellation from the I-axis to a paraboloid in the I-P plane, for 4-PAM and 4-IM, respectively. Fig. 5.11(b) shows that the splitting ratio $\rho \in (0,1)$ bends the received signal constellation from the I-Q plane to a paraboloid in the I-Q-P space.

5.3.3 Decision Region

Since all the transmitted symbols are of equal probability, the optimal signal detection method is the maximum likelihood (ML) method [130]. The decision region for the ith symbol is defined as

$$\mathcal{V}_i \triangleq \left\{\boldsymbol{v} | f(\boldsymbol{v}|i) \geq f(\boldsymbol{v}|j), \forall j \neq i, \boldsymbol{v} \in \mathbb{R}^3\right\}, \tag{5.26}$$

where $\boldsymbol{v} \triangleq (x, y, z)$ is the three-dimensional post-processing (noise added) signal in the splitting receiver, and $f(\cdot|\cdot)$ is the conditional pdf.

From Section 5.2, since both the CD and PD circuits introduce additive Gaussian noise, the received signal is surrounded by the noise sphere (ellipsoid) in the I-Q-P space, and $f(\boldsymbol{v}|i)$ is thus given by

$$f(\boldsymbol{v}|i) = \frac{1}{\sigma_{\text{cov}}^2\pi\sqrt{2\sigma_{\text{rec}}^2\pi}} \exp\left(-\frac{(x-x_i)^2}{\sigma_{\text{cov}}^2} - \frac{(y-y_i)^2}{\sigma_{\text{cov}}^2} - \frac{(z-z_i)^2}{2\sigma_{\text{rec}}^2}\right). \tag{5.27}$$

Therefore, (5.26) is rewritten as

$$\mathcal{V}_i \triangleq \left\{(x,y,z) : \, d_i(x,y,z) \leq d_j(x,y,z), \forall j \neq i\right\}, \tag{5.28}$$

where

$$d_j(x,y,z) \triangleq \frac{\left(x-x_j\right)^2}{\sigma_{\text{cov}}^2/2} + \frac{\left(y-y_j\right)^2}{\sigma_{\text{cov}}^2/2} + \frac{\left(z-z_j\right)^2}{\sigma_{\text{rec}}^2}. \tag{5.29}$$

From (5.28) and (5.29), after simplification, the decision region of the ith symbol, $\mathcal{V}_i$ is given by

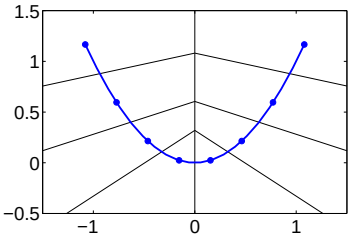

(a) 8-PAM decision regions in the I-P plane.

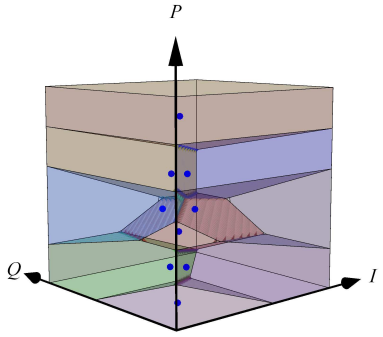

(b) Illustration of the decision regions for 36-QAM in the first quadrant, i.e., $x > 0$ and $y > 0$.

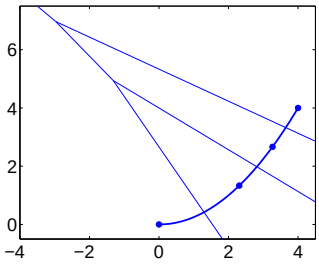

(c) 4-IM decision regions in the I-P plane.

Figure 5.12: Decision regions for 8-PAM, 36-QAM and 4-IM, $\mathcal{P} = 10$, $\sigma^2_{\text{cov}} = 2$, $\sigma^2_{\text{rec}} = 1$.

$$\mathcal{V}_i = \left\{ (x,y,z) : \frac{\check{x}_j - \check{x}_i}{\sigma^2_{\text{cov}}} x + \frac{\check{y}_j - \check{y}_i}{\sigma^2_{\text{cov}}} y + \frac{\check{z}_j - \check{z}_i}{2\sigma^2_{\text{rec}}} z \leq \frac{\check{x}_j^2 + \check{y}_j^2 - \check{x}_i^2 - \check{y}_i^2}{2\sigma^2_{\text{cov}}} + \frac{\check{z}_j^2 - \check{z}_i^2}{4\sigma^2_{\text{rec}}}, \forall j \neq i \right\}, \tag{5.30}$$

where $\check{x}_i$, $\check{y}_i$ and $\check{z}_i$ are defined in Section 5.3.2 above (5.25). It is easy to see that $\mathcal{V}_i$ is bounded by planes. The plane implied in (5.30), which divides the decision region between the ith and jth receive symbols, is given by

$$\mathcal{A}_{i-j} \triangleq \left\{ (x,y,z) : \frac{\check{x}_j - \check{x}_i}{\sigma^2_{\text{cov}}} x + \frac{\check{y}_j - \check{y}_i}{\sigma^2_{\text{cov}}} y + \frac{\check{z}_j - \check{z}_i}{2\sigma^2_{\text{rec}}} z = \frac{\check{x}_j^2 + \check{y}_j^2 - \check{x}_i^2 - \check{y}_i^2}{2\sigma^2_{\text{cov}}} + \frac{\check{z}_j^2 - \check{z}_i^2}{4\sigma^2_{\text{rec}}} \right\}. \tag{5.31}$$

The decision regions for 8-PAM, 36-QAM (only for the symbols within the first quadrant of the I-Q-P space) and 4-IM are illustrated in Figs. 5.12(a), 5.12(b), and 5.12(c), respectively.[7]

[7] Although for a practical M-QAM scheme, M is usually selected as a power of 2 so that the information bits can be easily mapped onto the QAM constellation, the M-QAM modulation (e.g. 36-QAM) that M is not a power of 2 are still useful for coded modulation schemes.

5.3.4 Joint Processing Gain in SER

To quantify the reduction in SER by the splitting receiver, we define the joint processing gain in terms of SER as:

Definition 4 (Joint processing gain in SER)**.** *Given a certain modulation scheme, the joint processing gain of the splitting receiver is*

$$G \triangleq \frac{\min_{\vec{\rho}=\vec{0},\vec{1}} P_e}{\inf\{P_e : \vec{\rho} \in [0,1]^K\}}, \tag{5.32}$$

where $\inf\{\cdot\}$ *denotes for the infimum, and* P_e *is the SER for a given* $\vec{\rho}$*.*

The joint processing gain represents the maximum SER reduction provided by the splitting receiver, compared with the best of the conventional receivers.

5.4 Splitting Receiver: SER Analysis

In this section, we derive the SER at a splitting receiver for practical modulation schemes with the transmitted signal constellation Ω_{gen} in the I-Q plane and the received signal constellation $\breve{\Omega}_{\text{gen}}$ in the I-Q-P space.

The SER can be written as

$$P_e = \frac{1}{M}\sum_{i=1}^{M}(1 - P_i), \tag{5.33}$$

where P_i is the symbol success probability of the ith symbol, which is given by

$$P_i = \iiint_{\mathcal{V}_i} \exp\left(-\frac{(x-\breve{x}_j)^2}{\sigma_{\text{cov}}^2/2} - \frac{(y-\breve{y}_j)^2}{\sigma_{\text{cov}}^2/2} - \frac{(z-\breve{z}_j)^2}{\sigma_{\text{rec}}^2}\right) \mathrm{d}x\mathrm{d}y\mathrm{d}z. \tag{5.34}$$

Based on Section 5.3.2, when $\mathsf{SNR} \to \infty$ and $\vec{\rho} \in [0,1]^K \setminus \{\vec{0},\vec{1}\}$, the received symbols $(\breve{x}_i, \breve{y}_i, \breve{z}_i)$ and $(\breve{x}_j, \breve{y}_j, \breve{z}_j)$ belonging to different power tiers, i.e., $\breve{z}_i \neq \breve{z}_j$, are easily distinguished because they are separated by a distance proportional to $\mathcal{P}$ in the power domain. In contrast, the symbols belonging to the same power tier are only separated with a distance proportional to $\sqrt{\mathcal{P}}$ on the I-Q plane. Thus, the intra-tier detection error probability dominates the overall SER in the high SNR regime.

Therefore, there are basically two cases for the SER analysis in the high SNR regime:

1. For Ω_{gen} having symbols that belong to the same tier as illustrated in Fig. 5.13(a), such as M-PAM, M-QAM and M-PSK (phase-shift keying), the intra-tier detection error

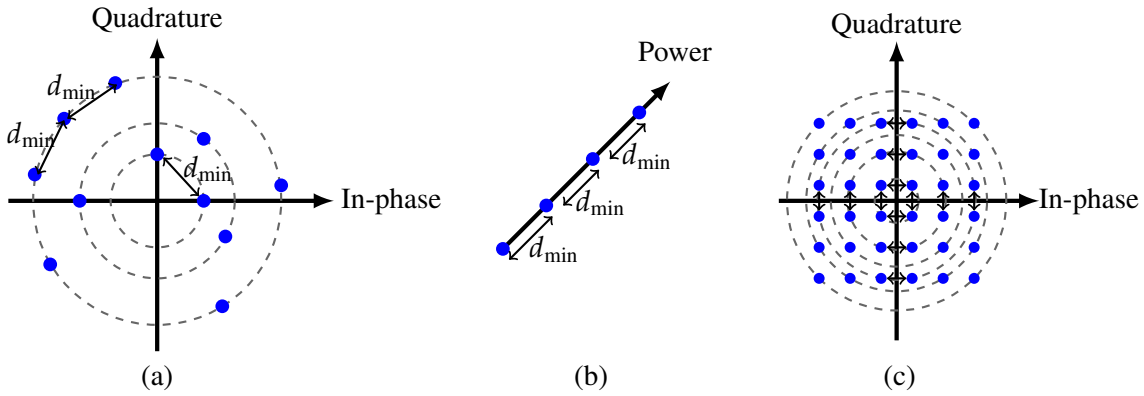

Figure 5.13: (a) and (b) Two transmitted signal constellation maps with 3 pairs of symbols that are dominant on detection error probability, plotted on the I-Q plane and the P-axis, respectively. (c) The transmitted signal constellation for 36-QAM, where 12 pairs of symbol that are dominant on detection error probability are illustrated.

probability is dominant. Moreover, the detection error caused by the pair symbols with the minimum distance on the I-Q plane is dominant (see Fig. 5.13(a)).

2. For Ω_{gen} in which every symbol belongs to a different tier as illustrated in Fig. 5.13(b), such as a M-IM, the inter-tier detection error probability is dominant. Moreover, the detection error caused by the pair of symbols with the minimum distance in the P-axis (power domain) is dominant.

Consider a transmitted signal constellation Ω_{gen} with W pairs of dominant symbols as mentioned above and the minimum distance being $d_{\min}$. The approximated SER is calculated as [130]

$$P_e \approx \frac{1}{M}\sum_{i=1}^{W} 2Q\left(\frac{d_{\min}}{2\sigma}\right), \tag{5.35}$$

where $\sigma = \sqrt{\sigma_{\text{cov}}^2/2}$ or σ_{rec} for cases 1) and 2), respectively.

It is straightforward to see that: For M-PAM, we have $W = 1$, i.e., the pair of symbols with the lowest power having the minimum distance given by $d_{\min} = 2\check{x}_1$. For M-QAM, we have $W = 2\sqrt{M}$, as illustrated in Fig. 5.13(c), and $d_{\min} = 2\check{x}_1$. For M-IM, we have $W = M - 1$, as illustrated in Fig. 5.13(b) and $d_{\min} = \check{x}_2 - \check{x}_1$. Then, based on (5.35), we can obtain the following results.

5.4.1 M-PAM

Proposition 8. *For the M-PAM scheme and* $\vec{\rho} \in [0,1]^K \setminus \{\vec{0}, \vec{1}\}$, *the SER in the high SNR regime is given by*

$$P_e \approx \frac{2}{M} Q\left(\frac{\sqrt{2}\check{x}_1}{\sigma_{\text{cov}}}\right). \tag{5.36}$$

Based on Proposition 8, we can see that when $\vec{\rho} \neq \vec{1}$ and $\vec{\rho} \to \vec{1}$, $\check{x}_1 \approx \sqrt{3H_2\mathcal{P}/(M^2-1)}$, and $P_e \approx \frac{2}{M}Q\left(\sqrt{\frac{6H_2\mathcal{P}}{\sigma_{\text{cov}}^2(M^2-1)}}\right)$, which is smaller than the SER of the $\vec{\rho} = \vec{1}$ case, i.e., $\frac{2(M-1)}{M} \times Q\left(\sqrt{\frac{6H_2\mathcal{P}}{\sigma_{\text{cov}}^2(M^2-1)}}\right)$, and is also smaller than the SER of the $\vec{\rho} = \vec{0}$ case in which the SER can be as large as 0.5. Thus, we have the following proposition:

Proposition 9. *For M-PAM, the asymptotic joint processing gain in the high SNR regime is*

$$G_{\text{PAM}} = \frac{\min\left\{0.5, \frac{2(M-1)}{M}Q\left(\sqrt{\frac{6H_2\mathcal{P}}{\sigma_{\text{cov}}^2(M^2-1)}}\right)\right\}}{\frac{2}{M}Q\left(\sqrt{\frac{6H_2\mathcal{P}}{\sigma_{\text{cov}}^2(M^2-1)}}\right)} = M-1. \tag{5.37}$$

Note that although the joint processing gain depends on $\mathcal{P}$, σ_{cov}^2 and σ_{rec}^2, the asymptotic joint processing gain is independent of the specific noise variance at the CD and PD circuits in the high SNR regime.

5.4.2 M-QAM

Proposition 10. *For M-QAM and $\vec{\rho} \in [0,1]^K \setminus \{\vec{0}, \vec{1}\}$, the SER in the high SNR regime is given by*

$$P_e \approx \frac{4}{\sqrt{M}}Q\left(\frac{\sqrt{2}\check{x}_1}{\sigma_{\text{cov}}}\right). \tag{5.38}$$

Letting $\vec{\rho} \to \vec{1}$, i.e., $\check{x}_1 \to \sqrt{\frac{3H_2\mathcal{P}}{2(M-1)}}$, the approximated SER in Proposition 10 is minimized as $P_e \approx \frac{4}{\sqrt{M}}Q\left(\sqrt{\frac{3H_2\mathcal{P}}{(M-1)\sigma_{\text{cov}}^2}}\right)$, which is smaller than the SER obtained by setting $\vec{\rho} = \vec{0}$ or $\vec{1}$. Thus, we have the following result:

Proposition 11. *For M-QAM, the asymptotic joint processing gain in the high SNR regime is*

$$\begin{aligned} G_{\text{QAM}} &= \lim_{\text{SNR}\to\infty} \frac{4\left(1-\frac{1}{\sqrt{M}}\right)Q\left(\sqrt{\frac{3H_2\mathcal{P}}{(M-1)\sigma_{\text{cov}}^2}}\right) - 4\left(1-\frac{1}{\sqrt{M}}\right)^2 Q\left(\sqrt{\frac{3H_2\mathcal{P}}{(M-1)\sigma_{\text{cov}}^2}}\right)^2}{\frac{4}{\sqrt{M}}Q\left(\sqrt{\frac{3H_2\mathcal{P}}{(M-1)\sigma_{\text{cov}}^2}}\right)} \\ &= \lim_{\text{SNR}\to\infty} \frac{4\left(1-\frac{1}{\sqrt{M}}\right)Q\left(\sqrt{\frac{3H_2\mathcal{P}}{(M-1)\sigma_{\text{cov}}^2}}\right)}{\frac{4}{\sqrt{M}}Q\left(\sqrt{\frac{3H_2\mathcal{P}}{(M-1)\sigma_{\text{cov}}^2}}\right)} = \sqrt{M}-1. \end{aligned} \tag{5.39}$$

Therefore, in the high SNR regime, for M-PAM and M-QAM, there always exists a non-trivial $\vec{\rho}$ that $\vec{\rho} \in [0,1]^K \setminus \{\vec{0}, \vec{1}\}$ and achieves a lower SER than the conventional receivers, i.e., $\vec{\rho} = \vec{0}$ or $\vec{1}$, no matter what values σ_{cov}^2 and σ_{rec} take.

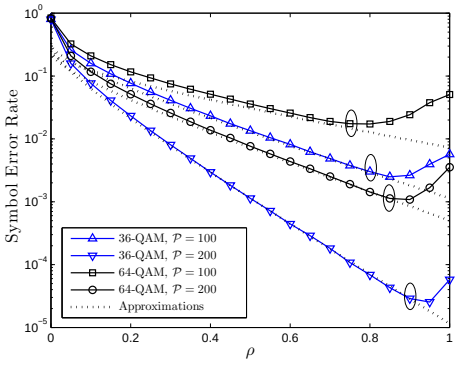

Figure 5.14: SER versus ρ, $\sigma^2_{\text{cov}} = 1$ and $\sigma^2_{\text{rec}} = 1$.

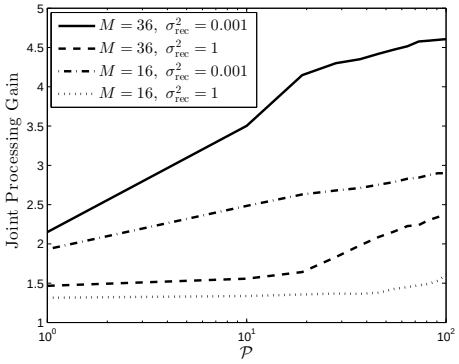

Figure 5.15: G_{QAM} versus $\mathcal{P}$, $\sigma^2_{\text{cov}} = 1$.

5.4.3 M-IM

Proposition 12. *For M-IM, the SER in the high SNR regime is given by*

$$P_e \approx \frac{2(M-1)}{M} Q\left(\frac{\sqrt{\Theta_2}\mathcal{P}}{(M-1)\sigma_{\text{rec}}}\right). \tag{5.40}$$

From Proposition 12, as $\vec{\rho} \to \vec{0}$, the minimum approximated SER is obtained as $P_e = \frac{2(M-1)}{M} \times Q\left(\frac{\sqrt{H_4}\mathcal{P}}{(M-1)\sigma_{\text{rec}}}\right)$, which equal to the SER when $\vec{\rho} = \vec{0}$. Thus, the splitting receiver cannot improve the SER performance compared with the conventional receivers, and we have the result:

Proposition 13. *For M-IM, the asymptotic joint processing gain in the high SNR regime is equal to one.*

5.4.4 Numerical Results

We present the numerical results using M-QAM for (i) the splitting receiver with single receiver antenna assuming $|\tilde{h}_1|^2 = 1$, and (ii) the simplified receiver with multiple receiver antennas. The SER results for M-QAM are plotted based on Monte Carlo simulation with 10^9 points using the detection rule (5.30). The results for M-PAM and M-IM are omitted for brevity.

5.4.4.1 Splitting receiver with single receiver antenna

Fig. 5.14 plots the SER versus the splitting ratio ρ for different M and different $\mathcal{P}$, where the approximation results are plotted using Proposition 10. It shows that the SER first decreases and then increases as ρ increases. We can see that the optimal ρ that minimizes the SER, increases with $\mathcal{P}$ and approaches 1 but decreases with the increasing of the order of constellation

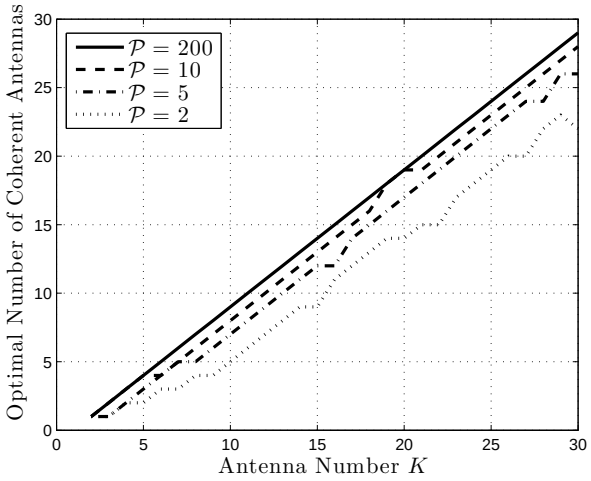

Figure 5.16: Optimal number of antennas allocated for coherent processing versus K for 16-QAM, $\sigma^2_{\text{cov}} = \sigma^2_{\text{rec}} = 1$.

M. Also we can see that when SNR is sufficiently large, e.g., 23 dB (i.e., $\mathcal{P} = 200$, and $\sigma^2_{\text{cov}} = \sigma^2_{\text{rec}} = 1$), the approximation of the SER is very close with the accurate SER for the value of ρ in the range $(0, \rho^\star)$, where $\rho^\star$ is the optimal splitting ratio. Note that $\rho^\star$ approaches 1 as SNR increases. This means the mismatch around $\rho = 1$ is minimized as SNR increases. *Therefore, the approximation in Proposition 10 is accurate for the values of* $\rho \in (0, 1)$ *when* SNR *is sufficiently large.*

Fig. 5.15 shows the joint processing gain versus $\mathcal{P}$ using Definition 4. We can see that the joint processing gain increase with $\mathcal{P}$ and approaches 3 and 5 for 16-QAM and 36-QAM, respectively, when $\mathcal{P} = 100$, $\sigma^2_{\text{cov}} = 1$ and σ^2_{rec} is sufficiently small, e.g., 10^{-3}. These results approach the asymptotic joint processing gain in Proposition 11. Also we see that only half the joint processing gain is achieved when $\mathcal{P} = 100$ and σ^2_{rec} is large, e.g., $\sigma^2_{\text{rec}} = 1$. However, the increasing trend of the joint processing gain in Fig. 15 suggest that the asymptotic joint processing gain can be eventually achieved, when $\mathcal{P}$ is much larger than 100. *Therefore, the asymptotic joint processing gain in Proposition 11 may not be approached in a normal range of the received signal power and the noise variance, but half of the joint processing gain is achievable.*

5.4.4.2 Simplified receiver with multiple receiver antennas

For the simplified receiver, we assume that the channel power gain at each antenna is independent and follows an exponential distribution with the mean of 1. Fig. 5.16 plots the optimal number of antennas allocated for coherent processing, i.e., $K_1^\star$, versus the total number of antennas for the 36-QAM scheme obtained by using 10^3 random channel realizations.

It shows that $K_1^\star$ increases with K, and approaches to $K-1$ in the high SNR regime, e.g, $K_1^\star \approx K-5,\ K-2$ and $K-1$ when $\mathcal{P} = 2,\ 10$ and 200, respectively. This is because that the optimal ratio $\vec{\rho} \to \vec{1}$ but never reaches $\vec{1}$ based on Proposition 8 in the high SNR regime. In other words, for the simplified receiver (where $\rho_k \in \{0,1\}$), most of the antennas should be connected to the CD circuits and at least one antenna should be connected to a PD circuit to achieve the highest joint processing gain.

Note that in practice, the degradation of ADC noise is usually modeled by the signal-to-quantization-noise ratio (SQNR), approximately given by $6K$ dB, where K is the number of quantization bits [26]. Here, by assuming $\mathcal{P} = 2$ and the noise variance of the ADC equals to 0.1 (i.e., less than σ_{cov}^2 and σ_{rec}^2), the SQNR equals to 13 dB, which implies $K \approx 2$ bits. Similarly, by assuming $\mathcal{P} = 200$, the SQNR equals to 33 dB, which implies $K \approx 5$ bits. Therefore, the parameter settings are practical.

5.5 Summary

In this chapter, we have proposed a splitting receiver, which fundamentally changes the way in which the signal is processed. With the same received signal power, the analytical results show that the splitting receiver provides excellent performance gain in the sense of both the mutual information (Gaussian input) and the SER (practical modulation), compared with the conventional coherent and non-coherent receivers.

Chapter 6

WPT-Based Backscatter Interference Networks

To prolong the life time of energy-constrained IoT network, EH and WPT are possible solutions, as investigated in Chapters 2, 3 and 4. Another solution is to consider passive communication technique, i.e., BackCom, to cut down the energy consumption of information transmission.

In this chapter, we study the passive BackCom system which consumes negligible energy for information transmission. In future IoT network, low-latency communication scheme is required especially in delay-sensitive application scenarios. Again, as battery replacement for the massive number of IoT devices is difficult if not infeasible, WPT is desirable. This motivates: (i) the design of *full-duplex* WIT to reduce latency and enable efficient spectrum utilization, and (ii) the implementation of *passive* IoT devices using backscatter antennas that enable WPT from one device (reader) to another (tag). However, the resultant increase in the density of simultaneous links exacerbates the interference issue. This issue is addressed in this chapter by proposing the design of full-duplex *backscatter communication* (BackCom) networks, where a novel multiple-access scheme based on *time-hopping spread-spectrum* (TH-SS)[1] is designed to enable both one-way WPT and two-way WIT in coexisting backscatter reader-tag links. Comprehensive performance analysis of BackCom networks is presented in this chapter, including forward/backward bit-error rates and WPT efficiency and outage probabilities, which accounts for energy harvesting at tags, non-coherent and coherent detection at tags and readers, respectively, and the effects of asynchronous transmissions.

This chapter is organized as follows. Sections 6.1 and 6.2 presents the system model and the time-hopping full-duplex BackCom scheme. Section 6.3 analyzes the farward and backward WIT performance of two-link BackCom network under both the static and fading channels. Section 6.4 analyzes the forward WPT performance. Sections 6.5 and 6.6 study

[1]The TH-SS scheme is one of the classical spread spectrum schemes. For example, the code-division multiple access (CDMA) scheme is another spread spectrum scheme.

the effects of asynchronous transmissions and the performance of K-link BackCom network, respectively. Section 6.7 presents the numerical results. Finally, Section 6.8 concludes the chapter.

6.1 System Model

We consider a BackCom system consisting of K coexisting single-antenna reader-tag pairs. Each reader is provisioned with a full-duplex antenna (see e.g.,[131]) allowing simultaneous transmission and reception. For simplicity, it is assumed that self-interference (from transmission to reception) at the reader due to the use of a full-duplex antenna is perfectly cancelled, *since the reader only transmits an unmodulated signal (i.e., the carrier wave), and the self-interference which can be easily cancelled by filtering in the analog domain.* Each passive tag uses a backscatter antenna for transmission by backscattering a fraction of the incident signal and an energy harvester for harvesting the energy in the remaining fraction. Each pair of intended reader and tag communicate by full-duplex transmission with robustness against interference using the design presented in the next section. The architecture of such a full-duplex passive tag is shown in Fig. 6.1. The baseband additive white Gaussian noise (AWGN) at Reader k is represented by the random variable $z_{\text{reader},k}$ with variance σ^2_{reader}. The passband noise signal at Tag k is $z_{\text{tag},k}(t)$ with variance σ^2_{tag}.

It is assumed that all the readers/tags share the same band for communication. Block fading is assumed such that the channel coefficients remain unchanged within a symbol duration but may vary from symbol-to-symbol. We consider both the static and Rayleigh fading channels, corresponding to the cases with or without mobility, respectively.[2] For the Rayleigh fading channel, we assume that the channel coefficient are composed of the large-scale path loss with exponent λ and the statistically independent small scale Rayleigh fading. The distance between Reader m and Tag n is denoted by d_{mn}. The *channel state information* (CSI) of the intended backscatter channel (reader-to-tag-to-reader) is available at the corresponding reader. However, the CSI of interference channels is not available at the reader. Moreover, tags have no knowledge of any channel.

It is important to note that the interference in a BackCom interference channel is more severe and complex than that in a conventional one. This is mainly due to *interference regeneration* by backscatter antennas at tags that reflect all incident signals including both data and interference signals. As an example, a two-link system is shown in Fig. 6.2 where interference regeneration is illustrated.

[2] Although a more general channel model, i.e., the Rician fading channel, is not considered in this chapter, the following analysis framework for the static and Rayleigh fading channels can be used directly for the Rician fading scenario.

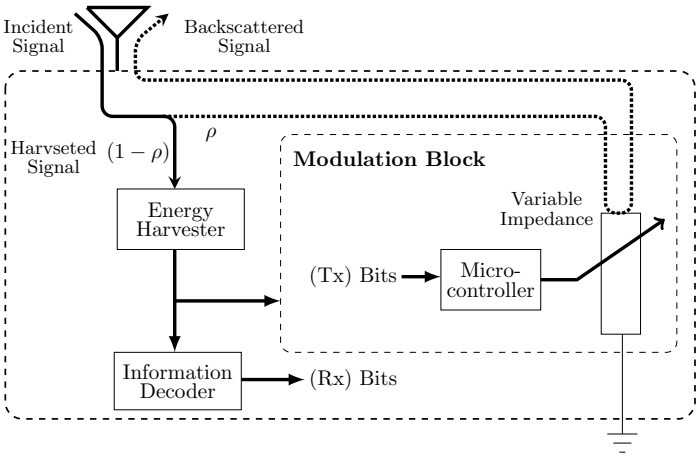

Figure 6.1: The architecture of a full-duplex tag.

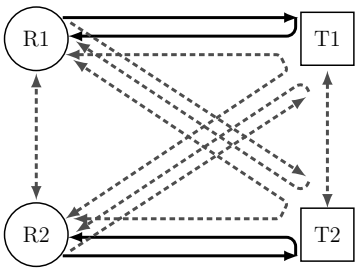

Figure 6.2: Two-link full-duplex interference channel. For example, signal R1-T1-R1 is the signal transmitted by Reader 1, then backscattered by Tag 1 and received by Reader 1.

The performance metrics are defined as follows. Both the BER for the backward and forward WIT are analyzed in the sequel. For the forward WPT, we consider two metrics: (i) the *expected* WPTR, denoted as $\mathcal{E}_{\text{tag}}$ and defined as the expected harvested energy at a tag per symbol, and (ii) the energy-outage probability [36], denoted as P_{out} and defined as the probability that the harvested energy at the tag during a symbol duration is below the tag's fixed energy consumption, denoted as $\mathcal{E}_0$.

Note that $\mathcal{E}_{\text{tag}}$ and P_{out} are related to the cases of large or small energy storage at tags, respectively. Specifically, a large energy storage battery accumulates the energy with random arrivals, and hence is able to constantly power the tag circuit especially when the instantaneous harvested energy is very small. Thus, we care about the expected harvested energy at a tag. Given a small or no storage, the instantaneous harvested energy is required to exceed the circuit power so as to operate the tag circuit, and cannot be accumulated for further usage. Thus, we care about the energy-outage probability.

6.2 Time-Hopping Full-Duplex BackCom Scheme

The proposed time-hopping full-duplex BackCom scheme comprises two components, namely the sequence-switch modulation and full-duplex BackCom, which are designed in the following sub-sections.

6.2.1 Sequence-Switch Modulation

The sequence-switch modulation used by each reader is designed for several purposes. The first is to suppress interference by TH-SS. The second is to enable simultaneous WIT and WPT under the constraint of non-coherent detection at the intended tag by energy detection [103]. Last, the modulation should support full-duplex BackCom by allowing a reader to transmit a carrier wave for backscatter by the intended tag.

Let a symbol duration T be uniformly divided into N slots called *chips*. For the mentioned purposes, define a *TH-SS sequence* as a N-chip random sequence comprising only a *single* randomly located nonzero chip while others are silent. Each link is assigned a pair of sequences with different nonzero chips to represent “0" and “1" of a bit. Then switching the sequences enables the transmission of a binary-bit stream, giving the name of sequence-switch modulation. Note that the sequence-switch modulation is also named as the *pulse-position modulation* in conventional UWB systems [96]. Consider the generation of a pair of TH-SS sequences. The first sequence can be generated by randomly placing a (nonzero) *on*-chip in one of the N chip positions and the second sequence by putting the corresponding nonzero chip randomly in one of those chip-positions corresponding to zeros of the first sequence. A pair of TH-SS sequences for a particular link, say the k-th link, can be represented by the indices (or positions) of the corresponding pair of on-chips, denoted as $\mathcal{S}_k \triangleq \{s_{k0}, s_{k1}\}$ and called a *TH-SS pattern* [see Fig. 6.3(a)], while all the other chips are the *off-chips*. Note that there exist $\frac{N(N-1)}{2}$ available patterns in total. The generation of the TH-SS patterns for different links are assumed independent. The transmission of a single bit by Reader k can be equivalently represented by a binary random variable C_k with support $\mathcal{S}_k$, called a transmitted on-chip. Assuming chip synchronization between links, their transmissions in an arbitrary symbol duration can be represented by a set of i.i.d. random variables $\{C_k\}$ and illustrated in Fig. 6.3(b).

How the above design of sequence-switch modulation serves the mentioned purposes is discussed as follows. First, interference between two links arises when their TH-SS patterns overlap and thereby causes detection errors at their intended tags. The likelihood of pattern overlapping reduces with the increasing sequence length N (the processing gain) as the patterns become increasingly sparse and different links are more likely to choose different patterns. Consider two coexisting links with TH-SS patterns $\mathcal{S}_1$ and $\mathcal{S}_2$. Given the design of sequence-switch modulation, there exist three scenarios for the relation between the two patterns, namely

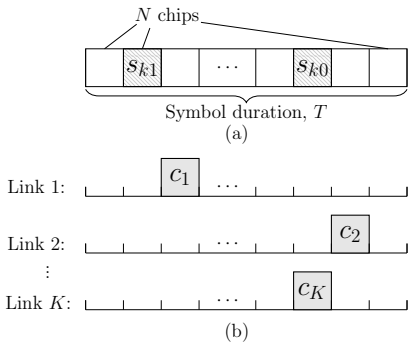

Figure 6.3: Sequence-switch modulation. (a) A TH-SS pattern. (b) Chip-synchronous transmissions of different links.

non-overlapping ($|\mathcal{S}_1 \cap \mathcal{S}_2| = 0$), *single-chip overlapping* ($|\mathcal{S}_1 \cap \mathcal{S}_2| = 1$), and *dual-chip overlapping* ($|\mathcal{S}_1 \cap \mathcal{S}_2| = 2$). For each scenario, the actual transmitted on-chips may or may not *collide* with each other. Thus each scenario can be further divided into multiple cases as illustrated in Fig. 6.4.

Next, the modulation design facilitates non-coherent detection at tags using energy detectors. For a particular link, since the assigned TH-SS pattern is known to both the reader and tag, the tag detects the transmitted bit by estimating which of the two on-chips (i.e., the chips s_{k0} and s_{k1}) in the pattern is transmitted using an energy detector. Specifically, if the harvested energy in the chip s_{k0} is larger than that in the chip s_{k1}, the estimated bit is '0', otherwise, it is '1'. Furthermore, the design of sequence-switch modulation enables WPT simultaneous with WIT by having an on-chip in every symbol duration for delivering energy to the intended tag. In addition, the tag also harvests energy from on-chips from the interference channels. As a result, the design achieves an WPT efficiency at least twice of that by using the on-off keying, namely switching between a TH-SS sequence and a all-zero sequence. Note that unlike the conventional active full-duplex transceiver, the full-duplex tag's transmission and reception are passive backscattering based and energy detection based, respectively. Thus, for such a passive transceiver, it is reasonable to assume that the backscattered (i.e., reflected) signal has no interference on the received signal for energy detection.

Last, this design feature of having an on-chip in every data symbol facilitate full-duplex BackCom. Specifically, the carrier wave modulating each on-chip is modulated and backscattered by the intended tag for backward WIT. The details are provided in the sequel.

6.2.2 Full-Duplex BackCom

Building on the sequence-switch modulation in the preceding subsection, the full-duplex BackCom is realized by the joint operation of the intended reader and tag designed as follows.

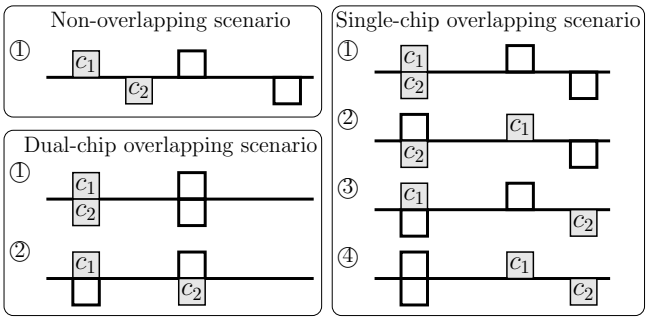

Figure 6.4: Two-link pattern-overlapping scenarios and transmission cases. The pairs of on-chips of Links 1 and 2 are the squares above and under the lines, respectively.

Consider the reader side of a particular link. A reader using one full-duplex antenna to transmit a forward bit stream using the sequence-switch modulation by sending a carrier wave represented by $\sqrt{2\mathcal{P}}\text{Real}\{e^{j\omega t}\}$ during the on-chip, where $\mathcal{P}$ is the transmission power and ω is the angular frequency. At the same time, the reader receives the tag's backscattered signal at the same antenna. After cancelling the self-interference from its transmission, the reader detects the backward bit stream by BPSK demodulation/detection of the backscattered signals in the intervals corresponding to the transmitted on-chips that are known to the reader. The reader discards the received signals in other intervals since they are interference. Note that this operation requires the chip-level synchronization between a pair of intended reader and tag.

Next, consider the tag side of the link. During the off-chips of the assigned TH-SS pattern, the tag disconnects the modulation block and harvests energy from the other readers' transmissions (see the tag architecture in Fig. 6.1). Given the RF energy harvesting efficiency η, only η portion of the RF receive power is harvested. During the two on-chip intervals of each instance of the pattern (or equivalently each symbol), the tag connects the modulation block and detects a forward bit by comparing the amounts of energy obtained from the two intervals using an energy detector. Based on the detection results, the tag estimates the transmitted on-chip positions and modulated/backscattered the signals in the corresponding chip intervals. Note that interference signal in either one or two of the on-chips may result in failure of the tag on detecting the corresponding forward bit. The variable impedance at the tag (see Fig. 6.1) is implemented by switching between two fixed impedances chosen to generate two reflection coefficients with the same magnitudes, namely $\sqrt{\rho}$, but different phase shifts, namely zero and 180 degrees. Then adapting the variable impedance to the backward bit streams modulates the backscatter signals with the bits by BPSK. Let the BPSK symbol transmitted by Tag k be denoted as q_k with $q_k \in \{1, -1\}$. Thus, during the two on-chip intervals, the tag backscatters a fraction, denoted as ρ with $\rho \in (0, 1)$, of the incident signal power and harvests the remaining fraction of $\eta(1-\rho)$.

Combining the aforementioned reader and tag operations realize the full-duplex BackCom with symmetric backward and forward WIT rates.

6.3 Time-Hopping Full-Duplex BackCom: WIT Performance

In this section, we analyze the BER for the backward and forward WIT. For simplicity, a two-link BackCom system is considered as shown in Fig. 6.2. The results are generalized for the K-link sysetm in Section 6.6. The analysis in this section focuses on the typical link, Link 1, without loss of generality.

6.3.1 BER at the Reader for Backward WIT

Consider demodulation and detection of an arbitrary bit at Reader 1. As discussed in Section 6.1 and Section 6.2, the receive baseband signal at Reader 1 during its transmitted on-chip C_1 can be written as

$$\begin{aligned} r_1 = &\sqrt{\mathcal{P}} f_{11} \sqrt{\rho} b_{11} q_1 + \mathbf{1}\left\{C_1 \in \mathcal{S}_2\right\} \sqrt{\mathcal{P}} f_{12} \sqrt{\rho} b_{21} q_2 \\ &+ \mathbf{1}\left\{C_1 = C_2\right\} \sqrt{\mathcal{P}} \left(h_{21} + f_{21} \sqrt{\rho} b_{11} q_1 + f_{22} \sqrt{\rho} b_{21} q_2\right) + z_{\text{reader},1}, \end{aligned} \tag{6.1}$$

where the two indicator functions indicate whether Tag 2 is backscattering and whether Reader 2 is transmitting during Reader 1's transmitted on-chip C_1, respectively. f_{mn} is the forward channel coefficient between Reader m and Tag n. b_{mn} is the backward channel coefficient between Tag m and Reader n. h_{mn} is the channel coefficient between Readers m and n, while g_{mn} is the channel coefficient between Tags m and n. We also assume reciprocity between the forward and backward channels, i.e., $f_{mn} = b_{nm}^*$. The first term and the second term in (6.1) correspond to the useful signal R1-T1-R1 and the interference signal R1-T2-R1, respectively, and the third term corresponds to the interference signals R2-R1, R2-T1-R1, and R2-T2-R1 as illustrated in Fig. 6.2.

Given interference at Reader 1, the BER of coherent detection can be close to the maximum of 0.5 and thus is assumed as 0.5 when Reader 1 suffers interference for simplicity. Then the BER at Reader 1 can be written as

$$P_{\text{reader}} = P_{\text{BPSK}} \Pr\left\{C_1 \notin \mathcal{S}_2\right\} + 0.5 \Pr\left\{C_1 \in \mathcal{S}_2\right\} = P_{\text{BPSK}} \left(p_0 + \frac{p_1}{2}\right) + \frac{1}{2} \left(\frac{p_1}{2} + p_2\right), \tag{6.2}$$

where P_{BPSK} denotes the BER for BPSK detection without interference, and together with the

probabilities $\{p_0, p_1, p_2\}$ are defined as follows:

$$\begin{aligned}
&P_{\text{BPSK}} = \mathbb{E}\left[Q\left(\sqrt{2\mathcal{P}\rho|f_{11}b_{11}|^2/\sigma^2_{\text{reader}}}\right)\right],\\
&p_0 \triangleq \Pr\{|\mathcal{S}_1 \cap \mathcal{S}_2| = 0\} = \binom{N-2}{2}\Big/\binom{N}{2} = \frac{(N-2)(N-3)}{N(N-1)},\\
&p_1 \triangleq \Pr\{|\mathcal{S}_1 \cap \mathcal{S}_2| = 1\} = 1 - \binom{N-2}{2}\Big/\binom{N}{2} - 1\Big/\binom{N}{2} = \frac{4(N-2)}{N(N-1)},\\
&p_2 \triangleq \Pr\{|\mathcal{S}_1 \cap \mathcal{S}_2| = 2\} = 1\Big/\binom{N}{2} = \frac{2}{N(N-1)}.
\end{aligned} \tag{6.3}$$

Substituting (6.3) into (6.2), we obtain the BER for the backward WIT at the reader:

Proposition 14. *The expected BER for the backward WIT is*

$$P_{reader} = \frac{N-2}{N}P_{BPSK} + \frac{1}{N}, \tag{6.4}$$

where it can be derived straightforwardly based on the statistics of the channel coefficients that

$$P_{BPSK} = \begin{cases} Q\left(\sqrt{2\mathcal{P}\rho|f_{11}b_{11}|^2/\sigma^2_{reader}}\right), & \textit{static channel,}\\ \dfrac{1}{2}\left(1 - \exp\left(\dfrac{d_{11}^{2\lambda}\sigma^2_{reader}}{4\mathcal{P}\rho}\right)\operatorname{erfc}\left(\dfrac{d_{11}^{\lambda}}{2}\sqrt{\dfrac{\sigma^2_{reader}}{\mathcal{P}\rho}}\right)\right), & \textit{Rayleigh fading channel,} \end{cases} \tag{6.5}$$

and $Q(\cdot)$ *and* $\operatorname{erfc}(\cdot)$ *are the Q-function and the complementary error function, respectively.*

The BER for the backward WIT decreases inversely with the reflection coefficient ρ. For the high SNR regime ($\mathcal{P}/\sigma^2_{\text{reader}} \to \infty$), the BER reduces to $P_{\text{reader}} \approx \frac{1}{N}$, which is caused by the interference and decreases inversely with the TH-SS sequence length N.

It is interesting to investigate the BER scaling law w.r.t. the sequence length N. We consider two schemes when increasing N: (i) the fixed chip power (FCP) scheme which fixes the chip transmit power $\mathcal{P}$, and (ii) the fixed chip energy (FCE) scheme which fixes the chip transmit energy denoted by $\mathcal{E}_{\text{chip}}$, and $\mathcal{E}_{\text{chip}} = \mathcal{P}\frac{T}{N}$, i.e., $\mathcal{P}$ increases linearly with N.

For the static channel, based on (6.4) and (6.5), as the sequence length $N \to \infty$, the asymptotic BER for the FCP scheme is $P_{\text{reader}} \approx \frac{N-2}{N}P_{\text{BPSK}}$, and noise is the dominant factor for causing detection errors. While the asymptotic BER for the FCE scheme is $P_{\text{reader}} \approx \frac{1}{N}$, and interference is the dominant factor for causing detection errors.

For Rayleigh fading channel, based on (6.4) and (6.5), as the sequence length $N \to \infty$, the asymptotic BER expression for both the FCP and FCE schemes is $P_{\text{reader}} \approx \frac{N-2}{N}P_{\text{BPSK}}$, and noise is the dominant factor for causing detection errors.

6.3.2 BER at the Tag for Forward WIT

We investigate the BER at Tag 1 in three different TH-SS pattern overlapping scenarios. Assuming that $P_{\text{tag}}^{(0)}$, $P_{\text{tag}}^{(1)}$ and $P_{\text{tag}}^{(2)}$ are the BER conditioned on the events $|\mathcal{S}_1 \cap \mathcal{S}_2| = 0$, $|\mathcal{S}_1 \cap \mathcal{S}_2| = 1$ and $|\mathcal{S}_1 \cap \mathcal{S}_2| = 2$, respectively, the BER at Tag 1 is

$$P_{\text{tag}} = \sum_{n=0}^{2} p_n P_{\text{tag}}^{(n)}. \tag{6.6}$$

We further calculate $P_{\text{tag}}^{(n)}$ as follows (see pattern-overlapping scenarios in Fig. 6.4):

6.3.2.1 BER Given Non-Overlapping Scenario

Tag 1's receive passband signal in the transmitted on-chip C_1 is

$$y_1(t) = \sqrt{2\mathcal{P}\eta(1-\rho)}\text{Real}\{f_{11}e^{j\omega t}\} + z_{\text{tag},1}(t). \tag{6.7}$$

Thus, the received signal power in the transmitted on-chip C_1 is

$$\mathcal{P}_0 \triangleq \mathcal{P}_{\text{rx}}^{(0)} = \mathcal{P}\eta(1-\rho)|f_{11}|^2, \tag{6.8}$$

while since neither Reader 1 nor Reader 2 is transmitting during the other on-chip $\mathcal{S}_1 \backslash C_1$, the received signal power in the other on-chip is $\check{\mathcal{P}}_{\text{rx}}^{(0)} = 0$.

Based on [103], scaling by the two-side power spectrum density of noise signal $z_{\text{tag},1}(t)$, the received energy during the transmitted on-chip C_1, E_1, follows a non-central chi-square distribution with 2 degrees of freedom and parameter $\gamma = \mathcal{P}_0/\sigma_{\text{tag}}^2$, i.e., $\chi'^2(\gamma)$. Similarly, for the other on-chip $\mathcal{S}_1 \backslash C_1$, the scaled received energy $\check{E}_1$, follows $\chi'^2(0)$. Therefore, comparing the scaled receive energy between the chips C_1 and $\mathcal{S}_1 \backslash C_1$, i.e., E_1 and $\check{E}_1$, the detection error probability is

$$P_{\text{tag}}^{(0)} = 1 - \Pr\left\{\check{E}_1 < E_1\right\} = 1 - \int_0^\infty F_{\check{E}_1}(x) f_{E_1}(x) \mathrm{d}x, \tag{6.9}$$

where $F_{\check{E}_1}(\cdot)$ and $f_{E_1}(\cdot)$ are the cumulative distribution function (cdf) and the probability density function (pdf) of the distributions $\chi'^2(0)$ and $\chi'^2(\mathcal{P}_0/\sigma_{\text{tag}}^2)$, respectively. For generality, we define function $G(a,b)$ as

$$G(a,b) \triangleq 1 - \Pr\{E_A < E_B\} = \int_0^\infty \frac{1}{2} Q_1(\sqrt{a}, \sqrt{x}) \exp\left(-(x+b)/2\right) I_0\left(\sqrt{bx}\right) \mathrm{d}x, \tag{6.10}$$

where E_A and E_B follows non-central chi-square distribution with 2 degrees of freedom and parameters a and b, respectively, and $Q_M(\cdot,\cdot)$ and $I_\alpha(\cdot)$ denotes the Marcum Q-function and

the modified Bessel function of the first kind, respectively [132]. Thus, the BER in (6.9) is represented as

$$P_{\text{tag}}^{(0)} = G(0, \mathcal{P}_0/\sigma_{\text{tag}}^2). \tag{6.11}$$

6.3.2.2 BER Given Single-Chip Overlapping Scenario

There are four transmission cases each with the same probability (see transmission cases in Fig. 6.4):

Case 1: The two readers are using the overlapping chip for transmission. Tag 1's received signal in the transmitted on-chip C_1 consists of four signals, i.e., R1-T1, R1-T2-T1, R2-T1 and R2-T2-T1, thus, the received signal power in the chip C_1 is

$$\mathcal{P}_1 \triangleq \mathcal{P}_{\text{rx}}^{(1)}(C_1 = C_2 = \mathcal{S}_1 \cap \mathcal{S}_2) = \eta(1-\rho)\mathcal{P}\left|f_{11} + f_{12}\sqrt{\rho}g_{21}q_2 + f_{21} + f_{22}\sqrt{\rho}g_{21}q_2\right|^2, \tag{6.12}$$

while the received signal power in the chip $\mathcal{S}_1 \backslash C_1$ is $\breve{\mathcal{P}}_{\text{rx}}^{(1)}(C_1 = C_2 = \mathcal{S}_1 \cap \mathcal{S}_2) = 0$. Based on (6.10), considering the randomness of both the channel coefficients[3] and Tag 2's modulated signal, the BER is

$$P_{\text{tag}}^{(1)}(C_1 = C_2 = \mathcal{S}_1 \cap \mathcal{S}_2) = \mathbb{E}_{f_{11},f_{12},f_{21},f_{22},g_{21},q_2}\left[G(0, \mathcal{P}_1/\sigma_{\text{tag}}^2)\right]. \tag{6.13}$$

Case 2: Reader 1 is using the non-overlapping chip, while Reader 2 is using the overlapping chip for transmission. The received signal in the chip C_1 is signal R1-T1, since both Reader 2 and Tag 2 are not active in the chip, thus, the received signal power in the chip C_1 is the same with (6.8), i.e., $\mathcal{P}_{\text{rx}}^{(1)}(C_1 \neq C_2 = \mathcal{S}_1 \cap \mathcal{S}_2) = \mathcal{P}_0$. While the received signal in $\mathcal{S}_1 \backslash C_1$ consists of signals R2-T1 and R2-T2-T1, and

$$\mathcal{P}_2 \triangleq \breve{\mathcal{P}}_{\text{rx}}^{(1)}(C_1 \neq C_2 = \mathcal{S}_1 \cap \mathcal{S}_2) = \eta(1-\rho)\mathcal{P}\left|f_{21} + f_{22}\sqrt{\rho}g_{21}q_2\right|^2. \tag{6.14}$$

Thus, the BER is

$$P_{\text{tag}}^{(1)}(C_1 \neq C_2 = \mathcal{S}_1 \cap \mathcal{S}_2) = \mathbb{E}_{f_{21},f_{22},g_{21},q_2}\left[G(\mathcal{P}_2/\sigma_{\text{tag}}^2, \mathcal{P}_0/\sigma_{\text{tag}}^2)\right]. \tag{6.15}$$

Case 3: Reader 1 is using the overlapping chip, while Reader-2 is using non-overlapping chip for transmission. The received signal in the chip C_1 consists of two signals, R1-T1 and

[3]Note that we have included all channel coefficients as the potential random variables over which the expectation is taken. In Rayleigh fading channel, all channel coefficients are random variables, while in the static channel they are constants. For ease of presentation, we continue to use such notations in the rest of the chapter.

R1-T2-T1, thus, the received signal power in the chip is

$$\mathcal{P}_3 \triangleq \mathcal{P}_{\text{rx}}^{(1)}(C_2 \neq C_1 = \mathcal{S}_1 \cap \mathcal{S}_2) = \eta(1-\rho)\mathcal{P}\left|f_{11} + f_{12}\sqrt{\rho}g_{21}q_2\right|^2, \tag{6.16}$$

and the received signal power in the chip $\mathcal{S}_1 \backslash C_1$ is $\breve{\mathcal{P}}_{\text{rx}}^{(1)}(C_2 \neq C_1 = \mathcal{S}_1 \cap \mathcal{S}_2) = 0$. Thus, the BER is

$$P_{\text{tag}}^{(1)}(C_2 \neq C_1 = \mathcal{S}_1 \cap \mathcal{S}_2) = \mathbb{E}_{f_{11},f_{12},g_{21},q_2}\left[G(0, \mathcal{P}_3/\sigma_{\text{tag}}^2)\right]. \tag{6.17}$$

Case 4: Reader 1 and Reader 2 are using non-overlapping chips for transmission. The received signal power in the chips C_1 and $\mathcal{S}_1 \backslash C_1$ are $\mathcal{P}_0$ and 0, respectively, and thus,

$$P_{\text{tag}}^{(1)}(C_1 \neq \mathcal{S}_1 \cap \mathcal{S}_2, C_2 \neq \mathcal{S}_1 \cap \mathcal{S}_2) = G(0, \mathcal{P}_0/\sigma_{\text{tag}}^2). \tag{6.18}$$

6.3.2.3 BER Given Dual-Chip Overlapping Scenario

There are two transmission cases each with the same probability (see transmission cases in Fig. 6.4):

Case 1: The two readers are using the same chip for transmission. We see that the received signal power in the chips C_1 and $\mathcal{S}_1 \backslash C_1$ are $\mathcal{P}_1$ and 0, respectively, and thus,

$$P_{\text{tag}}^{(2)}(C_1 = C_2) = \mathbb{E}_{f_{11},f_{12},f_{21},f_{22},g_{21},q_2}\left[G(0, \mathcal{P}_1/\sigma_{\text{tag}}^2)\right]. \tag{6.19}$$

Case 2: The two readers are using different chips for transmission. The received signal in the chip C_1 consists of signals R1-T1 and R1-T2-T1, thus, the received signal power in the non-overlapping chip is the same with (6.16), i.e., $\mathcal{P}_{\text{rx}}^{(2)}(C_1 \neq C_2) = \mathcal{P}_3$. While the received signal in $\mathcal{S}_1 \backslash C_1$ consists of signals R2-T1 and R2-T2-T1 which is the same with (6.14), i.e., $\breve{\mathcal{P}}_{\text{rx}}^{(2)}(C_1 \neq C_2) = \mathcal{P}_2$. Thus, the BER is

$$P_{\text{tag}}^{(2)}(C_1 \neq C_2) = \mathbb{E}_{f_{11},f_{12},f_{21},f_{22},g_{21},q_2}\left[G(\mathcal{P}_2/\sigma_{\text{tag}}^2, \mathcal{P}_3/\sigma_{\text{tag}}^2)\right]. \tag{6.20}$$

6.3.2.4 Main Results and Discussions

Based on the analysis above and (6.6), the expected BER for the forward WIT is

$$\begin{aligned} P_{\text{tag}} = \mathbb{E}_{f_{11},f_{12},f_{21},f_{22},g_{21},q_2} \Bigg\{ & \left(p_0 + \frac{1}{4}p_1\right) G(0, \mathcal{P}_0/\sigma_{\text{tag}}^2) \\ & + p_1\left(\frac{1}{4}G(0, \mathcal{P}_1/\sigma_{\text{tag}}^2) + \frac{1}{4}G(\mathcal{P}_2/\sigma_{\text{tag}}^2, \mathcal{P}_0/\sigma_{\text{tag}}^2) + \frac{1}{4}G(0, \mathcal{P}_3/\sigma_{\text{tag}}^2)\right) \\ & + p_2\left(\frac{1}{2}G(0, \mathcal{P}_1/\sigma_{\text{tag}}^2) + \frac{1}{2}G(\mathcal{P}_2/\sigma_{\text{tag}}^2, \mathcal{P}_3/\sigma_{\text{tag}}^2)\right)\Bigg\}. \end{aligned} \tag{6.21}$$

For tractability, we consider the high SNR regime which means $\mathcal{P}/\sigma_{\text{tag}}^2 >> 0$, and ignore the noise effect on information detection, and thus, $G(a,b) \approx \mathbf{1}\{a > b\}$.

From (6.21), we further obtain

$$\begin{aligned} P_{\text{tag}} &= \frac{N-2}{N(N-1)}\Pr\{\mathcal{P}_2 > \mathcal{P}_0\} + \frac{1}{N(N-1)}\Pr\{\mathcal{P}_2 > \mathcal{P}_3\} \\ &= \frac{N-2}{N(N-1)}\Pr\left\{|f_{21} + f_{22}\sqrt{\rho}g_{21}q_2|^2 > |f_{11}|^2\right\} \\ &+ \frac{1}{N(N-1)}\Pr\left\{|f_{21} + f_{22}\sqrt{\rho}g_{21}q_2|^2 > |f_{11} + f_{12}\sqrt{\rho}g_{21}q_2|^2\right\}. \end{aligned} \tag{6.22}$$

Thus, as the sequence length $N \to \infty$,

$$P_{\text{tag}} \approx \frac{1}{N}\Pr\left\{|f_{21} + f_{22}\sqrt{\rho}g_{21}q_2|^2 > |f_{11}|^2\right\}. \tag{6.23}$$

Therefore, increasing the sequence length N reduces the BER for the forward WIT.

Since q_2 takes value with the same probability from $\{e^{j0}, e^{j\pi}\}$, we have the following result:

Proposition 15. *For the static channel, the expected BER for the forward WIT is*

$$\begin{aligned} P_{tag} &= \frac{N-2}{2N(N-1)}\left(\mathbf{1}\left\{|f_{21} + f_{22}\sqrt{\rho}g_{21}|^2 > |f_{11}|^2\right\} + \mathbf{1}\left\{|f_{21} - f_{22}\sqrt{\rho}g_{21}|^2 > |f_{11}|^2\right\}\right) \\ &+ \frac{1}{2N(N-1)}\left(\mathbf{1}\left\{|f_{21} + f_{22}\sqrt{\rho}g_{21}|^2 > |f_{11} + f_{12}\sqrt{\rho}g_{21}|^2\right\}\right. \\ &\qquad \left. + \mathbf{1}\left\{|f_{21} - f_{22}\sqrt{\rho}g_{21}|^2 > |f_{11} - f_{12}\sqrt{\rho}g_{21}|^2\right\}\right). \end{aligned} \tag{6.24}$$

Although the effect of reflection coefficient ρ on the BER for the forward WIT depends on the specific values of the channel coefficients, for the typical case that the channel between reader-tag pair is better than the cross reader-tag channel, i.e., $|f_{11}|^2 > |f_{21}|^2$, $\rho = 0$ minimizes P_{tag} to approach zero since all the indicator functions in Proposition 15 is equal to zero.

Proposition 16. *For Rayleigh fading channel, the expected BER for the forward WIT is*

$$\begin{aligned} P_{tag} &= \frac{1}{N} - \frac{N-2}{N(N-1)}\frac{1}{\rho}\left(\frac{d_{22}d_t}{d_{11}}\right)^{\lambda}\exp\left(\frac{d_t^{\lambda}}{\rho}\left(\left(\frac{d_{22}}{d_{21}}\right)^{\lambda} + \left(\frac{d_{22}}{d_{11}}\right)^{\lambda}\right)\right)\Gamma\left(0,\ \frac{d_t^{\lambda}}{\rho}\left(\frac{d_{22}}{d_{21}}\right)^{\lambda} + \left(\frac{d_{22}}{d_{11}}\right)^{\lambda}\right) \\ &- \frac{1}{N(N-1)}\left(\frac{d_{22}^{\lambda}}{d_{12}^{\lambda} + d_{22}^{\lambda}} + \frac{d_t^{\lambda}}{\rho}\frac{\frac{1}{d_{11}^{\lambda}d_{22}^{\lambda}} - \frac{1}{d_{21}^{\lambda}d_{12}^{\lambda}}}{\left(\frac{1}{d_{12}^{\lambda}} + \frac{1}{d_{22}^{\lambda}}\right)^2}\exp\left(\frac{d_t^{\lambda}}{\rho}\frac{\frac{1}{d_{11}^{\lambda}} + \frac{1}{d_{21}^{\lambda}}}{\frac{1}{d_{12}^{\lambda}} + \frac{1}{d_{22}^{\lambda}}}\right)\Gamma\left(0,\ \frac{d_t^{\lambda}}{\rho}\frac{\frac{1}{d_{11}^{\lambda}} + \frac{1}{d_{21}^{\lambda}}}{\frac{1}{d_{12}^{\lambda}} + \frac{1}{d_{22}^{\lambda}}}\right)\right), \end{aligned} \tag{6.25}$$

where d_t is the distance between Tag 1 and Tag 2, and $\Gamma(\cdot,\cdot)$ is the incomplete gamma function.

Proof. See Appendix E.1. □

For the typical case that $d_{11} < d_{21}$ and $d_{22} < d_{12}$, i.e., each reader-tag pair distance is smaller than the cross reader-tag distance, we have $\frac{1}{d_{11}^{\lambda} d_{22}^{\lambda}} - \frac{1}{d_{21}^{\lambda} d_{12}^{\lambda}} > 0$ in Proposition 16, and thus, it can be shown that P_{tag} monotonically increases with ρ.

Therefore, for both the static and Rayleigh fading channels, a higher reflection coefficient leads to a higher BER for the forward WIT in the typical case, and there is a clear tradeoff between the BER for the forward and backward transmission in terms of ρ.

6.4 Time-Hopping Full-Duplex BackCom: WPT Performance

We analyze the expected PTR and the energy-outage probability in the following subsections.

6.4.1 Expected PTR

In Section 6.3.2, we have analyzed the harvested power (energy) in the pair of on-chips. While for the off-chips, Tag 1 can harvest energy from Reader 2's WIT and Tag 2's backscattering only if $C_2 \notin \mathcal{S}_1$. The probability $\Pr\{C_2 \notin \mathcal{S}_1\} = p_0 + \frac{1}{2}p_1$. Thus, Tag 1's received signal in the chip C_2 consists of two signals when $C_2 \notin \mathcal{S}_1$, i.e., R2-T1 and R2-T2-T1, and the received signal power in the chip is

$$\mathcal{P}_{\text{eh}} \triangleq \eta \mathcal{P} \left| f_{21} + f_{22}\sqrt{\rho} g_{21} q_2 \right|^2 . \tag{6.26}$$

Therefore, based on the analysis in Section 6.3.2, considering Tag 1's received signal power in the chips C_1, $\mathcal{S}_1 \backslash C_1$ and C_2, the expected PTR is

$$\begin{aligned} \mathcal{E}_{\text{tag}} &= \frac{T}{N} \left(\sum_{n=0}^{2} p_n \mathbb{E}\left[\mathcal{P}_{\text{rx}}^{(n)} + \check{\mathcal{P}}_{\text{rx}}^{(n)} \right] + \Pr\{C_2 \notin \mathcal{S}_1\} \mathbb{E}\left[\mathcal{P}_{\text{eh}}\right] \right) \\ &= \frac{T}{N} \mathbb{E}_{f_{11}, f_{12}, f_{21}, f_{22}, g_{21}, q_2} \left[\frac{N-2}{N} \left(\mathcal{P}_0 + \mathcal{P}_{\text{eh}} \right) + \frac{1}{N} \left(\mathcal{P}_1 + \mathcal{P}_2 + \mathcal{P}_3 \right) \right]. \end{aligned} \tag{6.27}$$

Proposition 17. *For the static channel, the expected PTR is*

$$\begin{aligned} \mathcal{E}_{tag} = \frac{\eta \mathcal{P} T}{N} \Bigg(& \frac{N-2}{N} \left((1-\rho)|f_{11}|^2 + \frac{1}{2} \left(|f_{21} + \sqrt{\rho} f_{22} g_{21}|^2 + |f_{21} - \sqrt{\rho} f_{22} g_{21}|^2 \right) \right) \\ & + \frac{(1-\rho)}{2N} \left(|f_{11} + f_{21} + \sqrt{\rho}(f_{21} + f_{22}) g_{21}|^2 + |f_{11} + f_{21} - \sqrt{\rho}(f_{21} + f_{22}) g_{21}|^2 \right) \\ & + \frac{(1-\rho)}{2N} \left(|f_{21} + \sqrt{\rho} f_{22} g_{21}|^2 + |f_{21} - \sqrt{\rho} f_{22} g_{21}|^2 + |f_{11} + \sqrt{\rho} f_{12} g_{21}|^2 + |f_{11} - \sqrt{\rho} f_{12} g_{21}|^2 \right) \Bigg). \end{aligned} \tag{6.28}$$

Although the effect of reflection coefficient ρ on the expected PTR for the forward WPT depends on the specific values of the channel coefficients, for the typical case that direct channel signal is much stronger than the backscattered signal, i.e., $|f_{12}g_{21}|^2 << |f_{11}|^2$ and $|f_{22}g_{21}|^2 << |f_{21}|^2$, $\mathcal{E}_{\text{tag}}$ increases inversely with ρ.

Proposition 18. *For Rayleigh fading channel, the expected PTR is*

$$\mathcal{E}_{tag} = \frac{\eta \mathcal{P} T}{N} \left(\nu_1 \rho^2 + \nu_2 \rho + \nu_3 \right), \tag{6.29}$$

where

$$\nu_1 = -\frac{2}{N} \left(\frac{1}{d_{12}^{\lambda} d_t^{\lambda}} + \frac{1}{d_{22}^{\lambda} d_t^{\lambda}} \right),\ \nu_2 = \frac{2}{N} \left(\frac{1}{d_{12}^{\lambda} d_t^{\lambda}} - \frac{1}{d_{21}^{\lambda}} \right) + \frac{1}{d_{22}^{\lambda} d_t^{\lambda}} - \frac{1}{d_{11}^{\lambda}},\ \nu_3 = \frac{1}{d_{11}^{\lambda}} + \frac{1}{d_{21}^{\lambda}}. \tag{6.30}$$

Proof. See Appendix E.2. □

Thus, for the typical case that $d_{12} d_t >> d_{21}$ and $d_{22} d_t >> d_{11}$, one can show that $\mathcal{E}_{\text{tag}}$ increases inversely with ρ.

From Propositions 17 and 18, as the sequence length $N \to \infty$, the asymptotic expected PTR for the static channel and Rayleigh fading channel are given by

$$\begin{aligned} \mathcal{E}_{\text{tag}} &\approx \frac{\eta \mathcal{P} T}{N} \left((1-\rho)|f_{11}|^2 + \frac{1}{2} \left(|f_{21} + \sqrt{\rho} f_{22} g_{21}|^2 + |f_{21} - \sqrt{\rho} f_{22} g_{21}|^2 \right) \right), \\ \mathcal{E}_{\text{tag}} &\approx \frac{\eta \mathcal{P} T}{N} \left((1-\rho) \frac{1}{d_{11}^{\lambda}} + \frac{1}{d_{21}^{\lambda}} + \rho \frac{1}{d_{22}^{\lambda} d_t^{\lambda}} \right), \end{aligned} \tag{6.31}$$

respectively.

Therefore, for the FCP scheme, the expected PTR decreases with the sequence length N and approaches zero, while for the FCE scheme, the expected PTR converges to a constant with the increasing of sequence length.

6.4.2 Energy-Outage Probability

Based on the analysis in Section 6.3.2 and Section 6.4.1, the energy-outage probability at Tag 1 is

$$\begin{aligned}P_{\text{out}} = p_0 \Pr\left\{\frac{T}{N}\left(\mathcal{P}_0+\mathcal{P}_{\text{eh}}\right)<\mathcal{E}_0\right\}+\frac{p_1}{4}\left(\Pr\left\{\frac{T}{N}\mathcal{P}_1<\mathcal{E}_0\right\}\right.\\ \left.+\Pr\left\{\frac{T}{N}\left(\mathcal{P}_0+\mathcal{P}_2\right)<\mathcal{E}_0\right\}+\Pr\left\{\frac{T}{N}\left(\mathcal{P}_3+\mathcal{P}_{\text{eh}}\right)<\mathcal{E}_0\right\}+\Pr\left\{\frac{T}{N}\left(\mathcal{P}_0+\mathcal{P}_{\text{eh}}\right)<\mathcal{E}_0\right\}\right)\\ +\frac{p_2}{2}\left(\Pr\left\{\frac{T}{N}\mathcal{P}_1<\mathcal{E}_0\right\}+\Pr\left\{\frac{T}{N}\left(\mathcal{P}_3+\mathcal{P}_2\right)<\mathcal{E}_0\right\}\right).\end{aligned} \tag{6.32}$$

For the static channel, the energy-outage probability can be easily derived using (6.32) and is omitted here for brevity. The result for Rayleigh fading channel is presented in the following proposition.

Proposition 19. *For Rayleigh fading channel, the energy-outage probability is*

$$\begin{aligned}P_{out} = \frac{(N-2)^2}{N(N-1)}M\left((1-\rho)\frac{1}{d_{11}^{\lambda}},0,\frac{1}{d_{21}^{\lambda}},\rho\frac{1}{d_{22}^{\lambda}}\frac{1}{d_t^{\lambda}}\right)+\frac{N-2}{N(N-1)}\times\\ \left(M\left((1-\rho)\frac{1}{d_{11}^{\lambda}},0,(1-\rho)\frac{1}{d_{21}^{\lambda}},(1-\rho)\rho\frac{1}{d_{22}^{\lambda}}\frac{1}{d_t^{\lambda}}\right)+M\left((1-\rho)\frac{1}{d_{11}^{\lambda}},(1-\rho)\rho\frac{1}{d_{12}^{\lambda}}\frac{1}{d_t^{\lambda}},\frac{1}{d_{21}^{\lambda}},\rho\frac{1}{d_{22}^{\lambda}}\frac{1}{d_t^{\lambda}}\right)\right)\\ +\frac{1}{N(N-1)}M\left((1-\rho)\frac{1}{d_{11}^{\lambda}},(1-\rho)\rho\frac{1}{d_{12}^{\lambda}}\frac{1}{d_t^{\lambda}},(1-\rho)\frac{1}{d_{21}^{\lambda}},(1-\rho)\rho\frac{1}{d_{22}^{\lambda}}\frac{1}{d_t^{\lambda}}\right)\\ +\frac{1}{N}\tilde{M}\left((1-\rho)\left(\frac{1}{d_{11}^{\lambda}}+\frac{1}{d_{21}^{\lambda}}\right),(1-\rho)\rho\left(\frac{1}{d_{12}^{\lambda}}\frac{1}{d_t^{\lambda}}+\frac{1}{d_{22}^{\lambda}}\frac{1}{d_t^{\lambda}}\right)\right),\end{aligned} \tag{6.33}$$

where

$$M(a,b,c,d)\triangleq 1-\int_0^{\infty}\frac{(a+bx)\exp\left(-\frac{\Xi}{(a+bx)}-x\right)-(c+dx)\exp\left(-\frac{\Xi}{(c+dx)}-x\right)}{a-c+(b-d)x}\mathrm{d}x,\ \Xi=\frac{N\mathcal{E}_0}{\eta\mathcal{P}T} \tag{6.34}$$

and

$$\tilde{M}(a,b)\triangleq 1-\int_0^{\infty}\exp\left(-\frac{\Xi}{a+bx}-x\right)\mathrm{d}x. \tag{6.35}$$

Proof. See Appendix E.3. □

For the typical case that $d_{12}d_t >> d_{11}$ and $d_{22}d_t >> d_{21}$, i.e., each of the terms $M(\cdot)$ in (19) is approximated by $M\left((1-\rho)\frac{1}{d_{11}^{\lambda}},0,\frac{1}{d_{21}^{\lambda}},0\right)$ and the term $\tilde{M}(\cdot)$ is approximated by

$\tilde{M}\left((1-\rho)\left(\frac{1}{d_{11}^{\lambda}}+\frac{1}{d_{21}^{\lambda}}\right),0\right)$. Since both functions $M(\cdot,\cdot,\cdot,\cdot)$ and $\tilde{M}(\cdot,\cdot)$ decrease with each of the parameters, P_{out} increases with ρ.

Based on (6.32), as the sequence length $N \to \infty$, the asymptotic P_{out} is given by

$$P_{\text{out}} \approx p_0 \Pr\left\{\frac{T}{N}\left(\mathcal{P}_0+\mathcal{P}_{\text{eh}}\right)<\mathcal{E}_0\right\} \approx \Pr\left\{(1-\rho)|f_{11}|^2+|f_{21}+\sqrt{\rho}f_{22}g_{21}q_2|^2<\Xi\right\}. \tag{6.36}$$

For the FCP scheme, as the sequence length $N \to \infty$, $\Xi \to \infty$ makes $P_{\text{out}} \to 1$. While for the FCE scheme, the asymptotic energy-outage probability for Rayleigh fading channel is given by

$$P_{\text{out}} = M\left((1-\rho)\frac{1}{d_{11}^{\lambda}},0,\frac{1}{d_{21}^{\lambda}},\rho\frac{1}{d_{22}^{\lambda}}\frac{1}{d_{t}^{\lambda}}\right). \tag{6.37}$$

6.5 Performance of Time-Hopping Full-Duplex BackCom with Asynchronous Transmissions

Considering the fact that the chip-synchronism is difficult to achieve in practical situations, in this section, we study BackCom with chip asynchronous transmissions.[4] Without loss of generality, it assumes that τ is the delay shift between Links 1 and 2, which is positive and given by

$$\tau = \beta\frac{T}{N},\ \beta \in [0,1), \tag{6.38}$$

where β is named as the delay offset. Hence, the delay is assumed to be within a chip duration.

Due to the lack of perfect synchronization, the pattern-overlapping scenarios are more complex than that of the chip-synchronous case (Section 6.2.1). Considering that Link 1's TH-SS pattern $\mathcal{S}_1$ may consists of disjunct chips or consecutive chips illustrated in Figs. 6.5(a) and 6.5(b), respectively. Note that if the pattern $\mathcal{S}_1$ consist of the first chip and the last chip of a symbol, we say this pattern consists of consecutive chips. Using p^{d} and p^{c} to denote the probability that Link 1's chips is (d)isjunct or (c)onsecutive, respectively, we have

$$p^{\text{d}} = 1-\frac{2}{N-1} = \frac{N-3}{N-1},\ p^{\text{c}} = \frac{2}{N-1}. \tag{6.39}$$

Then all the pattern overlapping scenarios are illustrated in Fig. 6.5, and p_{n-i}^{a} denotes the probability of each sub-scenarios, where $a \in \{\text{d},\text{c}\}$, $n = 0,1,2$ denotes the number of Link 2's chips overlapped by Link 1's chips, and $i = 1,2,3,4$ denotes the pattern overlapping scenario index in Fig. 6.5. Note that the chip overlapping duration is $1-\beta$ of a chip in the single-chip

[4] Although rake receivers have been used to combat synchronization for coherent detection based receivers, they cannot be directly implemented to a non-coherent receiver, i.e., a tag. Thus, we consider the asynchronous issue for the BackCom system in this section.

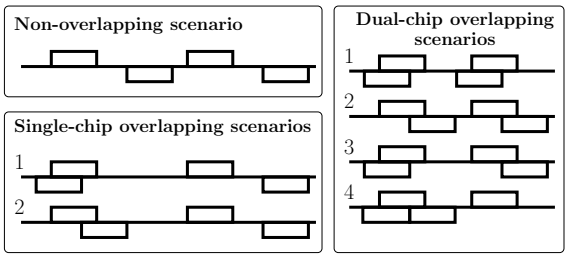

(a) Link 1 uses disjunct chips.

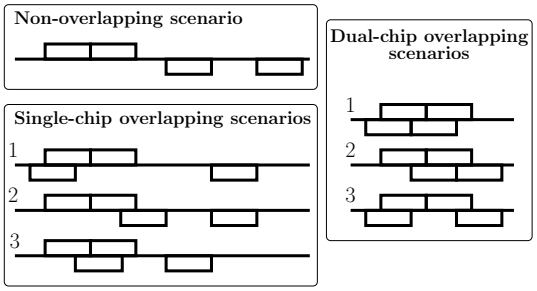

(b) Link 1 uses consecutive chips.

Figure 6.5: Different pattern-overlapping scenarios in the chip-asynchonous scenario. The pairs of on-chips of Links 1 and 2 are the rectangulars above and under the lines, respectively.

overlapping scenario 1 of Fig. 6.5(a), while it is β in the single-chip overlapping scenario 2. Thus, p^{d}_{n-i} and p^{c}_{n-i} can be obtained as

$$p^{\mathrm{d}}_0 = p^{\mathrm{d}}\frac{(N-4)(N-5)}{N(N-1)},\ p^{\mathrm{d}}_{1-1} = p^{\mathrm{d}}_{1-2} = p^{\mathrm{d}}\frac{4N-16}{N(N-1)}, p^{\mathrm{d}}_{2-1} = p^{\mathrm{d}}_{2-2} = p^{\mathrm{d}}\frac{2}{N(N-1)},$$
$$p^{\mathrm{d}}_{2-3} = p^{\mathrm{d}}_{2-4} = p^{\mathrm{d}}\frac{4}{N(N-1)},\ p^{\mathrm{c}}_0 = p^{\mathrm{c}}\frac{(N-3)(N-4)}{N(N-1)},\ p^{\mathrm{c}}_{1-1} = p^{\mathrm{c}}_{1-2} = p^{\mathrm{c}}_{1-3} = p^{\mathrm{c}}\frac{2N-6}{N(N-1)},$$
$$p^{\mathrm{c}}_{2-1} = p^{\mathrm{c}}_{2-2} = p^{\mathrm{c}}_{2-3} = p^{\mathrm{c}}\frac{2}{N(N-1)}. \tag{6.40}$$

6.5.1 BER at the Reader for Backward WIT

We assume that Reader 1 suffers interference when Link 1's transmitted on-chip C_1 is partially or entirely overlapped by either one or two of Link 2's on-chips s_{20} and s_{21}. Thus, the BER of coherent detection can be close to the maximum of 0.5 when the interference occurs (see Section 6.3.1). Calculating the probability that Reader 1 suffers interference and following the

similar steps for (6.2), the expected BER for the backward WIT is

$$\begin{aligned} P_{\text{reader}}^{\text{asyn}} &= P_{\text{BPSK}}\left(p_0^{\text{d}} + p_0^{\text{c}} + \frac{1}{2}\left(p_{1-1}^{\text{d}} + p_{1-2}^{\text{d}} + p_{2-4}^{\text{d}} + p_{1-1}^{\text{c}} + p_{1-2}^{\text{c}}\right)\right) \\ &+ 0.5 \times \left(\frac{1}{2}\left(p_{1-1}^{\text{d}} + p_{1-2}^{\text{d}} + p_{2-4}^{\text{d}} + p_{1-1}^{\text{c}} + p_{1-2}^{\text{c}}\right)\right. \\ &\left. + p_{2-1}^{\text{d}} + p_{2-2}^{\text{d}} + p_{2-3}^{\text{d}} + p_{1-3}^{\text{c}} + p_{2-1}^{\text{c}} + p_{2-2}^{\text{c}} + p_{2-3}^{\text{c}}\right). \end{aligned} \tag{6.41}$$

Substituting (6.40) into (6.41) gives the expected BER for the backward WIT as

$$P_{\text{reader}}^{\text{asyn}} = P_{\text{BPSK}}\frac{(N-3)(N-2)}{N(N-1)} + \frac{2N-3}{N(N-1)}. \tag{6.42}$$

Insights: We can make the following observations using (6.42): (i) For the high SNR regime, the BER reduces to $P_{\text{reader}}^{\text{asyn}} \approx \frac{2}{N}$. Comparing with the chip-synchronous case, we have $P_{\text{reader}}^{\text{asyn}}/P_{\text{reader}} \approx 2$, which is the *BER deterioration rate* due to the chip asynchronization. (ii) For the static channel, as the sequence length $N \to \infty$, the asymptotic BER for the FCP scheme is given by $P_{\text{reader}}^{\text{asyn}} \approx \frac{(N-2)(N-3)}{N(N-1)}P_{\text{BPSK}}$, thus, comparing with the chip-synchronous case, we have $P_{\text{reader}}^{\text{asyn}}/P_{\text{reader}} \approx 1$. While the asymptotic BER for the FCE scheme is given by $P_{\text{reader}} \approx \frac{2}{N}$, thus, $P_{\text{reader}}^{\text{asyn}}/P_{\text{reader}} \approx 2$. (iii) For Rayleigh fading channel, as the sequence length $N \to \infty$, the asymptotic BER for both the FCP and FCE schemes are given by $P_{\text{reader}}^{\text{asyn}} \approx \frac{(N-2)(N-3)}{N(N-1)}P_{\text{BPSK}}$, thus, comparing with the chip-synchronous case, $P_{\text{reader}}^{\text{asyn}}/P_{\text{reader}} \approx 1$. *From the above observations, we see that the BER deterioration rate for the backward WIT is either* 1 *(i.e., no deterioration) or* 2*, which is not too significant.* In the next subsection, we show that this is also comparable to the BER deterioration rate for the forward WIT.

6.5.2 BER at the Tag for Forward WIT

For tractability, we focus on the large sequence length scenario. Based on (6.40), as the sequence length $N \to \infty$, the dominant terms corresponding to the pattern overlapping scenarios are p_{1-1}^{d} and p_{1-2}^{d}, thus, the asymptotic BER for the forward WIT is

$$P_{\text{tag}}^{\text{asyn}} \approx p_{1-1}^{\text{d}}\mathbb{E}\left[P_{\text{tag}}^{(1-1)}\right] + p_{1-2}^{\text{d}}\mathbb{E}\left[P_{\text{tag}}^{(1-2)}\right] \approx \frac{4}{N}\mathbb{E}\left[P_{\text{tag}}^{(1-1)} + P_{\text{tag}}^{(1-2)}\right]. \tag{6.43}$$

Given disjunct pair of on-chips for Link 1, for the single-chip overlapping scenario 1 (see Fig. 6.5), we have the following transmission cases which occur with the same probability.

Case 1: The two readers are using the overlapping chip for transmission. The harvested

energy in the chips C_1, $\mathcal{S}_1 \backslash C_1$, the off-chips and the BER for the forward WIT are

$$\begin{aligned}
&\mathcal{E}_{\mathrm{rx}}^{(1-1)}(C_1 = C_2 = \mathcal{S}_1 \cap \mathcal{S}_2) = \frac{T}{N}\left((1-\beta)\mathcal{P}_1 + \beta\mathcal{P}_0\right),\ \breve{\mathcal{E}}_{\mathrm{rx}}^{(1-1)}(C_1 = C_2 = \mathcal{S}_1 \cap \mathcal{S}_2) = 0,\\
&\mathcal{E}_{\mathrm{eh}}^{(1-1)}(C_1 = C_2 = \mathcal{S}_1 \cap \mathcal{S}_2) = \frac{T}{N}\beta\mathcal{P}_{\mathrm{eh}},\ P_{\mathrm{tag}}^{(1-1)}(C_1 = C_2 = \mathcal{S}_1 \cap \mathcal{S}_2) = 0.
\end{aligned} \tag{6.44}$$

Case 2: Reader 1 is using the non-overlapping chip, while Reader 2 is using the overlapping chip for transmission.

$$\begin{aligned}
&\mathcal{E}_{\mathrm{rx}}^{(1-1)}(C_1 \neq C_2 = \mathcal{S}_1 \cap \mathcal{S}_2) = \frac{T}{N}\mathcal{P}_0,\ \breve{\mathcal{E}}_{\mathrm{rx}}^{(1-1)}(C_1 \neq C_2 = \mathcal{S}_1 \cap \mathcal{S}_2) = \frac{T}{N}(1-\beta)\mathcal{P}_2,\\
&\mathcal{E}_{\mathrm{eh}}^{(1-1)}(C_1 \neq C_2 = \mathcal{S}_1 \cap \mathcal{S}_2) = \frac{T}{N}\beta\mathcal{P}_{\mathrm{eh}},\ P_{\mathrm{tag}}^{(1-1)}(C_1 \neq C_2 = \mathcal{S}_1 \cap \mathcal{S}_2) = \Pr\left\{\mathcal{P}_0 < (1-\beta)\mathcal{P}_2\right\}.
\end{aligned} \tag{6.45}$$

Case 3: Reader 1 is using the overlapping chip, while Reader 2 is using the non-overlapping chip for transmission.

$$\begin{aligned}
&\mathcal{E}_{\mathrm{rx}}^{(1-1)}(C_2 \neq C_1 = \mathcal{S}_1 \cap \mathcal{S}_2) = \frac{T}{N}\left(\beta\mathcal{P}_0 + (1-\beta)\mathcal{P}_3\right),\ \breve{\mathcal{E}}_{\mathrm{rx}}^{(1-1)}(C_2 \neq C_1 = \mathcal{S}_1 \cap \mathcal{S}_2) = 0,\\
&\mathcal{E}_{\mathrm{eh}}^{(1-1)}(C_2 \neq C_1 = \mathcal{S}_1 \cap \mathcal{S}_2) = \frac{T}{N}\mathcal{P}_{\mathrm{eh}},\ P_{\mathrm{tag}}^{(1-1)}(C_2 \neq C_1 = \mathcal{S}_1 \cap \mathcal{S}_2) = 0.
\end{aligned} \tag{6.46}$$

Case 4: Reader 1 and Reader 2 are using non-overlapping chips for transmission.

$$\begin{aligned}
&\mathcal{E}_{\mathrm{rx}}^{(1-1)}(C_1 \neq \mathcal{S}_1 \cap \mathcal{S}_2, C_2 \neq \mathcal{S}_1 \cap \mathcal{S}_2) = \frac{T}{N}\mathcal{P}_0,\ \breve{\mathcal{E}}_{\mathrm{rx}}^{(1-1)}(C_1 \neq \mathcal{S}_1 \cap \mathcal{S}_2, C_2 \neq \mathcal{S}_1 \cap \mathcal{S}_2) = 0,\\
&\mathcal{E}_{\mathrm{eh}}^{(1-1)}(C_1 \neq \mathcal{S}_1 \cap \mathcal{S}_2, C_2 \neq \mathcal{S}_1 \cap \mathcal{S}_2) = \frac{T}{N}\mathcal{P}_{\mathrm{eh}},\ P_{\mathrm{tag}}^{(1-1)}(C_1 \neq \mathcal{S}_1 \cap \mathcal{S}_2, C_2 \neq \mathcal{S}_1 \cap \mathcal{S}_2) = 0.
\end{aligned} \tag{6.47}$$

Since the only difference between the single-chip overlapping scenarios 1 and 2 is the delay offset, which means by replacing β with $1-\beta$ in the above analysis, the relevant results for the single-chip overlapping scenario 2 can be obtained. Thus, based on (6.43), as the sequence length $N \to \infty$, the asymptotic BER for the forward WIT is

$$P_{\mathrm{tag}}^{\mathrm{asyn}} = \frac{1}{N}\left(\Pr\left\{\mathcal{P}_0 < (1-\beta)\mathcal{P}_2\right\} + \Pr\left\{\mathcal{P}_0 < \beta\mathcal{P}_2\right\}\right). \tag{6.48}$$

For the static channel, without loss of generality, assuming that $\beta \in (0, 1/2)$, if the random variable $\mathcal{P}_0/\mathcal{P}_2 \in [0, \beta)$ with probability 1, $P_{\mathrm{tag}}^{\mathrm{asyn}} = \frac{2}{N} > P_{\mathrm{tag}} = \frac{1}{N}$, whereas if the random variable $\mathcal{P}_0/\mathcal{P}_2 \in (1-\beta, 1)$ with probability 1, $P_{\mathrm{tag}}^{\mathrm{asyn}} = o(\frac{1}{N}) < P_{\mathrm{tag}} = \frac{1}{N}$. Thus, for some cases, the chip asynchronization deteriorates BER, but not for other cases.

For Rayleigh fading channel, based on (6.48), we further have

$$P_{\text{tag}}^{\text{asyn}} = \frac{1}{N}\left(2 - \int_0^{\infty}\left(\frac{e^{-x}}{1+\beta d_{11}^{\lambda}\left(\frac{1}{d_{21}^{\lambda}}+\frac{\rho x}{d_{21}^{\lambda}d_t^{\lambda}}\right)} + \frac{e^{-x}}{1+(1-\beta) d_{11}^{\lambda}\left(\frac{1}{d_{21}^{\lambda}}+\frac{\rho x}{d_{21}^{\lambda}d_t^{\lambda}}\right)}\right)\mathrm{d}x\right), \tag{6.49}$$

and $P_{\text{tag}}^{\text{asyn}}\big|_{\beta=0} = P_{\text{tag}}^{\text{asyn}}\big|_{\beta=1}$, $\frac{\mathrm{d}P_{\text{tag}}^{\text{asyn}}}{\mathrm{d}\beta}\Big|_{\beta=0} > 0$, $\frac{\mathrm{d}P_{\text{tag}}^{\text{asyn}}}{\mathrm{d}\beta}\Big|_{\beta=1} < 0$, $\frac{\mathrm{d}P_{\text{tag}}^{\text{asyn}}}{\mathrm{d}\beta}\Big|_{\beta=\frac{1}{2}} = 0$ and $\frac{\mathrm{d}^2 P_{\text{tag}}^{\text{asyn}}}{\mathrm{d}^2\beta} < 0$. Thus, $P_{\text{tag}}^{\text{asyn}}$ is a concave function of β, which increases first and then decreases. Therefore, any chip asynchronization deteriorates the BER, and the worst case of BER is obtained when $\beta = \frac{1}{2}$ as

$$P_{\text{tag}}^{\text{asyn}} = \frac{2}{N}\left(1 - \int_0^{\infty}\left(\frac{e^{-x}}{1+\frac{1}{2} d_{11}^{\lambda}\left(\frac{1}{d_{21}^{\lambda}}+\frac{\rho x}{d_{21}^{\lambda}d_t^{\lambda}}\right)}\right)\mathrm{d}x\right), \tag{6.50}$$

which can be proved to be greater than $1/N$ but less than $2/N$.

Insight: Therefore, the BER deterioration rate for the forward WIT due to the chip asynchronization, $P_{\text{tag}}^{\text{asyn}}/P_{\text{tag}} \in [1,2]$, when the TH-SS sequence length is sufficiently large.

6.5.3 Performance of Forward WPT

6.5.3.1 Expected PTR

Based on the analysis above for the single chip overlapping scenario 1 given Link 1's disjunct pair of on-chips, we see that the expected PTR in this scenario is

$$\mathbb{E}\left[\mathcal{E}_{\text{rx}}^{(1-1)} + \breve{\mathcal{E}}_{\text{rx}}^{(1-1)} + \mathcal{E}_{\text{eh}}^{(1-1)}\right] = \frac{T}{4N}\left((2+2\beta)\left(\mathcal{P}_0+\mathcal{P}_{\text{eh}}\right) + (1-\beta)\left(\mathcal{P}_1+\mathcal{P}_2+\mathcal{P}_3\right)\right). \tag{6.51}$$

Similarly, for the single chip overlapping scenario 2, we have

$$\mathbb{E}\left[\mathcal{E}_{\text{rx}}^{(1-2)} + \breve{\mathcal{E}}_{\text{rx}}^{(1-2)} + \mathcal{E}_{\text{eh}}^{(1-2)}\right] = \frac{T}{4N}\left((2+2(1-\beta))\left(\mathcal{P}_0+\mathcal{P}_{\text{eh}}\right) + \beta\left(\mathcal{P}_1+\mathcal{P}_2+\mathcal{P}_3\right)\right), \tag{6.52}$$

and thus, the expected PTR in the single-chip overlapping scenario given given Link 1's disjunct pair of on-chips, is the expectation of (6.51) and (6.52), i.e., $\frac{T}{4N}\left(3\left(\mathcal{P}_0+\mathcal{P}_{\text{eh}}\right) + \frac{1}{2}\left(\mathcal{P}_1+\mathcal{P}_2+\mathcal{P}_3\right)\right)$, which is independent of the delay offset β. Similarly, for the other pattern overlapping scenarios, the expected PTR also do not rely on β, thus, we have

$$\mathcal{E}_{\text{tag}}^{\text{asyn}} = \mathcal{E}_{\text{tag}} = \frac{T}{N}\mathbb{E}\left[\left(\frac{(N-2)}{N}\mathcal{P}_0 + \frac{1}{N}\left(\mathcal{P}_1+\mathcal{P}_2+\mathcal{P}_3\right) + \frac{(N-2)}{N}\mathcal{P}_{\text{eh}}\right)\right]. \tag{6.53}$$

Intuitively, the TH-SS scheme has averaged out the delay offset effect on the expected PTR. Thus, the chip asynchronization has zero effect on expected PTR.

6.5.3.2 Energy-Outage Probability

As the sequence length $N \to \infty$, for the FCP scheme, it is straightforward that the asymptotic energy-outage probability $P_{\text{out}}^{\text{asyn}} \to 1$. While for the FCE scheme, focusing on the dominant term, the asymptotic energy-outage probability is

$$P_{\text{out}}^{\text{asyn}} \approx p_0^{\text{d}} \Pr\left\{\frac{T}{N}\left(\mathcal{P}_0 + \mathcal{P}_{\text{eh}}\right) < \mathcal{E}_0\right\} \approx \Pr\left\{\frac{T}{N}\left(\mathcal{P}_0 + \mathcal{P}_{\text{eh}}\right) < \mathcal{E}_0\right\}. \tag{6.54}$$

Thus, $P_{\text{out}}^{\text{asyn}} / P_{\text{out}} \approx 1$. In other words, when the sequence length is sufficiently large, the chip asynchronization effect on the energy-outage probability is negligible.

Insight: Therefore, as the sequence length $N \to \infty$, the chip asynchronization has negligible effect on the performance of the forward WPT.

6.6 Performance of Time-Hopping Full-Duplex BackCom: K-Link Case

We study the K-link chip-synchronous transmissions in this section. Assuming that ϱ_n, $n = 0, 1, 2$, is the probability that Link 1 has n chips overlapped by the other links, i.e., $n = |\mathcal{S}_1 \cap (\mathcal{S}_2 \cup \mathcal{S}_3 \cup \cdots \cup \mathcal{S}_K)|$, we can obtain

$$\begin{aligned}
\varrho_0 &= p_0^{K-1} = \left(\frac{(N-2)(N-3)}{N(N-1)}\right)^{K-1} = \mathcal{O}(1), \\
\varrho_1 &= 2\left(\left(p_0 + \frac{1}{2}p_1\right)^{K-1} - p_0^{K-1}\right) = 2\left(\left(\frac{N-2}{N}\right)^{K-1} - \left(\frac{(N-2)(N-3)}{N(N-1)}\right)^{K-1}\right) = \mathcal{O}(\frac{1}{N}), \\
\varrho_2 &= 1 - \varrho_0 - \varrho_1 = 1 + \left(\frac{(N-2)(N-3)}{N(N-1)}\right)^{K-1} - 2\left(\frac{N-2}{N}\right)^{K-1} = o(\frac{1}{N}),
\end{aligned} \tag{6.55}$$

where $\mathcal{O}(\cdot)$ and $o(\cdot)$ are the big O and little o notations, respectively.

6.6.1 BER at the Reader for Backward WIT

Since Reader 1 suffers interference only if Link 1's transmitted on-chip $C_1 \in \mathcal{S}_2 \cup \mathcal{S}_3, \cdots \cup \mathcal{S}_K$, following the similar steps for (6.2), i.e., replacing p_n with ϱ_n in (6.2), the expected BER for the backward WIT is

$$P_{\text{reader}} = P_{\text{BPSK}}\left(\frac{N-2}{N}\right)^{K-1} + \frac{1}{2}\left(1 - \left(\frac{N-2}{N}\right)^{K-1}\right). \tag{6.56}$$

Insight: For the high SNR regime, the BER reduces to $P_{\text{reader}} \approx \frac{K-1}{N}$, and thus, P_{reader}

increases linearly with the number of BackCom Links, K.

For the static channel, as the sequence length $N \to \infty$, the asymptotic BER for the FCP scheme is given by $P_{\text{reader}} \approx \left(\frac{N-2}{N}\right)^{K-1} P_{\text{BPSK}}$. While the asymptotic BER for the FCE scheme is given by $P_{\text{reader}} \approx \frac{K-1}{N}$, which *increases linearly with the number of BackCom Links, K.* For Rayleigh fading channel, as the sequence length $N \to \infty$, the asymptotic BER for both the FCP and FCE schemes are given by $P_{\text{reader}} \approx \left(\frac{N-2}{N}\right)^{K-1} P_{\text{BPSK}}$, i.e., *increasing the number of the BackCom links has negligible effect on the BER for the backward WIT.*

6.6.2 BER at the Tag for Forward WIT

Based on Section 6.3.2, Tag 1 suffers interference only in the single-chip or dual-chip pattern-overlapping scenarios. Assuming ϱ is the probability that only one chip of the pattern $\mathcal{S}_1$ is overlapped and the overlapping is caused by just one link, we have

$$\varrho = 2\left((K-1)\frac{p_1}{2}(p_0)^{K-2}\right) = (K-1)\frac{4(N-2)}{N(N-1)}\left(\frac{(N-2)(N-3)}{N(N-1)}\right)^{K-2} = \mathcal{O}(\frac{1}{N}), \tag{6.57}$$

and it is easy to see that the sum probability of all the other single-chip overlapping and dual-chip overlapping scenarios is $\varrho_1 + \varrho_2 - \varrho$, which approaches zero with a higher order of $\frac{1}{N}$. Therefore, in the large sequence length regime, when analyzing the BER for the forward WIT, we only consider the pre-mentioned dominant case.

Thus, following the similar steps for (6.21), Tag 1's expected BER is

$$\begin{aligned} P_{\text{tag}} &\approx \varrho \frac{1}{K-1}\sum_{k=2}^{K}\frac{1}{4}\Pr\left\{\mathcal{P}_{\text{rx}}^{(1)}(C_1 \neq C_k = \mathcal{S}_1 \cap \mathcal{S}_k) > \mathcal{P}_0\right\} \\ &= \frac{N-2}{N(N-1)}\left(\frac{(N-2)(N-3)}{N(N-1)}\right)^{K-2}\sum_{k=2}^{K}\Pr\left\{\mathcal{P}_{\text{rx}}^{(1)}(C_1 \neq C_k = \mathcal{S}_1 \cap \mathcal{S}_k) > \mathcal{P}_0\right\}, \end{aligned} \tag{6.58}$$

where $\mathcal{P}_{\text{rx}}^{(1)}(C_1 \neq C_k = \mathcal{S}_1 \cap \mathcal{S}_k) \triangleq \eta(1-\rho)\mathcal{P}|f_{k1}u + f_{kk}\sqrt{\rho}g_{k1}q_k|^2$ which is the combined received signal power of the signals Rk-T1 and Rk-Tk-T1 during the chip $\mathcal{S}_1 \backslash C_1$.

As the sequence length $N \to \infty$, the asymptotic BER is

$$P_{\text{tag}} \approx \frac{1}{N}\sum_{k=2}^{K}\Pr\left\{\mathcal{P}_{\text{rx}}^{(1)}(C_1 \neq C_k = \mathcal{S}_1 \cap \mathcal{S}_k) > \mathcal{P}_0\right\}. \tag{6.59}$$

Insight: Therefore, the BER for the forward WIT increases with the number of BackCom links K.

6.6.3 Performance of Forward WPT

For simplicity, we focus on the large sequence length regime, and it is easy to see the probability that there is no overlapping between any of the K-link patterns, is

$$\Pr\left\{|\cup_{k=1}^{K}\mathcal{S}_k| = 2K\right\} = \frac{\frac{N(N-1)}{2}\frac{(N-2)(N-3)}{2}\cdots\frac{(N-2(K-1))(N-2(K-1)-1)}{2}}{\left(\frac{N(N-1)}{2}\right)^K} = \mathcal{O}(1). \quad (6.60)$$

Thus, as the sequence length $N \to \infty$, the asymptotic expected PTR and energy-outage probability are give by

$$\mathcal{E}_{\text{tag}} \approx \frac{T}{N}\mathbb{E}\left[\mathcal{P}_0 + \sum_{k=2}^{K}\mathcal{P}_{\text{eh},k}\right], \quad (6.61)$$

$$P_{\text{out}} \approx \Pr\left\{|\cup_{k=1}^{K}\mathcal{S}_k| = 2K\right\}\Pr\left\{\frac{T}{N}\left(\mathcal{P}_0+\sum_{k=2}^{K}\mathcal{P}_{\text{eh},k}\right) < \mathcal{E}_0\right\} \quad (6.62)$$

$$\approx \Pr\left\{\frac{T}{N}\left(\mathcal{P}_0+\sum_{k=2}^{K}\mathcal{P}_{\text{eh},k}\right) < \mathcal{E}_0\right\}, \quad (6.63)$$

respectively, where $\mathcal{P}_{\text{eh},k} \triangleq \eta\mathcal{P}|f_{k1} + f_{kk}g_{k1}|^2$ is the received signal power of the signal Rk-T1 in Tag 1's off-chips. The expected PTR and the energy-outage probability monotonically increases and decreases with K, respectively.

Insight: Therefore, when the sequence length is sufficiently large, increasing the number of BackCom Links improves the performance of the forward WPT.

6.7 Numerical Results

In this section, we only investigate the Rayleigh fading channel scenario (applicable to future IoT) and the FCP scheme for brevity. In general, we focus on the 2-link case, i.e., $K = 2$. We set the path loss exponent as $\lambda = 2.5$, and the distance (in meters) between the devices as $d_{11} = 10$, $d_{22} = 10$, $d_t = 20$, $d_{12} = 22$, $d_{21} = 22$. For the K-link case, i.e., $K > 2$, we assume that $d_{ii} = d_{11}$, and $d_{i1} = d_{21}$, $i = 3, 4, ..., K$. Also we set the noise variance at the reader and the tag as $\sigma^2_{\text{reader}} = \sigma^2_{\text{tag}} = -100$ dBm, and the RF energy harvesting efficiency as $\eta = 0.5$ [56] and [91]. Unless otherwise stated, we set the reader transmit power as $\mathcal{P} = 50$ mW, the sequence length as $N = 1000$, and the tag power consumption as $\frac{\mathcal{E}_0}{T} = 0.01$ μW.

In the following, we plot the BERs for the forward and backward WIT (i.e., P_{reader} and P_{tag}), and the energy-outage probability (i.e., P_{out}) for the forward WPT based on the analytical results derived in Sections 6.3, 6.4, 6.5 and 6.6. The Monte Carlo simulation results, averaged over 10^9 random channel realizations, are also presented. Specifically, the analytical results of

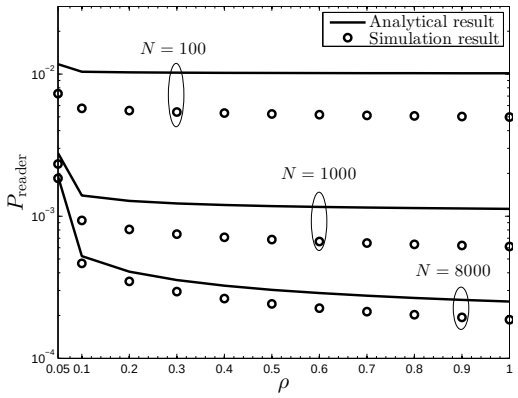

Figure 6.6: The BER of the reader, P_{reader}, versus the reflection coefficient, ρ.

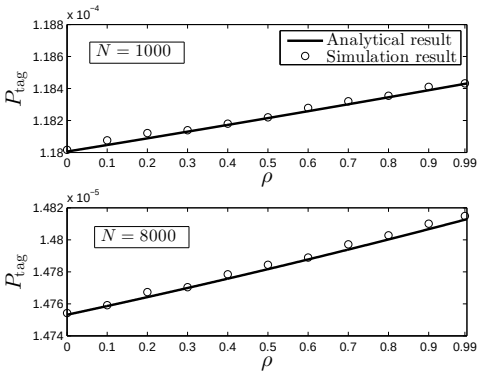

Figure 6.7: The BER of the tag, P_{tag}, versus the reflection coefficient, ρ.

BER for the forward and backward WIT in Section 6.3 are based on two modeling assumptions, respectively, i.e., the BER at the reader is 0.5 as long as the reader suffers from interference, and the BER at the tag does not take into account the noise effect. These modeling assumptions are verified by the simulation results.

6.7.1 Two-Link BackCom

In Fig. 6.6, curves of the BER for the backward WIT, P_{reader}, are plotted for different reflection coefficient, ρ, and TH-SS sequence length, N. The analytical result is plotted using Proposition 14. We see that the analytical result is an upper bound of the simulation result, and the gap diminishes as N increases, e.g., the gap is less than 10^{-4} when $N = 8000$. Thus, although the inter-link interference may not be fatal, i.e., inducing a BER of 0.5 at the reader, the analytical result is a tight upper bound especially when N is large.

In Fig. 6.7, curves of the BER for the forward WIT, P_{tag}, are plotted for different ρ and N. The analytical result is plotted using Proposition 16. We see that the analytical results perfectly match the simulation results, which verifies that the noise effect of the forward BER is negligible under the practical settings.

In Fig. 6.8, curves of the energy-outage probability for the forward WPT, P_{out}, are plotted for different ρ and N. The analytical result is plotted using Proposition 19, which perfectly matches the simulation result. Hence, the accuracy of the analytical result is verified.

From Figs. 6.6-6.8, we see that P_{reader} decreases while both P_{tag} and P_{out} increase with increasing ρ. This is because a larger ρ induces a stronger backscattered signal and a weaker received signal at the tag, which enhances the backward SNR but reduces the performance of the forward WIT and WPT. Also we see that both P_{reader} and P_{tag} decrease while P_{out} increases with increasing N. This is because a larger sequence length N suppresses the interference for both the forward and backward WIT by reducing the pattern-overlapping probability. However,

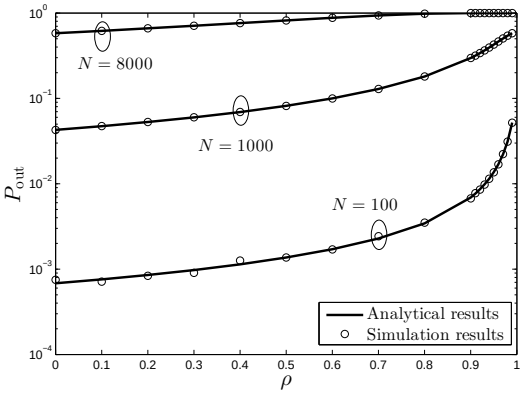

Figure 6.8: The energy outage probability, P_{out}, versus the reflection coefficient, ρ.

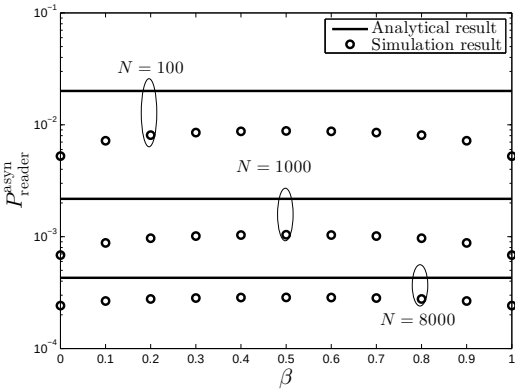

Figure 6.9: The BER of the reader, $P_{\text{reader}}^{\text{asyn}}$, versus the delay offset, β.

it makes the readers have a shorter time (i.e., each chip has a shorter time when N is larger) for active transmissions, which reduces the performance of the forward WPT.

Therefore, for practical BackCom system design, the tradeoff between the backward WIT and the forward WIT/WPT with reflection coefficient, and the tradeoff between the WIT and the WPT with TH-SS sequence length should be carefully considered. Moreover, the reflection coefficient and the sequence length should be optimized to satisfy the performance requirement of a certain BackCom system.

6.7.2 Asynchronous BackCom

In Fig. 6.9, curves of the BER for the backward WIT, $P_{\text{reader}}^{\text{asyn}}$, are plotted for different delay offset, β, and sequence length, N. The analytical result is plotted using (6.42). We see that the analytical result is an upper bound of the simulation result, and the gap diminishes quickly as N increases, e.g., the gap is about 10^{-3} when $N = 1000$, and is about 10^{-4} when $N = 8000$. From the simulation result, we see that the BER for the backward WIT is mostly affected when the delay offset caused by chip asynchronization is equal to a half chip duration. The influence on the BER caused by asynchronous transmissions is negligible when N is sufficiently large, i.e., the BER is almost the same with $\beta = 0$ and 0.5, when $N = 8000$. Therefore, although the analytical result is based on the assumption that the BER is the same no matter what the delay offset is, the result is a tight upper bound especially when N is large.

In Fig. 6.10, curves of the BER for the forward WIT, $P_{\text{tag}}^{\text{asyn}}$, are plotted for different β and N. The analytical result is plotted using (6.50), which matches the simulation result. Hence, the approximation in (6.50) is tight. It is observed that the chip asynchronization always increases the BER, i.e., the BER is larger for any $\beta \in (0,1)$ compared with $\beta = 0$ or 1. Furthermore, similar with the backward transmission, when the delay offset between the two links is equal to a half chip duration, i.e., $\beta = 0.5$, the BER is the worst. Also it is clear that

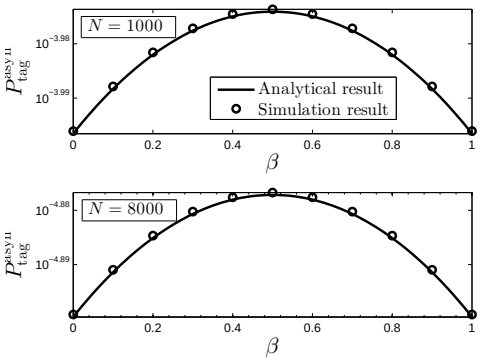

Figure 6.10: The BER of the tag, $P_{\text{tag}}^{\text{asyn}}$, versus the delay offset, β.

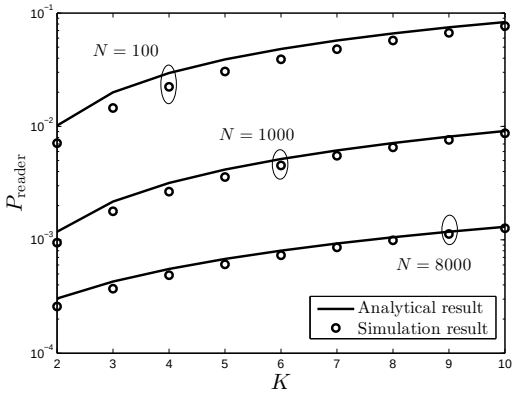

Figure 6.11: The BER of the reader P_{reader}, versus the number of the BackCom links, K.

the chip asynchronization effect on BER can be eliminated by increasing sequence length, for example, the worst chip-asynchronous BER with $N = 8000$ is much smaller than the BER of the chip-synchronous case with $N = 1000$.

Therefore, Figs. 6.9 and 6.10 jointly show that the chip-asynchronous effect on the forward and backward WIT is negligible as long as the sequence length is sufficiently large.

6.7.3 K-Link BackCom

In Fig. 6.11, curves of P_{reader} are plotted for different number of BackCom links, K, and different sequence length, N. The analytical result is plotted using (6.56), which is an upper bound of the accurate result since it assumes a BER of 0.5 when the interference occurs at the reader. We see that the analytical result is a tight upper bound of the simulation result, and the gap diminishes with the increasing sequence length and number of BackCom links. Also we see that P_{reader} increases with K, which is mainly because more BackCom links make the backward WIT more likely to suffer from interference. For a fixed N, the BER deteriorates as the number of BackCom links becomes large, and can even become close to 0.5, when the interference occurs.

In Fig. 6.12, curves of P_{tag} are plotted for different K and N. The analytical result is plotted using (6.58), which is a lower bound since it only takes into account the dominant term for a large N. We see that the analytical result is a tight lower bound of the simulation result. Also we see that P_{tag} increases with K, since more BackCom links make the backward WIT more likely to suffer from interference, and the interference is stronger when it occurs.

In Fig. 6.13, curves of the energy-outage probability, P_{out}, are plotted for different K and N. The analytical result is plotted using (6.62), which is a lower bound since it only takes into account the dominant term for a large N. We see that the analytical result is a tight lower bound of the simulation result. Also we see that P_{out} decreases with K, since a large number of

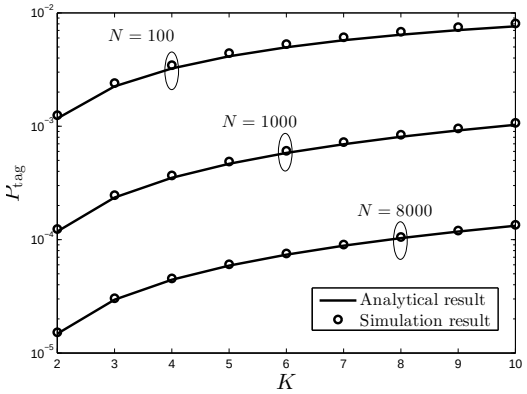

Figure 6.12: The BER of the tag, P_{tag}, versus the number of the BackCom links, K.

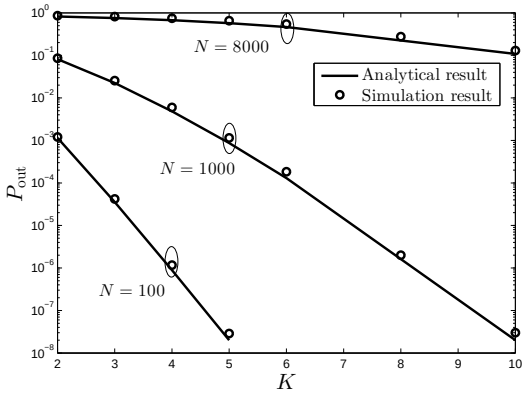

Figure 6.13: The energy outage probability, P_{out}, versus the number of the BackCom links, K.

BackCom links increases the harvested energy at the tag due to the multi-reader transmissions.

Figs. 6.11-6.13 jointly show the performance tradeoff between the WIT and the WPT with the number of BackCom links. Thus, for practical BackCom network design, this tradeoff should be carefully considered, and the number of BackCom links should be optimized to satisfy both the performance requirement of WIT and WPT.

6.8 Summary

In this chapter, we have proposed a full-duplex BackCom network, where a novel TH-SS based multiple-access scheme is designed. The scheme enables simultaneous forward/backward WIT and can also suppress interference from coexisting links. Moreover, the scheme not only supports dedicated WPT for every symbol but also allows wireless energy harvesting from interference. Several interesting design insights are obtained, such as: the performance tradeoff between the backward WIT and the forward WIT/WPT w.r.t. the reflection coefficients, the performance tradeoff between the forward WIT and WPT w.r.t. the TH-SS sequence length for power constrained reader, and also the performance tradeoff between the forward/backward WIT and the forward WPT w.r.t. the number of BackCom links.

Chapter 7

Conclusion

In this chapter, we summarize the general conclusions drawn from this thesis. We also outline some future research directions arising from this work.

In Chapter 2, we investigated the delay issue in EH WSN for status monitoring application scenario. Unlike most existing studies, we considered the energy costs of both sensing and transmission. We adopted two complementary metrics, i.e., update age and update cycle, to comprehensively study the delay performance. We showed that the consideration of sensing energy cost leads to an important tradeoff between the two metrics: more frequent updates result in less timely information available at the sink. Therefore, the chapter provides us a new perspective for delay measurement, which also serves the purpose of better quantification and better design of status monitoring network. Moreover, the complementary delay metrics can also be applied to the ultra-low-latency applications in the future.

In Chapter 3, we proposed to use a wireless-powered friendly jammer to enable low-complexity secure communication. We propose a WPT-then-WIT based secure communication protocol for the system. We also analytically characterized and maximized the long-term secure-communication behavior of the proposed protocol and derived a closed-form expression for the throughput. We showed that the throughput performance differs between the single-antenna jammer case and the multi-antenna jammer case. For example, as the source transmit power increases, the throughput quickly reaches an upper bound with single-antenna jammer, while the throughput grows unbounded with multi-antenna jammer. Moreover, this chapter also brings the new idea of 'energy trading' in energy-constrained IoT networks. In other words, the devices that are connected to the power grid or have high energy levels, can use their energy to buy service from the other devices that have low energy levels, such as cooperative jamming for secure services, or distributed computing for mobile-edge-computing services.

In Chapter 4, we studied a point-to-point SWIPT system adopting practical M-ary modulation for both the PS and the TS schemes. Unlike most existing studies, we consider a practical non-linear RF-EH converter. We also analyzed the performance tradeoff between energy har-

vesting and information decoding. We obtained several interesting results, such as channel fading is beneficial for energy harvesting in both PS- and TS-based SWIPT receivers. Therefore, this chapter opens a new research direction of the design and optimization of practical SWIPT systems, which also requires new methodologies. For instance, the optimal constellation design for SWIPT systems is very attractive but is also a difficult open problem.

In Chapter 5, we proposed a novel information receiver (i.e., the splitting receiver) inspired by the conventional PS-based SWIPT receiver, which involves joint coherent and non-coherent processing. We showed that the splitting receiver provides an achievable rate gain of 50% compared to either the conventional receivers in the high SNR regime. For practical communication systems, we also showed that the splitting receiver achieves asymptotic SER reduction by a factor of at least $M-1$ and $\sqrt{M}-1$ for M-PAM and M-QAM, respectively. Therefore, we have unlocked the great potential of joint coherent and non-coherent processing. Moreover, the proposed splitting receiver has a strong potential for future generation communication systems, including both the wireless and cable communications.

Finally, in Chapter 6, we proposed the design of full-duplex BackCom networks, where a novel multiple-access scheme based on TH-SS is designed to enable both one-way WPT and two-way WIT in coexisting backscatter reader-tag links. We comprehensively analyzed the performance of BackCom interference network, Also we showed some interesting design insights, such as: the performance tradeoff between the forward WIT and WPT w.r.t. the TH-SS sequence length, and also the performance tradeoff between the forward/backward WIT and the forward WPT w.r.t. the number of BackCom links. Moreover, the elaborate system design in this chapter has shed some light on multiple attractive research areas of BackCom networks, such as low-complexity interference suppression, full-duplex reader-tag communications, joint WPT and (opportunistic) RF energy harvesting of the passive tags.

7.1 Future Work

The field of EH or WPT-powered energy constrained IoT network is a vastly rich research area with tremendous potential. The following major research directions may be the focus of future work:

Massive MIMO and mmWave based WPT: The WPT efficiency, i.e., the ratio of harvested energy of the receiver to the transmitted power of the transmitter, in conventional WPT system is not good enough, and one of the main reasons is the significant propagation losses of radio wave due to its broadcast nature. Using massive multiple-input and multiple-output (MIMO) and millimeter wave (mmWave) technologies [133, 134, 135, 136, 137], a base station or an access point is able to transfer power to the nearby energy-constrained IoT devices using ultra-sharp energy beams [138, 139]. In this way, the WPT efficiency can be improved. As the the beam width of the massive MIMO and mmWave based WPT system is very small, effective initial beam association and beam alignment algorithms are thus desirable.

UAV-based WPT: Unmanned aerial vehicles (UAVs) have many potential applications in wireless communication systems in the near future, due to their maneuverability and increasing affordability [140, 141]. In particular, UAVs can be adopted for WPT since they can be easily deployed to provide WPT service in areas without infrastructure (e.g., power beacons) coverage in remote or hazardous environments. More importantly, due to the high maneuverability and flexible deployment of the UAVs, the wireless channel between an UAV and a energy-constrained IoT device are dominated by line-of-sight (LoS) links, and hence, the WPT efficiency can be improved. Since the UAVs are power-hungry devices, the optimal problems for UAV deployment and trajectory design should be considered such that the pure energy efficiency for WPT is within a reasonable range.

Near-field WPT: Near-field WPT has drawn significant interests recently due to its high efficiency for delivering power to electric loads wirelessly, compared with the far-field WPT techniques. There are two techniques to realize near-field WPT: inductive coupling (IC) for short-range applications within centimeters, and magnetic resonant coupling (MRC) for mid-range applications up to a couple of meters [142, 143]. Specifically, short-range WPT has been well-studied and is in widely commercial use, such as electric toothbrushes, however, midrange WPT is still largely under research and prototyping. For instance, optimal node placement and beamforming design for a midrange WPT system consisting of a single PB and multiple energy receivers, are very interesting.

BackCom MIMO: A key characteristic of BackCom is the double path-loss due to the fact that the backscatter signal received at a Reader propagates through the close-loop channel cascading the downlink and uplink channels. The resultant path loss is especially severe as the propagation distances in IoT are much longer than those for RFID applications. To enhance

link reliability, one solution is to deploy antenna arrays at Readers and Tags and apply spatial-diversity techniques. Furthermore, multi-antennas can enhance the efficiency of wireless power transfer by enabling transmit energy beamforming and increasing receive antenna apertures.

Backscattering introduces a special channel structure for the backward IT in a MIMO BackCom system, called a dyadic MIMO channel, which captures the composite fading in the forward and backward channels [144, 145]. To be specific, the CW signals sent by the transmit antennas of the Reader propagate through the forward MIMO channel, and are first combined at each antenna of the Tag and then backscattered, and lastly propagate through the backward MIMO channel to arrive at the receive antennas of the Reader. The resultant dyadic MIMO channel has a similar structure as the classic keyhole MIMO channel. The space-time coding is a simple but suitable technique for achieving the diversity gain of such a channel. Moreover, it is also attractive to study multi-user MIMO BackCom system.

Splitting receiver: The proposed splitting receiver in this thesis does not add much complexity and cost compared with the conventional receivers, but is able to provide a 1.5 times rate gain. Therefore, the single-antenna splitting receiver is very suitable for the energy-constraint IoT devices to enable either a more reliable, or lower-latency communication as each device's data reception can be finished with a much shorter time duration. Also the multi-antenna splitting receiver is suitable for 5G wireless communications, such that the user data rate can be significantly improved. Therefore, it is desirable to study the multiple splitting-receiver-based user scheduling and resource allocation problems.

Appendix A

This appendix contains the proofs needed in Chapter 2.

A.1 Proof of Lemma A1

We first define the block-wise harvest-then-use process, and then propose and prove Lemma A1.

Definition A1 (Block-wise harvest-then-use process)**.** A harvest-then-use process consists of energy harvesting blocks (EHBs) and energy consumption blocks (ECBs). It starts and keeps on harvesting energy with EHBs. Once the available, i.e., accumulated, energy is no less than a threshold of Q Joules, an ECB occurs, and consumes Q Joules of energy. If this condition for ECB is not satisfied, the process goes back to harvest energy with EHBs.

During the harvest-then-use process, the harvested energy in the ith EHB is represented by ξ_i, $i = 1, 2, 3, ...$, and the available energy after the jth ECB is represented by $\tilde{\Xi}_j$, $j = 1, 2, 3, ...$ Due to the randomness of the energy arrival process, i.e., ξ_i is a random variable, the available energy after each ECB, $\tilde{\Xi}_j$, is also a random variable which only depends on ξ_i. Furthermore, using the statistics of ξ_i, and modeling $\tilde{\Xi}_j$, $j = 1, 2, 3, ...$, as a random process, an important feature of the random process is revealed in Lemma A1.

Lemma A1. For block-wise harvest-then-use process with energy threshold Q, where the harvested energy in each EHB, ξ_i, $i = 1, 2, 3, ...$, is independent and identically distributed, each with pdf containing at least one positive right-continuous point, $f(x)$, the available energy after each ECB, $\tilde{\Xi}_j$, $j = 1, 2, 3, ...,$, consists of a positive recurrent Harris chain, with unique steady-state distribution which is given by

$$g(x) = \frac{1}{\rho}\left(1 - F(x)\right), \tag{A.1}$$

where $F(x)$ and ρ are respectively, the cdf and the mean of ξ_i.

Proof. The proof consists of two steps. In the first step, we prove that the energy state after the jth ECB, $\tilde{\Xi}_j$, constitutes a positive recurrent Harris chain (a collection of Markov chains

with uncountable state space). Thus, a unique steady-state distribution of $\tilde{\Xi}_j$ exists [146]. In the second step, we prove that (A.1) is the unique steady-state distribution.

Step 1: It is easy to see that the current state, $\tilde{\Xi}_j$ takes its value from a continuous state space and only relies on the previous energy state $\tilde{\Xi}_{j-1}$, thus $\tilde{\Xi}_j$, $j = 1,2,3,...$, forms a continuous-state Markov chain. Without loss of generality, we assume that $\sup\{\xi_i\} = B$, thus $\sup\{\tilde{\Xi}_j\} \leq B$ holds in this harvest-then-use process.[1] It is easy to see that the state space of Markov chain $\tilde{\Xi}_j$, $\mathcal{S}$, is a subset of $[0,B)$, and because of the harvest-then-use protocol, any current state which is higher than Q, will access the interval $[0,Q)$ in the following steps. Thus, we only need to prove that any state $s \in [0,\min\{B,Q\})$ can hit any arbitrary small interval $\boldsymbol{\tau} = (\tau^-,\tau^+)$ in $\mathcal{S}$ with non-zero probability within finite steps. Actually, in the following, we complete the proof with the assumption that $\mathcal{S} = [0,B)$, which also proves that the state space of Markov chain $\tilde{\Xi}_i$ is exactly $[0,B)$.

In the following, using a constructive method, we show that for Markov chain $\tilde{\Xi}_j$, given any current state $s \in [0,\min\{B,Q\})$, there is at least a probability, $q \times p$, that any arbitrary small interval $\boldsymbol{\tau}$ will be accessed with $\tilde{j}$ steps, where p, q, $\tilde{j}$ are defined below which only depend on the state s, the interval length τ and the pdf of the harvested energy in each EHB.

Since pdf function $f(x)$ has positive right-continuous points on $[0,B)$, there exists at least one interval $[D^-,D)$ that satisfies $[D^-,D) \subset [0,B)$, $D - D^- = \tau/2$, and $f(x)$ is positive right-continuous on $[D^-,D)$. We assume that $D^- \geq \tau^+$, and the $D^- < \tau^+$ case can be easily generated from the the following discussions, thus is omitted due to space limitation. Now we define $p \triangleq \int_{D^-}^{D} f(x)\mathrm{d}x$ as the probability that harvested energy in one EHB lies in the interval $[D^-,D)$. Also we define $\tilde{f}(x) = f(x)$ when $x \in [D^-,D)$, otherwise $\tilde{f}(x) = 0$, and $\tilde{f}_i(x)$ is the i-fold convolution of function $\tilde{f}(x)$.

Thus, it is easy to see that $\tilde{f}_i(x)$ is positive and continuous in the interval (iD^-,iD), and $\int_a^b \tilde{f}_i(x)\mathrm{d}x$ is the probability that the harvested energy by i EHBs lies in the interval $[a,b)$, while the energy harvested by each of the i EHBs lies in the interval $[D^-,D)$. Thus, letting $\tilde{i} \triangleq \lceil 4(Q+\tau)/\tau - 1 \rceil$ and $\tilde{j} \triangleq \lfloor ((\tilde{i}+1)D - \tau^+)/Q \rfloor$, given the current energy state s, after $\tilde{i}$ EHBs, the *accumulated energy level* lies in the interval $\mathcal{A} \triangleq (s+\tilde{i}D^-, s+\tilde{i}D)$ with positive probability distribution. Also we see that interval $\Delta \triangleq (\tilde{j}Q + \tau^- - D^-, \tilde{j}Q + \tau^+ - D) \subset \mathcal{A}$, thus, there is at least (because we have only considered the scenario that harvested energy by each EHB lies in $[D^-,D)$) a probability $q \triangleq \inf\{\int_{\tilde{\boldsymbol{\tau}}} \tilde{f}_{\tilde{i}}(x),\ \text{interval } \tilde{\boldsymbol{\tau}} \subset \mathcal{S}, \text{length of } \tilde{\boldsymbol{\tau}} = \text{length of } \Delta = \tau/2\}$ that the accumulated energy level lies in Δ. Therefore, after the next EHB with probability p that the harvested energy lies in $[D^-,D)$, the accumulated energy level lies in the interval $[\tilde{j}Q + \tau^-, \tilde{j}Q + \tau^+)$, which means that after the current state $\tilde{\Xi}_j = s$, with $\tilde{j}$ steps (each step consumes the amount of energy, Q), there is at least a probability, $q \times p$ to

[1] Note that although we assume B is finite, the infinite case can be easily generated from the discussions below, thus is omitted due to space limitation.

make the Markov chain hit the interval (τ^-, τ^+). Thus, Markov chain $\tilde{\Xi}_j$ is a positive recurrent Harris chain [146].

Step 2: In the aforementioned Markov chain, we still assume that the current state $\tilde{\Xi}_j = s$. Thus, in the previous state, the available energy could be higher than Q, i.e., $\tilde{\Xi}_{j-1} = s + Q$, and $\tilde{\Xi}_{j-1}$ could also be smaller than Q, i.e., based on energy level $\tilde{\Xi}_{j-1}$, there are i EHBs ($i = 1, 2, 3, ...$) to make the energy level reach $Q + s$, which makes $\tilde{\Xi}_j = s$. Based on the above and the Markovian property, the steady-state distribution of the process, $g(x)$, should satisfy the following conditions: (1) $\int_0^\infty g(x) = 1$ and (2) $g(x) = g(x+Q) + \sum_{i=1}^{\infty} \int_x^{Q+x} g_{i-1}(Q + x - y) f(y) \mathrm{d}y$. where $g_i(x)$ represents the pdf of energy level after i EHBs following a ECB, which is given by

$$g_i(x) = \begin{cases} g(x), & i = 0, \\ \left(g \underbrace{\star f \star f \star ... \star f}_{i \text{ convolutions}} \right)(x), & i > 0. \end{cases} \tag{A.2}$$

Because $f(x)$ and $g_i(x) \geq 0$ for all x and $i = 0, 1, 2, ...$, by using Tonelli's theorem for sums and integrals [147], we exchange the summation and integral operator in Condition 2, thus we have

$$g(x) = g(x+Q) + \int_x^{Q+x} \left(\sum_{i=0}^{\infty} g_i(Q + x - y) \right) f(y) \mathrm{d}y. \tag{A.3}$$

Taking (A.1) into (A.2), we have

$$g_i(x) = \frac{1}{\rho} \left(\left(F \underbrace{\star f \star f ... \star f}_{i-1 \text{ convolutions}} \right)(x) - \left(F \underbrace{\star f \star f ... \star f}_{i \text{ convolutions}} \right)(x) \right), \; i > 0. \tag{A.4}$$

Since $0 \leq F(x) \leq 1$, $f(x) \geq 0$ and $\int_0^\infty f(x) = 1$, when $i \to \infty$, we have [146]

$$\left(F \underbrace{\star f \star f ... \star f}_{i \text{ convolutions}} \right)(x) \to 0. \tag{A.5}$$

From (A.4) and (A.5), we have

$$\begin{aligned} &\sum_{i=0}^{\infty} g_i(Q + x - y) = \frac{1}{\rho} \left(1 - F(Q + x - y)\right) + \frac{1}{\rho} \left(F(Q + x - y) - (F \star f)(Q + x - y)\right) \\ &+ \frac{1}{\rho} \left((F \star f)(Q + x - y) - (F \star f \star f)(Q + x - y)\right) + ... = \frac{1}{\rho} \left(1 - \lim_{i \to \infty} \left(F \underbrace{\star f \star f ... \star f}_{i \text{ convolutions}} \right)(x) \right) = \frac{1}{\rho}. \end{aligned} \tag{A.6}$$

Taking (A.6) and (A.1) into the right side of (A.3), we have

$$g(x+Q)+\int_{x}^{Q+x}\left(\sum_{i=0}^{\infty}g_i(Q+x-y)\right)f(y)\mathrm{d}y=\frac{1}{\rho}(1-F(x+Q))+\int_{x}^{Q+x}\frac{1}{\rho}f(y)\mathrm{d}y$$
$$=\frac{1}{\rho}(1-F(x+Q))+\frac{1}{\rho}\left(F(Q+x)-(F(x)\right)=\frac{1}{\rho}\left(1-F(x)\right). \tag{A.7}$$

Thus, $g(x)$ in (A.2) satisfies Condition 2. Because of $\int_0^{\infty}(1-F(x))=\mathbb{E}\left[\xi_i\right]$ [146], Condition 1 is also satisfied, yielding the desired result. □

A.2 Proof of Lemma 1

For general random energy arrival processes, the proof is based on Lemma A1 given in Appendix A.1. First, we find an arbitrarily small Q which is a constant such that $\mathcal{E}_{\mathrm{SB}}$ and $\mathcal{E}_{\mathrm{TB}}$ are integer multiples of it. Then, from an energy perspective, we equivalently treat the proposed communication protocol with energy harvesting, sensing and transmission as a simple harvest-then-use process with EHBs and ECBs (each consumes energy, Q) as discussed in Lemma A1. Thus, the energy level after a TB, can be treated equivalently as that after a corresponding ECB. Therefore, the steady-state distribution of energy level after each TB is the same as that after each ECB, which is given in Lemma A1, completing the proof.

A.3 Event and Random Variable Definitions

To assist the proofs of the main results, we use UC to denote the sequence of time blocks from an arbitrary STB to the next STB. Also we define two events (according to [146]) and several discrete random variables (r.v.s) for convenience:

1) Event Λ_{suc}: Given a SB, its generated information is successfully transmitted to the sink, i.e., STB occurs during the W blocks after the SB.

2) Event Λ_{fail}: Given a SB, its generated information is not successfully transmitted to the sink, i.e., STB does not occur during the W blocks after the SB.

3) r.v. N, $1\leq N\leq W$: Given a SB, it is followed by N TBs before the next SB. I.e., if Λ_{suc} occurs, the N TBs include $N-1$ FTBs and one STB. While if Λ_{fail} occurs, all the N TBs are FTBs.

4) r.v. L, $1\leq L\leq W$: After a SB, the Lth block is the last TB before the next SB. I.e., if Λ_{suc} occurs, the Lth block is a STB, thus L is the update age. While if Λ_{fail} occurs, the Lth block is the last FTB during the time window for retransmissions, W.

5) r.v. $\tilde{V}$, $\tilde{V} \geq -1$: Given a SB, if Λ_{suc} occurs, $\tilde{V} = -1$, while if a Λ_{fail} occurs, $\tilde{V}$ is the number of the required EHBs after the time window for retransmissions, W, in order to harvest the amount of energy, $\mathcal{E}_{\text{TB}}$. Note that, after a Λ_{fail}, the amount of energy $\mathcal{E}_{\text{SB}} + \mathcal{E}_{\text{TB}}$ is required to be reached in order to support the following SB and TB. Without loss of generality, here we assume that the energy harvesting process first meets the energy level $\mathcal{E}_{\text{TB}}$, and the TB consumes the energy, $\mathcal{E}_{\text{TB}}$, (V)irtually. From Lemma 1 and its proof, the steady-state distribution of the available energy level after the $\tilde{V}$ EHBs is $g(\epsilon)$.

6) r.v. V, $V \geq 0$. Given a SB and conditioned on a Λ_{fail} occurs, V is the number of the required EHBs after the time window for retransmissions, W, in order to harvest the amount of energy, $\mathcal{E}_{\text{TB}}$. From the definition of V and $\tilde{V}$, it is easy to see that

$$\Pr\{V = v\} = \Pr\left\{\tilde{V} = v | \Lambda_{\text{fail}}\right\} = \frac{\Pr\left\{\tilde{V} = v\right\}}{\Pr\left\{\Lambda_{\text{fail}}\right\}}, v = 0, 1, 2, ... \tag{A.8}$$

7) r.v. $E(\mathcal{E})$, $E(\mathcal{E}) \geq 0$: Given the distribution of initial energy level, $g(\epsilon)$, and the amount of target energy, $\mathcal{E}$, the required number of energy harvesting block is $E(\mathcal{E})$.

For a deterministic energy arrival process, straightforwardly we have

$$\Pr\{E(\mathcal{E}) = i\} = 1, i = \mathcal{E}/\rho. \tag{A.9}$$

For a general random energy arrival process, from the definition of $E(\mathcal{E})$, Lemma 1 and its proof, we have

$$\Pr\{E(\mathcal{E}) = i\} = G_{i-1}(\mathcal{E}) - G_i(\mathcal{E}),\ i = 0, 1, 2, ... \tag{A.10}$$

where

$$G_i(x) = \begin{cases} 1, & i = -1, \\ \int_0^x g_i(u)\mathrm{d}u, & i \geq 0, \end{cases} \tag{A.11}$$

and $g_i(x)$ is defined in (A.2).

For *exponential* energy arrival process, we know that the energy accumulation process during EHBs after a TB is a *Poisson* process [146], thus, we have

$$\Pr\{E(\mathcal{E}) = i\} = G_{i-1}(\mathcal{E}) - G_i(\mathcal{E}) = \text{Pois}(i, \mathcal{E}/\rho) = \frac{(\mathcal{E}/\rho)^i e^{-\mathcal{E}/\rho}}{i!},\ i = 0, 1, 2, ... \tag{A.12}$$

8) r.v. M, $M \geq 0$: Given a UC, Λ_{fail} occur M times and followed by one Λ_{suc} in it.

From the definitions of events, we know that Λ_{suc} and Λ_{fail} are mutually exclusive events. Thus, we have

$$P_{\text{suc}} \triangleq \Pr\{\Lambda_{\text{suc}}\} \text{ and } \Pr\{\Lambda_{\text{fail}}\} = 1 - P_{\text{suc}}, \tag{A.13}$$

where Λ_{suc} and Λ_{fail} depend on transmit outage probability in each TB, and the available energy after the first TB following the SB. Because we have assumed that the success of each transmission is independent of one another, and from Lemma 1, the distribution of the available energy after each TB is the same, each event $\Lambda_{\text{suc}}/\Lambda_{\text{fail}}$ is independent with each other during the communication process. Therefore, r.v. M follows the geometric distribution

$$\Pr\{M = m\} = P_{\text{suc}}\left(1 - P_{\text{suc}}\right)^m, \; m = 0, 1, 2, ... \tag{A.14}$$

A.4 Pmf of Update Age

From the definitions in Appendix A.3, the pdf of T_{UA} can be calculated as

$$\Pr\{T_{\text{UA}} = k\} = \frac{\Pr\{L = k, \Lambda_{\text{suc}}\}}{\Pr\{\Lambda_{\text{suc}}\}}, \; k = 1, 2, ..., W. \tag{A.15}$$

Using the law of total probability and the r.v.s defined in Appendix A.3, we have

$$\begin{aligned}
\Pr\{L=k, \Lambda_{\text{suc}}\} &= \sum_{n=1}^{k} \Pr\{L=k, N=n, \Lambda_{\text{suc}}\} = \sum_{n=1}^{k} \Pr\{N=n, E((n-1)\mathcal{E}_{\text{TB}})=k-n, \Lambda_{\text{suc}}\} \\
&= \sum_{n=1}^{k} \Pr\{N=n, \Lambda_{\text{suc}} | E((n-1)\mathcal{E}_{\text{TB}})=k-n\} \Pr\{E((n-1)\mathcal{E}_{\text{TB}})=k-n\} \\
&= \sum_{n=1}^{k} (1-P_{\text{out}}) \left(P_{\text{out}}\right)^{n-1} \Pr\{E((n-1)\mathcal{E}_{\text{TB}}) = k-n\}.
\end{aligned} \tag{A.16}$$

Again using the law of total probability and using (A.16), (A.13) becomes

$$\begin{aligned}
P_{\text{suc}} &= \Pr\{\Lambda_{\text{suc}}\} = \sum_{l=1}^{W} \Pr\{L=l, \Lambda_{\text{suc}}\} = \Pr\{L=1, \Lambda_{\text{suc}}\} + \sum_{l=2}^{W} \Pr\{L=l, \Lambda_{\text{suc}}\} \\
&= 1 - P_{\text{out}} + \sum_{l=2}^{W} \sum_{n=2}^{l} \Pr\{L=l, N=n, \Lambda_{\text{suc}}\} \\
&= 1 - P_{\text{out}} + \sum_{l=2}^{W} \sum_{n=2}^{l} \Pr\{E((n-1)\mathcal{E}_{\text{TB}}) = l-n, N=n, \Lambda_{\text{suc}}\} \\
&= 1 - P_{\text{out}} + \sum_{l=2}^{W} \sum_{n=2}^{l} \Pr\{N=n, \Lambda_{\text{suc}} | E((n-1)\mathcal{E}_{\text{TB}})=l-n\} \Pr\{E((n-1)\mathcal{E}_{\text{TB}}) = l-n\}
\end{aligned} \tag{A.17}$$

$$= 1 - P_{\text{out}} + \sum_{l=2}^{W} \sum_{n=2}^{l} (1 - P_{\text{out}}) \left(P_{\text{out}}\right)^{n-1} \Pr\left\{E((n-1)\mathcal{E}_{\text{TB}}) = l - n\right\}.$$

By taking (A.9), (A.10) and (A.12) into (A.16) and (A.17), and then substituting (A.16) and (A.17) into (A.15), the pmfs of T_{UA} for deterministic, general random and exponential energy arrival process are given in Theorems 1, 2 and 3, respectively.

A.5 Pmf of Update Cycle

First, assuming that Λ_{fail} occurs m times during a UC, we define r.v.s E_0, V_i, E_i, $i = 1, 2, ..., m$, and $\tilde{L}$. E_0 is the number of EHBs at the beginning of the UC until the first SB occurs which follows the same pmf with r.v. $E(\mathcal{E}_{\text{SB}} + \mathcal{E}_{\text{TB}})$. V_i is the number of EHBs required to harvest the amount of energy, $\mathcal{E}_{\text{TB}}$, outside the time window for retransmissions of the ith Λ_{fail}. E_i is the number of EHBs required to harvest the amount of energy, $\mathcal{E}_{\text{SB}}$, following V_i EHBs after the ith Λ_{fail}. $\tilde{L}$ is the number of blocks after a SB to the last TB before the next SB, and the TB is a STB. From the r.v. definitions in Appendix A.3, E_0, V_i and E_i follow the same distribution with r.v.s $E(\mathcal{E}_{\text{SB}} + \mathcal{E}_{\text{TB}})$, V and $E(\mathcal{E}_{\text{SB}})$, respectively, and

$$\Pr\left\{\tilde{L} = l\right\} = \Pr\left\{L = l, \Lambda_{\text{suc}}\right\}, \; l = 1, 2, ..., W. \tag{A.18}$$

From Lemma 1, E_0, V_i, E_i, $i = 1, 2, ..., m$, and $\tilde{L}$ are mutually independent.

Then, the pmf of update cycle can be calculated as

$$\begin{aligned}
&\Pr\left\{T_{\text{UC}} = k\right\} = \sum_{m} \Pr\left\{T_{\text{UC}} = k, M = m\right\} \\
&= \sum_{m} \Pr\left\{E_0 + E_1 + ... + E_m + \tilde{V}_1 + ... + \tilde{V}_m + m \times (1+W) + \tilde{L} + 1 = k, \tilde{V}_1, \; \tilde{V}_2, \cdots, \; \tilde{V}_m \geq 0\right\} \\
&= \sum_{m=0}^{\hat{m}} \Pr\left\{E_0 + E_1 + ... + E_m + \tilde{V}_1 + ... + \tilde{V}_m + \tilde{L} = k - m \times (1+W) - 1, \tilde{V}_1, \; \tilde{V}_2, \cdots, \; \tilde{V}_m \geq 0\right\}, \\
&\qquad\qquad\qquad\qquad\qquad\qquad\qquad\qquad\qquad\qquad\qquad\qquad\qquad\qquad k = 2, 3, ...,
\end{aligned} \tag{A.19}$$

where $\hat{m} = \left\lfloor \frac{k-2}{W+1} \right\rfloor$. For simplicity, we define the following discrete functions:

$$\begin{aligned}
&\zeta(\mathcal{E}, i) \triangleq \Pr\left\{E(\mathcal{E}) = i\right\}, \; i = 0, 1, 2, ... \\
&\iota(l) \triangleq \Pr\left\{\tilde{L} = l\right\} = \Pr\left\{L = l, \Lambda_{\text{suc}}\right\}, \; l = 1, 2, ..., W \\
&\vartheta(v) \triangleq \Pr\left\{\tilde{V} = v\right\}, \; v = 0, 1, ...
\end{aligned} \tag{A.20}$$

where $\zeta(\mathcal{E}, i)$ and $\iota(l)$ are obtained directly from (A.9), (A.10), (A.12) and (A.16), respectively,

and $\vartheta(v)$ will be derived later. Therefore, pmf of T_{UC} in (A.19) can be calculated as

$$\Pr\{T_{\mathrm{UC}}=k\}=\sum_{m=0}^{\hat{m}}\left(\zeta(\mathcal{E}_{\mathrm{SB}}+\mathcal{E}_{\mathrm{TB}})\underbrace{*\zeta(\mathcal{E}_{\mathrm{SB}})*\cdots*\zeta(\mathcal{E}_{\mathrm{SB}})}_{m\text{ convolutions}}\underbrace{*\vartheta*\cdots*\vartheta}_{m\text{ convolutions}}*\iota\right)\times (k-m(1+W)-1). \tag{A.21}$$

Now we derive the expression for $\vartheta(i)$. From the definitions of r.v.s in Appendix A.3, we have

$$\begin{aligned}
\vartheta(v)&=\Pr\{\tilde{V}=v\}=\Pr\{\Lambda_{\mathrm{fail}},\tilde{V}=v\}=\sum_{n=1}^{W}\Pr\{\Lambda_{\mathrm{fail}},\tilde{V}=v,N=n\}\\
&=\Pr\{\Lambda_{\mathrm{fail}},\tilde{V}=v,N=1\}+\sum_{n=2}^{W}\Pr\{\Lambda_{\mathrm{fail}},\tilde{V}=v,N=n\}\\
&=\Pr\{\Lambda_{\mathrm{fail}},\tilde{V}=v,N=1\}+\sum_{l=2}^{W}\sum_{n=2}^{l}\Pr\{\Lambda_{\mathrm{fail}},\tilde{V}=v,N=n,L=l\}\\
&=\Pr\{\Lambda_{\mathrm{fail}},N=1,E(\mathcal{E}_{\mathrm{TB}})=W+v-1\}\\
&+\sum_{l=2}^{W}\sum_{n=2}^{l}\Pr\{\Lambda_{\mathrm{fail}},N=n,E((n-1)\mathcal{E}_{\mathrm{TB}})=l-n,E(\mathcal{E}_{\mathrm{TB}})=W+v-l\}\\
&=\Pr\{\Lambda_{\mathrm{fail}},N=1|E(\mathcal{E}_{\mathrm{TB}})=W+v-1\}\Pr\{E(\mathcal{E}_{\mathrm{TB}})=W+v-1\}\\
&+\sum_{l=2}^{W}\sum_{n=2}^{l}\Pr\{\Lambda_{\mathrm{fail}},N=n|E((n-1)\mathcal{E}_{\mathrm{TB}})=l-n,E(\mathcal{E}_{\mathrm{TB}})=W+v-l\}\times\\
&\qquad\Pr\{E((n-1)\mathcal{E}_{\mathrm{TB}})=l-n,E(\mathcal{E}_{\mathrm{TB}})=W+v-l\}\\
&=P_{\mathrm{out}}\Pr\{E(\mathcal{E}_{\mathrm{TB}})=W+v-1\}\\
&\quad+\sum_{l=2}^{W}\sum_{n=2}^{l}(P_{\mathrm{out}})^{n}\Pr\{E((n-1)\mathcal{E}_{\mathrm{TB}})=l-n\}\Pr\{E(\mathcal{E}_{\mathrm{TB}})=W+v-l\}.
\end{aligned} \tag{A.22}$$

By taking functions (A.22), $\zeta(\mathcal{E},i)$ and $\iota(l)$ in (A.20), into (A.21), and letting (A.9) and (A.10) substitute $\Pr\{E(\mathcal{E})=i\}$, the pmf of T_{UC} for deterministic and general random energy arrival process can be calculated, respectively, as given in Theorems 4 and 5. While for the exponential energy arrival process, by using the sum property of Poisson distribution, we have

$$\Pr\{E(\mathcal{E}_1)_1+E(\mathcal{E}_2)_2=i\}=\Pr\{E(\mathcal{E}_1+\mathcal{E}_2)=i\}, \tag{A.23}$$

where $E(\mathcal{E}_1)_1$ and $E(\mathcal{E}_2)_2$ are two independent random variables which have the same distribution with $E(\mathcal{E}_1)$ and $E(\mathcal{E}_2)$ defined in Appendix A.3, respectively. Therefore, letting (A.12)

substitute $\Pr\{E(\mathcal{E}) = i\}$, the pmf of T_{UC} for exponential energy arrival process can be further simplified as given in Theorem 6.

A.6 Average Update Cycle

Based on Appendix A.5, average update cycle can be calculated as

$$\begin{aligned}\bar{T}_{\mathrm{UC}} &= \mathbb{E}\left[\mathbb{E}\left[T_{\mathrm{UC}}|M\right]\right] = \sum_{m=0}^{\infty} \Pr\{M=m\}\,\mathbb{E}\left[T_{\mathrm{UC}}|M=m\right] \\ &= \sum_{m=0}^{\infty} \Pr\{M=m\}\,\mathbb{E}\left[E_0+E_1+\cdots+E_m+V_1+V_2+\cdots+V_m+m\times(1+W)+1+T_{\mathrm{UA}}\right] \\ &= \sum_{m=0}^{\infty} \Pr\{M=m\}\left(\mathbb{E}\left[E_0\right]+\mathbb{E}\left[E_1\right]+\cdots+\mathbb{E}\left[E_m\right]+m\times\bar{V}+m\times(W+1)+\bar{T}_{\mathrm{UA}}+1\right).\end{aligned} \tag{A.24}$$

From Appendix A.5, we have

$$\mathbb{E}\left[E_0\right] = \frac{\mathcal{E}_{\mathrm{SB}}+\mathcal{E}_{\mathrm{TB}}}{\rho},\ \mathbb{E}\left[E_i\right] = \frac{\mathcal{E}_{\mathrm{SB}}}{\rho}, i = 1,2,...,m. \tag{A.25}$$

After taking (A.22) and (A.13) into (A.8) and some simplifications, the expectation of V can be calculated as

$$\begin{aligned}\bar{V} &= \sum_{v=0}^{\infty} v\frac{\vartheta(v)}{1-P_{\mathrm{suc}}} \\ &= \frac{P_{\mathrm{out}}}{1-P_{\mathrm{suc}}}\left(\frac{\mathcal{E}_{\mathrm{TB}}}{\rho} - \sum_{i=0}^{W-2} i\Pr\{E(\mathcal{E}_{\mathrm{TB}})=i\} - (W-1)\left(1-\sum_{i=0}^{W-2}\Pr\{E(\mathcal{E}_{\mathrm{TB}})=i\}\right)\right) \\ &+ \frac{1}{1-P_{\mathrm{suc}}}\sum_{l=2}^{W}\sum_{n=2}^{l}\left(P_{\mathrm{out}}\right)^n \Pr\{E((n-1)\mathcal{E}_{\mathrm{TB}})=l-n\}\times \\ &\qquad\left(\frac{\mathcal{E}_{\mathrm{TB}}}{\rho} - \sum_{i=0}^{W-l-1} i\Pr\{E(\mathcal{E}_{\mathrm{TB}})=i\} - (W-l)\left(1-\sum_{i=0}^{W-l-1}\Pr\{E(\mathcal{E}_{\mathrm{TB}})=i\}\right)\right).\end{aligned} \tag{A.26}$$

By taking (A.25), (A.26) and (A.14) into (A.24), and further substituting P_{suc} and $\bar{T}_{\mathrm{UA}}$ given in Corollaries 1, 2 and 3, average update cycle for deterministic, general random and exponential energy arrival processes are given in Corollaries 5, 6 and 7, respectively.

A.7 Asymptotic Lower/Upper Bounds

From Corollaries 1 and 2, it is easy to see that $\bar{T}_{\mathrm{UA}}$ increases with W. While for $\bar{T}_{\mathrm{UC}}$, the monotonicity is not explicitly observed from Corollary 6. Due to space limitations, a sketch of

the proof is given: When W increases, more TBs are allowed, thus more STBs occur during the communication process, which also means shorter average update cycle.

When $W \to \infty$, the sensed information in each SB will be successfully transmitted to the sink, i.e., Λ_{suc} always occurs and $P_{\text{suc}} \to 1$. Thus, UC contains the EHBs to harvest the amount of energy, $\mathcal{E}_{\text{SB}} + \mathcal{E}_{\text{TB}}$, the SB, and the blocks in T_{UA}. Based on this explanation, for the average update age, we have

$$\begin{aligned}\lim_{W\to\infty} \bar{T}_{\text{UA}} &= \sum_{n=1}^{\infty} \Pr\{N=n\}\, \mathbb{E}\left[T_{\text{UA}}|N=n\right] = \sum_{n=1}^{\infty} (1-P_{\text{out}})\,(P_{\text{out}})^{n-1}\, \mathbb{E}\left[n + E((n-1)\mathcal{E}_{\text{TB}})\right] \\ &= \sum_{n=1}^{\infty} (1-P_{\text{out}})\,(P_{\text{out}})^{n-1} \left(n + (n-1)\frac{\mathcal{E}_{\text{TB}}}{\rho}\right) = 1 + \left(\frac{\mathcal{E}_{\text{TB}}}{\rho} + 1\right) \frac{P_{\text{out}}}{1-P_{\text{out}}}.\end{aligned} \tag{A.27}$$

For the average update cycle, we have

$$\begin{aligned}\lim_{W\to\infty} \bar{T}_{\text{UC}} &= \sum_{n=1}^{\infty} \Pr\{N=n\}\, \mathbb{E}\left[T_{\text{UC}}|N=n\right] \\ &= \sum_{n=1}^{\infty} (1-P_{\text{out}})\,(P_{\text{out}})^{n-1}\, \mathbb{E}\left[E(\mathcal{E}_{\text{SB}} + \mathcal{E}_{\text{TB}}) + 1 + n + E((n-1)\mathcal{E}_{\text{TB}})\right] \\ &= \sum_{n=1}^{\infty} (1-P_{\text{out}})\,(P_{\text{out}})^{n-1} \left(n+1+\frac{\mathcal{E}_{\text{SB}} + n\mathcal{E}_{\text{TB}}}{\rho}\right) \\ &= 2+\left(\frac{\mathcal{E}_{\text{TB}}}{\rho}+1\right) \frac{P_{\text{out}}}{1-P_{\text{out}}} + \frac{\mathcal{E}_{\text{SB}} + \mathcal{E}_{\text{TB}}}{\rho}.\end{aligned} \tag{A.28}$$

Appendix B

This appendix contains the proofs needed in Chapter 3.

B.1 Proof of Lemma 2

In one PT-IT cycle, once the available energy is higher than $\mathcal{P}_J T$, there will be Y opportunistic PT blocks. The probability of the discrete random variable Y being k is the probability that the successive k blocks suffer from connection outage of the $S \to D$ link, and the $(k+1)$th block does not have the $S \to D$ outage. Due to the i.i.d. channel gains in different blocks, Y follows a geometric distribution and the probability mass function (pmf) is given by

$$\mathbb{P}\{Y = k\} = p_{co}^{k}\left(1 - p_{co}\right), k = 0, 1, ... \tag{B.1}$$

The mean value of Y is given by

$$\mathbb{E}\{Y\} = \sum_{k=0}^{\infty} k\mathbb{P}\{Y = k\} = \sum_{k=0}^{\infty} k p_{co}^{k}\left(1 - p_{co}\right) = \frac{p_{co}}{1 - p_{co}}. \tag{B.2}$$

As we have defined ρ_J as the average harvested energy by one PT block, the average harvested energy by Y opportunistic PT blocks in one PT-IT cycle is given by

$$\mathcal{E}_Y = \mathbb{E}\{Y\}\rho_J = \frac{p_{co}}{1 - p_{co}}\rho_J. \tag{B.3}$$

If the average harvested energy by opportunistic PT blocks in a PT-IT cycle is higher than the required energy, $\mathcal{P}_J T$, for jamming in one IT block, the communication process leads to energy accumulation. Otherwise, we need dedicated PT blocks in some PT-IT cycles, and the communication process is energy balanced. Thus, we have the condition in Lemma 2.

B.2 Proof of Theorem 7

We derive information transmission probability p_{tx} in the following two cases.

Energy Accumulation Case: In this case, there is no dedicated PT blocks. We use a simple Markov chain with two states, IT and opportunistic PT, to model the communication process. When the fading channel of $S \rightarrow D$ link suffers connection outage, the block is in the opportunistic PT state, otherwise it is in the IT state. This Markov chain is ergodic since the fading channel of $S \rightarrow D$ link is i.i.d. between blocks. The information transmission probability is simply the probability that the $S \rightarrow D$ link does not suffer connection outage, hence we have

$$p_{tx} = 1 - p_{co} = \frac{1}{1 + \frac{p_{co}}{1-p_{co}}}. \tag{B.4}$$

Energy Balanced Case: In this case, the available energy at the jammer becomes directly relevant to whether a block is used for IT or PT. Following the recent works, such as [52], we model the energy state at the beginning/end of each time block as a Markov chain in order to obtain the information transmission probability. Since the energy state is continuous, we adopt Harris chain which can be treated as a Markov chain on a general state space (continuous state Markov chain).

It is easy to show that this Harris chain is recurrent and aperiodic, because any current energy state can be revisited in some future block, and one cannot find any two energy states that the transition from one to the other is periodic. Therefore, the Harris chain is ergodic [146], and there exists a unique stationary measure (stationary distribution), which means that the stationary distribution of available energy at the beginning/end of each block exists. Thus, the stationary probability of a block being used for IT (p_{tx}) or PT exists.

Instead of deriving the stationary distribution of energy states, we use time averaging which makes use of the ergodic property, to calculate the information transmission probability p_{tx} which is given by

$$p_{tx} = \lim_{\mathcal{N}_{total}\rightarrow\infty} \frac{\mathcal{N}_{IT}}{\mathcal{N}_{PT} + \mathcal{N}_{IT}} = \lim_{\mathcal{N}_{total}\rightarrow\infty} \frac{1}{1 + \mathcal{N}_{PT}/\mathcal{N}_{IT}}, \tag{B.5}$$

where $\mathcal{N}_{IT}$ and $\mathcal{N}_{PT}$ denote the numbers of IT and PT blocks in the communication process, respectively, and $\mathcal{N}_{total} \triangleq \mathcal{N}_{PT} + \mathcal{N}_{IT}$. By using the principle of conservation of energy (i.e., all the harvested energy in PT blocks are used for jamming in IT blocks) and the law of large numbers, we have

$$\lim_{\mathcal{N}_{total}\rightarrow\infty} \frac{\mathcal{N}_{PT}\,\rho_J}{\mathcal{N}_{IT}\,\mathcal{P}_J T} = 1, \tag{B.6}$$

where ρ_J is the average harvested energy in one PT block defined in (3.5) and $\mathcal{P}_J T$ is the energy used for jamming in one IT block. By taking (B.6) into (B.5) the information transmission

probability is given by

$$p_{tx} = \frac{1}{1+\frac{\mathcal{P}_J T}{\rho_J}}. \tag{B.7}$$

General Expression: Based on Lemma 2, (B.4) and (B.7), we can easily obtain the general expression for p_{tx} as

$$p_{tx} = \frac{1}{1+\max\left\{\frac{\mathcal{P}_J T}{\rho_J}, \frac{p_{co}}{1-p_{co}}\right\}}. \tag{B.8}$$

From (3.1), we have,

$$p_{co} = \mathbb{P}\left\{\log_2(1+\gamma_d) < R_t\right\} = \mathbb{P}\left\{\gamma_d < 2^{R_t}-1\right\} = F_{\gamma_d}\left(2^{R_t}-1\right). \tag{B.9}$$

By taking (3.9) into (B.9), we obtain the expression of p_{co} in (3.17).

B.3 Proof of Proposition 1

Case I: If optimal $(R_t, R_s) \in \mathcal{D}_1$, the optimization problem can be rewritten as

$$\max_{(R_t,R_s)\in\mathcal{D}_1} \quad \pi = \frac{R_s}{e^{\frac{\left(2^{R_t}-1\right)}{\rho_d}}\left(1+\frac{k_2\left(2^{R_t}-1\right)}{2^{R_t-R_s}-1}\right)}. \tag{B.10}$$

The optimal (R_t, R_s) should satisfies $\frac{\partial\,\pi}{\partial\,\varsigma} = 0$ and $\frac{\partial\,\pi}{\partial R_s} = 0$, where $\varsigma \triangleq 2^{R_t}$.

Since ς only appears in the denominator of (B.10), by taking the partial derivative of (B.10) about ς,

$$\frac{\partial\,\pi}{\partial\,\varsigma} = 0 \Leftrightarrow \frac{\partial\left(e^{\frac{(\varsigma-1)}{\rho_d}}\left(1+\frac{k_2(\varsigma-1)}{\frac{\varsigma}{2^{R_s}}-1}\right)\right)}{\partial\varsigma} = 0, \tag{B.11}$$

which can be further expanded and simplified as

$$e^{\frac{\varsigma}{\rho_d}}\left(\frac{1}{\rho_d}\left(1+\frac{k_2\left(\varsigma-1\right)}{\frac{\varsigma}{2^{R_s}}-1}\right)-\frac{k_2\left(1-\frac{1}{2^{R_s}}\right)}{\left(\frac{\varsigma}{2^{R_s}}-1\right)^2}\right) = 0. \tag{B.12}$$

Because $e^{\frac{\varsigma}{\rho_d}} > 0$, (B.12) is equivalent to

$$\begin{aligned}&\left(\frac{\varsigma}{2^{R_s}}-1\right)\left(\frac{\varsigma}{2^{R_s}}-1+k_2 2^{R_s}\left(\frac{\varsigma}{2^{R_s}}-1\right)+k_2 2^{R_s}\left(1-\frac{1}{2^{R_s}}\right)\right)\\ &-\rho_d k_2\left(1-\frac{1}{2^{R_s}}\right) = 0.\end{aligned} \tag{B.13}$$

By using $\xi \triangleq \frac{\varsigma}{2^{R_s}} - 1$, (B.13) can be further simplified as

$$\xi^2 + \frac{k_2 2^{R_s}\left(1-\frac{1}{2^{R_s}}\right)}{1+k_2 2^{R_s}}\xi - \frac{\rho_d k_2\left(1-\frac{1}{2^{R_s}}\right)}{1+k_2 2^{R_s}} = 0, \tag{B.14}$$

which has a single positive root as (since $\xi > 0$)

$$\xi = \frac{1}{2}\left(-\frac{k_2\left(2^{R_s}-1\right)}{1+k_2 2^{R_s}} + \left(\left(\frac{k_2\left(2^{R_s}-1\right)}{1+k_2 2^{R_s}}\right)^2 + \frac{4\rho_d k_2\left(1-\frac{1}{2^{R_s}}\right)}{1+k_2 2^{R_s}}\right)^{\frac{1}{2}}\right). \tag{B.15}$$

Also we have

$$\frac{\partial\,\pi}{\partial\,R_s} = \frac{\left(1+\frac{k_2\left(2^{R_t}-1\right)}{2^{R_t-R_s}-1}\right) - R_s\left(\frac{\ln 2\; k_2\; 2^{R_t-R_s}\left(2^{R_t}-1\right)}{\left(2^{R_t-R_s}-1\right)^2}\right)}{e^{\frac{2\left(2^{R_t}-1\right)}{\rho_d}}\left(1+\frac{k_2\left(2^{R_t}-1\right)}{2^{R_t-R_s}-1}\right)^2} = 0. \tag{B.16}$$

Since the denominator of the middle term of (B.16) is greater than zero, (B.16) reduces to

$$k_2\left(2^{R_s} + \frac{2^{R_s}-1}{\xi}\right)\left(\ln 2\; R_s - 1 + \frac{\ln 2\; R_s}{\xi}\right) = 1, \tag{B.17}$$

where k_2 is defined in (3.34).

Taking (B.15) into (B.17), optimal R_s, $R_s^\star$ can be obtained easily by linear search, since the left side of (B.17) is monotonically increasing with R_s which can be easily proved. The optimal R_t can be calculated as

$$R_t^\star = R_s^\star + \log_2\left(1+\xi^\star\right), \tag{B.18}$$

where $\xi^\star$ can be obtained by taking $R_s^\star$ into (B.15).

Case II: If optimal $(R_t, R_s) \in \hat{\mathcal{D}} \cup \mathcal{D}_2$, (3.22) can be rewritten as

$$\pi = \frac{R_s}{1+\frac{k_1}{2^{R_t-R_s}-1}}. \tag{B.19}$$

Because π in (B.19) increases with R_t, optimal R_t and R_s should be found at the boundary of $\mathcal{D}_1$ and $\mathcal{D}_2$, that is $\hat{\mathcal{D}}$. Letting $(a) = (b)$, we have

$$1 + \frac{k_1}{2^{R_t-R_s}-1} = e^{\frac{2^{R_t}-1}{\rho_d}} + \frac{k_2\, e^{\frac{2^{R_t}-1}{\rho_d}}\left(2^{R_t}-1\right)}{2^{R_t-R_s}-1}, \tag{B.20}$$

which can be further simplified as

$$2^{R_s} = \frac{2^{R_t}}{1+\zeta'}, \tag{B.21}$$

where

$$\zeta = \frac{k_1 - k_2\, e^{\frac{2^{R_t}-1}{\rho_d}}\left(2^{R_t}-1\right)}{e^{\frac{2^{R_t}-1}{\rho_d}}-1} > 0. \tag{B.22}$$

Thus, from (B.21) we have

$$R_s = R_t - \log_2\left(1+\zeta\right). \tag{B.23}$$

By taking (B.23) into (B.19), we have

$$\pi = \frac{R_t - \log_2\left(1+\zeta\right)}{1+\frac{k_1}{\zeta}}. \tag{B.24}$$

By taking the derivative of π about R_t in (B.24), optimal R_t should satisfy

$$\frac{\left(1-\frac{1}{\ln 2}\frac{\zeta'}{1+\zeta}\right)\left(1+\frac{k_1}{\zeta}\right)-\left(R_t-\log_2\left(1+\zeta\right)\right)\left(-\frac{k_1}{\zeta^2}\right)\zeta'}{\left(1+\frac{k_1}{\zeta}\right)^2}=0, \tag{B.25}$$

where

$$\zeta' \triangleq \frac{\mathrm{d}\zeta}{\mathrm{d}R_t} = \frac{\ln 2\, e^{\frac{2^{R_t}-1}{\rho_d}}}{\left(e^{\frac{2^{R_t}-1}{\rho_d}}-1\right)^2}\left(k_2\, 2^{R_t}\left(1+\frac{1}{\rho_d}-e^{\frac{2^{R_t}-1}{\rho_d}}\right)-\frac{k_1+k_2}{\rho_d}\right). \tag{B.26}$$

And (B.25) can be further simplified as

$$\zeta'\left(\frac{1+\frac{k_1}{\zeta}}{\ln 2\left(1+\zeta\right)}-\frac{k_1\left(R_t-\log_2\left(1+\zeta\right)\right)}{\zeta^2}\right)=1. \tag{B.27}$$

Thus, $R_t^\star$ can be calculated as the solution of (B.27), and from (B.23)

$$R_s^\star = R_t^\star - \log_2\left(1+\zeta^\star\right), \tag{B.28}$$

where $\zeta^\star$ is calculated by taking $R_t^\star$ into (B.22).

Note that, if the optimal (R_t, R_s) for problem (B.10) is obtained in region $\mathcal{D}_1$, they are the optimal rate parameters for problem (3.26). This is because, firstly, the above discussion and derivations show that the optimal rate parameters can only be obtained in region $\mathcal{D}_1$ and $\hat{\mathcal{D}}$. Secondly, by using the continuity of the function of throughput (3.22), if the optimal (R_t, R_s) for problem (B.10) are obtained in region $\mathcal{D}_1$, the maximal throughput in region $\mathcal{D}_1$ (i.e., the maximal value of the object function of (B.10) in $\mathcal{D}_1$), is larger than its boundary $\hat{\mathcal{D}}$. Thus, the optimal rate parameters are obtained and fall in region $\mathcal{D}_1$.

B.4 Proof of Corollary 9

We consider the asymptotically high SNR regime, i.e., $\rho_d \to \infty$ or equivalently $\mathcal{P}_s \to \infty$.

When $\rho_d \to \infty$, we firstly assume $(R_t^\star, R_s^\star)$ is obtained in the region $\mathcal{D}_1$. The value of R_s that satisfies (3.27) cannot go to infinity regardless of the value of ξ. Thus, we have $\xi \to \infty$ as $\rho_d \to \infty$, and (3.27) can be rewritten as

$$k_2 2^{R_s} (\ln 2 R_s - 1) = 1, \tag{B.29}$$

where k_2 is defined in (3.34). From (B.29) optimal R_s for the case $\rho_d \to \infty$ can be calculated as

$$R_s^\star = \frac{1 + \mathrm{W}_0\left(\frac{1}{k_2 2^{\frac{1}{\ln 2}}}\right)}{\ln 2} = \frac{1 + \mathrm{W}_0\left(\frac{1}{e k_2}\right)}{\ln 2}. \tag{B.30}$$

From (3.29), we know that $\xi = \mathcal{O}\left(\rho_d^{\frac{1}{2}}\right) = \mathcal{O}\left(\mathcal{P}_s^{\frac{1}{2}}\right)$, and because $\xi = \frac{2^{R_t}}{2^{R_s}} - 1$, we have $2^{R_t} = \mathcal{O}\left(\mathcal{P}_s^{\frac{1}{2}}\right)$. It can be easily verified that the assumption that optimal $(R_t, R_s) \in \mathcal{D}_1$ is correct. From Proposition 1 and (3.22), optimal (R_t, R_s) and π are obtained.

B.5 Proof of Proposition 2

Because (a) in (3.22) decreases with R_t, while (b) increases with R_t, optimal R_t can be obtained when the two parts become equal with each other, i.e., optimal $(R_t, R_s) \in \hat{\mathcal{D}}$. Thus, optimization problem (3.26) can be rewritten as

$$\begin{aligned} \max_{R_t, R_s} \quad & \frac{R_s}{1 + \max\left\{ \frac{d_{SJ}^m}{N_J \eta} \frac{d_{JE}^m}{d_{SE}^m} \frac{(N_J - 1)\left(\varepsilon^{-\frac{1}{N_J - 1}} - 1\right)}{2^{R_t - R_s} - 1}, e^{\frac{2^{R_t - 1}}{\rho_d}} - 1 \right\}} \\ \text{s.t.} \quad & \frac{d_{SJ}^m}{N_J \eta} \frac{d_{JE}^m}{d_{SE}^m} \frac{(N_J - 1)\left(\varepsilon^{-\frac{1}{N_J - 1}} - 1\right)}{2^{R_t - R_s} - 1} = e^{\frac{2^{R_t - 1}}{\rho_d}} - 1, R_t \geq R_s \geq 0. \end{aligned} \tag{B.31}$$

By solving the equality constraint, we have

$$2^{R_s} = \frac{2^{R_t}}{1 + \frac{M}{e^{\frac{2^{R_t - 1}}{\rho_d}} - 1}}, \tag{B.32}$$

where M is defined in (3.39). Certainly, $R_t \geq R_s$ is satisfied in (B.32). By taking (B.32) into

(B.31), the optimization problem can be rewritten as

$$\max_{R_t \geq 0} \frac{\log_2 \left(\frac{2^{R_t}}{1+\frac{M}{e^{\frac{2^{R_t}-1}{\rho_d}}-1}} \right)}{e^{\frac{2^{R_t}-1}{\rho_d}}}. \tag{B.33}$$

Now we use z to denote 2^{R_t}, thus $R_t = \log_2 z$. By taking the derivative of objective function about z in (B.33), and then setting it equal to 0, optimal z, $z^\star$, can be calculated as the solution of (3.38) which is monotone decreasing function with z on the left side.

B.6 Proof of Corollaries 10 and 11

When $\rho_d \to \infty$, (3.38) approximates as $2\frac{\rho_d}{z} - \ln z = 0$. Thus, we have $z^\star = \frac{2\rho_d}{\mathrm{W}_0(2\rho_d)}$. From (3.22) and Proposition 2, the Corollary 10 can be easily obtained. When $N_J \to \infty$, from (3.39), we have $M = \frac{d_{SJ}^m}{N_J \eta} \frac{d_{JE}^m}{d_{SE}^m}(N_J - 1)\left(\varepsilon^{-\frac{1}{N_J - 1}} - 1\right) \to 0$. Therefore, (3.38) approximates to $\frac{\rho_d}{z} - \ln z = 0$. Thus, we have the expression of optimal z in $N_J \to \infty$ regime as $z^\star = e^{\mathrm{W}_0(\rho_d)}$. From (3.22) and Proposition 2, Corollary 11 can be easily obtained.

Appendix C

This appendix contains the proofs needed in Chapter 4.

C.1 Proof of Proposition 3

Given channel fading power gain v, average power for PT $\mathcal{P}_{\text{tx},1}$, time for PT τ, we assume that an energy signal is an N-level power signal, with power levels in ascending sort as, $\tilde{P}_i$, $i = 1, 2, ..., N$. $\tilde{P}_i$ holds for q_i percentage of the time duration, τ, and we have $\sum_{i=1}^{N} q_i \tilde{P}_i = \mathcal{P}_{\text{tx},1}$.

Assuming that $\tilde{P}_{n-1} \leq \mathcal{P}_{\text{th}}$ and $\tilde{P}_n > \mathcal{P}_{\text{th}}$, we propose the following optimization problem to find the optimal energy signal which maximizes the harvested energy during τ as:

$$\begin{aligned} \textbf{PA}: \quad & \underset{P_{\text{low}}, P_{\text{high}}, q_{\text{low}}, q_{\text{high}}}{\text{Maximize}} \quad q_{\text{high}} \left(P_{\text{high}} - \mathcal{P}_{\text{th}} \right) \\ & \text{Subject to} \quad q_{\text{low}} P_{\text{low}} + q_{\text{high}} P_{\text{high}} = \mathcal{P}_{\text{tx},1}, \\ & \qquad\qquad 0 \leq P_{\text{low}} \leq \mathcal{P}_{\text{th}} \leq P_{\text{high}} \leq \mathcal{P}_{\text{peak}}, \\ & \qquad\qquad q_{\text{low}} + q_{\text{high}} = 1, q_{\text{low}}, q_{\text{high}} \geq 0, \end{aligned} \tag{C.1}$$

where $q_{\text{low}} = \sum_{i=1}^{n-1} q_i$, $q_{\text{high}} = \sum_{i=n}^{N} q_i$, $P_{\text{low}} = \sum_{i=1}^{n-1} q_i \tilde{P}_i / q_{\text{low}}$ and $P_{\text{high}} = \sum_{i=n}^{N} q_i \tilde{P}_i / q_{\text{high}}$.

Because the target function of **PA** is a monotonically increasing function w.r.t. both q_{high} and P_{high}, we let $q_{\text{low}} P_{\text{low}} = 0$ in the first constraint of **PA**, i.e., $q_{\text{high}} P_{\text{high}} = \mathcal{P}_{\text{tx},1}$. Then, **PA** can be easily solved as $P^{\star}_{\text{high}} = \mathcal{P}_{\text{peak}}, q^{\star}_{\text{high}} = \mathcal{P}_{\text{tx},1} / \mathcal{P}_{\text{peak}}, P^{\star}_{\text{low}} = 0$, and $q^{\star}_{\text{low}} = 1 - \mathcal{P}_{\text{tx},1} / \mathcal{P}_{\text{peak}}$. Therefore, an optimized energy signal is proposed in Proposition 3.

C.2 Proof of Proposition 4

In order to solve **P2**, we first relax the peak power constraint for $\mathcal{P}_{\text{tx},2}$, i.e., replace $\varphi_i \mathcal{P}_{\text{tx},2} \leq \mathcal{P}_{\text{peak}}$ with $\mathcal{P}_{\text{tx},2} \leq \mathcal{P}_{\text{peak}}$.

From (4.17), $1 - \text{SER}(v)$ is a monotonically increasing function w.r.t. $\mathcal{P}_{\text{tx},2}$. Thus, from (4.26), the target function of **P2**, $\overline{\text{SSR}}$, is a monotonically increasing and decreasing function

w.r.t. $\mathcal{P}_{\text{tx},2}$ and ρ_{TS}, respectively. Therefore, the first and the second constraints of **P2** are active constraints, i.e., the equalities hold, which are given by (after simplification)

$$\rho_{\text{TS}}\mathcal{P}_{\text{tx},1} = \frac{\bar{\mathcal{P}}_0 d^{\lambda}}{\eta\Psi}, \tag{C.2}$$

$$(1-\rho_{\text{TS}}) = \frac{1}{\mathcal{P}_{\text{tx},2}}\left(\mathcal{P}_{\text{ave}} - \frac{\bar{\mathcal{P}}_0 d^{\lambda}}{\eta\Psi}\right), \tag{C.3}$$

respectively. Taking (C.3) into (4.26), we have

$$\overline{\text{SSR}} = \int_0^{\infty} \frac{1}{\mathcal{P}_{\text{tx},2}} \left(1-\text{SER}(v)\right) f_v(v)\mathrm{d}v. \tag{C.4}$$

Given v, taking (4.17) into (C.4) and using the property that $Q'(x) = -\frac{1}{\sqrt{2\pi}}\exp\left(-x^2/2\right)$, we verify that $\frac{1}{\mathcal{P}_{\text{tx},2}}\left(1-\text{SER}(v)\right)$ is a monotonically decreasing function w.r.t. $\mathcal{P}_{\text{tx},2}$. Thus, $\overline{\text{SSR}}$ in (C.4) monotonically decreases with $\mathcal{P}_{\text{tx},2}$. From (C.3), in order to minimize $\mathcal{P}_{\text{tx},2}$, we need to find the minimum ρ_{TS}, which can be obtained by letting $\mathcal{P}_{\text{tx},1} = \mathcal{P}_{\text{peak}}$ in (C.2). Thus, the optimal ρ_{TS} can be derived, and then the optimal $\mathcal{P}_{\text{tx},2}$ is obtained from (C.3), which are shown in Proposition 4.

From the above solution, we obtain the optimal $\mathcal{P}_{\text{tx},2}$ which is no larger than $\mathcal{P}_{\text{ave}}$. Based on our explanation for peak power constraint in Sec. 4.1.2, the optimal $\mathcal{P}_{\text{tx},2}$ satisfies the constraint $\varphi_i\mathcal{P}_{\text{tx},2} \leq \mathcal{P}_{\text{peak}}$ naturely. Thus, the calculated optimal $\mathcal{P}_{\text{tx},2}$ is exactly the global optimal $\mathcal{P}_{\text{tx},2}$.

Appendix D

This appendix contains the proofs needed in Chapter 5.

D.1 Proof of Lemma 3

We assume that $\vec{\rho} \in [0,1]^K \backslash \{\vec{0}, \vec{1}\}$. Thus, based on (5.6), $\Theta_1 > 0$ and $\Theta_2 > 0$.

D.1.1 Proof of (5.16a)

Based on the property of mutual information invariance under scaling of random variables [148], a scaled received signal expression based on (5.7) is given by

$$\begin{aligned} \tilde{Y}_1 &= \sqrt{\Theta_1}\tilde{X} + \frac{\tilde{Z}}{\sqrt{\mathcal{P}}}, \\ Y_2 &= \sqrt{\Theta_2} k \sqrt{\mathcal{P}} |\tilde{X}|^2 + k\frac{N}{\sqrt{\mathcal{P}}}, \end{aligned} \tag{D.1}$$

where $k \triangleq \frac{\sigma_{\text{cov}}}{\sqrt{2}\sigma_{\text{rec}}}$. Thus, it is easy to verify that the real and imaginary parts of $\frac{\tilde{Z}}{\sqrt{\mathcal{P}}}$ and $k\frac{N}{\sqrt{\mathcal{P}}}$ are independent with each other and follow the same distribution $\mathcal{N}(0, \frac{\sigma_{\text{cov}}^2}{2\mathcal{P}})$.

We define two random variables as

$$\tilde{X}_1 \triangleq \sqrt{\Theta_1}\tilde{X}, \text{ and } X_2 \triangleq \sqrt{\Theta_2} k \sqrt{\mathcal{P}} |\tilde{X}|^2. \tag{D.2}$$

Because of the Markov chain $\sqrt{\mathcal{P}}\tilde{X} \to (\tilde{X}_1, X_2) \to (\tilde{Y}_1, Y_2)$ and the smooth and uniquely invertible map from $\sqrt{\mathcal{P}}\tilde{X}$ to $(\tilde{X}_1, X_2)$, we have

$$\mathcal{I}(\sqrt{\mathcal{P}}X; \tilde{Y}_1, Y_2) = \mathcal{I}(\tilde{X}_1, X_2; \tilde{Y}_1, Y_2). \tag{D.3}$$

Before the analysis of $\mathcal{I}(\tilde{X}_1, X_2; \tilde{Y}_1, Y_2)$, we first define a new coordinate system named as paraboloid-normal (PN) coordinate system which is based on a paraboloid $\mathcal{U}$. The paraboloid

$\mathcal{U}$ is defined by the equation

$$c_P = k\sqrt{\mathcal{P}}\frac{\sqrt{\Theta_2}}{\Theta_1}(c_I^2 + c_Q^2), \tag{D.4}$$

where c_I, c_Q and c_P are the three axes of Cartesian coordinate system of the I-Q-P space. By changing coordinate system, the point (c_1, c_2, c_3) is represented as $(\tilde{a}, l)$ in the PN coordinate system, where $\tilde{a}$ is the nearest point on the paraboloid $\mathcal{U}$ to the point (c_1, c_2, c_3), and $|l|$ is the distance. In other words, the point (c_1, c_2, c_3) is on the normal line at the point $\tilde{a}$ on the paraboloid. Specifically, the sign of l is positive when the point (c_1, c_2, c_3) is above the parabolic, otherwise, it is negative.

Based on the property of mutual information invariance under a change of coordinates [148], representing Cartesian coordinate based random variables $(\tilde{X}_1, X_2)$ and $(\tilde{Y}_1, Y_2)$ under the PN coordinate system as $(\tilde{A}_X, L_X)$ and $(\tilde{A}_X + \tilde{A}_{\tilde{Z},N}, L_{\tilde{Z},N})$, respectively, gives

$$\mathcal{I}(\tilde{X}_1, X_2; \tilde{Y}_1, Y_2) = \mathcal{I}(\tilde{A}_X, L_X; \tilde{A}_X + \tilde{A}_{\tilde{Z},N}, L_{\tilde{Z},N}), \tag{D.5}$$

where the noise-related random variables $\tilde{A}_{\tilde{Z},N}$ and $L_{\tilde{Z},N}$, which are generated by $\tilde{Z}$ and N, are correlated with the random variable $\tilde{A}_X$. Since $X_2 = k\sqrt{\mathcal{P}}\frac{\sqrt{\Theta_2}}{\Theta_1}|\tilde{X}_1|^2$, $(\tilde{X}_1, X_2)$ lies on the paraboloid $\mathcal{U}$, i.e., L_X is a constant which is equal to zero, $\tilde{A}_X$ can be represented by $(\tilde{X}_1, X_2)$ for brevity. Thus, we have

$$\begin{aligned}
\mathcal{I}(\tilde{X}_1, X_2; \tilde{Y}_1, Y_2) &= \mathcal{I}(\tilde{A}_X; \tilde{A}_X + \tilde{A}_{\tilde{Z},N}, L_{\tilde{Z},N}) \\
&= h(\tilde{A}_X + \tilde{A}_{\tilde{Z},N}, L_{\tilde{Z},N}) - h(\tilde{A}_X + \tilde{A}_{\tilde{Z},N}, L_{\tilde{Z},N}|\tilde{A}_X) \\
&= h(\tilde{A}_X + \tilde{A}_{\tilde{Z},N}) + h(L_{\tilde{Z},N}|\tilde{A}_X + \tilde{A}_{\tilde{Z},N}) \\
&\quad - \left(h(\tilde{A}_X + \tilde{A}_{\tilde{Z},N}|\tilde{A}_X) + h(L_{\tilde{Z},N}|\tilde{A}_X, \tilde{A}_X + \tilde{A}_{\tilde{Z},N})\right).
\end{aligned} \tag{D.6}$$

Since the expectations $\mathbb{E}\left[\tilde{Z}\right] = (0,0)$ and $\mathbb{E}\left[N\right] = 0$, and the variances $\mathrm{Var}(\frac{\tilde{Z}}{\sqrt{\mathcal{P}}}) \to 0$ and $\mathrm{Var}(k\frac{N}{\sqrt{\mathcal{P}}}) \to 0$ as $\mathcal{P} \to \infty$, it is easy to see that the noise variable $\tilde{A}_{\tilde{Z},N}$ converges in probability towards $(0,0)$. Thus, $\tilde{A}_X + \tilde{A}_{\tilde{Z},N}$ converges in probability towards $\tilde{A}_X$.

Furthermore, since convergence in probability implies convergence in distribution and the entropy function $h(\cdot)$ is continuous and defined based on the probability distribution of the input random variable [128], we have $h(\tilde{A}_X + \tilde{A}_{\tilde{Z},N}) \to h(\tilde{A}_X)$ as $\mathcal{P} \to \infty$. Similarly, we have the convergence of the random variable, i.e., $\left(L_{\tilde{Z},N}, \tilde{A}_X + \tilde{A}_{\tilde{Z},N}\right) \to \left(L_{\tilde{Z},N}, \tilde{A}_X\right)$, hence the convergence of entropy, i.e., $h(L_{\tilde{Z},N}, \tilde{A}_X + \tilde{A}_{\tilde{Z},N}) \to h(L_{\tilde{Z},N}, \tilde{A}_X)$.

Therefore, the conditional entropy $h(L_{\tilde{Z},N}|\tilde{A}_X + \tilde{A}_{\tilde{Z},N}) \triangleq h(L_{\tilde{Z},N}, \tilde{A}_X + \tilde{A}_{\tilde{Z},N}) - h(\tilde{A}_X + \tilde{A}_{\tilde{Z},N})$ converges to $h(L_{\tilde{Z},N}|\tilde{A}_X) \triangleq h(L_{\tilde{Z},N}, \tilde{A}_X) - h(\tilde{A}_X)$, i.e., $h(L_{\tilde{Z},N}|\tilde{A}_X + \tilde{A}_{\tilde{Z},N}) \to h(L_{\tilde{Z},N}|\tilde{A}_X)$. Similarly, we have $h(L_{\tilde{Z},N}|\tilde{A}_X, \tilde{A}_X + \tilde{A}_{\tilde{Z},N}) \to h(L_{\tilde{Z},N}|\tilde{A}_X, \tilde{A}_X)$. Together

with the fact that $h(L_{\tilde{Z},N}|\tilde{A}_X) = h(L_{\tilde{Z},N}|\tilde{A}_X, \tilde{A}_X)$ [128], we have $h(L_{\tilde{Z},N}|\tilde{A}_X + \tilde{A}_{\tilde{Z},N}) - h(L_{\tilde{Z},N}|\tilde{A}_X, \tilde{A}_X + \tilde{A}_{\tilde{Z},N}) \to 0$ as $\mathcal{P} \to \infty$. Thus, the mutual information in (D.6) can asymptotically be rewritten as

$$\mathcal{I}(\tilde{X}_1, X_2; \tilde{Y}_1, Y_2) = h(\tilde{A}_X) - h(\tilde{A}_X + \tilde{A}_{\tilde{Z},N}|\tilde{A}_X). \tag{D.7}$$

Then we calculate $h(\tilde{A}_X)$ and $h(\tilde{A}_X + \tilde{A}_{\tilde{Z},N}|\tilde{A}_X)$ as follows.

D.1.1.1 $h(\tilde{A}_X)$

Due to the fact that the probability contained in a differential area should not alter under a change of variables, we have

$$|f_{\tilde{X}}(\tilde{x})\mathrm{d}S| = |f_{\tilde{A}_X}(\tilde{a})\mathrm{d}\Sigma|, \tag{D.8}$$

where $\mathrm{d}S = \mathrm{d}u\mathrm{d}v$, $u = \mathrm{Real}\{\tilde{x}\}$, $v = \mathrm{Imag}\{\tilde{x}\}$, $\tilde{a}$ is the PN coordinate system representation of the point $(\tilde{x}_1, x_2)$, $\mathrm{d}\Sigma$ is the differential area on the paraboloid $\mathcal{U}$, $f_{\tilde{A}_X}(\tilde{a})$ and $f_{\tilde{X}}(\tilde{x})$ are the pdfs of $\tilde{A}_X$ and $\tilde{X}$, respectively, and

$$f_{\tilde{X}}(\tilde{x}) = \frac{1}{\pi}\exp\left(-|\tilde{x}|^2\right). \tag{D.9}$$

Assuming that $\mathbf{r} = (\mathrm{Real}\{\tilde{x}_1\}, \mathrm{Imag}\{\tilde{x}_1\}, x_2)$, which is a point on the paraboloid $\mathcal{U}$, and thus, based on (D.2), we have

$$\begin{aligned} &\frac{\partial \mathbf{r}}{\partial u} = (\sqrt{\Theta_1}, 0, 2k\sqrt{\mathcal{P}}\sqrt{\Theta_2}u),\ \frac{\partial \mathbf{r}}{\partial v} = (0, \sqrt{\Theta_1}, 2k\sqrt{\mathcal{P}}\sqrt{\Theta_2}v), \\ &\mathrm{d}\Sigma = \left|\frac{\partial \mathbf{r}}{\partial u} \times \frac{\partial \mathbf{r}}{\partial v}\right| \mathrm{d}u\mathrm{d}v = \Theta_1\sqrt{4\frac{k^2\mathcal{P}\Theta_2}{\Theta_1^2}|\tilde{x}_1|^2 + 1}\ \mathrm{d}u\mathrm{d}v, \end{aligned} \tag{D.10}$$

where $\times$ is the cross product operator. Taking (D.10), (D.9) and $\tilde{x} = \frac{\tilde{x}_1}{\sqrt{\Theta_1}}$ into (D.8), after simplification, we have

$$f_{\tilde{A}_X}(\tilde{a}) = f_{\tilde{A}_X}(\tilde{x}_1, x_2) = \frac{1}{\pi\Theta_1\sqrt{4\frac{k^2\mathcal{P}\Theta_2}{\Theta_1^2}|\tilde{x}_1|^2 + 1}}\exp\left(-\frac{|\tilde{x}_1|^2}{\Theta_1}\right). \tag{D.11}$$

The differential entropy of $\tilde{A}_X$ is derived as

$$h(\tilde{A}_X) = \iint -f_{\tilde{A}_X}(\tilde{a})\log_2\left(f_{\tilde{A}_X}(\tilde{a})\right)\mathrm{d}\Sigma. \tag{D.12}$$

Taking (D.11) and (D.10) into (D.12), we have

$$\begin{aligned} h(\tilde{A}_X) &= \int_{-\infty}^{\infty}\int_{-\infty}^{\infty} -\frac{\exp\left(-\frac{|\tilde{x}_1|^2}{\Theta_1}\right)}{\pi}\log_2\left(\frac{\exp\left(-\frac{|\tilde{x}_1|^2}{\Theta_1}\right)}{\pi\Theta_1\sqrt{4\frac{k^2\mathcal{P}\Theta_2}{\Theta_1^2}|\tilde{x}_1|^2+1}}\right)\mathrm{d}u\mathrm{d}v \\ &\overset{(a)}{=} 2\pi\int_0^{\infty} -\frac{\exp\left(-\frac{r^2}{\Theta_1}\right)}{\pi\Theta_1}\log_2\left(\frac{\exp\left(-\frac{r^2}{\Theta_1}\right)}{\pi\Theta_1\sqrt{4\frac{k^2\mathcal{P}\Theta_2}{\Theta_1^2}r^2+1}}\right)r\mathrm{d}r \\ &= \log_2(\pi e\Theta_1) + \frac{1}{2\log(2)}\exp\left(\frac{\Theta_1}{4k^2\mathcal{P}\Theta_2}\right)\mathrm{Ei}\left(\frac{\Theta_1}{4k^2\mathcal{P}\Theta_2}\right), \end{aligned} \tag{D.13}$$

where (a) is because of the polar transformation.

D.1.1.2 Asymptotic $h(\tilde{A}_X + \tilde{A}_{\tilde{Z},N}|\tilde{A}_X)$

For a given value of $\tilde{A}_X$, based on the definition of the PN coordinate system, the random variable $\tilde{A}_X + \tilde{A}_{\tilde{Z},N}$ is treated as the projection of the three-dimensional circular symmetric Gaussian noise, i.e., $(\frac{\tilde{Z}}{\sqrt{\mathcal{P}}}, k\frac{N}{\sqrt{\mathcal{P}}})$ shifted by $\tilde{A}_X$, on the parabolic $\mathcal{U}$ by the normal vectors of it.

As $\mathcal{P}\to\infty$, $\tilde{A}_X + \tilde{A}_{\tilde{Z},N}$ converges in probability toward $\tilde{A}_X$, thus, for a given value of $\tilde{A}_X$, the effective range of the random variable $\tilde{A}_X + \tilde{A}_{\tilde{Z},N}$ on the paraboloid $\mathcal{U}$, is very small, which is close to the tangent plane of $\mathcal{U}$ at the point $\tilde{A}_X$. Therefore, the random variable $\tilde{A}_X + \tilde{A}_{\tilde{Z},N}$ converges in probability toward the random variable generated by the projection of the three-dimensional circular symmetric Gaussian noise on the tangent plane of $\mathcal{U}$ at the point $\tilde{A}_X$ by the normal vector of the point $\tilde{A}_X$, which is the well-known two-dimensional complex Gaussian random variable with variance $\sigma_{\mathrm{cov}}^2/\mathcal{P}$. Therefore, given $\tilde{A}_X$, the entropy $h(\tilde{A}_X + \tilde{A}_{\tilde{Z},N})$ is approaching to $\log_2(\pi e\sigma_{\mathrm{cov}}^2/\mathcal{P})$ which does not rely on $\tilde{A}_X$. Thus, as $\mathcal{P}\to\infty$, the asymptotic conditional entropy is

$$h(\tilde{A}_X + \tilde{A}_{\tilde{Z},N}|\tilde{A}_X) = \mathbb{E}_{\tilde{A}_X}\left[h(\tilde{A}_X + \tilde{A}_{\tilde{Z},N}|\tilde{A}_X = \tilde{a}_X)\right] \approx \log_2\left(\frac{\pi e\sigma_{\mathrm{cov}}^2}{\mathcal{P}}\right). \tag{D.14}$$

D.1.1.3 Asymptotic $\mathcal{I}(\sqrt{\mathcal{P}}X; \tilde{Y}_1, Y_2)$

Taking (D.13) and (D.14) into (D.7), (5.16a) is obtained.

D.1.2 Proof of (5.16b)

Based on the power series expansion of the exponential integral function [132]

$$\mathrm{Ei}(x) = -\gamma - \ln x - \sum_{n=1}^{\infty} \frac{(-x)^n}{n\, n!},\ x > 0, \tag{D.15}$$

where $\gamma \approx 0.5772$ is Euler's constant, as $\mathcal{P}$ is sufficiently large, we have

$$\lim_{\mathcal{P}\to\infty} \exp\left(\frac{\Theta_1\sigma_{\mathrm{rec}}^2}{2\sigma_{\mathrm{cov}}^2\mathcal{P}\Theta_2}\right) \mathrm{Ei}\left(\frac{\Theta_1\sigma_{\mathrm{rec}}^2}{2\sigma_{\mathrm{cov}}^2\mathcal{P}\Theta_2}\right) = -\gamma + \ln\left(\frac{2\sigma_{\mathrm{cov}}^2\mathcal{P}\Theta_2}{\Theta_1\sigma_{\mathrm{rec}}^2}\right). \tag{D.16}$$

Substituting (D.16) into (5.16a), (5.16b) is obtained.

Appendix E

This appendix contains the proofs needed in Chapter 6.

E.1 Proof of Proposition 16

Based on (6.22), in order to calculate the BER for the forward IT, we need to calculate $\Pr\{\mathcal{P}_2 > \mathcal{P}_0\}$ and $\Pr\{\mathcal{P}_2 > \mathcal{P}_3\}$ as follows:

$$\begin{aligned}
&\Pr\{\mathcal{P}_2 > \mathcal{P}_0\} \overset{(a)}{=} 1 - \mathbb{E}_{g_{21},q_2}\left[\int_0^\infty \exp\left(-\mu_1 x\right)\mu_2 \exp\left(-\mu_2 x\right)\mathrm{d}x\right] \\
&= 1 - \mathbb{E}_{g_{21},q_2}\left[\frac{\mu_2}{\mu_1+\mu_2}\right] \\
&= 1 - \frac{1}{\rho}\left(\frac{d_{22}d_t}{d_{11}}\right)^\lambda \exp\left(\frac{d_t^\lambda}{\rho}\left(\left(\frac{d_{22}}{d_{21}}\right)^\lambda + \left(\frac{d_{22}}{d_{11}}\right)^\lambda\right)\right)\Gamma\left(0,\ \frac{d_t^\lambda}{\rho}\left(\frac{d_{22}}{d_{21}}\right)^\lambda + \left(\frac{d_{22}}{d_{11}}\right)^\lambda\right),
\end{aligned} \tag{E.1}$$

where (a) is because given g_{21} and q_2, both $|f_{11}|^2$ and $\left|f_{21} + \sqrt{\rho} f_{22} g_{21} q_2\right|^2$ follow exponential distribution with parameters $\mu_1 = 1 \Big/ \left(\frac{1}{d_{11}^\lambda}\right)$ and $\mu_2 = 1 \Big/ \left(\frac{1}{d_{21}^\lambda} + \frac{\rho|g_{21}|^2}{(d_{22}d_t)^\lambda}\right)$, respectively.

Similarly, we have

$$\Pr\{\mathcal{P}_2 > \mathcal{P}_3\} = 1 - \left(\frac{d_{22}^\lambda}{d_{12}^\lambda + d_{22}^\lambda} + \frac{d_t^\lambda}{\rho}\frac{\frac{1}{d_{11}^\lambda d_{22}^\lambda} - \frac{1}{d_{21}^\lambda d_{12}^\lambda}}{\left(\frac{1}{d_{12}^\lambda}+\frac{1}{d_{22}^\lambda}\right)^2}\exp\left(\frac{d_t^\lambda}{\rho}\frac{\frac{1}{d_{11}^\lambda}+\frac{1}{d_{21}^\lambda}}{\frac{1}{d_{12}^\lambda}+\frac{1}{d_{22}^\lambda}}\right)\Gamma\left(0,\ \frac{d_t^\lambda}{\rho}\frac{\frac{1}{d_{11}^\lambda}+\frac{1}{d_{21}^\lambda}}{\frac{1}{d_{12}^\lambda}+\frac{1}{d_{22}^\lambda}}\right)\right). \tag{E.2}$$

Taking (E.1) and (E.2) into (6.22), the BER for the forward IT is obtained.

E.2 Proof of Proposition 18

Using the fact that $\mathbb{E}\left[|X+YZ|^2\right] = \mathbb{E}\left[|X|^2\right] + \mathbb{E}\left[|Y|^2\right]\mathbb{E}\left[|Z|^2\right]$ if X, Y and Z are independent random variables and have zero mean, we thus have

$$\mathbb{E}_{f_{11},q_2}[\mathcal{P}_0] = \eta(1-\rho)\mathcal{P}\frac{1}{d_{11}^{\lambda}}, \tag{E.3}$$

$$\mathbb{E}_{f_{11},f_{12},f_{21},f_{22},g_{21},q_2}[\mathcal{P}_1] = \eta(1-\rho)\mathcal{P}\left(\frac{1}{d_{11}^{\lambda}}+\frac{1}{d_{21}^{\lambda}}+\rho\left(\frac{1}{d_{12}^{\lambda}}\frac{1}{d_t^{\lambda}}+\frac{1}{d_{22}^{\lambda}}\frac{1}{d_t^{\lambda}}\right)\right), \tag{E.4}$$

$$\mathbb{E}_{f_{21},f_{22},g_{21},q_2}[\mathcal{P}_2] = \eta(1-\rho)\mathcal{P}\left(\frac{1}{d_{21}^{\lambda}}+\rho\frac{1}{d_{22}^{\lambda}}\frac{1}{d_t^{\lambda}}\right), \tag{E.5}$$

$$\mathbb{E}_{f_{11},f_{12},g_{21},q_2}[\mathcal{P}_3] = \eta(1-\rho)\mathcal{P}\left(\frac{1}{d_{11}^{\lambda}}+\rho\frac{1}{d_{12}^{\lambda}}\frac{1}{d_t^{\lambda}}\right), \tag{E.6}$$

$$\mathbb{E}_{f_{21},f_{22},g_{21},q_2}[\mathcal{P}_{\text{eh}}] = \mathcal{P}_2/(1-\rho). \tag{E.7}$$

Taking these results into (6.27), the expected ETR is obtained.

E.3 Proof of Proposition 19

Given g_{21} and q_2, then $\mathcal{P}_0/(\eta\mathcal{P})$ and $\mathcal{P}_{\text{eh}}/(\eta\mathcal{P})$ are independent with each other and follow exponential distribution with mean parameters $(1-\rho)\frac{1}{d_{11}^{\lambda}}$ and $\left(\frac{1}{d_{21}^{\lambda}}+\rho\frac{1}{d_{22}^{\lambda}}\frac{1}{d_t^{\lambda}}|g_{21}|^2\right)$, respectively. Thus, we have

$$\begin{aligned}
&\Pr\left\{\frac{T}{N}\left(\mathcal{P}_0+\mathcal{P}_{\text{eh}}\right)<\mathcal{E}_0\right\} = \mathbb{E}_{g_{21},q_2}\left[\Pr\left\{\frac{(\mathcal{P}_0+\mathcal{P}_{\text{eh}})}{\eta\mathcal{P}}<\frac{N\mathcal{E}_0}{\eta\mathcal{P}T}\middle| g_{21},q_2\right\}\right]\\
&=1-\mathbb{E}_{g_{21}}\left[\frac{(1-\rho)\frac{1}{d_{11}^{\lambda}}\exp\left(-\frac{\Xi}{(1-\rho)\frac{1}{d_{11}^{\lambda}}}\right)-\left(\frac{1}{d_{21}^{\lambda}}+\rho\frac{1}{d_{22}^{\lambda}}\frac{1}{d_t^{\lambda}}|g_{21}|^2\right)\exp\left(-\frac{\Xi}{\left(\frac{1}{d_{21}^{\lambda}}+\rho\frac{1}{d_{22}^{\lambda}}\frac{1}{d_t^{\lambda}}|g_{21}|^2\right)}\right)}{(1-\rho)\frac{1}{d_{11}^{\lambda}}-\left(\frac{1}{d_{21}^{\lambda}}+\rho\frac{1}{d_{22}^{\lambda}}\frac{1}{d_t^{\lambda}}|g_{21}|^2\right)}\right]\\
&= M\left((1-\rho)\frac{1}{d_{11}^{\lambda}},0,\frac{1}{d_{21}^{\lambda}},\rho\frac{1}{d_{22}^{\lambda}}\frac{1}{d_t^{\lambda}}\right).
\end{aligned} \tag{E.8}$$

where $\Xi \triangleq \frac{N\mathcal{E}_0}{\eta\mathcal{P}T}$, and function $M(\cdot,\cdot,\cdot,\cdot)$ is defined in (6.34). Similarly, we can obtain $\Pr\left\{\frac{T}{N}\left(\mathcal{P}_0+\mathcal{P}_2\right)<\mathcal{E}_0\right\}$, $\Pr\left\{\frac{T}{N}\left(\mathcal{P}_3+\mathcal{P}_{\text{eh}}\right)<\mathcal{E}_0\right\}$, $\Pr\left\{\frac{T}{N}\left(\mathcal{P}_3+\mathcal{P}_2\right)<\mathcal{E}_0\right\}$, $\Pr\left\{\frac{T}{N}\mathcal{P}_1<\mathcal{E}_0\right\}$. Taking these results and (6.3), (E.8), and (6.34) into (6.32), the energy-outage probability is obtained.

Bibliography

[1] V. Gungor and G. Hancke, "Industrial wireless sensor networks: Challenges, design principles, and technical approaches," *IEEE Trans. Ind. Electron.*, vol. 56, no. 10, pp. 4258–4265, Oct. 2009. (cited on pages xxvii, 5, 17, and 19)

[2] X. Lu, P. Wang, D. Niyato, D. I. Kim, and Z. Han, "Wireless networks with RF energy harvesting: A contemporary survey," *IEEE Commun. Surveys Tuts.*, vol. 17, no. 2, pp. 757–789, Second quarter 2015. (cited on pages xxvii, 9, 13, 25, 65, and 81)

[3] E. Dahlman, G. Mildh, S. Parkvall, J. Peisa, J. Sachs, Y. Selén, and J. Sköld, "5G wireless access: Requirements and realization," *IEEE Commun. Mag.*, vol. 52, no. 12, pp. 42–47, Dec. 2014. (cited on page 1)

[4] S. Sudevalayam and P. Kulkarni, "Energy harvesting sensor nodes: Survey and implications," *IEEE Commun. Surveys Tuts.*, vol. 13, no. 3, pp. 443–461, Third Quarter 2011. (cited on pages 1, 5, 14, 32, and 54)

[5] R. Roman, P. Najera, and J. Lopez, "Securing the internet of things," *Computer*, vol. 44, no. 9, pp. 51–58, Sep. 2011. (cited on page 2)

[6] X. Zhou, L. Song, and Y. Zhang, *Physical Layer Security in Wireless Communications*. CRC Press, 2013. (cited on pages 2 and 20)

[7] R. Zhang and C. K. Ho, "MIMO broadcasting for simultaneous wireless information and power transfer," *IEEE Trans. Wireless Commun.*, vol. 12, no. 5, pp. 1989–2001, May 2013. (cited on pages 3, 7, 10, 11, 12, 13, 14, 25, 65, 72, 73, 74, 75, 81, and 82)

[8] A. Al-Fuqaha, M. Guizani, M. Mohammadi, M. Aledhari, and M. Ayyash, "Internet of Things: A survey on enabling technologies, protocols, and applications," *IEEE Commun. Surveys Tuts.*, vol. 17, no. 4, pp. 2347–2376, Fourth Quarter 2015. (cited on pages 4 and 22)

[9] H. Mahdavi-Doost and R. Yates, "Energy harvesting receivers: Finite battery capacity," in *Proc. IEEE ISIT*, Jul. 2013, pp. 1799–1803. (cited on pages 5 and 34)

[10] Z. A. Eu, H.-P. Tan, and W. K. Seah, "Design and performance analysis of MAC schemes for wireless sensor networks powered by ambient energy harvesting," *Ad Hoc Networks*, vol. 9, no. 3, pp. 300–323, 2011. (cited on pages 5, 34, and 43)

[11] C. Huang, R. Zhang, and S. Cui, "Throughput maximization for the Gaussian relay channel with energy harvesting constraints," *IEEE J. Sel. Areas Commun.*, vol. 31, no. 8, pp. 1469–1479, Aug. 2013. (cited on pages 5 and 34)

[12] D. Niyato, E. Hossain, and A. Fallahi, "Sleep and wakeup strategies in solar-powered wireless sensor/mesh networks: Performance analysis and optimization," *IEEE Trans. Mobile Comput.*, vol. 6, no. 2, pp. 221–236, Feb. 2007. (cited on pages 6, 18, and 35)

[13] J. Lei, R. Yates, and L. Greenstein, "A generic model for optimizing single-hop transmission policy of replenishable sensors," *IEEE Trans. Wireless Commun.*, vol. 8, no. 2, pp. 547–551, Feb. 2009. (cited on pages 6, 18, and 35)

[14] C. K. Ho and R. Zhang, "Optimal energy allocation for wireless communications with energy harvesting constraints," *IEEE Trans. Signal Process*, vol. 60, no. 9, pp. 4808–4818, Sep. 2012. (cited on pages 6 and 35)

[15] A. Seyedi and B. Sikdar, "Energy efficient transmission strategies for body sensor networks with energy harvesting," *IEEE Trans. Commun.*, vol. 58, no. 7, pp. 2116–2126, Jul. 2010. (cited on page 6)

[16] S. Zhang, A. Seyedi, and B. Sikdar, "An analytical approach to the design of energy harvesting wireless sensor nodes," *IEEE Trans. Wireless Commun.*, vol. 12, no. 8, pp. 4010–4024, Aug. 2013. (cited on page 6)

[17] S. Luo, R. Zhang, and T. J. Lim, "Optimal save-then-transmit protocol for energy harvesting wireless transmitters," *IEEE Trans. Wireless Commun.*, vol. 12, no. 3, pp. 1196–1207, Mar. 2013. (cited on pages 6, 7, 24, 32, 35, 43, and 44)

[18] R. Morsi, D. Michalopoulos, and R. Schober, "On-off transmission policy for wireless powered communication with energy storage," in *Proc. Asilomar Conference on Signals, Systems and Computers*, Nov. 2014, pp. 1676–1682. (cited on pages 6 and 35)

[19] Y. Dong, F. Farnia, and A. Ozgur, "Near optimal energy control and approximate capacity of energy harvesting communication," *IEEE J. Sel. Areas Commun.*, vol. 33, no. 3, pp. 540–557, Mar. 2015. (cited on pages 6 and 35)

[20] N. Michelusi, L. Badia, and M. Zorzi, "Optimal transmission policies for energy harvesting devices with limited state-of-charge knowledge," *IEEE Trans. Commun.*, vol. 62, no. 11, pp. 3969–3982, Nov. 2014. (cited on page 6)

[21] O. Ozel, K. Tutuncuoglu, J. Yang, S. Ulukus, and A. Yener, "Transmission with energy harvesting nodes in fading wireless channels: Optimal policies," *IEEE J. Sel. Areas Commun.*, vol. 29, no. 8, pp. 1732–1743, Sep. 2011. (cited on page 7)

[22] J. Yang and S. Ulukus, "Transmission completion time minimization in an energy harvesting system," in *Proc. CISS*, Mar. 2010, pp. 1–6. (cited on page 7)

[23] J. Yang and S. Ulukus, "Delay-minimal transmission for energy constrained wireless communications," in *Proc. IEEE ICC*, May 2008, pp. 3531–3535. (cited on page 7)

[24] Y. Mao, G. Yu, and Z. Zhang, "On the optimal transmission policy in hybrid energy supply wireless communication systems," *IEEE Trans. Wireless Commun.*, vol. 13, no. 11, pp. 6422–6430, Nov. 2014. (cited on page 7)

[25] N. Michelusi and M. Zorzi, "Optimal random multiaccess in energy harvesting wireless sensor networks," in *Proc. IEEE ICC*, Jun. 2013, pp. 463–468. (cited on page 7)

[26] X. Zhou, R. Zhang, and C. K. Ho, "Wireless information and power transfer: Architecture design and rate-energy tradeoff," *IEEE Trans. Commun.*, vol. 61, no. 11, pp. 4754–4767, Nov. 2013. (cited on pages 7, 10, 13, 14, 25, 50, 65, 75, 86, 87, and 108)

[27] H. Ju and R. Zhang, "Throughput maximization in wireless powered communication networks," *IEEE Trans. Wireless Commun.*, vol. 13, no. 1, pp. 418–428, Jan. 2014. (cited on pages 7, 13, 14, 25, and 65)

[28] I. Krikidis, "Simultaneous information and energy transfer in large-scale networks with/without relaying," *IEEE Trans. Commun.*, vol. 62, no. 3, pp. 900–912, Mar. 2014. (cited on page 7)

[29] W. Liu, X. Zhou, S. Durrani, and P. Popovski, "Secure communication with a wireless-powered friendly jammer," *IEEE Trans. Wireless Commun.*, vol. 15, no. 1, pp. 401–415, Jan. 2016. (cited on pages 8 and 26)

[30] W. Liu, X. Zhou, S. Durrani, H. Mehrpouyan, and S. D. Blostein, "Energy harvesting wireless sensor networks: Delay analysis considering energy costs of sensing and transmission," *IEEE Trans. Wireless Commun.*, vol. 15, no. 7, pp. 4635–4650, Jul. 2016. (cited on pages 8, 20, and 25)

[31] A. A. Nasir, X. Zhou, S. Durrani, and R. A. Kennedy, "Wireless-powered relays in cooperative communications: Time-switching relaying protocols and throughput analysis," *IEEE Trans. Commun.*, vol. 63, no. 5, pp. 1607–1622, May 2015. (cited on pages 8, 11, 24, 25, 32, 35, 43, 44, and 50)

[32] B. Clerckx and E. Bayguzina, "Waveform design for wireless power transfer," *IEEE Trans. Signal Process.*, vol. 64, no. 23, pp. 6313–6328, Dec. 2016. (cited on pages 10, 11, and 12)

[33] E. Boshkovska, D. W. K. Ng, N. Zlatanov, and R. Schober, "Practical non-linear energy harvesting model and resource allocation for SWIPT systems," *IEEE Commun. Lett.*, vol. 19, no. 12, pp. 2082–2085, Dec. 2015. (cited on page 10)

[34] T. Wu and H.-C. Yang, "On the performance of overlaid wireless sensor transmission with RF energy harvesting," *IEEE J. Sel. Areas Commun.*, vol. 33, no. 8, pp. 1693–1705, Aug. 2015. (cited on pages 10, 24, 32, 35, 39, 43, 44, 72, and 81)

[35] W. Liu, X. Zhou, S. Durrani, and P. Popovski, "SWIPT with practical modulation and RF energy harvesting sensitivity," in *Proc. ICC*, May 2016, pp. 1–7. (cited on pages 10, 27, and 86)

[36] K. Huang and V. K. N. Lau, "Enabling wireless power transfer in cellular networks: Architecture, modeling and deployment," *IEEE Trans. Wireless Commun.*, vol. 13, no. 2, pp. 902–912, Feb. 2014. (cited on pages 10, 13, 14, and 111)

[37] J. Guo, S. Durrani, X. Zhou, and H. Yanikomeroglu, "Outage probability of ad hoc networks with wireless information and power transfer," *IEEE Wireless Commun. Lett.*, vol. 4, no. 4, pp. 409–412, Aug. 2015. (cited on page 11)

[38] J. Xu and R. Zhang, "Energy beamforming with one-bit feedback," *IEEE Trans. Signal Process.*, vol. 62, no. 20, pp. 5370–5381, Oct. 2014. (cited on pages 11 and 14)

[39] S. Lee and R. Zhang, "Distributed energy beamforming with one-bit feedback," in *Proc. IEEE WCNC*, Apr. 2016, pp. 1–6. (cited on pages 11 and 14)

[40] Z. Wang, L. Duan, and R. Zhang, "Adaptively directional wireless power transfer for large-scale sensor networks," *IEEE J. Sel. Areas Commun.*, vol. 34, no. 5, pp. 1785–1800, May 2016. (cited on page 11)

[41] S. Bi and R. Zhang, "Placement optimization of energy and information access points in wireless powered communication networks," *IEEE Trans. Wireless Commun.*, vol. 15, no. 3, pp. 2351–2364, Mar. 2016. (cited on page 11)

[42] Y. Zeng, H. Chen, and R. Zhang, "Bidirectional wireless information and power transfer with a helping relay," *IEEE Commun. Lett.*, vol. 20, no. 5, pp. 862–865, May 2016. (cited on page 11)

[43] I. Krikidis, S. Timotheou, S. Nikolaou, G. Zheng, D. W. K. Ng, and R. Schober, "Simultaneous wireless information and power transfer in modern communication systems," *IEEE Commun. Mag.*, vol. 52, no. 11, pp. 104–110, Nov 2014. (cited on page 12)

[44] X. Zhou, J. Guo, S. Durrani, and I. Krikidis, "Performance of maximum ratio transmission in ad hoc networks with wireless energy harvesting," *IEEE Wireless Commun. Lett.*, vol. 4, no. 5, pp. 529–532, Oct. 2015. (cited on page 12)

[45] S. Luo, J. Xu, T. J. Lim, and R. Zhang, "Capacity region of miso broadcast channel for simultaneous wireless information and power transfer," *IEEE Trans. Commun.*, vol. 63, no. 10, pp. 3856–3868, Oct. 2015. (cited on page 12)

[46] X. Zhou, C. K. Ho, and R. Zhang, "Wireless information and power transfer in multiuser OFDM systems," *IEEE Trans. Wireless Commun.*, vol. 13, no. 4, pp. 2282–2294, Apr. 2014. (cited on page 12)

[47] K. Huang and E. Larsson, "Simultaneous information and power transfer for broadband wireless systems," *IEEE Trans. Signal Process.*, vol. 61, no. 23, pp. 5972–5986, Dec. 2013. (cited on page 12)

[48] L. Liu, R. Zhang, and K.-C. Chua, "Wireless information and power transfer: A dynamic power splitting approach," *IEEE Trans. Commun.*, vol. 61, no. 9, pp. 3990–4001, Sep. 2013. (cited on pages 12, 13, 72, 73, and 74)

[49] R. Morsi, D. Michalopoulos, and R. Schober, "Multi-user scheduling schemes for simultaneous wireless information and power transfer over fading channels," *IEEE Trans. Wireless Commun.*, vol. 14, no. 4, pp. 1967–1982, Apr. 2015. (cited on pages 12 and 74)

[50] S. Bi, Y. Zeng, and R. Zhang, "Wireless powered communication networks: An overview," *IEEE Wireless Commun. Mag.*, vol. 23, no. 2, pp. 10–18, Apr. 2016. (cited on page 13)

[51] H. Ju and R. Zhang, "Optimal resource allocation in full-duplex wireless-powered communication network," *IEEE Trans. Commun.*, vol. 62, no. 10, pp. 3528–3540, Oct. 2014. (cited on page 13)

[52] S. Lee, R. Zhang, and K. Huang, "Opportunistic wireless energy harvesting in cognitive radio networks," *IEEE Trans. Wireless Commun.*, vol. 12, no. 9, pp. 4788–4799, Sep. 2013. (cited on pages 13 and 152)

[53] Y. Zeng and R. Zhang, "Optimized training design for wireless energy transfer," *IEEE Trans. Commun.*, vol. 63, no. 2, pp. 536–550, Feb. 2015. (cited on page 14)

[54] Y. Zeng and R. Zhang, "Optimized training for net energy maximization in multi-antenna wireless energy transfer over frequency-selective channel," *IEEE Trans. Commun.*, vol. 63, no. 6, pp. 2360–2373, Jun. 2015. (cited on page 14)

[55] J. Xu and R. Zhang, "A general design framework for MIMO wireless energy transfer with limited feedback," *IEEE Trans. Signal Process.*, vol. 64, no. 10, pp. 2475–2488, May 2016. (cited on page 14)

[56] K. Huang and X. Zhou, "Cutting the last wires for mobile communications by microwave power transfer," *IEEE Commun. Mag.*, vol. 53, no. 6, pp. 86–93, 2015. (cited on pages 14, 21, and 131)

[57] C. Boyer and S. Roy, "Backscatter communication and RFID: Coding, energy, and MIMO analysis," *IEEE Trans. Commun.*, vol. 62, no. 3, pp. 770–785, Mar. 2014. (cited on pages 14 and 18)

[58] V. Chawla and D. S. Ha, "An overview of passive RFID," *IEEE Commun. Mag.*, vol. 45, no. 9, pp. 11–17, Sep. 2007. (cited on page 15)

[59] K. Sohraby, D. Minoli, and T. Znati, *Wireless Sensor Networks: Technology, Protocols, and Applications*. Wiley, 2007. (cited on page 16)

[60] H. Yetgin, K. T. K. Cheung, M. El-Hajjar, and L. Hanzo, "A survey of network lifetime maximization techniques," *IEEE Commun. Surveys Tuts.*, vol. 19, no. 2, pp. 828–854, Second-quarter 2017. (cited on page 16)

[61] V. Raghunathan, S. Ganeriwal, and M. Srivastava, "Emerging techniques for long lived wireless sensor networks," *IEEE Commun. Mag.*, vol. 44, no. 4, pp. 108–114, Apr. 2006. (cited on pages 18, 32, and 43)

[62] W. Liu, K. Huang, X. Zhou, and S. Durrani, "Full-duplex backscatter interference networks based on time-hopping spread spectrum," *IEEE Trans. Wireless Commun.*, vol. 16, no. 7, pp. 4361–4377, Jul. 2017. (cited on pages 18 and 30)

[63] S. Mao, M. H. Cheung, and V. Wong, "Joint energy allocation for sensing and transmission in rechargeable wireless sensor networks," *IEEE Trans. Veh. Technol.*, vol. 63, no. 6, pp. 2862–2875, Jul. 2014. (cited on page 18)

[64] M. Costa, M. Codreanu, and A. Ephremides, "Age of information with packet management," in *Proc. IEEE ISIT*, Jun. 2014, pp. 1583–1587. (cited on pages 20 and 24)

[65] S. Kaul, R. Yates, and M. Gruteser, "Real-time status: How often should one update?" in *Proc. IEEE INFOCOM*, Mar. 2012, pp. 2731–2735. (cited on pages 20, 24, and 35)

[66] Y. Sun, E. Uysal-Biyikoglu, R. Yates, C. E. Koksal, and N. B. Shroff, "Update or wait: How to keep your data fresh," in *Proc. IEEE INFOCOM*, Apr. 2016, pp. 1–9. (cited on page 20)

[67] M. Bloch and J. Barros, *Physical-Layer Security: From Information Theory to Security Engineering*. Cambridge University Press, 2011. (cited on page 20)

[68] A. Mukherjee, S. Fakoorian, J. Huang, and A. L. Swindlehurst, "Principles of physical layer security in multiuser wireless networks: A survey," *IEEE Commun. Surveys Tuts.*, vol. 16, no. 3, pp. 1550–1573, Aug. 2014. (cited on page 20)

[69] L. Dong, Z. Han, A. P. Petropulu, and H. V. Poor, "Amplify-and-forward based cooperation for secure wireless communications," in *Proc. IEEE ICASSP*, Apr. 2009, pp. 2613–2616. (cited on page 20)

[70] V. Aggarwal, L. Sankar, A. Calderbank, and H. Poor, "Secrecy capacity of a class of orthogonal relay eavesdropper channels," *EURASIP J. Wireless Commun. Netw.*, vol. 2009, Jul. 2009. (cited on page 20)

[71] J. Li, A. Petropulu, and S. Weber, "On cooperative relaying schemes for wireless physical layer security," *IEEE Trans. Signal Process.*, vol. 59, no. 10, pp. 4985–4997, Oct. 2011. (cited on page 20)

[72] S. Goel and R. Negi, "Guaranteeing secrecy using artificial noise," *IEEE Trans. Wireless Commun.*, vol. 7, no. 6, pp. 2180–2189, Jun. 2008. (cited on page 20)

[73] E. Tekin and A. Yener, "The general gaussian multiple-access and two-way wiretap channels: Achievable rates and cooperative jamming," *IEEE Trans. Inform. Theory*, vol. 54, no. 6, pp. 2735–2751, Jun. 2008. (cited on page 20)

[74] O. Simeone and P. Popovski, "Secure communications via cooperating base stations," *IEEE Commun. Lett.*, vol. 12, no. 3, pp. 188–190, Mar. 2008. (cited on page 20)

[75] I. Krikidis, J. Thompson, and S. McLaughlin, "Relay selection for secure cooperative networks with jamming," *IEEE Trans. Wireless Commun.*, vol. 8, no. 10, pp. 5003–5011, Oct. 2009. (cited on page 20)

[76] G. Zheng, L.-C. Choo, and K.-K. Wong, "Optimal cooperative jamming to enhance physical layer security using relays," *IEEE Trans. Signal Process.*, vol. 59, no. 3, pp. 1317–1322, Apr. 2011. (cited on page 20)

[77] R. Zhang, L. Song, Z. Han, and B. Jiao, "Physical layer security for two-way untrusted relaying with friendly jammers," *IEEE Trans. Veh. Technol.*, vol. 61, no. 8, pp. 3693–3704, Oct. 2012. (cited on page 20)

[78] L. Dong, Z. Han, A. P. Petropulu, and H. V. Poor, "Improving wireless physical layer security via cooperating relays," *IEEE Trans. Signal Process.*, vol. 58, no. 3, pp. 1875–1888, Mar. 2010. (cited on pages 20 and 65)

[79] J. Huang and A. L. Swindlehurst, "Cooperative jamming for secure communications in MIMO relay networks," *IEEE Trans. Signal Process.*, vol. 59, no. 10, pp. 4871–4884, Oct. 2011. (cited on page 20)

[80] S. Fakoorian and A. L. Swindlehurst, "Solutions for the MIMO Gaussian wiretap channel with a cooperative jammer," *IEEE Trans. Signal Process.*, vol. 59, no. 10, pp. 5013–5022, Oct. 2011. (cited on page 20)

[81] J. Yang, I.-M. Kim, and D. I. Kim, "Optimal cooperative jamming for multiuser broadcast channel with multiple eavesdroppers," *IEEE Trans. Wireless Commun.*, vol. 12, no. 6, pp. 2840–2852, Jun. 2013. (cited on page 20)

[82] H. Xing, L. Liu, and R. Zhang, "Secrecy wireless information and power transfer in fading wiretap channel," *IEEE Trans. Veh. Technol.*, vol. 65, no. 1, pp. 180–190, Jan. 2016. (cited on page 20)

[83] L. Liu, R. Zhang, and K.-C. Chua, "Secrecy wireless information and power transfer with MISO beamforming," *IEEE Trans. Signal Process.*, vol. 62, no. 7, pp. 1850–1863, Apr. 2014. (cited on page 20)

[84] R. Feng, Q. Li, Q. Zhang, and J. Qin, "Robust secure transmission in MISO simultaneous wireless information and power transfer system," *IEEE Trans. Veh. Technol.*, vol. 64, no. 1, pp. 400–405, Jan. 2015. (cited on page 20)

[85] D. Ng, E. Lo, and R. Schober, "Robust beamforming for secure communication in systems with wireless information and power transfer," *IEEE Trans. Wireless Commun.*, vol. 13, no. 8, pp. 4599–4615, Aug. 2014. (cited on page 20)

[86] A. Bletsas, S. Siachalou, and J. N. Sahalos, "Anti-collision backscatter sensor networks," *IEEE Trans. Wireless Commun.*, vol. 8, no. 10, pp. 5018–5029, 2009. (cited on page 21)

[87] J. Kimionis, A. Bletsas, and J. N. Sahalos, "Increased range bistatic scatter radio," *IEEE Trans. Commun.*, vol. 62, no. 3, pp. 1091–1104, 2014. (cited on page 21)

[88] A. Alma'aitah, H. S. Hassanein, and M. Ibnkahla, "Tag modulation silencing: Design and application in RFID anti-collision protocols," *IEEE Trans. Commun.*, vol. 62, no. 11, pp. 4068–4079, 2014. (cited on page 21)

[89] J. Wang, H. Hassanieh, D. Katabi, and P. Indyk, "Efficient and reliable low-power backscatter networks," in *Proc. ACM SIGCOMM*, 2012, pp. 61–72. (cited on page 21)

[90] K. Han and K. Huang, "Wirelessly powered backscatter communication networks: Modeling, coverage and capacity," vol. 16, no. 4, pp. 2548–2561, Apr. 2017. (cited on page 21)

[91] S. Bi, C. Ho, and R. Zhang, "Wireless powered communication: opportunities and challenges," *IEEE Commun. Mag.*, vol. 53, no. 4, pp. 117–125, Apr. 2015. (cited on pages 21 and 131)

[92] G. Yang, C. K. Ho, and Y. L. Guan, "Multi-antenna wireless energy transfer for backscatter communication systems," *IEEE J. Sel. Areas Commun.*, vol. 33, no. 12, pp. 2974–2987, 2015. (cited on page 21)

[93] S. Lee, L. Liu, and R. Zhang, "Collaborative wireless energy and information transfer in interference channel," *IEEE Trans. Wireless Commun.*, vol. 14, no. 1, pp. 545–557, 2015. (cited on page 21)

[94] V. Liu, A. Parks, V. Talla, S. Gollakota, D. Wetherall, and J. R. Smith, "Ambient backscatter: Wireless communication out of thin air," in *Proc. ACM SIGCOMM*, Jun. 2013, pp. 39–50. (cited on page 21)

[95] V. Liu, V. Talla, and S. Gollakota, "Enabling instantaneous feedback with full-duplex backscatter," in *Proc. ACM MobiCom*, 2014, pp. 67–78. (cited on pages 22 and 29)

[96] M. Z. Win, R. A. Scholtz *et al.*, "Ultra-wide bandwidth time-hopping spread-spectrum impulse radio for wireless multiple-access communications," *IEEE Trans. Commun.*, vol. 48, no. 4, pp. 679–689, 2000. (cited on pages 22 and 112)

[97] D. Dardari, R. D. Errico, C. Roblin, A. Sibille, and M. Z. Win, "Ultrawide bandwidth RFID: The next generation?" *Proc. IEEE*, vol. 98, no. 9, pp. 1570–1582, Sep. 2010. (cited on page 22)

[98] A. Sabharwal, P. Schniter, D. Guo, D. Bliss, S. Rangarajan, and R. Wichman, "In-band full-duplex wireless: Challenges and opportunities," *IEEE J. Sel. Areas Commun.*, vol. 32, no. 9, pp. 1637–1652, Sept 2014. (cited on page 22)

[99] W. Liu, X. Zhou, S. Durrani, H. Mehrpouyan, and S. D. Blostein, "Performance of wireless-powered sensor transmission considering energy cost of sensing," in *Proc. IEEE GLOBECOM*, Dec. 2015, pp. 1–7. (cited on page 25)

[100] W. Liu, X. Zhou, and S. Durrani, "Wireless-powered friendly jammer for physical layer security," in *Proc. IEEE WCSP*, Oct. 2015, pp. 1–5. (cited on page 26)

[101] W. Liu, X. Zhou, S. Durrani, and P. Popovski, "A novel receiver design with joint coherent and non-coherent processing," *IEEE Trans. Commun.*, vol. 65, no. 8, pp. 3479–3493, Aug. 2017. (cited on page 28)

[102] S. Verdú and S. Shamai, "Spectral efficiency of CDMA with random spreading," *IEEE Trans. Inform. Theory*, vol. 45, no. 2, pp. 622–640, 1999. (cited on page 29)

[103] H. Urkowitz, "Energy detection of unknown deterministic signals," *Proc. IEEE*, vol. 55, no. 4, pp. 523–531, Apr. 1967. (cited on pages 29, 112, and 117)

[104] W. Liu, K. Huang, X. Zhou, and S. Durrani, "Time-hopping multiple-access for backscatter interference networks," to appear in Proc. IEEE GLOBECOM 2017, pp. 1–7. (cited on page 30)

[105] P. Lee, Z. A. Eu, M. Han, and H. Tan, "Empirical modeling of a solar-powered energy harvesting wireless sensor node for time-slotted operation," in *Proc. IEEE WCNC*, Mar. 2011, pp. 179–184. (cited on page 32)

[106] C. Wang, K. Sohraby, B. Li, M. Daneshmand, and Y. Hu, "A survey of transport protocols for wireless sensor networks," *IEEE Netw.*, vol. 20, no. 3, pp. 34–40, May 2006. (cited on page 33)

[107] *MICAz*, Crossbow Technology, 2008. [Online]. Available: http://www.openautomation.net/uploadsproductos/micaz-datasheet.pdf (cited on page 43)

[108] F. Zhang and V. Lau, "Closed-form delay-optimal power control for energy harvesting wireless system with finite energy storage," *IEEE Trans. Signal Process*, vol. 62, no. 21, pp. 5706–5715, Nov. 2014. (cited on page 43)

[109] Z. Ding, S. Perlaza, I. Esnaola, and H. V. Poor, "Power allocation strategies in energy harvesting wireless cooperative networks," *IEEE Trans. Wireless Commun.*, vol. 13, no. 2, pp. 846–860, Feb. 2014. (cited on pages 43 and 44)

[110] A. J. Goldsmith, *Wireless Communications*. New York: Cambridge University Press, 2005. (cited on page 43)

[111] J. Yang and S. Ulukus, "Optimal packet scheduling in a multiple access channel with energy harvesting transmitters," *J. Commun. Netw.*, vol. 14, no. 2, pp. 140–150, Apr. 2012. (cited on page 50)

[112] L. Liu, R. Zhang, and K.-C. Chua, "Wireless information transfer with opportunistic energy harvesting," *IEEE Trans. Wireless Commun.*, vol. 12, no. 1, pp. 288–300, Jan. 2013. (cited on page 50)

[113] A. Nasir, X. Zhou, S. Durrani, and R. Kennedy, "Relaying protocols for wireless energy harvesting and information processing," *IEEE Trans. Wireless Commun.*, vol. 12, no. 7, pp. 3622–3636, Jul. 2013. (cited on pages 50 and 74)

[114] X. Zhou and M. McKay, "Secure transmission with artificial noise over fading channels: Achievable rate and optimal power allocation," *IEEE Trans. Veh. Technol.*, vol. 59, no. 8, pp. 3831–3842, Oct. 2010. (cited on pages 51 and 56)

[115] A. D. Wyner, "The wire-tap channel," *Bell Syst. Tech. J.*, vol. 54, no. 8, pp. 1355–1387, Oct. 1975. (cited on page 51)

[116] X. Tang, R. Liu, P. Spasojevic, and H. Poor, "On the throughput of secure hybrid-arq protocols for gaussian block-fading channels," *IEEE Trans. Inform. Theory*, vol. 55, no. 4, pp. 1575–1591, Apr. 2009. (cited on page 52)

[117] X. Zhou, M. McKay, B. Maham, and A. Hjørungnes, "Rethinking the secrecy outage formulation: A secure transmission design perspective," *IEEE Commun. Lett.*, vol. 15, no. 3, pp. 302–304, Mar. 2011. (cited on page 52)

[118] X. Zhang, X. Zhou, and M. McKay, "On the design of artificial-noise-aided secure multi-antenna transmission in slow fading channels," *IEEE Trans. Veh. Technol.*, vol. 62, no. 5, pp. 2170–2181, Jun. 2013. (cited on pages 52 and 57)

[119] R. Corless, G. Gonnet, D. Hare, D. Jeffrey, and D. Knuth, "On the Lambert W function," *Adv. Comput. Math.*, vol. 5, no. 1, pp. 329–359, 1996. (cited on page 62)

[120] U. Baroudi, A. Qureshi, V. Talla, S. Gollakota, S. Mekid, and A. Bouhraoua, "Radio frequency energy harvesting characterization: an experimental study," in *Proc. IEEE TrustCom*, Feb. 2012, pp. 1976–1981. (cited on page 72)

[121] A. Boaventura and N. Carvalho, "Maximizing DC power in energy harvesting circuits using multisine excitation," in *Proc. IEEE MTT-S*, Jun. 2011, pp. 1–4. (cited on page 72)

[122] M. Khoshnevisan and J. Laneman, "Power allocation in wireless systems subject to long-term and short-term power constraints," in *Proc. IEEE ICC*, Jun. 2011, pp. 1–5. (cited on page 73)

[123] M. K. Simon and M. S. Alouini, *Digital Communication over Fading Channels: A Unified Approach to Performance Analysis*. Wiley, 2000. (cited on pages 73, 75, and 77)

[124] S. de la Kethulle de Ryhove and G. Oien, "Rate-optimal power adaptation in average and peak power constrained fading channels," in *Proc. IEEE WCNC*, Mar. 2007, pp. 1773–1778. (cited on page 81)

[125] Y. Wu, Y. Liu, Q. Xue, S. Li, and C. Yu, "Analytical design method of multiway dual-band planar power dividers with arbitrary power division," *IEEE Trans. Microw. Theory Techn.*, vol. 58, no. 12, pp. 3832–3841, Dec. 2010. (cited on page 86)

[126] *DC to 18 GHz Power Splitter*, Agilent Technologies, 2001. [Online]. Available: http://cp.literature.agilent.com/litweb/pdf/5990-5351EN.pdf (cited on page 86)

[127] A. Lapidoth, S. Moser, and M. Wigger, "On the capacity of free-space optical intensity channels," *IEEE Trans. Inform. Theory*, vol. 55, no. 10, pp. 4449–4461, Oct. 2009. (cited on pages 87, 90, and 91)

[128] T. Cover and J. Thomas, *Elements of Information Theory*. Wiley, 2006. (cited on pages 91, 92, 162, and 163)

[129] E. Grushka, "Characterization of exponentially modified Gaussian peaks in chromatography," *Analytical Chemistry*, vol. 44, no. 11, pp. 1733–1738, 1972. (cited on page 91)

[130] D. Tse and P. Viswanath, *Fundamentals of wireless communication*. Cambridge university press, 2005. (cited on pages 95, 96, 100, 101, and 104)

[131] D. Bharadia, E. McMilin, and S. Katti, "Full duplex radios," in *Proc. ACM SIGCOMM*, 2013, pp. 375–386. (cited on page 110)

[132] M. Abramowitz and I. A. Stegun, *Handbook of mathematical functions: with formulas, graphs, and mathematical tables*. Courier Corporation, 1964, vol. 55. (cited on pages 118 and 165)

[133] A. L. Swindlehurst, E. Ayanoglu, P. Heydari, and F. Capolino, "Millimeter-wave massive MIMO: The next wireless revolution?" *IEEE Commun. Mag.*, vol. 52, no. 9, pp. 56–62, Sep. 2014. (cited on page 139)

[134] F. Boccardi, R. W. Heath, A. Lozano, T. L. Marzetta, and P. Popovski, "Five disruptive technology directions for 5G," *IEEE Commun. Mag.*, vol. 52, no. 2, pp. 74–80, Feb. 2014. (cited on page 139)

[135] E. G. Larsson, O. Edfors, F. Tufvesson, and T. L. Marzetta, "Massive MIMO for next generation wireless systems," *IEEE Commun. Mag.*, vol. 52, no. 2, pp. 186–195, Feb. 2014. (cited on page 139)

[136] A. Alkhateeb, J. Mo, N. Gonzalez-Prelcic, and R. W. Heath, "MIMO precoding and combining solutions for millimeter-wave systems," *IEEE Commun. Mag.*, vol. 52, no. 12, pp. 122–131, Dec. 2014. (cited on page 139)

[137] J. G. Andrews, T. Bai, M. N. Kulkarni, A. Alkhateeb, A. K. Gupta, and R. W. Heath, "Modeling and analyzing millimeter wave cellular systems," *IEEE Trans. Commun.*, vol. 65, no. 1, pp. 403–430, Jan. 2017. (cited on page 139)

[138] T. A. Khan, A. Alkhateeb, and R. W. Heath, "Millimeter wave energy harvesting," *IEEE Trans. Wireless Commun.*, vol. 15, no. 9, pp. 6048–6062, Sep. 2016. (cited on page 139)

[139] L. Wang, M. Elkashlan, R. W. Heath, M. D. Renzo, and K. K. Wong, "Millimeter wave power transfer and information transmission," in *in Proc. IEEE GLOBECOM*, Dec. 2015, pp. 1–6. (cited on page 139)

[140] D. W. Matolak and R. Sun, "Unmanned aircraft systems: Air-ground channel characterization for future applications," *IEEE Vehic. Tech. Mag.*, vol. 10, no. 2, pp. 79–85, Jun. 2015. (cited on page 139)

[141] Y. Zeng, R. Zhang, and T. J. Lim, "Wireless communications with unmanned aerial vehicles: Opportunities and challenges," *IEEE Commun. Mag.*, vol. 54, no. 5, pp. 36–42, May 2016. (cited on page 139)

[142] S. Y. R. Hui, W. Zhong, and C. K. Lee, "A critical review of recent progress in mid-range wireless power transfer," *IEEE Trans. Power Electron.*, vol. 29, no. 9, pp. 4500–4511, Sep. 2014. (cited on page 139)

[143] G. Yang, M. R. V. Moghadam, and R. Zhang, "Magnetic MIMO signal processing and optimization for wireless power transfer," *IEEE Trans. Signal Process.*, vol. 65, no. 11, pp. 2860–2874, Jun. 2017. (cited on page 139)

[144] J. D. Griffin and G. D. Durgin, "Gains for RF tags using multiple antennas," *IEEE Trans. Antennas Propag.*, vol. 56, no. 2, pp. 563–570, Feb. 2008. (cited on page 140)

[145] C. He, Z. J. Wang, C. Miao, and V. C. M. Leung, "Block-level unitary query: Enabling orthogonal-like space-time code with query diversity for MIMO backscatter RFID," *IEEE Trans. Wireless Commun.*, vol. 15, no. 3, pp. 1937–1949, Mar. 2016. (cited on page 140)

[146] R. Durrett, *Probability: Theory and Examples*. Cambridge University Press, 2010. (cited on pages 142, 143, 144, 145, and 152)

[147] T. Tao, *An Introduction to Measure Theory*. American Mathematical Soc., 2011. (cited on page 143)

[148] A. Kraskov, H. Stögbauer, and P. Grassberger, "Estimating mutual information," *Physical review E*, vol. 69, no. 6, 2004. (cited on pages 161 and 162)